

The Pennsylvania State University
The Graduate School

NUMERICAL MODELING OF LIGHTNING, BLUE JETS, AND
GIGANTIC JETS

A Dissertation in
Electrical Engineering
by
Jérémy A. RiOUSset

© 2010 Jérémy A. RiOUSset

Submitted in Partial Fulfillment
of the Requirements
for the Degree of

Doctor of Philosophy

August 2010

The dissertation of J  r  my A. Rioussset was reviewed and approved* by the following:

Victor P. Pasko
Professor of Electrical Engineering
Dissertation Advisor, Chair of Committee

John D. Mathews
Professor of Electrical Engineering
Communications and Space Sciences Laboratory Director

Hampton N. Shirer
Associate Professor of Meteorology
Associate Head of Meteorology for Undergraduate Programs

Douglas H. Werner
Professor of Electrical Engineering

W. Kenneth Jenkins
Professor of Electrical Engineering
Head of Department of Electrical Engineering

*Signatures are on file in the Graduate School.

Abstract

Blue jets and gigantic jets are transient luminous events in the middle atmosphere that form when conventional lightning leaders escape upward from thundercloud tops and propagate toward the lower ionosphere. These events are believed to be initiated by ‘classic’ parent lightning discharges, when they escape upward from cloud tops. The present study builds upon a previously introduced lightning model that combines the hypotheses of equipotentiality and overall charge neutrality of the lightning channel with the fractal approach allowing to describe the stochasticity and branching of the discharge [Riousset, 2006]. The lightning model has been validated by comparison of the simulated lightning discharge with lightning mapping observations made by the New Mexico Tech Lightning Mapping Array (LMA) during a thunderstorm on July 31, 1999. This validation allows us to confidently apply the model to investigation of the conditions for the initiation of jet discharges, which represents one of the key goals of the research of this dissertation.

Although the various types of intracloud and cloud-to-ground lightning are reasonably well understood, the cause and nature of upward discharges remains a subject of active research. Based on the idea first expressed by *Petrov and Petrova* [1999] that jets could be the extension of classic lightning discharges initiated within the cloud boundaries, this dissertation demonstrates the fundamental physical similarities between the various kinds of electrical discharges known to occur in the thundercloud. In collaboration with colleagues at New Mexico Tech, a combination of observational and modeling results is reported and indicates two principal ways in which upward discharges can be produced. The modeling indicates that blue jets occur as a result of electrical breakdown between the upper storm charge and screening charge attracted to the cloud top; they are predicted to occur 5–10 s or less after a cloud-to-ground or intracloud discharge produces a sudden charge imbalance in the storm. A new observation is also presented of an upward discharge that supports this basic mechanism. Gigantic jets are indicated

to begin as a normal intracloud discharge between dominant midlevel charge and a screening-depleted upper level charge that continues to propagate out the top of the storm. Observational support for this mechanism comes from similarity with ‘bolt-from-the-blue’ discharges and from data on the polarity of gigantic jets. Upward discharges are analogous to cloud-to-ground lightning and their explanation provides a unifying view of how lightning escapes from a thundercloud.

How charge imbalances form in the thundercloud has been first suggested by *Wilson* [1921], but their impact on the initiation and early stages of development of blue and gigantic jets has not been addressed in the refereed literature. To address this question, a two-dimensional axisymmetric model of charge relaxation in the conducting atmosphere is developed. It is used in conjunction with the lightning model to demonstrate how realistic cloud electrodynamics leads to the development of blue and gigantic jets. This model accounts for the time-dependent conduction currents and screening charges formed under the influence of the thundercloud charge sources. Particular attention is given to numerical modeling of the screening charges near the cloud boundaries. The results demonstrate the important role of the screening charges in local enhancement of the electric field and/or reduction of net charge in the upper levels of the thundercloud. This model shows that the accumulation of screening charges near the thundercloud top produces a charge configuration leading to the initiation of blue jets, and the effective mixing of these charges with the upper thundercloud charge may lead to the formation of gigantic jets.

The visual appearance of the observed jet discharges indicates that these events may be associated with significant heating of the air in the regions of atmosphere near cloud tops through which they propagate. Many of the small-scale features observed in jets can be interpreted in terms of streamers, which are needle-shaped filaments of ionization embedded in originally cold (~ 300 K) air. After appropriate scaling with air density, these features are fully analogous to those that initiate spark discharges in relatively short (several cm) gaps at near-ground pressure. Thus, we develop a model of the streamer-to-spark transition to study this transition from cold, weakly ionized plasma to thermalized spark at various altitudes (or equivalently, ambient air densities) in the Earth atmosphere. The model is a fully one-dimensional (1-D) axisymmetric, axially invariant thermodynamics model coupled to a zero-dimensional (0-D) chemical kinetics scheme. In this dissertation, the model is applied to study the scaling properties of air heating in streamer channels under conditions of constant electric field. The model results on characteristic heating times τ_{br} appear to be in excellent agreement with the available laboratory measurements conducted in short discharge gaps at ground and near-ground pressures. The results demonstrate a significant acceleration of the heating at lower air densities, with effective heating times appearing to scale closer to $1/N$ than

to $1/N^2$ predicted on the basis of simple similarity laws for Joule heating, where N is the ambient air density. This acceleration is attributed to strong reduction in electron losses owing to three-body attachment and electron-ion recombination with reduction of air pressure. The results also indicate that at low ambient air densities, the channel conductivity and the air temperature increase very rapidly in comparison with the gas dynamic expansion time (i.e., $\tau_{br} \leq r_s/c_s$, where r_s is the streamer channel radius and c_s is speed of sound). Thus both constant-density and constant-pressure approximations to channel dynamics commonly used in previous studies at ground pressure lead to nearly identical streamer-to-spark transition times.

Table of Contents

List of Figures	ix
List of Tables	xix
List of Symbols	xx
Acknowledgments	xxiv
Chapter 1	
Introduction	1
1.1 Thundercloud, Lightning, Jets, and Streamer-to-Leader Transition	1
1.1.1 Tripolar Structure of the Thundercloud	1
1.1.2 Plasma Nature of Lightning, Blue Jets, and Gigantic Jets .	8
1.2 Problem Formulation	19
1.3 Organization of the Dissertation	19
1.4 Scientific Contributions	21
Chapter 2	
Three-Dimensional Fractal Model of a Lightning Discharge	23
2.1 Lightning Models in the Refereed Literature	23
2.2 Formulation of the Fractal Model	29
2.3 Summary of Results	37
Chapter 3	
Modeling of an Intracloud Discharge in a New Mexico Thunderstorm and Comparison with LMA Observations	38
3.1 Results of Modeling of an Intracloud Discharge	38
3.2 Discussion	45

3.3	Summary of Results	55
Chapter 4		
	Unified Theory of Lightning and Jet Discharges: Role of the Charge Imbalance	56
4.1	Observations of Blue and Gigantic Jets	56
4.2	Lightning and Jets: New Observations and Unified Charge Imbalance Theory	57
4.3	Summary of Results	67
Chapter 5		
	Two-Dimensional Model for Studies of the Thundercloud Screening Charges in the Conducting Atmosphere	69
5.1	Fundamental Principles of Maxwellian Charge Relaxation	70
5.2	Formulation of the Charge Relaxation Model	76
5.3	Summary of Results	84
Chapter 6		
	Self-Consistent Modeling of Thundercloud Screening Charges: Implications for Blue and Gigantic Jets	85
6.1	Results of Modeling of Storm Dynamics and Jet Initiations	86
6.2	Discussion	92
6.3	Summary of Results	98
Chapter 7		
	Model of Air Heating in Streamer Discharges Under Constant Applied Electric Field	99
7.1	Physics and Modeling of the Streamer-to-Spark Transition	100
7.2	Formulation of the Model of Streamer-to-Spark Transition	109
7.3	Summary of Results	120
Chapter 8		
	Investigation of Timescales of Air Heating in Streamer Discharges at Different Altitudes in the Earth Atmosphere	121
8.1	Results of Modeling of the Streamer-to-Spark Transition	122
8.2	Discussion	133
8.2.1	Comparison with experimental data, and approximations of constant pressure and gas density	133
8.2.2	Role of $N_2(B^3\Pi_g)$ and $N_2(C^3\Pi_u)$ excited species	135
8.2.3	Role of atomic oxygen in detachment collisions	135

8.2.4	Role of ambient NO, O ₃ , O, and CO ₂	136
8.2.5	Effects of positive ion chemistry	137
8.2.6	Role of associative ionization reactions	138
8.2.7	Scaling of heating time with air density, and thermal con- duction and diffusion losses	139
8.3	Summary of Results	140
Chapter 9		
	Conclusions	142
9.1	Summary of Results	142
9.1.1	Fractal Modeling of an Intracloud Discharge	142
9.1.2	Unified Theory of Lightning and Jet Discharges	143
9.1.3	Self-Consistent Modeling of Thundercloud Screening Charges: Implications for Blue and Gigantic Jets	143
9.1.4	Investigations of the Timescales of Air Heating in Streamer Discharges at Different Altitudes in the Earth Atmosphere	144
9.2	Suggestions for Future Research	145
9.2.1	Modeling of the Dynamics of the Thunderstorm	145
9.2.2	Modeling of the Streamer-to-Spark Transition	146
Appendix A		
	Flowchart Representations of the Numerical Models	147
Appendix B		
	Supplementary Information for the Unified Theory of Lightning and Jet Discharges	151
B.1	Lightning mapping and radar observations	151
B.2	Electrodynamic Model	152
B.3	Jets in Normal and Inverted-Polarity Thunderclouds	152
Appendix C		
	Supplementary Information for the Maxwellian Charge Relax- ation Model	155
C.1	Necessity of Charge Compensation in a Conducting Medium	155
C.2	Performance of the Charge Relaxation Model: Comparison with the Results of <i>Holzer and Saxon</i> [1952]	157
References		163

List of Figures

1.1	Example of cloud structure [<i>Marshall et al.</i> , 2005, Figure 1]. Lightning inferred storm charge structure for a 6-min time interval of LMA data collected during the descent of the sounding balloon. Yellow/red regions indicate positive charge; the blue region indicates negative charge. The letters A–D show the initiation points of the cloud-to-ground (CG) flashes and number 3 and 5 show the initiation points of intracloud (IC) flashes that occurred in the part of the storm observed by the balloon. The occurrence times of the flashes are shown in the upper panels, and the red part of the balloon trajectory corresponds to the time interval of the lightning data.	3
1.2	(a) Inferred cloud structure from Figure 1.1c with charging currents from [<i>Krehbiel et al.</i> , 2004]. (b) Equivalent representation using the tripole model with the parameters shown in Table 1.1 and used in Chapter 3. The main positive and lower positive layers are colored in red, and the main negative charge is colored in blue. The solid red line represents the ambient potential, the solid blue line the ambient electric field, and the dot-dashed green line the electric field threshold for initiation of lightning.	4

1.3	Conceptual model of the charge structure of an MCS [<i>Stolzenburg et al.</i> , 1998a; <i>Rakov and Uman</i> , 2003, p. 93]. Positive charge layers are indicated by the light red shading and negative layers are indicated by the light blue shading. The solid lines are radar reflectivity contours. In the convective region and the transition zone, the thick solid arrows depict convective updrafts and downdrafts, and the thin solid arrows show divergent outflows. The smaller open arrows represent system-relative flows, which are mainly horizontal. The mesoscale updraft and downdraft in the stratiform region are depicted by large open arrows (black and white outlines, respectively). There are four horizontally extensive cloud charge layers in the part of the stratiform precipitation region farthest behind the convective region, the fifth (lowermost) charge layer being seen in the stratiform region entirely below the cloud. An additional (negative) charge layer extends from the convective region through the nearest part of the stratiform region above all the other layers [<i>Stolzenburg et al.</i> , 1998a; <i>Rakov and Uman</i> , 2003, p. 93].	6
1.4	Schematic of the basic charge structure in the convective region of a thunderstorm [<i>Stolzenburg et al.</i> , 1998a; <i>Rakov and Uman</i> , 2003, p. 83]. Four charge layers are represented in the updraft region, and six charge layers are represented outside the updraft region (to the left of the updraft diagram). The charge structure shown in this figure is applicable to the convective elements of Mesoscale Convective Systems (MCS), isolated supercell storms, and New Mexican air-mass storms. Note that there is a variability about this basic structure, especially outside the updraft [<i>Stolzenburg et al.</i> , 1998a; <i>Rakov and Uman</i> , 2003, p. 83].	8
1.5	Sketch of the leader/leader-corona system, with the main characteristics of the different discharge regions [<i>Comtois et al.</i> , 2003]. . .	10
1.6	Positive (or cathode directed) streamer. (a) Streamer at two consecutive moments of time, with secondary avalanches moving towards the positive head of the streamer, and wavy arrows showing photons that generate seed (i.e., initial) electrons for avalanches. (b) Lines of force of the field near the streamer head. Adapted from [<i>Raizer</i> , 1991, p. 335; <i>Bazelyan and Raizer</i> , 2000, p. 33].	12

1.7	Negative (or anode directed) streamer. (a) Streamer at two consecutive moments of time, with secondary avalanches moving away from the negative head of the streamer (bubble shapes), and wavy arrows showing photons that generate seed (i.e., initial) electrons for avalanches. (b) Field in the vicinity of the head. Adapted from [Raizer, 1991, p. 338].	13
1.8	Development of a positive leader. Panels (a), (b), (c), (d), (e) and (f) represent different stages of the development; 1, leader tip; 2, leader channel; 3, streamer zone. See text for details.	15
1.9	Development of a negative leader. Panels (a), (b), (c), (d), (e), (f), (g), (h) and (i) represent different stages of the development. 1, leader tip; 2, primary leader channel; 3, negative streamers in the streamer zone; 4, space stem or plasma spot; 5, negative streamers of the streamer zone associated with the negative space leader; 6, space leader developing from the plasma spot; 7, positive streamers of the streamer zone associated with the positive space leader; 8, negative end of the space leader; 9, positive end of the space leader; 10, leader step; 11, burst of negative streamers. See text for details. Note that the streamer zones are not reproduced in panels (f) and (g) for the sake of clarity.	17
2.1	A cross-sectional view in the y - z plane at $x=6$ km of the model thundercloud with upper positive (P), central negative (N) and lower positive (LP) charge layers. Electric field lines produced by the model cloud are also shown for reference.	30
2.2	Channel extension in a 2-D geometry. (a) Channel links (solid lines) and link candidates (dashed lines); (b) Probability associated with each link. (The values of the probabilities given on this plot are arbitrary and are shown only for two representative points on the existing discharge tree for the purposes of illustration. Actual values are derived based on the analysis of potential differences involving all grid points of the existing discharge tree—see text for details.) .	34
3.1	Electric field line pattern of the thundercloud with parameters specified in Table 3.1 in a simulation domain with (a) equipotential boundaries; (b) open boundaries. (c) Comparison of the electric field magnitudes using equipotential (dashed line) and open boundary conditions (solid line) at an altitude of 9.8 km.	40

3.2	Representation in Lightning Mapping Array (LMA) data form of a simulated intracloud discharge. We use the same formatting as for the LMA data shown in Figure 3.3. In panel (c), the total number of grid points crossed by the discharge (497) corresponds to the sum of the number of grid points crossed by the upper branches (299) and lower branches (199) minus one because, the initiation point is counted twice, being part of both the upper and lower branches. Adapted from [Riousset <i>et al.</i> , 2007a, Figures 4, 6, and 7].	41
3.3	An actual bilevel intracloud flash measured by the LMA during the thunderstorm on July 31, 1999 at 22:23 (local time).	43
3.4	(a) 3-D view of the intracloud discharge shown in Figure 3.2 after 496 steps; (b) Electric field before the flash (solid line), and after (dashed line) along the central vertical axis of the simulation domain. The electric field initiation threshold is shown for reference by dash-dotted lines; (c) Electric potential before (solid line), and after (dashed line) the discharge development along the same axis.	44
3.5	Parameters of the simulated discharge shown in Figure 3.2 at each step of the development: (a) Channel potential ϕ_0 ; (b) Charge carried by the positive leaders Q_{cha}^+ ; (c) Magnitude of the discharge electric dipole moment $p = \vec{p} $; (d) x -, y - and z - components of the dipole moment \vec{p}	45
4.1	Basic scenario leading to blue jet formation. (a) Lightning-inferred charge structure [Marshall <i>et al.</i> , 2005] and model-estimated charging currents in a normally electrified storm over Langmuir Laboratory on July 31, 1999, including the expected screening charge at the upper cloud boundary (dashed line). (b,c) Vertical electric field (E_z) and potential (V) profiles before and after a negative cloud-to-ground discharge, showing how the discharge increases V and E_z in the upper part of the storm, and the assumed breakdown threshold vs. altitude. (d,e,f) Simulated and predicted occurrence of an upward discharge 6 s after the negative cloud-to-ground discharge. Here \times 's denote E_z and V where each discharge is initiated. The net charge content of each layer in C is indicated next to the charge region in panel (d) [Krehbiel <i>et al.</i> , 2008].	58

4.2	Upward negative jet from an inverted polarity storm on June 12 UTC during STEPS 2000. (a-d) VHF mapping observations of the jet (bold black sources) and preceding intracloud discharge, projected onto the closest vertical radar scan through the storm (panel a; line in plan projection, panel b). The jet developed ~2 km above the echo top, beginning immediately above where the intracloud discharge locally removed positive charge from the lower storm level (b). Plan radar scans show that the radar top was essentially constant at ~11.5 km altitude above the flash and in the vicinity of the jet. (e) Numerical simulation of the jet discharge. The net charge content of each layer in C is indicated next to the charge region. Red regions correspond to the positive charge centers, and blue regions represent the negative charge center. [<i>Krehbiel et al.</i> , 2008].	60
4.3	Two ‘bolt-from-the-blue’ (BFB) discharges. (a) Lightning mapping observations of a negative bolt-from-the-blue discharge, superimposed on a vertical radar scan through the storm. The lightning began as an upward intracloud discharge between midlevel negative charge (red sources) and upper positive charge (blue sources), then exited the cloud and went to ground as a negative leader, well away from the storm. ‘ Δ ’ denotes the negative cloud-to-ground strike point. (b) A cloud-enshrouded bolt-from-the-blue lightning that started to develop upward above the storm top before branching horizontally back into the upper part of the storm and turning downward to ground, causing a negative cloud-to-ground discharge on the lower right. The photograph of was taken with a 38 s time exposure from Langmuir laboratory at 3230 m altitude, 30 km distance from the storm, using an IR-modified 6-megapixel Canon 300D digital SLR fitted with a Nikon 35 mm/2.0 lens set at f/5.6. ISO-setting was 100, without noise reduction [<i>Krehbiel et al.</i> , 2008].	63
4.4	Simulated discharges illustrating the different known and postulated lightning types in a normally electrified storm (panels a–f). Blue and red contours and numbers indicate negative and positive charge regions and charge amounts (in C), respectively, each assumed to have a Gaussian spatial distribution. A partially analogous set of discharges occurs or would be predicted to occur in storms having inverted electrical structures (Figure B.1) [<i>Krehbiel et al.</i> , 2008].	65

- 5.1 Charge dissipation in a conductive medium as a function of the altitude. (a) Geometry of the illustrative example. (b) Cross-sectional view of the charge density distribution at $t \sim 15.8$ s. The positive charge (+) has almost disappeared and the negative charge (−) has only slightly dissipated. Letters A–E indicate the loci of observation of the evolution of the electric field and charge density in panels (c) and (d), respectively. In panel (d), B_{th} and D_{th} indicate the analytically calculated approximations of the evolutions of the charge densities at points B and D. The total charge Q in the simulation domain is represented using a solid purple line with corresponding scale shown on the right vertical axis. (See Supplementary Video 1 in [Riousset *et al.*, 2010a] for the animated version of panel (b) plot.) 72
- 5.2 Formation of the screening charge at the boundary of a cylindrically symmetric thundercloud with reduced conductivity. (a) Geometry of the illustrative example. (b) Cross-sectional view of the charge density distribution at $t \sim 2.15$ s. The screening charge develops much faster on the upper boundary of the cylinder than on the lower one due to the exponential increase of conductivity with altitude z . Points A–I indicate the locations where the temporal evolution of the electric field and charge density are shown in panels (c) and (d), respectively. The total charge in the simulation domain Q is represented using a solid purple line with corresponding scale shown on the right vertical axis. (See Supplementary Videos 2a and 2b in [Riousset *et al.*, 2010a] for the animated version of panel (b) plot.) 73
- 5.3 Geometry and conductivity distribution inside and nearby the model cloud employed for the simulation of (a) blue jets and (b) gigantic jets. Dashed green lines represent the electric field threshold E_{th}^{\pm} for lightning initiation. The solid blue lines represent the electric field at $r=0$ prior to the development of the jets. The solid rectangles marked LP, N and P depict the altitude and dimensions of the lower positive, central negative and upper positive thundercloud charge regions, respectively (Tables 5.1 and 5.2). The vertical arrows indicate the charging currents I_1 and I_2 77

6.1	Model-calculated temporal variations of the storm charges leading to initiation of: (a) a blue jet discharge between the upper positive layer and the screening charge layer at $t=299.4$ s; (b) gigantic jet discharges between the central negative layer and upper positive charge layer reduced by the screening charge. The first gigantic jet occurs at $t\sim 46$ s. Sudden vertical jumps in the curves correspond to occurrence of intracloud discharges unless marked otherwise. Asterisks indicate that the gigantic jets could instead be bolt-from-the-blue discharges.	87
6.2	Total charge density (a), and electric field magnitude (b) at the moment of the blue jet initiation $t\sim 299.4$ s (see Figure 6.1a). At this instant, the electric field exceeds the lightning initiation threshold near the cloud upper boundary leading to an upward positive discharge (marked as +BJ in Figure 6.1a). (c) Modeling of the jet discharge using the 3-D fractal model, with charge densities as background. (See Supplementary Video 3 in [Riousset <i>et al.</i> , 2010a] for the animated version of panels (a) and (b).)	88
6.3	Same as Figure 6.2, except for the gigantic jet discharge at $t\sim 46$ s in Figure 6.1b, initiates between the central negative and screening depleted upper positive charge regions. (See Supplementary Video 4 in [Riousset <i>et al.</i> , 2010a] for the animated version of panels (a) and (b).)	89
7.1	(a) A black and white image of a 2-min time exposure of a blue jet [Wescott <i>et al.</i> , 2001]. The image is provided through the courtesy of G. Wescott, University of Alaska. (b) Processed image obtained by averaging of sequence of video fields from observations reported in [Pasko <i>et al.</i> , 2002, http://pasko.ee.psu.edu/Nature/]. Reprinted from [Pasko and George, 2002] with permission from American Geophysical Union.	102
7.2	Fractions of Joule energy spent in fast heating η_T (solid line), and vibrational excitation of N_2 molecules η_V (dashed line) as a function of the applied reduced field E/N in Td. The results are based on BOLSIG+ software calculations [Hagelaar and Pitchford, 2005].	113

7.3	Algorithm for the 1-D axisymmetric, axially invariant model of streamer-to-spark transition. The time notation t represents the timeline for the gas dynamics model, and t' denotes that of the kinetics scheme. If ρ , \bar{v} , ε , ε_v are known at $t(n)$ (step (a)), then the model calculates the values of N , T_g , and ε_v at step (b) and uses them as input values for the kinetics scheme to derive the densities of each species α in the interval $[t'(0), t'(n')]$ (step (c)). Then the model calculates the electronic and ionic conductivities of the plasma σ_e^0 and σ_i^0 and density of atomic oxygen on the axis ($r=0$) at $t(n+1/2)$ by averaging the values of σ_e^0 , σ_i^0 and n_O calculated at $t=t'(0)$ and $t=t'(n')$ (step (d)). Afterward, the terms corresponding to the electronic and ionic Joule energy deposition per unit volume Q_e and Q_i and energy transfer from the vibrational energy levels of nitrogen to translational energy Q_{VT} per unit volume are calculated at every point r of the simulation domain at $t=t(n+1/2)$ (step (e)). Finally the values of ρ , \bar{v} , ε , ε_v are calculated at $t(n+1)$ using the quantities obtained from steps (a) and (e) (step (f)/(a)). The process is repeated until T_g reaches a breakdown value $T_{br}=5000$ K.	115
8.1	(a) Experimental and model streamer-to-spark transition times for various applied voltages. The solid lines represent the transition times under normal pressure ($p = 10^5$ Pa) and reduced pressure ($p=0.75 \times 10^5$ Pa). The broken line shows the breakdown time of a Joule heated channel with constant neutral gas density corresponding to $p=10^5$ Pa and assuming a constant plasma conductivity in the channel. The symbols '◻' show the experimental results obtained by Černák <i>et al.</i> [1995], and '◊' and '●' show the results obtained by Larsson [1998]. The data obtained reduced density are shown with full circle '●', while data taken at atmospheric pressure are shown with open circles '◊'. (b) Same model and experimental data as in panel (a) but using reduced values of the applied field (EN_0/N) and of the transition times ($\tau_{br}N/N_0$).	123
8.2	Comparison of 0-D models under constant pressure p , constant density N , and 1-D model of Chapter 7 at different altitudes and for two different kinetic schemes: including O_2^+ only at $z=0$ km (a) and $z=70$ km (c); and including O_2^+ , O_4^+ , and $O_2^+N_2$ at $z=0$ km (b) and $z=70$ km (d).	124

8.3	Time dynamics of the streamer-to-spark transition at altitude 0 km and $EN_0/N=19$ kV/cm. (a) Changes in the reduced neutral gas density N/N_0 at the axis of the channel; (b) Variations of the reduced pressure p/p_0 at the axis of the channel, where p_0 is the ambient pressure at the altitude considered; (c) evolution of the neutral gas temperature T_g (solid line) and vibrational temperature T_v of N_2 at the axis of the channel (dashed lined); (d) Electric current flowing along the channel and defined as $I=\pi r_s^2 (\sigma_e^0 + \sigma_i^0) E^2$	126
8.4	Time dynamics of the streamer-to-spark transition at altitude 0 km and $EN_0/N=19$ kV/cm (cont. from Figure 8.3). (a), (b) densities of charged species (e , O^- , O_2^- , O_3^- , O_2^+ , O_4^+ , and $O_2^+N_2$), and densities of neutral species (O , N , NO , $O_2(a^1\Delta_g)$, $N_2(A^3\Sigma_u^+)$, and $N_2(a'^1\Sigma_u^-)$) at the axis of the discharge, respectively. (c) Contributions from the fast heating ($\eta_T Q_e = \eta_T \sigma_e^0 E^2$), ionic Joule heating ($Q_i = \sigma_i^0 E^2$), and vibrational-translational relaxation energy transfer (Q_{VT}) (in $eV m^{-3} s^{-1}$) appearing on the right hand side of the equation for translational energy (7.5). (d) Rates of generation and loss of electrons as a function of time.	127
8.5	Time dynamics of the streamer-to-spark transition at altitude 70 km and $EN_0/N=19$ kV/cm. (a)–(d) Same as in Figure 8.3.	128
8.6	Time dynamics of the streamer-to-spark transition at altitude 70 km and $EN_0/N=19$ kV/cm (cont. from Figure 8.5). (a)–(d) Same as in Figure 8.4.	129
8.7	Contributions of all reactions of detachment (R13–R22 in Table 7.2) to the total detachment rate F_d throughout the duration of the streamer-to-spark transition at 0 km (a), and 70 km (b).	130
8.8	Distribution of the reduced gas density on the radial coordinate (a) at 0 km at $t=0, 0.3, 0.6$, and $0.9 \mu s$, and (b) at 70 km at $t=10, 20, 30$, and 40 ms.	131
8.9	Scaling of the breakdown times as a function of the neutral density for various applied electric fields and altitudes (0, 30, 50, and 70 km). (a) $\tau_{br} \propto 1/N^1$: the scaling is the same as that of the vibrational-translational relaxation timescale. (b) $\tau_{br} \propto 1/N^2$: the scaling is the same as that of the Joule heating timescale, assuming constant air density N and time independent conductivity of the channel.	132
A.1	Algorithm for development of the discharge trees [<i>Riousset et al.</i> , 2007a, and Chapter 2 of this document](based on hypotheses by <i>Kasemir</i> [1960] and <i>Niemeyer et al.</i> [1984]).	148

A.2	Flowchart of the model of Maxwellian relaxation of the atmosphere. The charge reduction is based on [Krehbiel <i>et al.</i> , 2004, 2008].	149
A.3	Flowchart of the model of streamer-to-spark transition.	150
B.1	Illustrative lightning simulations for normal- and inverted-polarity storms, showing the four possible types of upward discharges, classified by initiation mechanism (blue jet and gigantic jet) and upward polarity (+ and -). Blue and red contours and numbers indicate negative and positive charge regions and charge amounts (in C), respectively, each assumed to have a Gaussian spatial distribution. Also shown for reference are the common forms of IC and CG flashes in normal and inverted storms. Blue jets will tend to be initiated by a precursor discharge (either CG or IC) that causes a charge imbalance in the storm [Krehbiel <i>et al.</i> , 2008, Supplementary Information].	154
C.1	A spherical charge Q of radius a placed in the center of a sphere of conductivity σ' and radius b embedded in a medium of conductivity σ	158
C.2	Comparison of numerical and analytical solutions to the problem of Figure C.1 at $t=2.5 \times 10^4$ s. (a) Total charge density $\rho_t = \rho_s + \rho_f$. (b) Amplitude of the electric field $E = \sqrt{E_r^2 + E_z^2}$, where E_r and E_z are the horizontal and vertical component of the electric field. (c) Source and free induced charge densities (ρ_s and ρ_f , respectively) at $r=0$ km. (d) Numerical (solid line) and analytical (broken line) solutions for the amplitude of the vertical component of the electric field E_z at $r=0$ km.	161

List of Tables

1.1	Charge heights and extents for the cylindrical disk model used in [Riousset <i>et al.</i> , 2007a] and reproduced in Chapter 2, and charge amounts required to initiate the intracloud discharge discussed in Chapter 3.	2
1.2	Electric field thresholds at ground pressure [Pasko, 2006, and references therein].	9
1.3	Streamer characteristics at ground level [Gallimberti <i>et al.</i> , 2002; Pasko, 2006].	11
1.4	Leader characteristics at ground level [Helsdon <i>et al.</i> , 1992; Gallimberti <i>et al.</i> , 2002; Mansell <i>et al.</i> , 2002; Comtois <i>et al.</i> , 2003].	14
3.1	Charge values, heights and extents for the cylindrical disk model. .	39
5.1	Parameters used in the simulations.	78
5.2	Geometrical and electrical parameters of the model thundercloud. .	79
7.1	Model parameters	111
7.2	Reaction list	116

List of Symbols

Symbols introduced in Chapters 2, 3, and 4

$\delta x, \delta y, \delta z$	Discretization steps in x -, y -, and z -directions (m)
ε_0	Permittivity of free space ($\varepsilon_0=8.85 \times 10^{-12}$) (F/m)
η	Probability sensitivity (dimensionless)
ϕ	Total electric potential ($\phi = \phi_{\text{amb}} + \phi_{\text{cha}}$, see below) (V)
ϕ_0	Total electric potential of the channel(V)
ϕ_{amb}	Ambient electric potential due to cloud charges (V)
ϕ_{cha}	Electric potential due to polarization charges on the channel (V)
ϕ_{gnd}	Total electric potential of the ground boundary (V)
ρ_{amb}	Thundercloud charge density (C/m ³)
$\rho_{\text{amb}}^{\text{i}}$	Ground image of the thundercloud charge density (C/m ³)
ρ_{cha}	Polarization charge density in the channel (C/m ³)
$\rho_{\text{cha}}^{\text{i}}$	Ground image of the polarization charge density in the channel (C/m ³)
$\rho_{\text{cha}}^{\text{l}}$	Average linear charge density of the discharge tree (C/m)
$d_{\text{LP}}, d_{\text{N}}, d_{\text{P}}$	Depths of the lower positive, central negative and upper positive charge layers (m)
\vec{E}	Total electric field ($\vec{E} = \vec{E}_{\text{amb}} + \vec{E}_{\text{cha}}$, see below) (V/m)
\vec{E}_{amb}	Ambient electric field due to cloud charges (V/m)

\vec{E}_{cha}	Electric field due to polarization charges on the channel (V/m)
E_{init}	Electric field threshold for discharge initiation (V/m)
E_{cr}^+	Electric field threshold for propagation of positive streamers (V/m)
E_{cr}^-	Electric field threshold for propagation of negative streamers (V/m)
E_{k}	Electric field conventional breakdown threshold (V/m)
E_{th}^+	Electric field threshold for propagation of positive leaders (V/m)
E_{th}^-	Electric field threshold for propagation of negative leaders (V/m)
I_1, I_2	Upper and lower charging currents (A)
l	Length of a link (m)
L	Total length of the discharge (m)
L_x, L_y, L_z	Dimensions of the simulation domain in the x -, y -, and z -directions (m)
N	Neutral density (m^{-3})
N_0	Neutral density at sea level (m^{-3})
N_x, N_y, N_z	Number of discretization points of the simulation domain in the x -, y -, and z -directions (dimensionless)
\vec{p}	Electric dipole moment of the discharge (C·m)
p_i	Probability of propagation for a candidate link i ($p_i \in [0, 1]$)
Q_{cha}^+	Net charge carried by the positive leaders (i.e., charge transfer) (C)
$Q_{\text{LP}}, Q_{\text{N}}, Q_{\text{P}}$	Net charges in the lower positive, central negative and upper positive charge layers (C)
$R_{\text{LP}}, R_{\text{N}}, R_{\text{P}}$	Radii of the lower positive, central negative and upper positive charge layers (m)
z_{gnd}	Altitude of the ground level (m)

Additional symbols introduced in Chapter 5 and 6

α	Thickness of the cloud boundary (m)
ρ_s	Source charge density brought by the charging currents (C/m ³)
ρ_f	Induced free charge density (C/m ³)
σ	Electrical conductivity of the thundercloud (S/m)
δr	Discretization step in the radial direction (m)
I_{SC}	Screening current flowing from the thundercloud top into the ionosphere (A)
L_r	Radial dimension of the simulation domain (m)
N_r	Number of discretization points of the simulation domain in the radial direction (dimensionless)
Q_{SC}	Screening charge accumulating around the thundercloud upper boundary (C)
Q_{mix}	Free induced screening charge mixed with the upper positive layer (C)
r_c	Radius of the thundercloud (m)
z_c	Height of the thundercloud (m)

Additional symbols introduced in Chapter 7 and 8

δt	Discretization step in time (s)
η_β^α	Fraction of the rates of energy losses for a given species α in the process β over the sum of the loss rates in all the processes (dimensionless)
η_T, η_V	Fast heating and fraction of the Joule heating transferred to the vibrational energy levels of the nitrogen molecules (dimensionless)
$\varepsilon, \varepsilon_v, \varepsilon_{v,eq}(T_g)$	Energy density, vibrational energy density of N ₂ , and equilibrium value of ε_v at the temperature $T_v=T_g$ (eV)
γ	Adiabatic index or ratio of specific heats (dimensionless)

ρ	Mass density of the plasma (kg/m ³)
σ_e, σ_i	Electronic and ionic conductivity (S/m)
τ_{VT}, τ_{VTO}	Timescales of the vibrational–translational (VT) relaxation of N ₂ (v) on air molecules (N ₂ and O ₂) and atomic oxygen (O) (s)
ΔE_v	Quantum of vibrational energy (eV)
c_s	Velocity of sound (m/s)
E	Applied electric field between the electrodes (V/m)
k_B	Boltzmann constant (J/K)
m_g	Average mass of a molecules of air (kg)
N_α	Number density of the species α (m ⁻³)
N ₂ (X ^{2S+1} Λ_Ω^\pm)	Electronic levels of nitrogen, in this dissertation: N ₂ (X ^{2S+1} Λ_Ω^\pm)=N ₂ (A ³ Σ_u^+), N ₂ (B ³ Π_g), N ₂ (C ³ Π_u), and N ₂ (a' ¹ Σ_u^-) [e.g., <i>Gilmore</i> , 1965]
O ₂ (a ¹ Δ_g)	Electronic level of oxygen [<i>Lieberman and Lichtenberg</i> , 2005, p. 242]
p	Neutral gas pressure (Pa)
Q_e, Q_i	Electronic and ionic Joule energies per unit volume, per unit time (J m ⁻³ s ⁻¹)
Q_{VT}	Rate of energy transfer from the vibrational energy levels of nitrogen to the translational energy of the gas (J m ⁻³ s ⁻¹)
q_β^α	Rate of energy loss coefficient for the species α in the process β
r_s	Streamer radius (m)
t, t'	Timelines of the gas dynamics and kinetics processes (s)
U	Applied voltage between the electrodes (V)
U_c	Voltage drop at the cathode (V)
T_g, T_v	Neutral gas temperature and vibrational temperature of N ₂ (K)
T_{br}	Temperature of spark breakdown (K)
\vec{v}	Radial velocity of the neutral particles in the plasma (m/s)
x_{N_2}, x_{O_2}, x_{Ar}	Fraction of N ₂ , O ₂ , and Ar in air (dimensionless)

Acknowledgments

A couple of years ago, when the organization of this dissertation was starting to shape up in my mind, I never realized that the acknowledgement section would be the last one I would write, and I would have never believed that it would be the most difficult to write. This Ph.D. represents six years of my life, and so many people participated in it, one way or another, and I would feel so ungrateful to forget any of them.

So when it comes to thanks, I must express first and foremost my deepest gratitude to my advisor Professor Victor P. Pasko, who introduced me to the physics of electrical discharges and phenomenology of transient luminous events. His yearning for excellence pushed me to always perform at my best, and his guidance and confidence are no stranger to the recognition of my work by the atmospheric science community.

I also have to acknowledge my coworkers, in particular Professor Paul R. Krehbiel, whose exceptional analytical skills and suggestions led to the piece of work I am most proud of to date. I would like to extend thanks also to Professors William Rison, Ronald J. Thomas, and the whole group I had the chance to work with at New Mexico Tech for our very constructive and worthwhile collaboration.

During these six years as a Master's and then a Ph.D. student, I was given the opportunity to meet more outstanding scientists than I could possibly fit in these pages, but I would like to particularly recognize two of them: Professor Davis D. Sentman, whose passion for and pioneering work on blue jets remains to this day a source of inspiration, and Professor Anne Bourdon, whose help inside and outside the academic microcosm was no less than invaluable. I remain truly impressed by these scientists, whose sagacity is rivaled only by their modesty, simplicity and availability.

I feel equally indebted to the members of my doctoral committee for their insightful directions and contributions. I am particularly grateful to Professor Hampton N. Shirer for his communicative enthusiasm and his teaching on the Norwegian cyclone model and surface maps as they provided me with a better

understanding of the meteorological aspects involved in the development of lightning, blue jets, and gigantic jets. But my approach to the problems discussed in this dissertation would have been incomplete without the suggestions of Professors Douglas H. Werner, and John D. Mathews. Professor Werner offered an expertise on fractal modeling, which encouraged me to look deeper in the capabilities of such models, while Professor Mathews' conceptual thinking forced me to break down the complex questions involved in my research into elementary problems and to analyze my results with the most fundamental principles of physics. I also have a particular a sense of gratitude for Professor Timothy J. Kane for his class on remote sensing, which will remain in my memory one of my most enjoyable at Penn State, and for helping me throughout my Ph.D., particularly during the past year.

But the Ph.D. program was more than a professional experience for me; it was a personal journey, which I could have never walked alone. I feel that some people have shared it all along and that I would be very ungrateful to forget them. First of all, I remember my parents, who have always been there and will always be there. Without them, I am not sure where I would be at the moment, and I feel that this dissertation is theirs at least as much as it is mine. I also dedicate this dissertation to my brother Nicolas and my sister Pauline. Both of them so tremendously contributed to this work by their constant support and encouragement. I would like to address them directly here. Pauline, through your ever-positive attitude in times of success as well as in time of frustration and disappointment, you made this accomplishment possible. Should you decide to start a Ph.D. too, there is no question in mind that you will perform spectacularly. Nicolas, thank you for reminding me how attached I was to this doctoral program, when I almost forgot. Your words undoubtedly helped to keep me on track. So did this quote from you Sonia: *"Faut que tu kiffes ton Ph.D.!"* ("You gotta love your Ph.D.!"), as it reminded me that research is not all about the results. One must also enjoy the process, so I would like to thank you too.

I should also give many thanks to the people with whom I shared my days (and some nights as well) in the laboratory in the past several years. In particular, thank you Jon, Ningyu, Jianqi, and Seb². We spent so many hours talking not only about research, ideas, and concepts, but politics, sports, music, movies as well. These discussions have been sometimes stimulating, sometimes enlightening, and sometimes simply entertaining. Some also proofread my dissertation—I am particularly thankful to Céline (G.-W. & C.), Don, Jeremy, Jianqi, Lucie, Okhtay, Sebs (C. & d. L.), and Zikri for their time and patience. They motivated me when I needed it and took my mind away from work when necessary. And how could I forget the many friends that supported me throughout the years. I cannot possibly name them all but as I am writing, I am thinking to Ju', the oldest, Peter and

Okhtay the craziest, Claire, Clém', Mel', and Maryam, the sweetest, Zikri, Nino, Jeremy, the most protective, Lucie and Amp, the motivational, Olivier and Kris, the coolest, and all the others that would be worth making this section longer than the dissertation itself. For you all, I would like to borrow this quote from J.R.R. Tolkien, which I discover thanks to Okhtay, "I don't know half of you half as well as I should like; and I like less than half of you half as well as you deserve."

Lastly, I would like to thank you, who are reading this dissertation, because your interest in my work justifies the six years I invested in it.

Jérémy A. RiOUSset,
University Park, PA
August 2, 2010

This research was supported by the National Science Foundation under grant AGS-0134838 to the Pennsylvania State University.

Dedication

to my loving mother and father,

Michèle *and* Christian Riousset

pour leur affection et leur soutien indéfectible

and to my ever-caring brother and sister,

Nicolas *and* Pauline Riousset

pour leur confiance aussi ferme qu'inaltérable.

For turning the light on when I was in the dark...

Introduction

In this chapter, we introduce the background information about the structure of the thundercloud and the physics of the lightning channel necessary to understand the original work presented in this dissertation. The description of the thundercloud is used to model the environment in which lightning and jet occur. The remainder of the chapter is dedicated to the discussion of the scientific questions addressed in this dissertation, the organization of this dissertation, and the summary of the specific scientific contributions this dissertation makes.

1.1 Thundercloud, Lightning, Jets, and Streamer-to-Leader Transition

This section is devoted to the description of the electrical structure of the thundercloud and of the physics of the lightning discharge. This background information is extensively used throughout the remainder of the dissertation for the development of models and analysis of the simulation results.

1.1.1 Tripolar Structure of the Thundercloud

Knowledge of the charge structure of the thundercloud is a necessity in studies of lightning and jet discharges. This information is needed to derive the electric field everywhere, especially at the location of the initiation of the lightning channel. Based on the data from the Lightning Mapping Array (LMA) [*Rison et al.*, 1999],

we can infer this structure on a global scale. Knowing that a lightning flash preferentially propagates in a region of large charge density [e.g., *Williams et al.*, 1985; *Mansell et al.*, 2002, and Chapter 2 of this dissertation] allows one to retrieve to the location of the denser charge regions [*Coleman et al.*, 2003] from the superposition of sequences of lightning discharges obtained with the LMA. The values of charges in these inferred charge regions can be deduced from balloon soundings (Figure 1.1). This method provides one with a good quantitative idea of the global “electrical shape” of the thundercloud. The initiation of the lightning occurs in regions of intense electric field. Such regions could be of relatively small dimension compared with the size of the charge layers [*Dwyer et al.*, 2005] and hence would not clearly appear on the lightning inferred cloud structure. That is one of the reasons why it is difficult to accurately determine the electric field threshold required for lightning initiation. The only available data are the local values of charge density and electric field provided by balloon soundings, which might not be at the exact location of the initiation at the time when the lightning flash starts. Numerous series of soundings have been done to investigate the electrical structure of the thunderclouds. Some of these investigations are mainly based on balloon soundings, other also involve rocket soundings [e.g., *Marshall et al.*, 1995], or radar data [e.g., *Shepherd et al.*, 1996; *Marshall et al.*, 2001].

From the measurements cited above, the authors deduce the charge structure of the thundercloud, a common description of which is based on a tripole model [e.g., *Williams*, 1989; *Rakov and Uman*, 2003, p. 69]. This model is often regarded as an adequate approximation of the charge structure involved in lightning discharges in the convective parts of normally electrified storms. It employs a three-layer charge

Table 1.1. Charge heights and extents for the cylindrical disk model used in [*Riousset et al.*, 2007a] and reproduced in Chapter 2, and charge amounts required to initiate the intracloud discharge discussed in Chapter 3.

Charge Layer	Altitude, km AGL ^a	Depth, km	Radius, km	Charge, C
Upper positive	6.75	1.5	4.0	48.7
Main negative	3.75	1.5	3.0	−51.6
Lower positive	2.0	1.5	1.5	2.92

^a AGL, above ground level

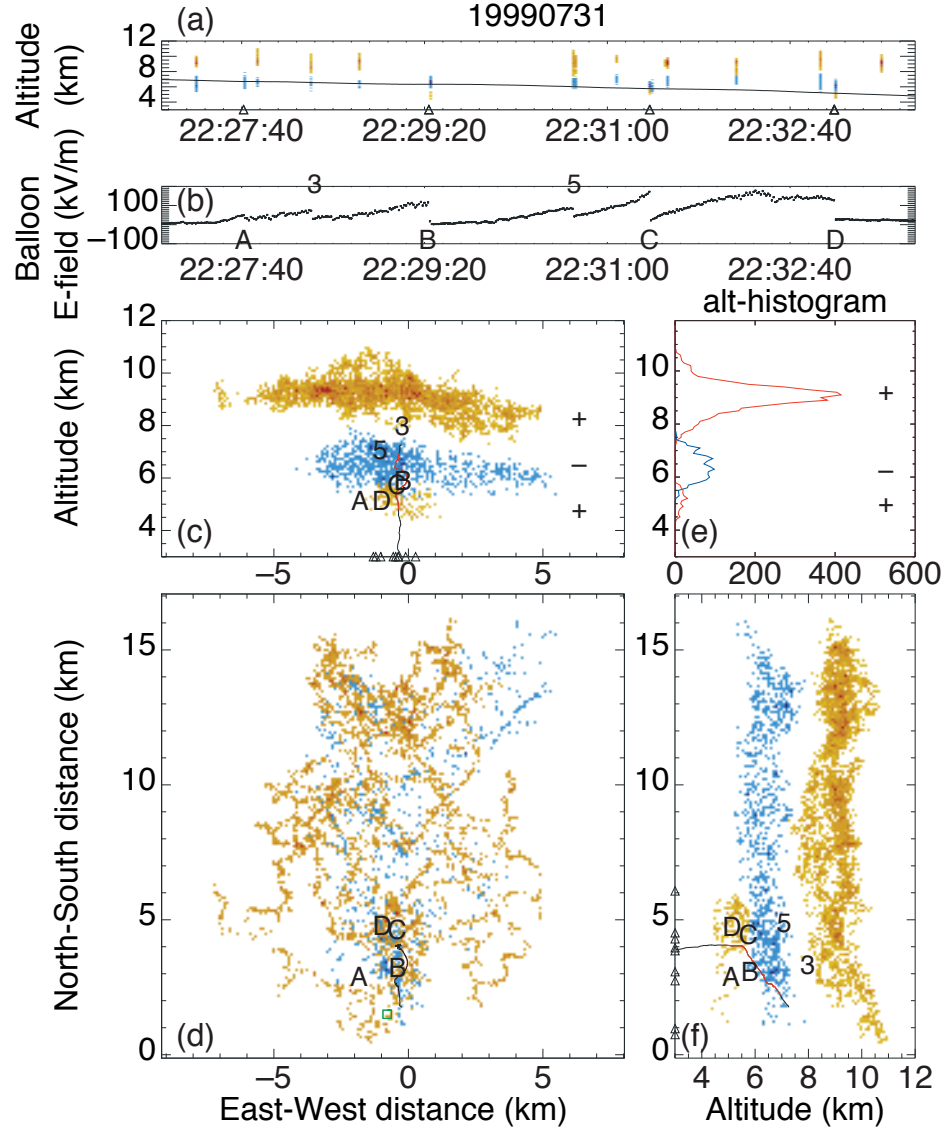


Figure 1.1. Example of cloud structure [Marshall *et al.*, 2005, Figure 1]. Lightning inferred storm charge structure for a 6-min time interval of LMA data collected during the descent of the sounding balloon. Yellow/red regions indicate positive charge; the blue region indicates negative charge. The letters A–D show the initiation points of the cloud-to-ground (CG) flashes and number 3 and 5 show the initiation points of intracloud (IC) flashes that occurred in the part of the storm observed by the balloon. The occurrence times of the flashes are shown in the upper panels, and the red part of the balloon trajectory corresponds to the time interval of the lightning data.

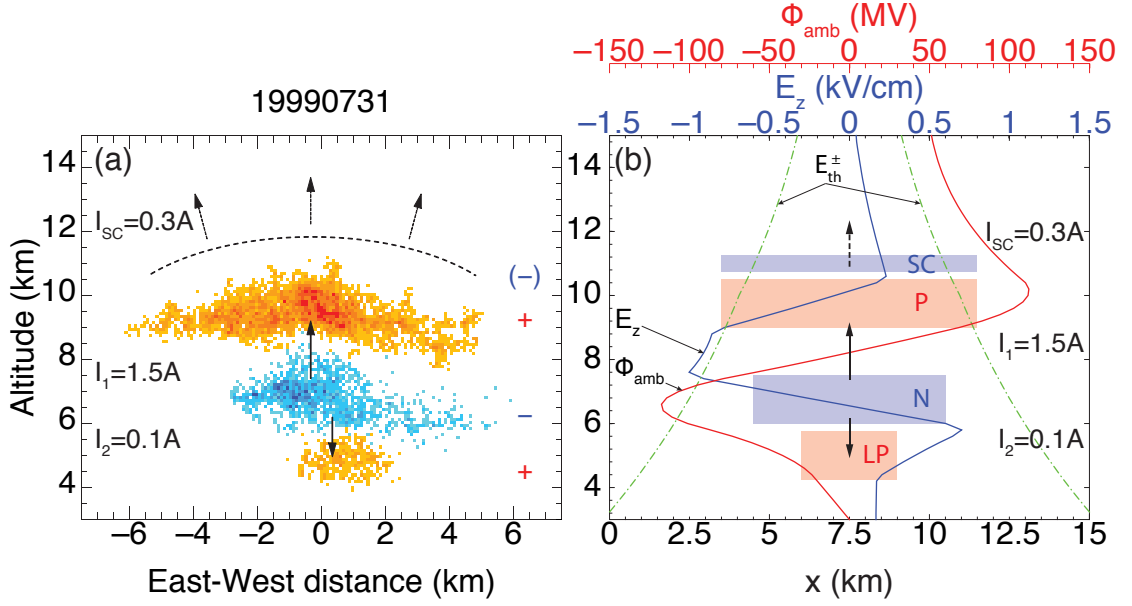


Figure 1.2. (a) Inferred cloud structure from Figure 1.1c with charging currents from [Krehbiel *et al.*, 2004]. (b) Equivalent representation using the tripole model with the parameters shown in Table 1.1 and used in Chapter 3. The main positive and lower positive layers are colored in red, and the main negative charge is colored in blue. The solid red line represents the ambient potential, the solid blue line the ambient electric field, and the dot-dashed green line the electric field threshold for initiation of lightning.

structure above a perfectly electrically conducting (PEC) ground plane. A main negative charge (Q_N) is located at midlevels in the storm, with comparable upper positive charge (Q_P) above the negative and a weaker lower positive charge (Q_{LP}) below the negative (see Figure 1.2). The model can also be extended to include a negative screening charge (Q_{SC}) at the top of the cloud. An important aspect of storm charge structure, which is reflected by means of cylindrical disk models and is important in simulating the lightning produced by the storm, is that the upper positive and main negative charge regions are distributed horizontally within the confines of the storm, in a region of low conductivity (see Chapter 5). We give an illustration of this model in Figures 1.2 and 5.3, which are based on the parameters suggested by Krehbiel *et al.* [2004] (Table 1.1).

An obvious advantage of this charge model is its simplicity. Moreover, it has been successfully applied to reproduce certain features of the thunderstorm such

as the lightning leader initial velocity [Behnke *et al.*, 2005] or lightning path and branching [e.g., Rioussel *et al.*, 2007a]. Mazur and Ruhnke [1998] use a slightly modified tripole model to investigate the relationships among cloud charges, potentials and electric fields, and the induced charges, currents, and electric fields associated with the lightning channel. In this model, the lower positive charge is enclosed at the lower part of the main negative charge, which is split in two to better reproduce the updraft region. Recent studies of the cloud structure based on LMA data [e.g., Marshall *et al.*, 2005] have not confirmed that the lower positive charge is enclosed at the bottom of the main negative layer. This choice of modeling still remains fairly close to a tripole structure, which the Marshall *et al.* [2005] argue to be especially suitable for modeling of isolated thunderstorms. Furthermore, the tripolar structure tends to be reproduced by recent numerical models of the global electrification of the thundercloud [e.g., Barthe *et al.*, 2005; Altaratz *et al.*, 2005].

Not all authors agree on the validity of the tripole model as an accurate description of the thundercloud electrical structure. In particular, Marshall and Rust [1993] suggest that large thundercloud complexes, so-called mesoscale convective systems (MCSs), are too complicated to be described by the simple tripole model (for further information about MCSs, see [e.g., Stolzenburg *et al.*, 1998a]). Investigations based on balloon soundings in the stratiform precipitation region of the MCSs (represented in the left part of Figure 1.3) led Marshall and Rust [1993] and Shepherd *et al.* [1996] to define alternative structures of so-called “Type A” and “Type B” to describe the charge configuration in this region. A type A structure is composed of four main regions of charge equally spaced with alternating polarities. The lowest charge region is negative, and a fifth screening region is added at the top. A type B structure seems to be associated with either bow-echo MCSs or with the presence of a well-defined trailing mesovortex at midlevels [Marshall and Rust, 1993]. The type B vertical structures consist of four main regions with alternating polarities, with the lowest region being negative. The main differences between the two electrical structures are the following: type B has fewer charge regions and a positive charge-density layer at 0 °C, and type A is more complex and tends to have a negative charge-density layer at 0 °C [Marshall and Rust, 1993; Shepherd *et al.*, 1996].

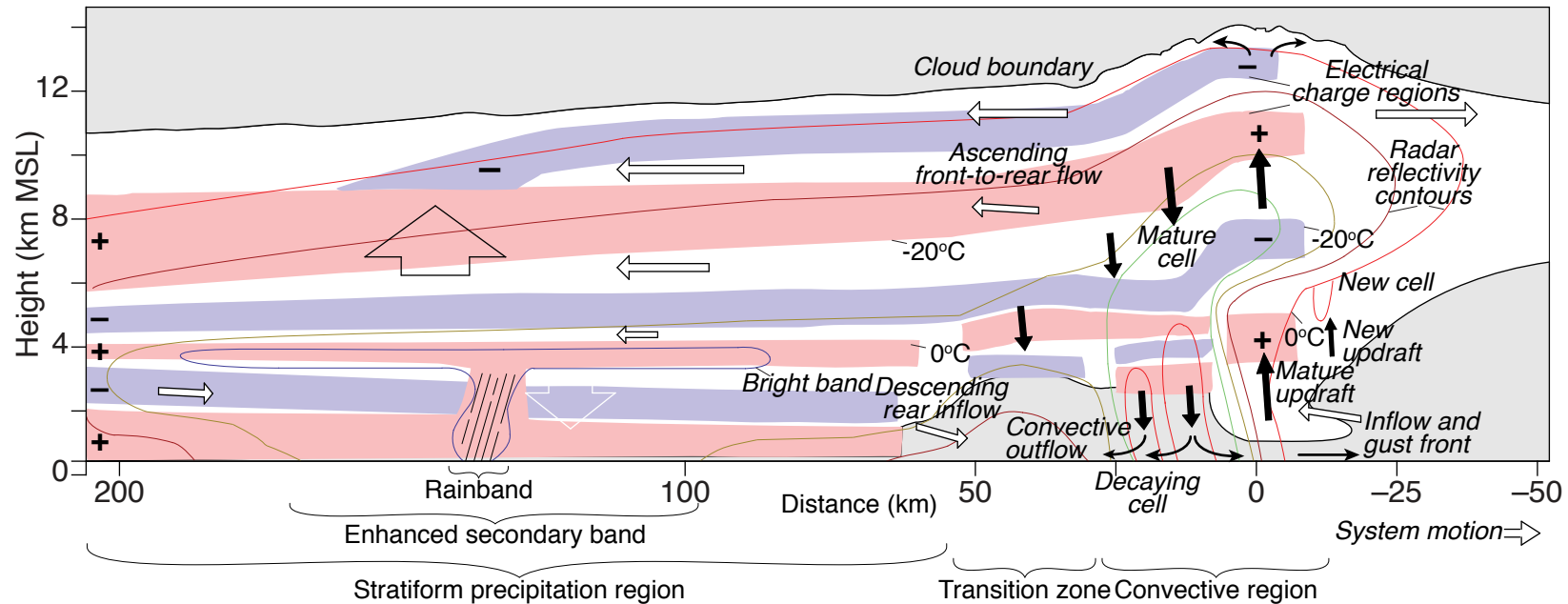


Figure 1.3. Conceptual model of the charge structure of an MCS [Stolzenburg *et al.*, 1998a; Rakov and Uman, 2003, p. 93]. Positive charge layers are indicated by the light red shading and negative layers are indicated by the light blue shading. The solid lines are radar reflectivity contours. In the convective region and the transition zone, the thick solid arrows depict convective updrafts and downdrafts, and the thin solid arrows show divergent outflows. The smaller open arrows represent system-relative flows, which are mainly horizontal. The mesoscale updraft and downdraft in the stratiform region are depicted by large open arrows (black and white outlines, respectively). There are four horizontally extensive cloud charge layers in the part of the stratiform precipitation region farthest behind the convective region, the fifth (lowermost) charge layer being seen in the stratiform region entirely below the cloud. An additional (negative) charge layer extends from the convective region through the nearest part of the stratiform region above all the other layers [Stolzenburg *et al.*, 1998a; Rakov and Uman, 2003, p. 93].

Stolzenburg et al.'s [1998a] picture of the MCS (Figure 1.3) supports the idea that the stratiform region of the MCS cannot be described based on the assumption of a tripole structure. How type A and type B structures fit in *Stolzenburg et al.*'s [1998a] picture of the thundercloud is unclear however. In the same study, *Stolzenburg et al.* [1998a, b, c] also establish that convective regions of MCSs, supercells, and New Mexican thunderstorms, which are three types of thunderstorms, present similar electric structures. They notice that the convective updraft region of an MCS (shown in the right part of Figure 1.3), the updraft region of a supercell, and the region near the center of a New Mexican storm (Figure 1.4) could be accurately described by a tripole structure with an additional negative screening layer at its top. Within the convective region of the thundercloud but outside of the updraft (to the left of the updraft diagram in Figure 1.4), the cloud electrical structure is similar to that described in the stratiform region of MCSs (Figure 1.3), with possible variability between the three types of thunderstorms. Nevertheless, it remains consistent with the idea that this region needs more than three charge layers to be properly described.

Finally, we conclude this section by noting that all interpretations of the measurements converge toward the idea of a stratified structure, but no consensus exists on the validity of the tripole model as an accurate description of the thundercloud. Yet, some authors argue that a tripole charge model is not unreasonable for the mature stage of an isolated storm [e.g., *Mazur and Ruhnke*, 1998]. In addition, *Rakov and Uman* [2003, p. 81] question the distinction established by *Marshall and Rust* [1993] and justify the classical tripolar charge structure of the cloud interior by suggesting that those extra charge regions might be related to transitions between different stages of the thunderstorm evolution. Similarly, *Coleman et al.* [2003] suggest that the definition of type A and B structures may be due to a misqualification of charges deposited by previous discharges as charge centers and reaffirm in their study that the tripole structure is a good electrical equivalent of the thundercloud. From the above discussion, it appears that the tripole model (with additional screening layer) is at least accurate in the region where lightning discharges mainly occur. Therefore, we adopt the tripole structure for the simulation of lightning and jet-producing clouds in this thesis.

Although the exact physics of the formation of the charge layers is still not fully

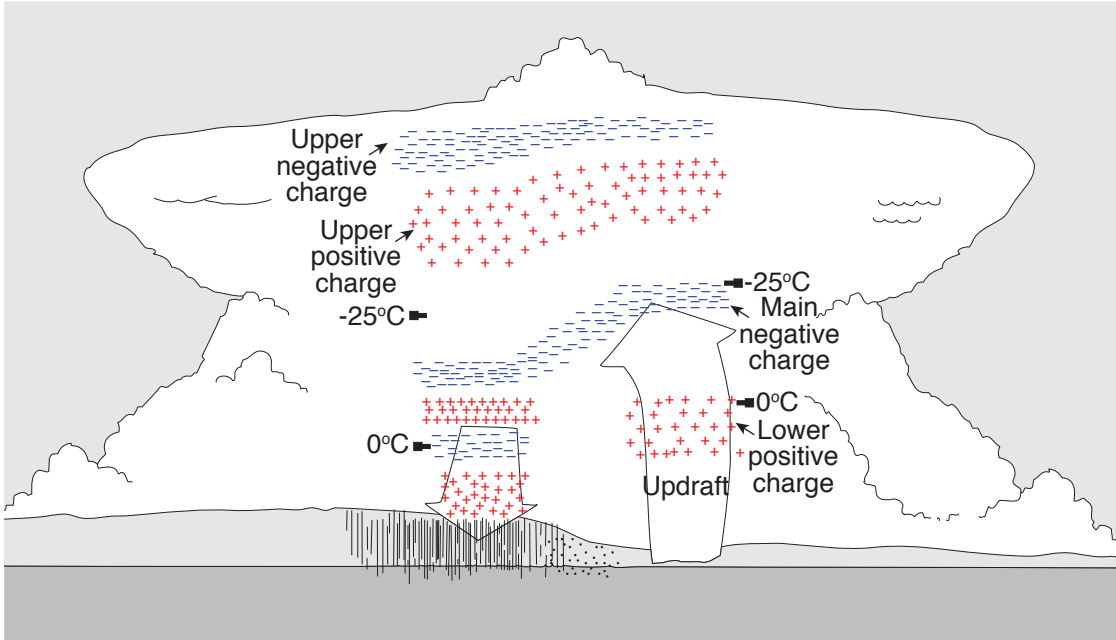


Figure 1.4. Schematic of the basic charge structure in the convective region of a thunderstorm [Stolzenburg *et al.*, 1998a; Rakov and Uman, 2003, p. 83]. Four charge layers are represented in the updraft region, and six charge layers are represented outside the updraft region (to the left of the updraft diagram). The charge structure shown in this figure is applicable to the convective elements of Mesoscale Convective Systems (MCS), isolated supercell storms, and New Mexican air-mass storms. Note that there is a variability about this basic structure, especially outside the updraft [Stolzenburg *et al.*, 1998a; Rakov and Uman, 2003, p. 83].

understood, it is known that each charge layer grows during the early stages of the thunderstorm and consequently enhances the local electric field. A discharge process is therefore required to prevent the electric field in the cloud from reaching unrealistic values. This initiation is achieved through lightning and jet discharges. The next section is therefore dedicated to a review of the mechanisms governing their development.

1.1.2 Plasma Nature of Lightning, Blue Jets, and Gigantic Jets

In this section, we present the physics of the plasma channels in electrical discharges in the context of lightning, blue jets, and gigantic jets.

Streamer and Leader: Pertinence to Lightning and Jet Physics

Many forms of lightning develop within the thundercloud (in particular, intracloud lightning: IC, cloud-to-ground discharge: CG, bolt-from-the-blue: BFB [e.g., *Rison et al.*, 1999; *Thomas et al.*, 2001]). They develop within and out of the thundercloud (see Chapter 4) by means of the well-documented leader process [*Uman*, 2001, p. 82]. The head of the highly ionized and conducting leader channel is normally preceded by a streamer zone looking as a diverging column of diffuse glow and filled with highly branched streamers [*Bazelyan and Raizer*, 1998, pp. 203, 253]. Figure 1.5 provides illustration of the leader-streamer corona system, and Table 1.2 summarizes the typical electric field thresholds for streamer and leader discharges at ground pressure.

The same leader-to-streamer corona is believed to constitute most of the visible part of blue jets and gigantic jets [e.g., *Pasko and George*, 2002; *Riousset et al.*, 2006a; *Raizer et al.*, 2006, 2007; *Krehbiel et al.*, 2008]. Blue and gigantic jets belong to a class of transient luminous events (TLEs). These jets are vertically extensive optical flashes developing from the top of the thundercloud upwards and have been the object of numerous undocumented reports about unusual large-scale luminous phenomena above thunderclouds. Blue jets were discovered first by *Wescott et al.* [1995] and then gigantic jets were later reported by *Pasko et al.* [2002]. The video recording taken at the Arecibo Observatory, Puerto Rico, of a gigantic jet propagating upwards from a thundercloud top to an altitude of about 70 km, i.e., above the altitude of 42 km, usually regarded as the upper limit for

Table 1.2. Electric field thresholds at ground pressure [*Pasko*, 2006, and references therein].

Threshold Name	Notation	Value
Thermal Runaway	E_c	~ 260 kV/cm
Conventional Breakdown	E_k	~ 32 kV/cm
Negative Streamer Propagation	E_{cr}^-	~ 12.5 kV/cm
Positive Streamer Propagation	E_{cr}^+	~ 4.4 kV/cm
Relativistic Runaway	E_t	~ 2 kV/cm
Leader Propagation	E_l or E_{th}^\pm	$\sim \pm 1$ kV/cm

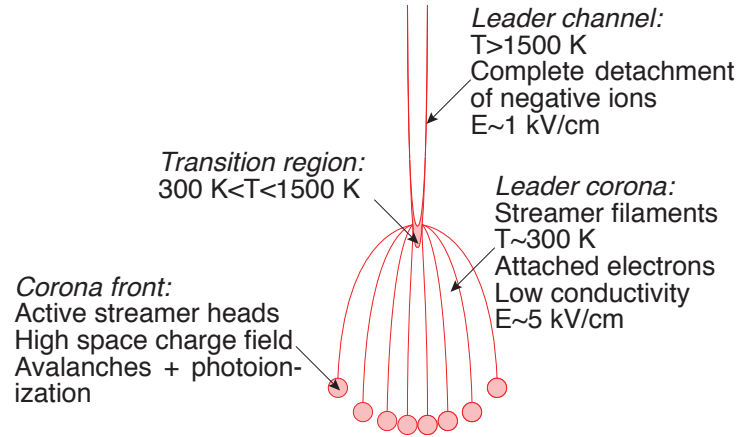


Figure 1.5. Sketch of the leader/leader-corona system, with the main characteristics of the different discharge regions [Comtois *et al.*, 2003].

blue jets, established conclusively for the first time the existence of a direct path of electrical contact between a thundercloud and the lower ionosphere, as was first theoretically suggested by *Wilson* [1921] over 80 years ago. Blue and gigantic jets are believed to be initiated by ‘classic’ parent lightning discharges [*Petrov and Petrova*, 1999; *Krehbiel et al.*, 2008]; therefore, the description of the leader physics provided hereafter is also relevant to the early stages of the development of jets.

In the remainder of this section, we review essential physical processes involved in the formation and propagation of leader discharges. Although the current understanding of the leader process is still far from complete [e.g., *Raizer*, 1991, p. 370; *Bazelyan and Raizer*, 2000, pp. 84–85; *Uman*, 2001, p. 79; *Rakov and Uman*, 2003, p. 136; *Pasko*, 2006], this information provides important physical background for the formulation of the lightning model presented in the next chapter.

Concept of a Streamer

Raizer [1991, p. 334] defines the streamer as “a moderately, one can even say, weakly ionized thin channel formed from the primary avalanche in a sufficiently strong electric field”. Some types of gas discharges are produced based on the streamer phenomenon only, but streamers also serve as precursors to the more complicated leader phenomena, which is discussed later in this chapter. A classic distinction is usually made between the streamer head (or active region), where

the luminous emission and the ionization process occur, and the streamer tail (or passive region). The streamer head contains a net electrical charge, which defines its polarity [Gallimberti *et al.*, 2002]. Owing to its weak ionization, a streamer has low conductivity, with a voltage drop along its path often quoted as ~ 5 kV/cm for positive streamers and ~ -10 kV/cm for negative streamers at ground pressure [Bazelyan and Raizer, 1998, pp. 156–158, 2000, p. 84; Pasko and George, 2002].

Gallimberti *et al.* [2002] summarize the streamer head and the streamer body characteristics. Those values are given at ground level and reproduced in Table 1.3. We note however that these values must be scaled with altitude. Pasko [2006] reviews useful similarity relationships using the neutral density N (or, equivalently, the total pressure p assuming constant temperature of the neutral gas). The scaling factors are shown in the third column of Table 1.3, where N_0 denotes the neutral density at sea level.

In both positive and negative streamer discharges, the strong field near the tip is created mainly by the charge in the streamer head. In this region, electrons are accelerated and get enough energy to ionize air molecules by electron impact. The streamer head also represents a source of UV photons, which are able to ionize neutral gas ahead of the streamer head [e.g., Liu and Pasko, 2004, and

Table 1.3. Streamer characteristics at ground level [Gallimberti *et al.*, 2002; Pasko, 2006].

Parameter	Value	Similarity relationship
<i>Streamer head</i>		
Head radius	10–30 μm	$\propto (N/N_0)^{-1}$
Rotational temperature	330 K	$\propto (N/N_0)^0$
Vibrational temperature	≥ 1000 K	$\propto (N/N_0)^0$
Electron energy	5–15 eV	$\propto (N/N_0)^0$
Electric field in front of the head	100–150 kV/cm	$\propto (N/N_0)^{+1}$
Electron density	10^{15} cm^{-3}	$\propto (N/N_0)^{+2}$
<i>Streamer channel</i>		
Channel radius	10–30 μm	$\propto (N/N_0)^{-1}$
Electron density	$10^{13} - 10^{15}$ cm^{-3}	$\propto (N/N_0)^{+2}$

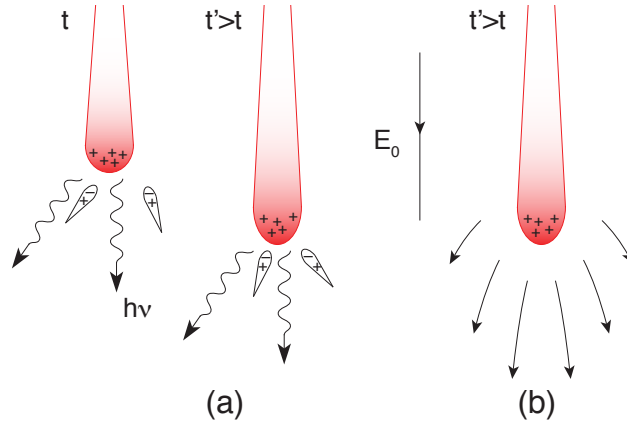


Figure 1.6. Positive (or cathode directed) streamer. (a) Streamer at two consecutive moments of time, with secondary avalanches moving towards the positive head of the streamer, and wavy arrows showing photons that generate seed (i.e., initial) electrons for avalanches. (b) Lines of force of the field near the streamer head. Adapted from [Raizer, 1991, p. 335; Bazelyan and Raizer, 2000, p. 33].

references therein]. The radiation is mostly absorbed, but its intensity is high enough to provide an initial electron density of 10^5 – 10^6 cm^{-3} in a range of a couple of millimeters in front of the streamer tip. The electrons so-produced gain energy due to the strong local electric field (Figures 1.6b and 1.7b), generating the electron avalanches. Because the number of avalanches developing simultaneously is large, they create in front of the plasma tip a new plasma region leading to spatial extension of the streamer [Bazelyan and Raizer, 2000, p. 33].

In a positive streamer (Figure 1.6a), electrons are avalanching towards the streamer head and neutralize positive charges in there to create a new section of the streamer body. Meanwhile, a positive charge density appears at the other end of the avalanches, which becomes the new streamer head [Bazelyan and Raizer, 2000, p. 33].

Negative streamers propagate in a similar way to positive ones. The different charge sign at the streamer tip introduces a few differences however. Unlike in positive streamers, electrons drift away from the streamer tip. The negative charges in the streamer tip move rapidly in this strong field and join the positive charges of the avalanches ahead to form a plasma region. There, electrons at the front of the plasma region move away, repelled by the negative head, while electrons in

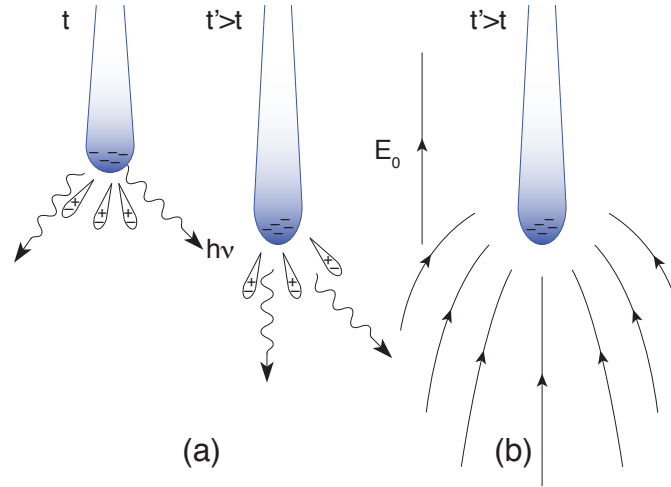


Figure 1.7. Negative (or anode directed) streamer. (a) Streamer at two consecutive moments of time, with secondary avalanches moving away from the negative head of the streamer (bubble shapes), and wavy arrows showing photons that generate seed (i.e., initial) electrons for avalanches. (b) Field in the vicinity of the head. Adapted from [Raizer, 1991, p. 338].

the back (hence, in a weaker field) do not separate from ions and form with them a quasi-neutral plasma, which extends the streamer body (Figure 1.7a) [Raizer, 1991, p. 335].

Concept of a Leader

It is known that the electric field in a thunderstorm hardly exceeds 1.5 kV/cm [e.g., Marshall *et al.*, 1995]. This field is insufficient for the propagation of positive or negative streamers [Pasko, 2006]. Thus, the lightning breakdown must be of another nature. The lightning body extends as “a thin, highly conductive, highly ionized channel [...] from the strong field region along the path prepared by the preceding streamers;” this channel carries the potential along the discharge much more efficiently than a streamer, and is known as a leader. This description, written by Raizer [1991, p. 364] for long-gap discharges, equally applies for lightning. The voltage drop in a leader is much less than that of a streamer; Mansell *et al.* [2002] quote the value of 5×10^{-3} kV/cm in their stochastic lightning model.

The leader channel is not uniform. One can usually distinguish the main body, the transition region and the leader tip (see Figure 1.5). Most of the ionization

occurs in the latter, where the gas is also gradually heated and the conductivity increased. The plasma in the rest of the channel is usually in a quasi-stationary state at high temperature of a few thousands of Kelvins [*Bazelyan and Raizer*, 2000, p. 75; *Gallimberti et al.*, 2002]. Although the main difference between positive and negative streamers lies in the direction of the electron avalanches at the tip of the channel [*Raizer*, 1991, pp. 336 and 338], the difference between leaders of different polarities is far more complex. In particular, the propagation mechanisms and streamer zone structure of a negative leader are much more complicated than those of a positive leader and are still poorly understood [*Bazelyan and Raizer*, 2000, pp. 84–85; *Gallimberti et al.*, 2002]. Below we provide a summary of characteristics for positive and then for negative leaders.

The plasma in the leader body (or thermalized leader) is heated up to thousands of Kelvins, and consequently the conductivity of the channel is highly increased (to $\sim 10^4 \Omega^{-1}\text{m}^{-1}$ [*Rakov and Uman*, 2003, p. 227]). Therefore, the leader head approximately carries the same potential as at the point where the discharge has been initiated. From this point of view, the leader can be considered roughly equipotential or with a very low voltage drop ($\sim 5 \times 10^{-3}$ kV/cm, see [*Mansell et al.*, 2002] and Table 1.4). Hence, the leader channel is analog to a metallic wire placed in a non-zero ambient field: it becomes polarized by the ambient field (i.e., the thundercloud electric field in the case of a lightning discharge). The resulting accumulation of charge at the tip of the leader enhances the surrounding electric field above the

Table 1.4. Leader characteristics at ground level [*Helsdon et al.*, 1992; *Gallimberti et al.*, 2002; *Mansell et al.*, 2002; *Comtois et al.*, 2003].

Parameter	Value
<i>Leader head (Transition region)</i>	
Temperature	330 K < T < 1500 K
<i>Leader channel</i>	
Temperature	> 1500 K
Luminous diameter	0.5–4 mm
Thermal diameter	0.2–1 mm
Voltage drop	$\sim 0.5\text{--}1 \times 10^{-3}$ kV/cm
Linear charge density	~ 1 mC/m

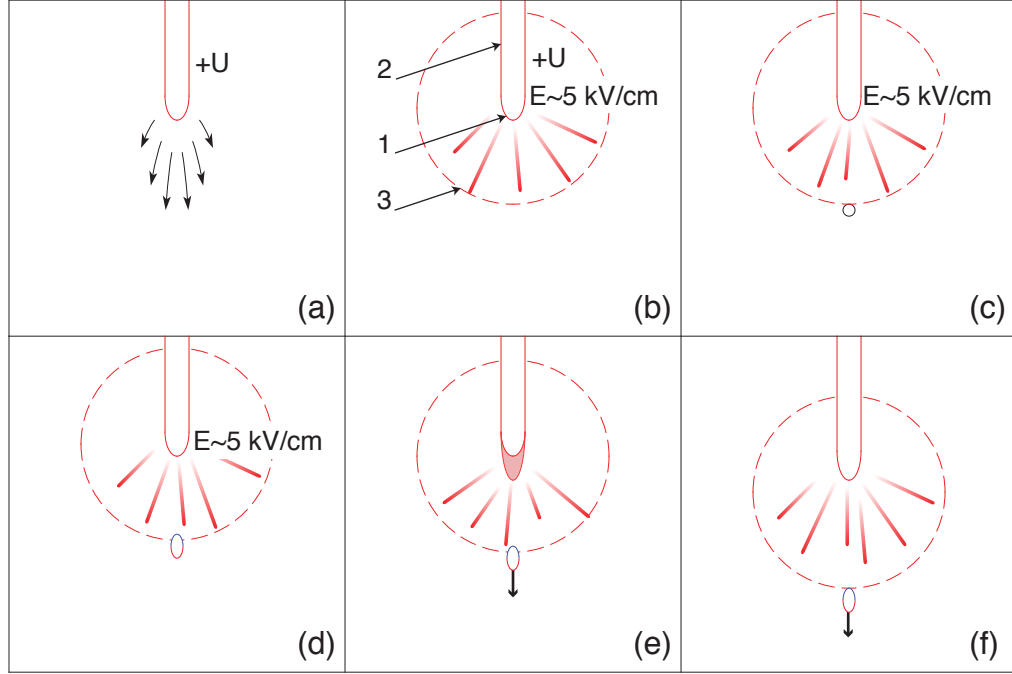


Figure 1.8. Development of a positive leader. Panels (a), (b), (c), (d), (e) and (f) represent different stages of the development; 1, leader tip; 2, leader channel; 3, streamer zone. See text for details.

threshold required for initiation of streamers. The plot of the electric field lines around the tip of leader of positive polarity (Figure 1.8a) clearly illustrates this process. Their convergence towards the leader head indicates the increase of the E -field in this region. Consequently, streamers continuously develop in the region surrounding the tip with a generation frequency on the order of 10^9 s^{-1} [Bazelyan and Raizer, 2000, p. 71] (Figure 1.8b). The charge density associated with streamers leads to self-consistent reduction of the electric field in the leader streamer zone to values comparable to the streamer propagation threshold. Besides, currents of all streamers starting from a leader tip are summed up (Figure 1.8d), leading to Joule heating of the region ahead of the tip (Figure 1.8e) and therefore to an increase of its thermal energy. This energy input provokes a temperature increase of the gas molecules, a hydrodynamic expansion, a reduction of the gas density, and finally the detachment of the negative ions due to both the increase of the gas temperature and the low reduced electric field, defined as the ratio of electric field over the neutral density. These processes are discussed in detail in the con-

text of streamer-to-spark transition at various pressures in Chapters 7 and 8. The aforementioned effects tremendously increase the conductivity at the leader head, permitting further propagation of the leader channel (Figure 1.8f). This mechanism, the so-called current contraction in the front region of a leader channel, is not quite clear yet, especially quantitatively. One may assume the existence of ionization–thermal instability [*Bazelyan and Raizer*, 2000, pp. 53–64 and p. 255; *Gallimberti et al.*, 2002; *Rakov and Uman*, 2003, pp. 136 and 226].

A plasma spot formation is represented in Figure 1.8c. It is polarized in Figure 1.8d. The existence of this plasma spot has been shown for negative leader development (see further discussion in this section), but is still uncertain for positive leaders. Even if present, the electric field in the streamer zone of positive leader ($\lesssim 5$ kV/cm [e.g., *Pasko*, 2006]) is not strong enough to allow negative streamer development toward the leader head and consequently to modify the mechanism of development of the positive leader (recall that a field on the order of -12.5 kV/cm is needed for the propagation of negative streamers [e.g., *Pasko*, 2006]). A streak picture of a positive leader discharge [*Gallimberti et al.*, 2002] shows that the leader tip and the leader streamer zone advance at roughly constant velocity ($\sim 2 \times 10^4$ m/s for a typical laboratory leader [e.g., *Lalande et al.*, 2002]).

The initial stages of the development of a negative leader are the same as those of a positive leader and the values of the electric field for their initiations are also similar: ~ 1 kV/cm [e.g., *Raizer*, 1991, p. 375; *Bazelyan and Raizer*, 1998, pp. 253; *Rakov and Uman*, 2003, p. 322]. The temperature of the leader body is increased up to several thousands of Kelvins; the electric field is also increased around the leader tip (Figure 1.9a) up to values exceeding the propagation threshold for negative streamers (~ -12.5 kV/cm). Consequently, negative streamers develop to form the leader corona (Figure 1.9b). A plasma spot arises near the external boundary of the negative streamer zone (Figure 1.9c). The physical nature of the plasma spot is not understood at present. Under the effect of the ambient electric field, the plasma body becomes polarized (Figure 1.9d). The positive plasma dipole end, which is directed towards the main leader tip, serves as a starting point for positive streamers. We note that positive streamers require only 5 kV/cm fields for their propagation [e.g., *Raizer*, 1991, p. 335]) and can therefore easily propagate toward the negative leader head in streamer zone fields on the order of 12.5 kV/cm. The

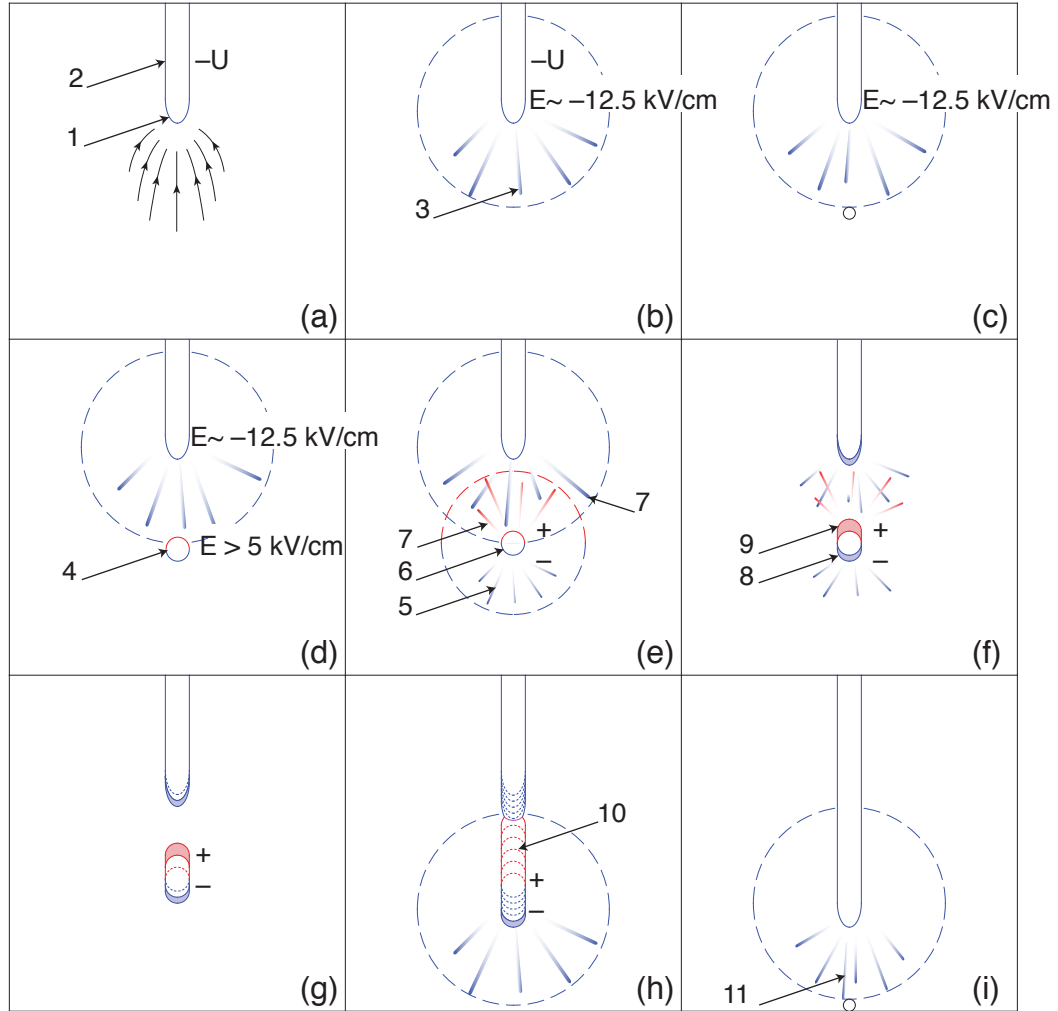


Figure 1.9. Development of a negative leader. Panels (a), (b), (c), (d), (e), (f), (g), (h) and (i) represent different stages of the development. 1, leader tip; 2, primary leader channel; 3, negative streamers in the streamer zone; 4, space stem or plasma spot; 5, negative streamers of the streamer zone associated with the negative space leader; 6, space leader developing from the plasma spot; 7, positive streamers of the streamer zone associated with the positive space leader; 8, negative end of the space leader; 9, positive end of the space leader; 10, leader step; 11, burst of negative streamers. See text for details. Note that the streamer zones are not reproduced in panels (f) and (g) for the sake of clarity.

negative streamers can develop on the other end of the plasma body thanks to the field enhancement around it (Figure 1.9e). A current contraction process similar to that for positive leaders probably occurs at the tip of the plasma spot, allowing the development of a secondary leader, known as volume or space leader [Bazelyan and

Raizer, 1998, pp. 254–255, 2000, pp. 85–88; *Rakov and Uman*, 2003, pp. 136–137]. The leader main channel slowly advances towards the space leader. The positive end of the space leader develops towards the main leader and the negative end propagates in the opposite direction (Figures 1.9f and 1.9g). Normally, the positive streamer zone of the positive space leader almost immediately reaches the main negative leader. Therefore, the junction between the main negative leader and the positive space leader is very quick, and develops in a way similar to the final stage of development of positive leader [*Bazelyan and Raizer*, 1998, p. 212]. When the space leader comes into contact with the main channel, they form a common conducting channel. A process of partial charge neutralization and redistribution occurs and results in the modification of the potential of the former space leader. The latter acquires a potential close to that of the former main negative channel. This process resembles a miniature lightning return stroke, accompanied by a rapidly rising and just as rapidly falling current impulse in the channel. During this stage, the optical emission of the channel strongly increases, giving the impression to the observer that the channel moves by steps (Figure 1.9h). What causes this strong emission is still unclear, even if some processes such as the temperature rise, or the ionization in the channel cover may be suggested. Finally, the negative end of the former space leader turns into the new leader head, a burst of negative streamers develops, and the process is repeated (Figure 1.9i) [*Bazelyan and Raizer*, 2000, pp. 83–89 and p. 255; *Gallimberti et al.*, 2002; *Rakov and Uman*, 2003, p. 136].

The description presented above has been reconstructed from streak photographs of laboratory negative leader discharges [*Bazelyan and Raizer*, 2000, p. 85; *Rakov and Uman*, 2003, p. 136]. The first negative discharge of a lightning or of any laboratory experiment is usually referred to as the “stepped” leader and is often said to be discontinuous in opposition to the continuous nature of the positive leader discharge. The motion of a negative leader is continuous, but secondary positive leaders, also continuous, produce a stepwise effect, which originates in the terminology “stepped” leaders [*Bazelyan and Raizer*, 1998, pp. 255–256; 2000, p. 87].

The previous section introduces the physical concepts behind the atmospheric processes modeled and discussed throughout this dissertation. Next, we discuss the issues addressed in this work, its organization, and contributions to knowledge.

1.2 Problem Formulation

This dissertation addresses some of the unanswered questions pertaining to lightning and jet physics. The present study builds upon a previously introduced lightning model that is able to reproduce the stochasticity and branching of the lightning channel, and respects the fundamental principles of the leader equipotentiality and overall charge neutrality [Riousset, 2006]. The lightning model is further validated, refined and applied in this dissertation work to shed a new light on important processes in lightning and jets.

Shortly after the discovery of blue jets by Wescott *et al.* [1995], Petrov and Petrova [1999] hypothesized that blue jets could be a visible manifestation of regular lightning escaping from the thundercloud top upward. A unified theory of lightning and jets still remained to be developed and supported by observations. The development of this theory constitutes an important part of the studies presented in this dissertation.

The work on the unified theory of lightning and jet discharges reveals the importance of local and global electric charge imbalances in the thundercloud. Their existence has been demonstrated as early as in 1921 by *C.T.R. Wilson*, but their impact on the initiation and early stages of the development of blue and gigantic jets remained to be understood and is also addressed in this dissertation.

Finally, Section 1.1.2 emphasizes that the propagation of the leader channel is associated with significant heating of air in the plasma channel. The mechanisms behind the heating of the plasma channel are still the topic of active research, and much remains to be understood. In particular, how the heating characteristics scale with altitude, and particularly at the altitudes of known propagation of blue and gigantic jets, is an open question that is discussed in the last part of this dissertation.

1.3 Organization of the Dissertation

Chapter 1 starts with a general description of the thundercloud and of the physical processes creating the lightning and jet discharges. This chapter permits the building of the background for understanding the lightning model detailed in Chapter 2,

the model of thundercloud and charge relaxation in Chapter 5, and the model of streamer-to-spark¹ transition developed in Chapter 7. These models can be represented using a flowchart format, and such flowcharts are provided in Appendix A.

More specifically, Chapter 2 is devoted to the description of a stochastic model of the lightning leader trees, whose results are presented in Chapters 3 and 4. In Chapter 3, we test the performance of the model through the modeling of a representative intracloud discharge produced by a common New Mexico thunderstorm. This study additionally allows us to explain how and why lightning channels develop within regions of higher charge density. In Chapter 4, we explore the reasons behind the escape of the lightning channel from the thundercloud in the form of classic cloud-to-ground lightning, bolt-from-the-blue lightning, and blue and gigantic jets. This work leads to the formulation of a unified theory of lightning and jet discharges based on the concepts of local and global charge imbalances inside the thundercloud. The theory is complemented by discussions specific to inverted-polarity thunderstorms in Appendix B.

These charge imbalances are further investigated in Chapters 5 and 6. A model of thundercloud charging, including cloud conductivity and charge relaxation in a conducting atmosphere is developed in Chapter 5, and applied to investigate the formation of charge imbalances in the thundercloud in Chapter 6. In particular, we study the mechanisms likely to be responsible for the initiation of blue and gigantic jets. Supplementary material pertaining to the modeling of Maxwellian relaxation of charges in a conducting medium is provided in Appendix C.

Chapters 7 and 8 examine the heating processes relevant to streamers and transient luminous events. We present a model of heating of the air in a streamer channel from ambient temperature (~ 300 K) to breakdown temperature (~ 5000 K) in Chapter 7. The model accounts for the effects of gas dynamics and chemical kinetics of the discharge, and for the vibrational–translational relaxation of N_2 molecules. We report the results of modeling the streamer-to-spark transition based on this model in Chapter 8. We also compare the results obtained with two

¹The word “spark” usually refers to the electrical breakdown between two still points. It is a high-conductivity, high-temperature thermalized plasma, whose last stage can be regarded as an arc-flash [e.g., *Bazelyan and Raizer*, 1998, p. 8]. In contrast, the term leader conventionally designates a progressing channel. Note that the terminology is not clearly established at present, and use of these terms may vary from one author to another.

different schemes for the chemistry of positive ions and test the results against both experimental data from [Černák *et al.*, 1995] and [Larsson, 1998] and from previous numerical modeling by Naidis [1999, 2005].

Finally, the results presented in this dissertation are summarized in Chapter 9.

1.4 Scientific Contributions

The research accomplished as part of the doctoral studies makes several contributions to the fields of atmospheric electricity and gas discharge modeling, which can be summarized as follows:

1. A unified theory of lightning and jet discharges is developed based on the concept of bi-directional, overall neutral and equipotential lightning leaders. A three-dimensional fractal model of lightning is applied to model typical lightning and jet discharges using realistic cloud configurations emphasizing charge imbalance as a principal factor that allows the formation of leader with high enough potential that enables it to escape from the thundercloud.
2. A new two-dimensional (2-D) axisymmetric model of Maxwellian charge relaxation in the conducting atmosphere is developed to understand the dynamic formation of the screening charges at the thundercloud boundaries. The results emphasize the role of the screening charges in the magnification of the electric field near the cloud top and/or the formation of charge imbalances. Blue and gigantic jets are successfully modeled in the framework of the fractal model of lightning using realistic cloud configurations produced by the Maxwellian relaxation model.
3. A streamer-to-spark transition model is developed that allows studies of gas dynamics and chemical kinetics involved in heating of air in streamer channels for a given air density N under assumption of constant applied electric field E . The model closely agrees with results of experimental measurements of streamer-to-spark transition times τ_{br} at ground and near-ground air pressures. It is demonstrated that for the air densities N corresponding to a broad altitude range of 0–70 km in the Earth atmosphere, the kinetic effects lead to a significant acceleration of the air heating in streamer channels, with

effective heating times appearing to scale closer to $1/N$ than to $1/N^2$, which is predicted on the basis of simple similarity laws for Joule heating assuming constant channel conductivity. This acceleration is attributed to strong reduction in electron losses due to three-body attachment and electron-ion recombination processes with reduction of air pressure.

The model presented in Chapter 2 and the results presented in Chapter 3 have been published in the form of a full-length paper in the *Journal of Geophysical Research-Atmospheres* [Riousset et al., 2007a]. This work builds upon previous work [Riousset, 2006] recently published in the form of a book by LAP publishing [Riousset, 2010]. The theory developed in Chapter 4 has been published in *Nature Geoscience* [Krehbiel et al., 2008]. Mr. J  r  my Riousset equally contributed to the conception of the physical mechanisms and to the formulation of all results related to the modeling, and carried out all lightning simulations presented in [Krehbiel et al., 2008]. The numerical modeling of the formation of the screening charge near the thundercloud boundaries described in Chapter 5 and its impact on the initiation and early stages of development of blue and gigantic jets presented in Chapter 6, have been published as part of the special issue of the *Journal of Geophysical Research-Space Physics* [Riousset et al., 2010a], related to the 2009 AGU Chapman Conference on the Effects of Thunderstorms and Lightning on the Upper Atmosphere. The last part of this work, related to air heating in streamer channels, constitutes a subject of a paper to be submitted to the *Journal of Geophysical Research* [Riousset et al., 2010b].

Three-Dimensional Fractal Model of a Lightning Discharge

The material covered in this chapter has been published in the form of a full length article in the *Journal of Geophysical Research–Atmospheres* [Riousset *et al.*, 2007a]. Chapter 1 is devoted to the description of the thundercloud charge configurations and of the mechanisms behind the formation of lightning leader channels. This chapter is devoted to the description of the fractal model developed by Riousset *et al.* [2007a]. Following the discussion about the thunderstorm cloud electric structure presented in Section 1.1.1, we employ a tripole charge configuration as an essential part of the fractal model of lightning propagation.

2.1 Lightning Models in the Refereed Literature

The leader process as a propagation mechanism of cloud-to-ground lightning was determined photographically as early as the 1930s by Schonland, Malan and co-workers in South Africa (as summarized by Uman [1984, p. 5, 2001, pp. 7, 83]). This basic mechanism is now known to be also valid for intracloud discharges [Ogawa and Brook, 1964; Proctor, 1981, 1983; Uman, 1984, p. 10; Liu and Krehbiel, 1985; Shao and Krehbiel, 1996; Rakov and Uman, 2003, p. 322]. The understanding of the internal physics of the leader process is still far from complete, however [e.g., Bazelyan and Raizer, 2000, pp. 84–85; Gallimberti *et al.*, 2002; Pasko, 2006, and references therein]. The complexity of the phenomenon and the lack of a complete

theory on lightning propagation led some authors to consider only the bulk effects of the lightning discharges in the development of cloud electrification models [e.g., *Ziegler and MacGorman*, 1994; *Krehbiel et al.*, 2004]. The model presented in [*Riousset et al.*, 2007a] continues a long-lasting effort started in the 1950s directed towards a theoretical description of the interaction between the lightning channel and the surrounding thunderstorm electric field [e.g., *Kasemir*, 1960, and references therein].

Kasemir [1960] models the lightning channel as an equipotential, overall neutral, prolonged spheroid placed in the thundercloud electric field. The spheroid is vertical and lies on the main axis of the system, which is assumed to possess a rotational symmetry. The induced linear charge density in the channel is derived based on the surrounding ambient potential of the thundercloud. *Mazur and Ruhnke* [1998] revisit *Kasemir's* [1960] model with the same assumptions of overall neutrality and equipotentiality in order to investigate the relationships among cloud charges, potentials, and electric fields, and the induced charges, currents, and electric field changes associated with the lightning channel. The linear charge density in the channel is no longer derived analytically based on the assumption of spheroid channel but is determined numerically to account for the geometry of the channel used in their model. This work utilizes a tripolar-like charge model to study the development of cloud-to-ground and intracloud discharges, but the system remains axisymmetric and does not allow for branching or horizontal development. Unlike *Kasemir's* [1960] model, in which the estimation of the potential is done for a channel of fixed length, *Mazur and Ruhnke* [1998] introduce a dynamical variation of the channel length to simulate the discharge progression.

In their three-dimensional simulations of electric fields within a thunderstorm, *Hager et al.* [1989] introduce a deterministic lightning model, which allows branching of the discharge channels. In this model, whenever some component of the electric field reaches a predefined breakdown threshold, the conductivity between the corresponding mesh points is taken to infinity. As the conductivity tends to infinity, the potential is adjusted throughout the domain, so that in the breakdown region, the potential is constant. This adjustment of the potential, which does not account for the overall neutrality of the discharge, often leads to cascades; in the process of equilibrating the potential between two nodes, the electric field between

an adjacent pair of nodes reaches the breakdown threshold [*Hager et al.*, 1989].

Recently, *Behnke et al.* [2005] applied the principles of *Mazur and Ruhnke's* [1998] model to investigate the evolution of initial leader velocities during intracloud lightning. Instead of *Mazur and Ruhnke's* [1998] model of a thundercloud, the authors use a more realistic model derived from lightning mapping and electric field sounding observations of actual storms. As in the work by *Mazur and Ruhnke* [1998], *Behnke et al.* [2005] ensure the overall neutrality of the channel by adequately shifting the electric potential of the channel.

Helsdon et al. [1992] use *Kasemir's* [1960] equipotential, spheroid, overall neutral representation of the lightning in their model of storm electrification. The problem is solved in a two-dimensional (2-D) Cartesian domain, with no hypothesis concerning the symmetry of the channel. To overcome the difficulty of deriving a linear charge density in 2-D, *Helsdon et al.* [1992] derive an analytical expression for the linear charge density carried by a channel of the designated spheroid geometry. In this model, the lightning propagates with no branching along the field lines defined by the ambient field configuration regardless of the electric field due to the lightning channel itself. *Helsdon et al.* [2002] extend the previous model to a 3-D geometry. The channel is again neutral and equipotential and propagates bi-directionally between the grid points of the three-dimensional Cartesian space, with essentially the same limitations as in the 1992 model. Other models based on the same concepts have been developed but are not described here for the sake of brevity. A review of those can be found in [*Poepfel*, 2005, pp. 1–5].

A significant limitation of the aforementioned models is related to the deterministic character of the propagation of the model lightning. Indeed, none of these models is able to reproduce the observed morphology of the highly distorted and branched path of the lightning in a realistic way. This issue cannot be resolved at present using a microscopic approach to the lightning propagation because of insufficient knowledge of the related processes and also because of the lack of computational power. Instead, *Petrov and Petrova* [1993] use *Niemeyer et al.'s* [1984] dielectric breakdown model to introduce stochasticity in the modeling of the lightning discharge. The original model by *Niemeyer et al.* [1984] is further discussed, refined and improved in [*Satpathy*, 1986; *Niemeyer et al.*, 1986; *Wiesmann and Zeller*, 1986; *Niemeyer and Wiesmann*, 1987; *Niemeyer et al.*, 1989; *Femia et al.*,

1993]. The idea of these models is to simulate the observed macroscopic behavior of the leader by using a probabilistic approach rather than by describing its internal physics. Such models have been successfully applied to reproduce other atmospheric phenomena such as sprites [e.g., *Pasko et al.*, 2000, 2001]. *Petrov and Petrova*'s [1993] model use a dipole electrode representation of a thundercloud in a 2-D Cartesian space. The links between grid points resembling lightning channels are initiated from a central circular region in the simulation domain where the potential is constant. The model uses unusually high electric field values for the discharge initiation threshold and employs a variable voltage drop along the channel to simulate its resistivity. *Petrov et al.* [2003] further extend this model to a 3-D Cartesian geometry to predict the probability of lightning strikes to practical structures. As in their previous model, the potential at a point of a new link at the moment of its connection with the discharge remains unchanged for the remainder of the simulation. No assumptions concerning the channel neutrality are employed and no charge densities are derived.

Mansell et al. [2002] also extend *Niemeyer et al.*'s [1984] model to a 3-D Cartesian geometry. In addition, they add bi-directional propagation of the model lightning trees, and integrate it in a numerical thunderstorm model. As in *Petrov and Petrova* [1993], the channel is resistive but with a fixed voltage drop between adjacent channel grid points. As in the work by *Kasemir* [1960], *Mansell et al.* [2002] assume the overall neutrality of the channel, which is ensured by favoring the development of a part of the bi-directional tree having a charge deficit. In particular, if the overall net charge carried by the discharge trees after an iteration is positive (respectively negative), then the threshold field needed for advancement of branches of negative (respectively positive) polarity is lowered to enhance their development until neutrality is achieved [*Mansell et al.*, 2002].

The aforementioned channel-based simulations of lightning only model the leader part of the discharge. Nonetheless, it is well known that a streamer zone, not described in the previous models, develops at the leader tip and plays an important role in leader advancement [e.g., *Bazelyan and Raizer*, 2000, p. 71]. Because of its high conductivity, the leader is analogous to an equipotential metallic wire, which gets polarized when placed in the thundercloud ambient electric field. The resulting accumulation of charge at the tip of the leader enhances the surrounding

electric field above the threshold required for initiation of streamers. Consequently, streamers continuously develop in the region surrounding the tip with a generation frequency on the order of 10^9 s^{-1} [Bazelyan and Raizer, 2000, p. 71]. The charge density associated with streamers leads to a self-consistent reduction of the electric field in the leader streamer zone to values comparable to the streamer initiation threshold [Bazelyan and Raizer, 2000, pp. 56–71]. In addition, currents of all streamers starting from a leader tip are summed up, heating the region ahead of the tip and therefore increasing its conductivity, permitting further propagation of the leader channel [Bazelyan and Raizer, 2000, pp. 53–64 and p. 255; Rakov and Uman, 2003, pp. 136 and 226]. The exclusion of the direct modeling of the streamer zone in existing models is justified by the lack of knowledge of the detailed physics of this region as well as by the computational expenses involved in a thorough description of it.

Kupershtokh et al. [2001] propose to introduce the streamer zone in probabilistic lightning models using a cellular automata approach. *Kupershtokh et al.*'s [2001] model does not deal with the underlying physics of the process. Thus, from this point of view it remains close to *Niemeyer et al.*'s [1984] original model. The previous models consider only two states for any grid point in the domain—a conducting state, if the point is crossed by the leader, and a dielectric state otherwise. The use of a cellular automata approach described in [Kupershtokh et al., 2001] allows the introduction of a third, streamer state, reproducing the streamer zone. Moreover, *Kupershtokh et al.* [2001] introduce time in their model to overcome the absence of an actual timescale in the *Niemeyer et al.*'s [1984]-based models. The model developed in [Kupershtokh et al., 2001] has not yet been applied to the modeling of leader development in realistic thundercloud configurations.

Agoris et al. [2004] also introduce leader–streamer zone effects but still based their model on the “classical” *Niemeyer et al.*'s [1984] dielectric breakdown model. In addition, they use a timescale for the propagation of streamer and leader bounds. The formation time for each streamer segment likely to propagate the discharge is derived using the assumption of a Weibull probability distribution function and compared with the time step of the current iteration (defined as the average of the times of formation of all candidate streamer bounds). Hence at each step, if the time of formation of a candidate streamer link is smaller than the time step of

the current iteration, then the link is added to the existing tree. Unlike the leader streamer corona mechanism described above, the formation of leader channels is considered to be done at constant velocity compared with streamer propagation (and therefore with a constant time step). Its driving mechanisms are the same as in [Femia *et al.*, 1993], except that candidate leader bounds are now defined between the leader channels and points occupied by a streamer link. This model is run in a 2-D Cartesian simulation domain and no charge considerations are accounted for at any stage of the development of either streamer or leader channels. Agoris *et al.*'s [2004] model is applied to the study of Franklin rod height impact on the striking distance and produces results in good agreement with experiments.

In Kupershtokh *et al.*'s [2001] model as well as in any other model based on approaches proposed by Niemeyer *et al.* [1984], the channel propagates through grid points of a discretized 2-D or 3-D simulation domain. Therefore, the channel propagation often takes unrealistically sharp angles. This issue is addressed by Helsdon and Poeppel [2005]. These authors propose to avoid grid dependency in a 3-D geometry by deriving the direction of the lightning propagation based on the location of random free electrons near the leader tip, and no longer in terms of the probability introduced by Niemeyer *et al.* [1984]. Stochasticity in this model is therefore introduced by the location of the free electrons, which is derived using a Monte Carlo technique [Helsdon and Poeppel, 2005]. The channel is assumed to be equipotential and the linear charge density is derived using the theory for unbranched conductors [e.g., Mazur and Ruhnke, 1998]. Helsdon and Poeppel [2005] are able to identify numerical parameters of the model leading to the realistic behavior of the channel (e.g., branching, arresting of propagation, etc.), and the model produces positive leaders developing in the negative charge regions, and negative leaders propagating in the positive charge center, generally consistent with observations.

The purpose of this chapter is to present a new fractal model of lightning derived from Niemeyer *et al.*'s [1984] dielectric breakdown model. The model is three-dimensional and uses Kasemir's [1960] equipotential hypotheses to describe the channel properties. Special emphasis is placed on obtaining self-consistent solutions preserving complete charge neutrality of discharge trees at any stage of the simulation. This model is applied to the investigation of changes in the configu-

ration of the thunderstorm electric field by an intracloud lightning discharge. The model results are directly compared with an intracloud discharge detected by the LMA.

The study of cloud-to-ground discharges involves the modeling of additional processes (e.g., the development of the return stroke), which requires further discussion and validation. This chapter and the following one focus on an intracloud discharge.

2.2 Formulation of the Fractal Model

The thundercloud and lightning discharge are modeled in a 3-D Cartesian domain. The domain is discretized using equidistant grids (specific parameters are given in Section 3.1).

The thundercloud charge distribution is based on a tripole model [e.g., *Williams*, 1989; *Rakov and Uman*, 2003, p. 69, and Chapter 1 of this dissertation]. This model is often regarded as an adequate approximation of the charge structure involved in lightning discharges in the convective parts of normally electrified storms. It employs a three-layer charge structure above a perfectly electrically conducting (PEC) flat ground plane. A main negative charge (Q_N) is located at midlevels in the storm, with comparable upper positive charge (Q_P) above the negative and a weaker lower positive charge (Q_{LP}) below the negative, as illustrated in Figure 2.1. The model can also be extended to include negative screening charge (Q_{SC}) at the top of the cloud, but this extension is not implemented in our study of intracloud discharges. An important aspect of storm charge structure is that the upper positive and main negative charge regions are spread in horizontally extended regions within the confines of the storm as is further described below.

The particular charge configuration used in Chapters 2 and 3 closely follows the approach of *Krehbiel et al.* [2004] and *Behnke et al.* [2005]. Each charge layer is assumed to have a cylindrically symmetric disk shape with dimensions chosen based on observations of a storm over the Langmuir Laboratory on July 31, 1999, as determined by *Krehbiel et al.* [2004] and summarized in Table 3.1 (see [*Marshall et al.*, 2005] for results concerning the initiation conditions of cloud-to-ground lightning discharges in this storm). In the study by *Krehbiel et al.* [2004], charging currents

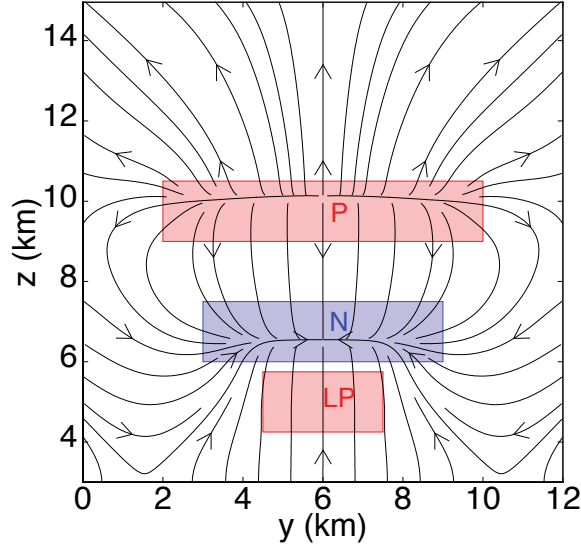


Figure 2.1. A cross-sectional view in the y - z plane at $x=6$ km of the model thundercloud with upper positive (P), central negative (N) and lower positive (LP) charge layers. Electric field lines produced by the model cloud are also shown for reference.

I_1 and I_2 are introduced between the upper and lower dipolar structures (i.e., $Q_N - Q_P$ and $Q_N - Q_{LP}$, respectively) that reproduce the average lightning rates of both cloud-to-ground and intracloud flashes, as determined by the three-dimensional Lightning Mapping Array (LMA). The charging currents are $I_1 = +1.5$ A between the main negative and upper positive, and $I_2 = -90$ mA between the main negative and lower positive charge regions. The resulting variation of the electric field profiles with space and time along the axis of the modeled charge structure reproduce the basic features of balloon-borne electric field soundings through the storm [Krehbiel *et al.*, 2004].

In the present study, the above charging currents are applied until the conditions for initiation of an intracloud discharge between the main negative and upper positive charge regions are satisfied (discussed later in this section). The charge brought by the currents is uniformly distributed in cylindrical disk volumes with dimensions specified in Table 3.1 (see also Figure 2.1). The values of the thundercloud charges at the time of the lightning initiation are also included in Table 3.1 for reference. The charge density of the model thunderstorm at the time of discharge initiation is discretized on the grid points of the simulation domain

and referred to as the ambient charge density ρ_{amb} . From the charge density, the ambient electric field and potential (\vec{E}_{amb} and ϕ_{amb}) are determined at all grid points within and on the boundaries of the simulation domain.

The potential on the side and upper boundaries is calculated so that the contributions of all the charges within the simulation domain as well as the ground images of these charges are accounted for. Those boundary conditions are further referred to as “open boundaries.” The ground is assumed to be a perfect conductor with potential $\phi_{\text{gnd}}=0$ V. Consequently, the electric potential at the boundaries prior to the discharge can be obtained directly from the following expression [e.g., *Liu and Pasko, 2006*]:

$$\phi(\vec{r}) = \phi_{\text{amb}}(\vec{r}) = \frac{1}{4\pi\epsilon_0} \iiint_{V'} \frac{\rho_{\text{amb}}(\vec{r}')}{|\vec{r} - \vec{r}'|} dV' + \frac{1}{4\pi\epsilon_0} \iiint_{V'} \frac{\rho_{\text{amb}}^i(\vec{r}'_i)}{|\vec{r} - \vec{r}'_i|} dV' \quad (2.1)$$

where \vec{r} defines the coordinate vector of a point at a boundary and $\phi(\vec{r})$ the total potential at this point. The quantity $\rho_{\text{amb}}(\vec{r}')$ refers to the ambient charge density at point \vec{r}' , and $\rho_{\text{amb}}^i(\vec{r}'_i)$ designates the ground image of the ambient charge distribution at point \vec{r}'_i . Having calculated potential values on the boundaries, we numerically solve Poisson’s equation $\nabla^2\phi_{\text{amb}}=-\rho_{\text{amb}}/\epsilon_0$ using a successive overrelaxation (SOR) algorithm [e.g., *Hockney and Eastwood, 1981*, p. 179] to calculate ϕ_{amb} and $\vec{E}_{\text{amb}}=-\nabla\phi_{\text{amb}}$ inside of the simulation domain. The development of discharge trees starts when the cloud charges reach values such that the ambient field exceeds a predefined initiation threshold E_{init} for a lightning discharge by 10% somewhere in the simulation domain (the related charge values are shown in Table 3.1). From this moment on, the ambient charge distribution remains unchanged.

The exact value of the initiation threshold (i.e., of the electric field E_{init} required to initiate the lightning) is not well established, nor are the mechanisms of the lightning initiation [e.g., *Marshall et al., 1995; Dwyer, 2003; Behnke et al., 2005*, and references therein]. A general consensus exists in the present literature that values around $\sim 1\text{--}2$ kV/cm at sea level represent a reasonable estimate of fields needed for lightning initiation [e.g., *Gurevich and Zybin, 2001; MacGorman et al., 2001; Behnke et al., 2005; Helsdon and Poepfel, 2005; Mansell et al., 2005; Marshall et al., 2005*]. For the purposes of modeling discussed in this dissertation, we adopt

a value $E_{\text{init}}=2.16$ kV/cm similar to that used in recent studies of *Krehbiel et al.* [2004] and *Marshall et al.* [2005].

We note that the field value $\simeq 2.16$ kV/cm at sea level is the minimum field needed to balance the dynamic friction force in air on a relativistic electron with ~ 1 MeV energy [e.g., *McCarthy and Parks*, 1992; *Gurevich et al.*, 1992; *Rousset-Dupré et al.*, 1994; *Lehtinen et al.*, 1999; *Gurevich and Zybin*, 2001]. We emphasize however that similarly to previous work [e.g., *Pasko and George*, 2002] we use 2.16 kV/cm only as a reference field, making no direct association of the relativistic runaway phenomenon and lightning initiation in our model. The intracloud discharge develops as a bi-directional leader from the inception point. Although controlled by different processes, the propagation of the positive or negative branches is known to require nearly identical electric fields [e.g., *Raizer*, 1991, p. 375; *Bazelyan and Raizer*, 1998, p. 253; *Rakov and Uman*, 2003, p. 322]. This propagation threshold, denoted E_{th}^{\pm} , is about 1 kV/cm in large laboratory gaps (several tens of meters long) [*Raizer*, 1991, p. 362] and can be substantially lower in the case of lightning leaders [*Gallimberti et al.*, 2002, and references therein]. Both the lightning initiation E_{init} and propagation E_{th}^{\pm} thresholds represent input parameters in our model. In the framework of the present work, the increases or decreases in these thresholds would lead to corresponding increases or decreases in thundercloud charge values and densities and would not affect any principal conclusions derived from the present study. In the remainder of this dissertation, we simply assume the same initiation and propagation thresholds $E_{\text{init}}=E_{\text{th}}^{\pm}=\pm 2.16$ kV/cm, where E_{th}^{+} is positive and represents the propagation threshold of positive leaders, and E_{th}^{-} is negative and represents the propagation threshold of negative leaders. These values are given at sea level, and it is assumed that they vary proportionally to the neutral atmospheric density N at other altitudes. Practical considerations have led us to define every altitude z in our model with respect to the ground level (i.e., $z=0$ is always referred to as ground level). Sea level is the usual reference for neutral atmospheric density N however. Because ground level and sea level do not always coincide (e.g., when considering measurements in New Mexico thunderstorms), it is judicious to introduce explicitly the difference between ground level and sea level and to denote it as z_{gnd} . Therefore, the initiation and propagation thresholds can be derived at any altitude z above ground using the following

representation:

$$E_{\text{init}}(z) = E_{\text{th}}^{\pm}(z) = \pm 2.16 \frac{N(z+z_{\text{gnd}})}{N_0} [\text{kV/cm}] \quad (2.2)$$

where N_0 is the value of the neutral density at sea level.

As already noted above, the model thundercloud achieves a maturity state sufficient for initiation of the model intracloud discharge discussed in Chapter 3 when the corresponding ambient electric field exceeds the initiation threshold field by 10% somewhere in the simulation domain. As a result of this process, a region of high electric field exceeding the initiation threshold by 0 to 10% is created around the central vertical axis of the simulation domain between the upper positive and central negative charge layers. The inception point is chosen randomly in this region with no weighting based on the ambient electric field magnitude. Thus, every point at which $E_{\text{amb}} \geq E_{\text{init}}$ has equal probability to initiate the discharge. The leader channel propagates iteratively from this starting point; at each step, one and only one link is added (at either the upper or the lower end of the tree) and the potential is updated to ensure the overall neutrality of the channel. To illustrate the procedure, we start from an existing channel and describe each step required to achieve the next stage of the development of the discharge tree.

We first define the total potential ϕ , which can be viewed as the ambient potential due to thundercloud charges modified by the presence of the lightning trees up to the current stage of development. Further propagation of the channel requires the knowledge of ϕ inside of the domain. How ϕ is determined is discussed later in this section. At this point, we assume that the total potential has already been established and show how the next segment of the discharge tree is added. By the choice of the new link, we introduce stochasticity in the model. Starting from the existing channel, a new link is chosen among the candidates, which are defined as the possible links between the channel points and the neighboring points where the local electric field exceeds E_{th}^{\pm} . For each candidate link i , the local electric field E_i is calculated as $E_i = (\phi^{\text{start}} - \phi^{\text{end}})/l$, where ϕ^{start} and ϕ^{end} are the total potentials at the tips of the candidate link, and l is the length of the link. Consequently, a positive or negative leader will be able to propagate through a candidate link i if $E_i \geq E_{\text{th}}^+$ or $E_i \leq E_{\text{th}}^-$, respectively. Examples of candidates originating from two

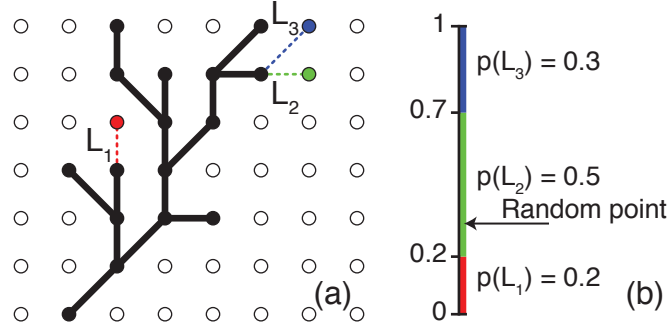


Figure 2.2. Channel extension in a 2-D geometry. (a) Channel links (solid lines) and link candidates (dashed lines); (b) Probability associated with each link. (The values of the probabilities given on this plot are arbitrary and are shown only for two representative points on the existing discharge tree for the purposes of illustration. Actual values are derived based on the analysis of potential differences involving all grid points of the existing discharge tree—see text for details.)

representative points on an existing discharge tree are shown in Figure 2.2a. The existing tree is represented using solid lines, and the candidate links are represented by dashed lines. Figure 2.2a is plotted in 2-D for the sake of clarity, and an extension to the 3-D geometry actually used by the model is straightforward. The probability p_i of the channel growth associated with candidate link i is assigned as follows [e.g., *Wiesmann and Zeller*, 1986; *Femia et al.*, 1993]:

$$p_i = \frac{|E_i - E_{th}^\pm|^\eta}{\sum_i |E_i - E_{th}^\pm|^\eta} \quad (2.3)$$

where η is called the probability sensitivity. The value of η has been derived by *Popov* [2002] to be 1 for streamer discharges in air. No similar derivation exists for the case of leader discharges. For all calculations presented in this dissertation, we adopt $\eta=1$, which is a common choice in existing fractal models [e.g., *Niemeyer and Wiesmann*, 1987; *Mansell et al.*, 2002]. The probability associated with each link can be represented as a portion of a segment of unity length (see Figure 2.2b). By picking randomly a point between 0 and 1 on this segment, we select the new link. Therefore, this procedure accounts for both the propensity of the channel to develop in regions of strong electric field and for the stochastic nature of the leader development.

Once the new link has been selected, the potential needs to be redefined in the channel, inside of the domain and at its boundaries. This potential adjustment, which has formerly been used for simple deterministic models [e.g., *Mazur and Ruhnke*, 1998], is the salient component of the model compared with the previous fractal modeling of the lightning discharge [e.g., *Mansell et al.*, 2002], and must account for the overall neutrality of the discharge tree and its equipotentiality, which is achieved in the following way. From the principle of superposition, the total potential in the presence of a conducting tree at each point M inside the simulation domain can be written as $\phi(M)=\phi_{\text{amb}}(M)+\phi_{\text{cha}}(M)$, where $\phi_{\text{cha}}(M)$ is the potential due to the charges induced on the channel. In particular, for points P on the channel, $\phi_{\text{cha}}(P)=\phi_0-\phi_{\text{amb}}(P)$ to make the channel an equipotential characterized by the constant potential ϕ_0 . A simple iterative procedure is used to determine the value of channel potential ϕ_0 that minimizes the net charge on the channel as described below in this section. The updated values of ϕ_{cha} after the addition of a new link are derived by solving Laplace's equation $\nabla^2\phi_{\text{cha}}=0$ using the SOR algorithm with Dirichlet's conditions (i.e., fixed potential) on the interior and exterior boundaries defined hereafter. The grid points occupied by the channel serve as an interior boundary, and the potential $\phi_{\text{cha}}(P)$ at these points is fixed and set to $\phi_0-\phi_{\text{amb}}(P)$ as detailed above. The values of the potential on the boundaries of the simulation domain define the exterior boundary. They are taken from potential solutions obtained after the previous link was added and are also assumed fixed. Having applied Poisson's equation to the new result for ϕ_{cha} , but now including the points on the channel in the calculation of the Laplacian, we can estimate the charge density ρ_{cha} associated with the channel as $\rho_{\text{cha}}=-\epsilon_0\nabla^2\phi_{\text{cha}}$. Because $\nabla^2\phi_{\text{cha}}=0$ everywhere outside the grid points that belong to the discharge trees, ρ_{cha} is confined only to the grid points on the channel. The total charge Q_{cha} on the channel can then be obtained by performing an integration of ρ_{cha} over the volume V of grid points associated with the discharge trees as follows: $Q_{\text{cha}}=\iiint_V \rho_{\text{cha}}(\vec{r})dV$. In addition, the electric dipole moment \vec{p} of the discharge trees is derived for diagnostic purposes as: $\vec{p}=\iiint_V \vec{r}\rho_{\text{cha}}(\vec{r})dV$ [e.g., *Zahn*, 1987, p. 139].

The value of ϕ_0 to achieve overall neutrality of the channel, namely $Q_{\text{cha}}=0$ C, is determined by applying a bisection method [e.g., *Press et al.*, 1992, p. 353].

This root-finding algorithm requires that the solution is known to lie inside a given interval. For the present model, the total potential ϕ_0 of the channel will necessarily lie between the minimum and the maximum of the ambient potential. Because the algorithm quickly converges to the solution, we simply use the extrema of ϕ_{amb} to bound the solution instead of attempting to estimate ϕ_0 based on its value at the previous stage of the channel development.

Having determined ϕ_0 and ϕ_{cha} as described above, the effect of the channel is known everywhere in the simulation domain following addition of each new link. In particular, the determination of ρ_{cha} enables us to update the contribution of the channel to the potential at the simulation domain boundaries. This contribution is calculated using (2.1) with ϕ_{amb} , ρ_{amb} , and ρ_{amb}^i respectively replaced by ϕ_{cha} , ρ_{cha} , and ρ_{cha}^i , where ρ_{cha}^i is the ground image of the channel charge. The recalculated values are used for the boundary conditions during the next step of the discharge development. Thus, the update of the simulation domain boundary conditions is always one link behind with respect to advancement of the channel. This delay is due to the impossibility of determining the effect of a link on the boundary conditions prior to its establishment. Because the difference is only that due to the addition of a single link, the errors introduced by this approach are expected to be small. Typically, for the simulation results presented in the next chapter, a link modifies the total potential at the boundary by less than 1%. Even though the changes are small ($\leq 1\%$) during every step of the model execution, we fully recalculate the potential at the side and upper boundaries after each addition of a new link for maximum accuracy.

Finally, recalling that ϕ_{amb} has been previously derived inside of the domain and at its boundaries, the potential at any point M of the domain can be obtained using the principle of superposition $\phi(M) = \phi_{\text{cha}}(M) + \phi_{\text{amb}}(M)$. At this stage, all requirements are fulfilled and model execution proceeds to development of the next link. This procedure is repeated until no candidate links for further extension can be found or until a channel link reaches the ground. In the next chapter, we focus on studies of intracloud discharges, which are more probable for the thundercloud charge configuration specified at the beginning of this section.

2.3 Summary of Results

In this chapter, a three-dimensional model of intracloud lightning discharge is described, based on *Kasemir's* [1960] hypotheses of equipotentiality and neutrality of the channel, and on the dielectric breakdown model proposed by *Niemeyer et al.* [1984]. This model is applied in Chapter 3 to the study of the development of intracloud discharges, and is used in the framework of the theory of charge imbalances developed in Chapter 4 to explain the physical similarities between lightning and jet discharges.

Modeling of an Intracloud Discharge in a New Mexico Thunderstorm and Comparison with LMA Observations

In this chapter, we apply the model introduced in Chapter 2 to simulate an intracloud lightning discharge. The simulation results give insight into the fundamental mechanisms of the propagation of the lightning channel and provide a quantitative validation of the lightning leader model. The results presented in this chapter are published in [Riousset *et al.*, 2007a].

3.1 Results of Modeling of an Intracloud Discharge

In this section, we report results from a representative simulation run corresponding to an intracloud discharge. The results are obtained in a 12 km×12 km×12 km simulation domain, which is discretized using 41×41×61 equidistant grid points. Hence, the spatial resolution is 300 m in the horizontal x - and y -directions and 200 m in the vertical z -direction. We note that the ground level for lightning simulations is different from the reference altitude for the LMA measurements (which is usually within 10 m of the mean sea level [Rison *et al.*, 1999]). As discussed in the Chapter 2, our model uses ground level

as the zero altitude ($z=0$ km) reference point. To ease direct comparison with LMA results, all plot results produced by our model are shifted by adding z_{gnd} to z such that all altitudes in Figures 2.1 and 3.1 through 3.4 are given with reference to sea level. After ~ 32.5 seconds of application of charging currents I_1 and I_2 with magnitudes defined in Chapter 2, the conditions for lightning initiation are fulfilled (i.e., the electric field at one of the points inside of the simulation domain exceeds E_{init} threshold by 10%). These currents produce cloud charge density ρ_{amb} in the two upper charge layers on the order of ± 1 nC/m³. These values are smaller than those inferred from measurements by *Williams et al.* [1985] or *Coleman et al.* [2003], but still are of the same order of magnitude. The positions, dimensions and integral charge values corresponding to each charge layer at this moment of time are summarized in Table 3.1.

Figure 2.1 shows a cross-sectional view of the model thundercloud (in the y - z plane positioned in the center of the simulation domain at $x=6$ km). The upper and lower positive charge layers are identified by the letters ‘P’ and ‘LP’ respectively, and the central negative charge layer is identified by the letter ‘N’. In addition, Figure 2.1 also illustrates the electric field lines produced by this charge configuration just before the initiation of the discharge. The electric field lines converge toward the negative charge center and diverge from the upper positive one, consistent with expectations. At the lower boundary, the field is normal to the equipotential ground surface, also consistent with field theory.

If equipotential boundaries with potential equal to ϕ_{gnd} were used, then the field line pattern would be conspicuously modified close to the side and top boundaries, where the field lines would be normal to the edges of the domain. This modification is best seen if the number of field lines in Figure 2.1 is increased (Figure 3.1b),

Table 3.1. Charge values, heights and extents for the cylindrical disk model.

Charge Layer	Altitude (km AGL ^a)	Depth (km)	Radius (km)	Charge (C)
P	6.75	1.5	4.0	48.7
N	3.75	1.5	3.0	-51.6
LP	2.00	1.5	1.5	2.92

^aAGL, above ground level

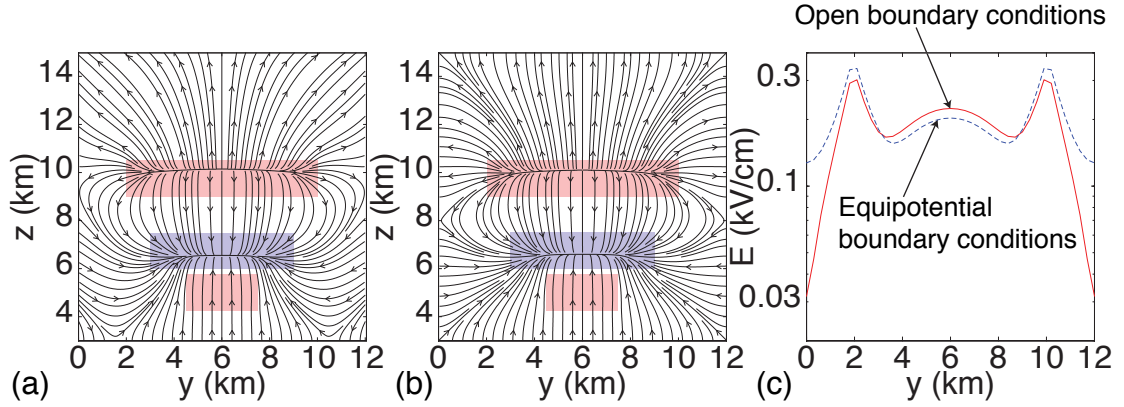


Figure 3.1. Electric field line pattern of the thundercloud with parameters specified in Table 3.1 in a simulation domain with (a) equipotential boundaries; (b) open boundaries. (c) Comparison of the electric field magnitudes using equipotential (dashed line) and open boundary conditions (solid line) at an altitude of 9.8 km.

and the resulting field line pattern compared with that of the same thundercloud when equipotential boundaries are employed (Figure 3.1a). The magnitude of the electric field would also be modified by the use of equipotential boundary conditions. A comparison of the y -span of the field magnitude at 9.8 km altitude (in the middle of the upper positive charge layer) and at the center of the simulation domain at $x=6$ km (Figure 3.1c) shows that the use of equipotential boundary conditions introduces a noticeable error, in particular close to the boundaries. In particular, at $y=0$ km, the field magnitude is $\sim 3.2 \times 10^3$ V/m using the open boundary simulation domain, and $\sim 1.2 \times 10^4$ V/m using equipotential boundaries. Hence equipotential boundaries are not suitable for narrow simulation domains such as the one employed in this study. We additionally note that in both cases, the field magnitude is much greater than the fair weather field magnitude at the same altitude ~ 4.7 V/m [Rakov and Uman, 2003, p. 9].

Figure 3.2 shows an example of a fully developed discharge. The discharge trees are projected on the x - y , y - z and x - z planes (shown, respectively in panels (b), (d) and (e) of Figure 3.2). Panel (c) in Figure 3.2 shows a histogram representing the numbers of grid points occupied by the discharge links as a function of the altitude. Finally, the altitude of each new link at each step is plotted in the upper panel (i.e., panel (a) of Figure 3.2). The sequence of steps in our model can be considered as resembling the temporal development of lightning flashes in the actual LMA

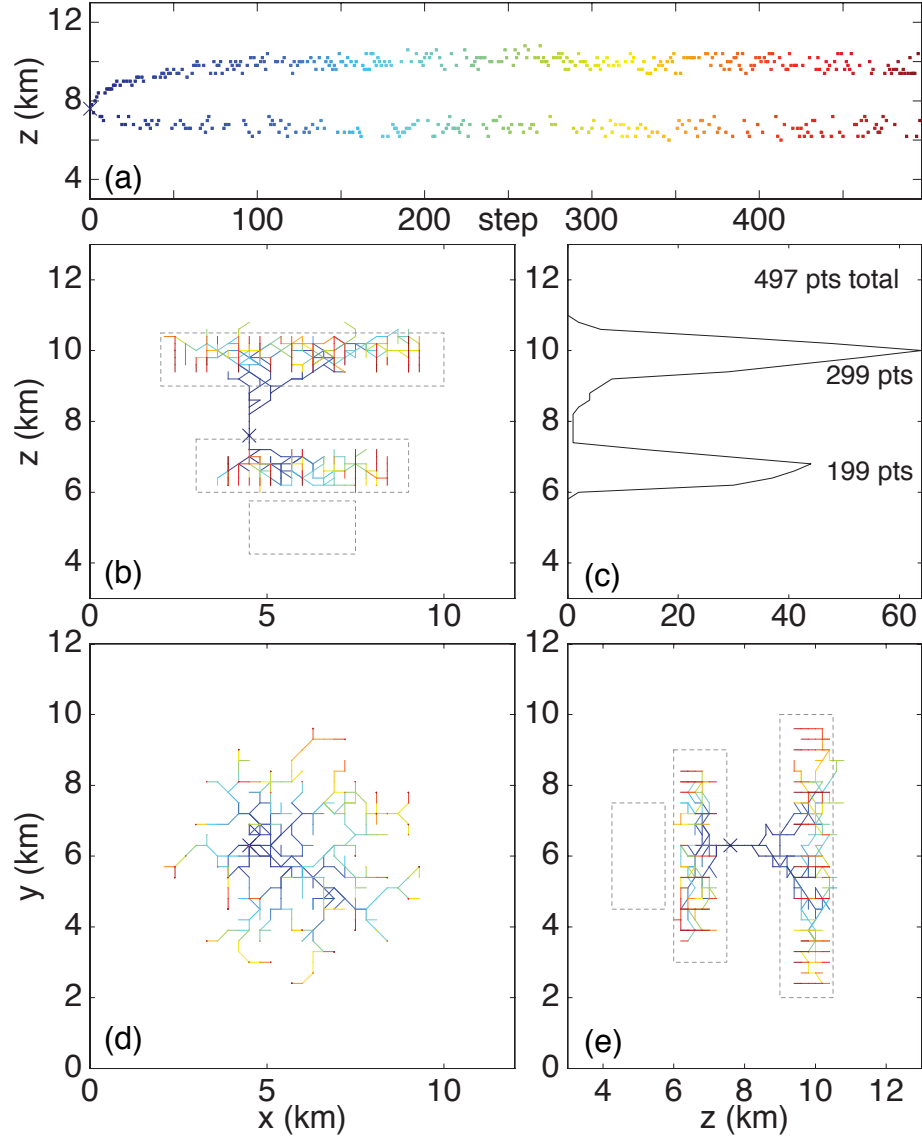


Figure 3.2. Representation in Lightning Mapping Array (LMA) data form of a simulated intracloud discharge. We use the same formatting as for the LMA data shown in Figure 3.3. In panel (c), the total number of grid points crossed by the discharge (497) corresponds to the sum of the number of grid points crossed by the upper branches (299) and lower branches (199) minus one because, the initiation point is counted twice, being part of both the upper and lower branches. Adapted from [Riousset *et al.*, 2007a, Figures 4, 6, and 7].

measurements. The step number gives the sequence of creation of new links in the model, and a color-scale similar to actual LMA data is used. For this run, ground level is set at 3 km above sea level (the approximate altitude of the ground for measurements of the lightning activity near Langmuir Laboratory in central New Mexico). The topographic profile at the location of the LMA observations is presented in [Rison *et al.*, 1999, (Figures 3, 4 and 6)] and justifies the assumption of a flat ground plane at the above altitude, due to the relatively small variations of the ground elevation (≤ 1 km) in comparison with the altitudes of the charge centers and that of the development of the intracloud discharge (between 6 and 11 km, see Figure 3.3). The simulated discharge is initiated at an altitude of 7.6 km above sea level (4.6 km above ground level), ~ 1.5 km radially away from the central vertical axis of the simulation domain. The developing leader initially extends vertically without showing much branching structure between ~ 7.0 and ~ 9.2 km before spreading horizontally in the volume of the main negative and upper positive charge layers (at altitudes around 6.5 and 10 km, respectively). In addition, we show the contours of the charge centers in panels (b) and (e) by dashed gray lines. Inspection of this figure shows that the negative leaders are essentially contained in the upper positive charge layer while positive leaders are mainly “trapped” in the central negative charge layer.

Figure 3.3 presents an actual intracloud lightning event detected by the LMA over Langmuir Laboratory on July 31, 1999 at 22:23 (local time). This event is similar to the bilevel discharge first reported by Rison *et al.* [1999]. We note that the inception point of the discharge is at an altitude of ~ 8.0 km on the southeastern edge of the storm. The discharge then propagates vertically between altitudes around 7.0 and 9.0 km, where horizontal propagation then becomes dominant.

Figure 3.4a shows the model discharge of Figure 3.2 in a 3-D representation, and Figures 3.4b and 3.4c compare respectively the total electric field and potential before and after the flash at the center of the simulation domain, along the vertical axis. The propagation threshold given by (2.2) is also shown for reference in Figure 3.4b. A positive value of the electric field indicates an upward directed field.

Figure 3.5a shows the evolution of the discharge tree total potential ϕ_0 . The charge carried by the positive leaders is illustrated in Figure 3.5b. We note that

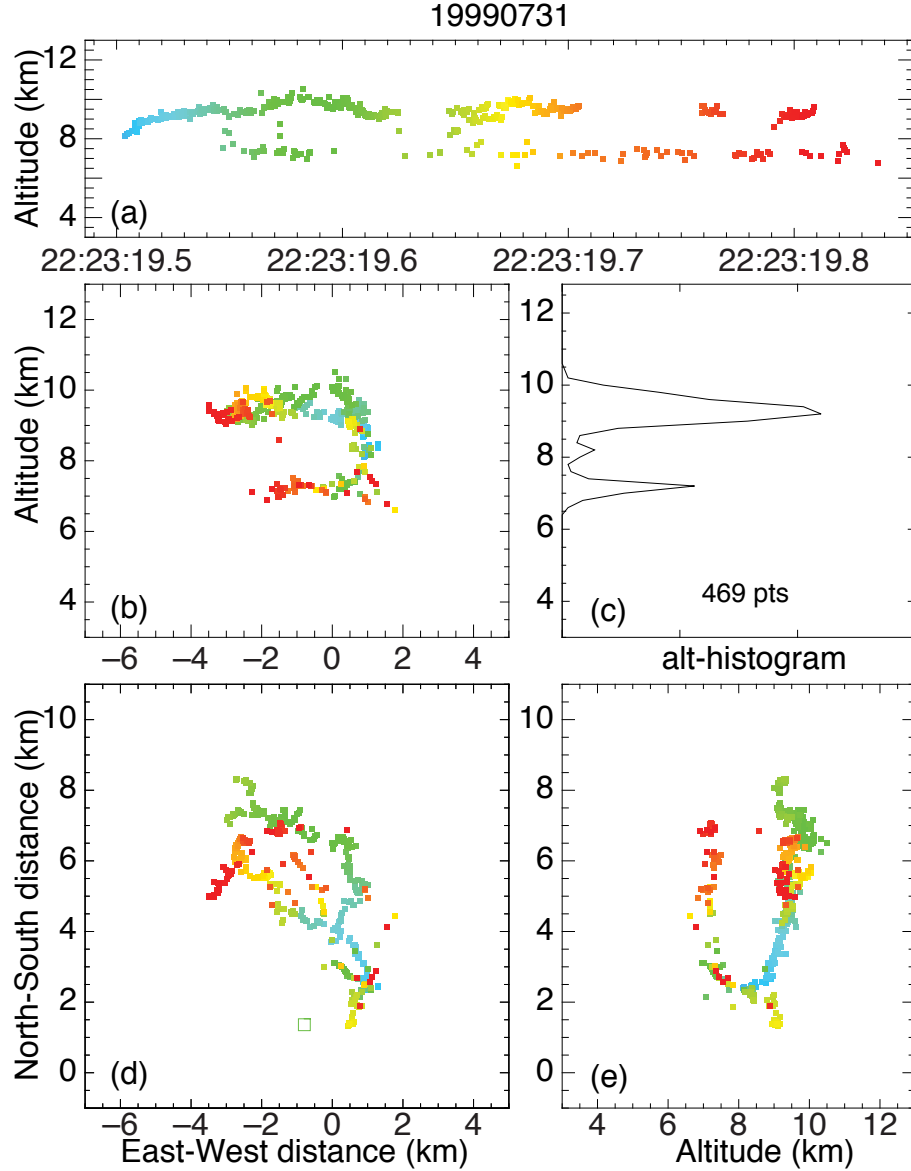


Figure 3.3. An actual bilevel intracloud flash measured by the LMA during the thunderstorm on July 31, 1999 at 22:23 (local time).

negative leaders carry an equal amount of negative charge, and the charge shown in Figure 3.5b can be interpreted as the total charge transferred by the discharge. Figures 3.5c and 3.5d illustrate the evolution of the discharge dipole moment as the simulation progresses. Figure 3.5a shows a rapid increase of the channel potential at the early stages of the discharge development, from an initial value of -47.5 MV at the inception point, followed by a smoother increase after which ϕ_0

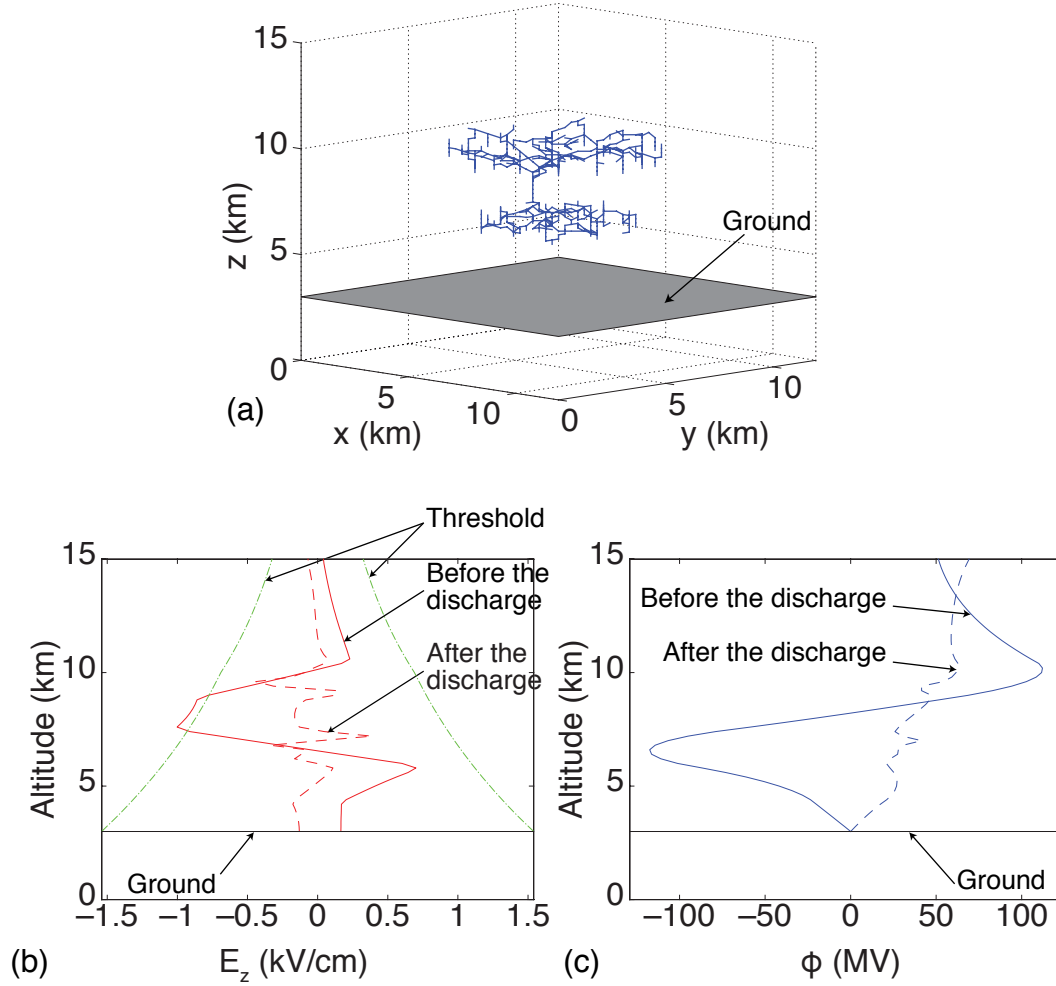


Figure 3.4. (a) 3-D view of the intracloud discharge shown in Figure 3.2 after 496 steps; (b) Electric field before the flash (solid line), and after (dashed line) along the central vertical axis of the simulation domain. The electric field initiation threshold is shown for reference by dash-dotted lines; (c) Electric potential before (solid line), and after (dashed line) the discharge development along the same axis.

reaches the final value of ~ 41.5 MV. Figure 3.5c shows a progressive growth of the charge transferred by the discharge that reaches value ~ 37.5 C by the end of the simulation. The magnitude of the dipole moment \vec{p} shown in Figure 3.5d also smoothly increases reaching ~ 122 C \cdot km. Figure 3.5b shows that \vec{p} is predominantly vertical and directed downward. This trend is consistent with the development of the trees, because the horizontal components of \vec{p} (i.e., p_x and p_y) become more and more negligible compared with the vertical component p_z .

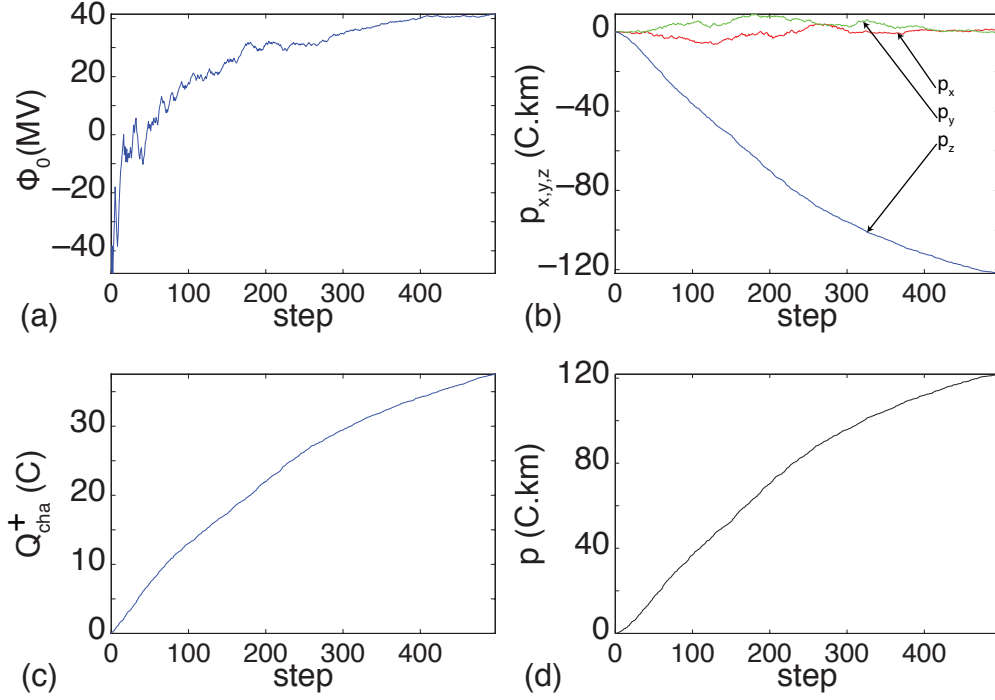


Figure 3.5. Parameters of the simulated discharge shown in Figure 3.2 at each step of the development: (a) Channel potential ϕ_0 ; (b) Charge carried by the positive leaders Q_{cha}^+ ; (c) Magnitude of the discharge electric dipole moment $p = |\vec{p}|$; (d) x -, y - and z -components of the dipole moment \vec{p} .

A comparison of the total charge in the system before and after the development of the discharge trees allows us to check the charge conservation. The system remains approximately neutral, with differences between absolute values of positive and negative charges not exceeding ~ 30 mC during different stages of the model execution. This difference is mainly due to numerical noise and is negligible compared with the charge in the cloud or in the upper and lower channel structures. As already noted above, the amount of charge carried by the positive and negative leaders is ~ 37.5 C, which constitutes $\sim 75\%$ of thundercloud charges of each polarity (i.e., 51.6 C) as shown in Table 3.1.

3.2 Discussion

Advanced fractal modeling accounting for the charge neutrality of the discharge is reported by *Mansell et al.* [2002]. Although both this model and ours make

use of similar hypotheses (namely neutrality of the channel and equipotentiality or quasi-equipotentiality of the channel), the treatments of the channel neutrality and of the boundary conditions differ and constitute two salient improvements of our model.

Unlike other fractal models referenced in Chapter 2, our model modifies the channel potential as the discharge propagates. Previous models involving the charge neutrality of the channel have employed mathematical artifacts to ensure electric neutrality of the discharge, e.g., by varying the propagation thresholds [Mansell *et al.*, 2002]. In contrast to these models, we have chosen to develop a solution involving a physics-based potential variation. This solution avoids the introduction of additional parameters such as the percentage of charge imbalance allowed during the simulation run and the range of variation of the propagation thresholds. Furthermore, it ensures the neutrality at each stage of advancement of the discharge.

The treatment of the boundary conditions also represents a significant improvement compared with previous lightning models. Although simple, fixed Dirichlet's and/or Neumann's conditions have commonly been used in previous modeling [e.g., Mansell *et al.*, 2002], the choice of a similar Dirichlet's condition at the ground but open boundary conditions on the upper and side boundaries (see Chapter 2) allows us to simulate an open domain in order to obtain a better modeling of the mirror charges. Also, this solution lets us place the boundaries closer to the charge centers, hence yielding an increased resolution in the simulation domain, which is of major importance for further advancement of lightning simulation studies.

The simulation run described in Section 3.1 is typical for intracloud discharges produced by our model. As is discussed in this section, it shows many similarities with the bi-level discharge observed during the thunderstorm over Langmuir Laboratory on July 31, 1999, which is reproduced in Figure 3.3. Comparability between fractal modeling and lightning mapping data is mentioned by Mansell *et al.* [2002]. This chapter further develops the comparison between actual and model lightning discharges and introduces a quantitative evaluation of the simulation results.

The LMA observations (Figure 3.3) show the initial 2–3 km vertical propagation followed by two distinct regions of roughly horizontal propagation at altitudes of ~6.5 and ~9.5 km. The upper region corresponds to the propagation of the

negative leaders in the thundercloud positive charge, and the lower one to that of the positive leaders in the main negative charge. The propagation altitudes of the model discharge are mostly defined by the chosen positions of the model thundercloud charges, which are inferred directly from observations of actual lightning discharges following the conclusions in [Coleman *et al.*, 2003]. Consequently, the model discharge (Figure 3.2) develops in the two upper charge layers at altitudes matching the altitudes of propagation of the actual discharge (Figure 3.3).

Comparison of Figures 3.2 and 3.3 shows that both the simulated and measured discharges are not initiated on the axis of the inferred storm charges, although they both propagate in a rather symmetric manner toward and in the upper positive and central negative charge layers. It is recalled that the x - and y -directions in our simulation are arbitrary and do not necessarily correspond to East-West and North-South directions in Figure 3.3. Thus, no conclusions should be drawn from the horizontal position of the initiation point; it should merely be noticed instead, that our initiation algorithm produces realistic horizontal displacement of the initiation point with respect to the axis of the storm charge layers. The random initiation algorithm employed in the simulation uses the idea that the lightning is probably not initiated immediately upon the threshold being exceeded at some point in the cloud, but after the threshold is over-exceeded over some larger horizontal area. Initiating the discharge once the threshold is exceeded by 10% somewhere in the simulation domain allows the growing charges Q_{LP} , Q_N and Q_P to create such a region around the central vertical axis. The lightning is then initiated randomly within this area of high electric field (exceeding the initiation threshold E_{init}).

The initiation point should be regarded primarily as an indicator of the locations of strongest vertical fields. In realistic situations, the initiation point is also expected to depend on the non-uniformity of the actual storm charges. It is quite improbable that the actual thundercloud has the perfect cylindrical symmetry assumed by the model. Therefore, a non-uniform charge distribution is considered as a primary factor, which would lead to the lightning being initiated away from the center of the charge region as in the case of Figure 3.3.

Tests have also been conducted with non-random initiation (the related results are not shown in this work for the sake of brevity). In this case, the discharge is always initiated at the point of maximum electric field magnitude. Due to the

cylindrical geometry of the modeled thundercloud, this point is always on the main axis of the inferred charge layers at an altitude of 7.6 km. The same initial 2–3 km vertical extension of the tree followed by the horizontal propagations at altitudes around 6.5 and 10.0 km is observed. The main difference is that the discharge takes a more symmetric form because the horizontal shift of the initiation point is suppressed. Quantitatively, the values for the channel potential, transferred charge, linear charge density and dipole moments remain very close to those discussed for the simulation presented in Figures 3.2 and 3.4 with parameters shown in Figure 3.5.

When the contours outlining the positions of the charge layers are superimposed with the discharge channels, as in Figure 3.2, it becomes obvious that simulated trees tend to propagate more or less through the full extent of the parent storm charges. A similar effect is observed for dielectric breakdown in polymethylmethacrylate (PMMA) [*Williams et al.*, 1985]. This property has also been suggested for real intracloud discharges [e.g., *Shao and Krehbiel*, 1996; *Coleman et al.*, 2003] and has been noticed in previous fractal modeling of lightning [*Mansell et al.*, 2002]. The complexity of the charge structures involved in both observations and *Mansell et al.*'s [2002] simulation results makes it difficult to interpret the full extent of the effects of net charges on the development of the channel. In particular, although *Mansell et al.*'s [2002] results show that the leader channels penetrate regions of net charge, the use of a simpler thundercloud charge structure in our model demonstrates that the discharge tends to be strongly limited or confined to such charge regions. This approach is comparable to *Williams et al.*'s [1985] experiments in charged and uncharged polymethylmethacrylate to test the effects of net charge on propagation of discharge trees (see also *Mansell et al.*'s [2002] numerical modeling interpretation of these experiments). This phenomenon can be explained by considering the dramatic changes in the field configuration prior to the discharge (represented in Figure 2.1) caused by the development of the lightning leader tree. In the leader breakdown process, the electric field lines are along the potential gradient between the channel potential and the surrounding ambient potential (see Figures 1.8 and 1.9). Specifically, when a conducting leader channel approaches and progresses into a region of intense charge, the field lines will connect the negative (respectively positive) charges induced on the channel

and the surrounding positive (respectively negative) charges of the charge regions. Due to the large horizontal extension of the charge centers, the field lines become primarily horizontal and the field intensity is also increased in this direction. Because the discharge path is mainly driven by the direction of the local electrostatic field, both in actual [Williams *et al.*, 1985] and simulated clouds, it is expected that the upper and lower ends of the discharge tree would propagate horizontally inside of the charge layers.

A comparison of panels (a), (b) and (c) of Figures 3.2 and 3.3 reveals a far greater number of points for the propagation of the simulated positive leaders when compared with the actual measurements. Rison *et al.* [1999] note that negative breakdown in positive charge regions is inherently noisier at radio frequencies than is positive breakdown in a negative layer. The LMA primarily detects the negative breakdown in the positive charge region. In the negative charge regions, VHF radiation is produced primarily by recoil-type breakdown in which negative leaders re-ionize the channels formed by positive leader breakdown [Shao and Krehbiel, 1996; Shao *et al.*, 1996]. It appears that the LMA is locating such recoil activity in the negative charge regions. Recoil processes are not accounted for in our model. The model thus simulates what the LMA detects due to negative leaders, but not positive leaders. Yet, comparison of positive and negative leader trees in Figure 3.2 reveals that positive trees developing in the lower portion of the discharge occupy fewer grid points than negative ones. This effect is purely numerical (i.e., is not related to physical differences between different types of leaders observed in LMA data). Indeed, the upper positive and central negative charge centers have different radii (4 and 3 km, respectively) but are discretized using grids with identical grid size. Thus, to extend through the entire volume of each charge layer, the discharge should require $(\pi R_P^2 d_P)/(\pi R_N^2 d_N)$ times as many steps in the positive as in the negative charge region. Here, R_P , d_P designate, respectively, the radius and depth of the upper positive charge layer, and R_N , d_N refer to the same quantities for the central negative charge region. Using values tabulated in Table 3.1, we calculate this ratio to be ~ 1.78 , which is in good agreement with the ratio derived ~ 1.51 from Figures 3.2c.

Comparison of Figures 3.2d and 3.3d emphasizes a major difference in the horizontal development of the simulated discharges compared with that of the mea-

sured ones, namely the horizontal structure of the simulated trees looks far more complex. As noted previously, LMA measurements appear primarily to detect negative polarity, recoil-type breakdown associated with positive leaders. Therefore the LMA map of negative leaders closely matches the map of modeled negative channels but the LMA map of positive leaders has a different and simpler pattern than that of the modeled positive channels (see Figure 3.2). Additionally, inspection of Figure 3.2 shows little difference between horizontal developments of positive and negative trees. The present version of the model does not include any differences between positive and negative leaders, and their streamer zones in particular, and an extension of the model to account for related effects represents a subject of future studies. It is also most likely that the details and complexities of the storm charge structure, which are not reproduced in our model (but have been studied by *Poulos et al.* [2008]), are largely responsible for the observed discharge structure shown in Figure 3.3.

The calculated value of the charge carried by the leader trees is estimated at every step of the simulation and is plotted for positive branches in Figure 3.5b. The value at the end of the discharge development, ~ 37.5 C is of particular interest and can be compared with the values obtained from both observational and modeling studies. From multi-station electric field change measurements, *Krehbiel* [1981] determined that the charge transfer during the first twelve intracloud discharges in a small developing Florida thunderstorm steadily increased from about 3 C for the initial intracloud discharge to 21 C for the twelfth discharge (see also [*Krehbiel et al.*, 1984a]). In addition, the charge transfer for an energetic intracloud discharge in a fully developed storm is estimated to be about 50 C [*Krehbiel et al.*, 1984b; *Shao and Krehbiel*, 1996]. *Helsdon et al.* [1992] quote typical values for the charge transferred ranging between 0.3 and 100 C. *Shao and Krehbiel* [1996] estimate charge transfer to be 8.5 and 49 C for two intracloud discharges in Florida based on interferometer data and single-station electric field change measurements. *Rakov and Uman* [2003, p. 325] list the charge transfer values between 21 and 32 C for an intracloud discharge in a New Mexico thunderstorm. Previous fractal modeling of intracloud discharges estimates the charge transfer between 36.3 and 52.4 C [*Mansell et al.*, 2002, Figures 7 and 8]. Our model results are generally consistent with values documented in the literature.

The average linear charge density of discharge trees in our model can also be estimated and compared with previously published values. This calculation is done by summing the absolute value of the charge carried by channels of each polarity and dividing it by the total length of the channels (~ 147 km), leading to an estimate ~ 0.5 mC/m. This value is below but still is in a reasonable agreement with a value of 1 mC/m referred to by *Helsdon et al.* [1992] and *Mazur and Ruhnke* [1998]. It is also in good agreement with the linear charge densities between 0.7 and 8.7 mC/m estimated by *Proctor* [1997] for intracloud flashes with origin similar to that of the simulated discharge presented in this chapter.

Figure 3.5a shows the evolution of the channel potential during the development of the discharge trees. Being initiated just above the central negative layer, the initial channel potential ϕ_0 is strongly negative ($\simeq -47.5$ MV). In the early stages of the development (~ 30 steps), while the breakdown tree is developing vertically, ϕ_0 rapidly increases to approximately 0 MV. This change in potential is required to maintain channel neutrality in an asymmetric potential environment. In particular, the induced charge density along a linear, vertical equipotential channel is proportional to the difference between the channel potential and the ambient thundercloud potential at the same altitude. To maintain overall charge neutrality in the presence of an asymmetric potential profile, the leader potential changes as the breakdown increases in vertical extent [e.g., *Mazur and Ruhnke*, 1998; *Bazelyan and Raizer*, 2000, pp. 152–153; *Behnke et al.*, 2005, Figures 5 and 6]. For the simulation of this study, the negative and upper positive charges are nearly equal and opposite and the lower positive charge is relatively weak, so that the ambient potential profile becomes approximately symmetric when the channel potential ϕ_0 reaches about 0 MV (Figure 3.4c). Beyond ~ 30 iteration steps, the channel has entered the upper positive charge region and starts developing horizontally (Figure 3.2a). The channel potential continues to increase at a slower rate due to changes in the neutral midpoint location as the discharge develops, but more importantly due to substantial changes in the ambient potential profile and as the thundercloud becomes increasingly discharged. The channel potential at the end of the simulated discharge is about +41.5 MV, indicative of the potential of the discharged storm at the end of the discharge (Figure 3.4c).

The regions of intense charge correspond to wells of ambient potential [*Coleman*

et al., 2003], i.e., extrema of the ambient potential bounded by strong potential gradients. For the simulation of this study, the potential wells are at altitudes of 6.6 km and 10.2 km (Figure 3.4c). Equation (2.3) emphasizes that the discharge develops into regions where the difference between the channel potential ϕ_0 and the surrounding potential (i.e., the ambient potential as modified by the presence of the channel) is maximized. The region where the discharge is initiated is a region of large potential gradients; therefore the discharge rapidly propagates “downhill,” that is to say in the direction of the strongest gradients, into and within the potential wells. The wells extend largely in horizontal directions (5–6 km), but are fairly narrow in the vertical direction (1–2 km). Thus, when the channel reaches the bottom of a well, further propagation in the z -direction would require it to go “uphill,” i.e., towards a decreased potential difference, but horizontal propagation allows the development of the discharge trees into the region where the difference between the channel potential and the surrounding potential is still large. In other words, the discharge starts developing horizontally due to greater potential gradients in the horizontal direction than in the vertical direction. Similar dynamics are observed by *Coleman et al.* [2003] for discharges detected by the LMA.

The altitudes of the potential extrema are slightly different than the altitudes of the charge centers (10.2 km versus 9.75 km for the upper positive charge, respectively, and 6.6 km versus 6.75 km for the negative charge). As noted by *Coleman et al.* [2003], the extrema in the vertical potential profile occur where the vertical component of the electric field E_z happens to pass through zero (Figure 3.4b). The zero crossings are influenced by the presence of multiple charge layers as well as by their locations, polarities and charge contents, causing the altitudes of the potential extrema to be different from those of the isolated charge centers. An important question is where the lightning-deposited charge will be centered. In terms of grid points involved in the simulated discharge, the number of grid points occupied by a discharge channel peaks at altitudes of 10.0 km and 6.8 km in the upper positive and midlevel negative regions, respectively (Figure 3.2c). These peaks are thus displaced somewhat from the altitudes of the potential wells, closer to or at the charge centers themselves. A more detailed understanding of these effects is the subject of continued study.

The overall symmetry of the thunderstorm charge configuration in our model suggests that the resulting discharge electric dipole moment would be essentially vertical. The Q_P and Q_N charge layers form a normal polarity dipole in the upper part of the cloud in which leaders of opposite polarities propagate. It is therefore expected that the fully developed channels would form an opposite polarity dipole (i.e., vertical and preferentially downward-directed). Results presented in Figure 3.5d are consistent with these expectations. Figure 3.5d also indicates that the dipole moment of the discharge is dominated by its vertical component during the full period of propagation of the leader channels. The magnitude of the dipole moment of the fully developed discharge is calculated to be ~ 122 C·km, as compared with the observational values reported by *Krehbiel* [1981] of 13–102 C·km for the initial intracloud discharges in a developing storm and ~ 200 C·km for the energetic intracloud discharge in a fully developed storm, and inferred dipole moment changes of 17 C·km and 147 C·km for the two intracloud discharges studied by *Shao and Krehbiel* [1996]. The results are also consistent with modeling results by *Mansell et al.* [2002], whose simulations estimate $|\vec{p}|=173\text{--}241$ C·km.

The model also allows direct investigation of the reduction of the electric field inside of the thundercloud due to the growth of the discharge trees. The results shown in Figure 3.4b demonstrate that the simulated intracloud leader structure significantly reduces the electric field in the cloud. In particular, the fractional decrease of the electric field by $\sim 80\%$ at an altitude around 8 km is in reasonable agreement with the values $\sim 60\%$ and $\sim 75\%$ measured by *Winn and Byerley* [1975] and *Stolzenburg et al.* [2007], respectively. This reduction is especially pronounced at altitudes ~ 6.5 km and ~ 10.0 km, where most of discharge trees develop (see Figure 3.4b). The field is lowered far below the propagation threshold. Our results therefore demonstrate that under model conditions discussed in this chapter the bulk charge carried by the integral action of positive and negative lightning leaders is sufficient to significantly reduce the value of the electric field in the thundercloud. Alternatively, these results also suggest that the location of the charge deposited by the lightning leader channels can be inferred from the location of strong field reduction in balloon sounding data.

Results of the present study demonstrate the ability of the model to produce realistic intracloud discharges. In so doing, our results further support and expand

upon the idea that lightning propagates through regions of net charge in a thunderstorm, and indicate the extent to which the two are coupled. The simulations also demonstrate that branching occurs primarily within the charge regions and, except for the leaders connecting the charge regions, the breakdown is effectively confined to these charge regions.

A simple explanation for the propagation of lightning through regions of net charge rests on the assumption that discharges will tend to minimize the overall electrical energy of a storm, and that this will not be accomplished if the lightning deposited charges are displaced from the centers of the storm charges themselves (or from the potential wells). *Vonnegut* [1983] raises the question of the simplicity of the relationship between the lightning and storm charges for a phenomenon as complex as lightning. The issue is partly resolved by the laboratory experiments of *Williams et al.* [1985] and by the recent observational studies by *Coleman et al.* [2003] and *Rust et al.* [2005]. These studies clearly establish the existence of a close relationship between the lightning and storm charges and show that lightning charge deposition partially explains the complex charge structures observed by in-situ measurements [*Rust and Marshall*, 1996; *Stolzenburg et al.*, 1998c]. Complete validation of the hypothesis, however, requires simulation of the physics of the process as in the present study and the study by *Mansell et al.* [2002].

The present study tests the above ideas by (a) using lightning data to infer a realistic storm charge structure, (b) growing the charge structure to the point where it would be expected to produce lightning, (c) simulating the lightning with physical models, and (d) comparing the results. The fact that the results compare favorably shows not only that the modeling has been successfully implemented, but more importantly just how lightning responds to the storm charge distribution. Further studies and development of the model are expected to advance these ideas further yet. The results of Figure 3.4b demonstrate that the simulated intracloud leader structure reduces the overall electric field inside the thundercloud. At the same time, the field will be locally enhanced in the vicinity of the lightning channels, which can be investigated with further refinements of the model.

3.3 Summary of Results

In this chapter, we use a realistic thundercloud charge distribution to show that the model developed in Chapter 2 is able to reproduce a realistic pattern of an intracloud discharge (in particular, the altitude of initiation and extensive horizontal propagation of leader channels) comparable to an actual discharge observed over Langmuir Laboratory on July 31, 1999. In addition, it is shown that the parameters of the discharge such as the carried charge, dipole moment and average linear charge density associated with the leader trees, are in good agreement with previous modeling and related measurements reported in the refereed literature. The model of lightning discharge is applied to study the reduction of electric field in the thunderstorm due to the growth of the bipolar structure of leader trees resembling development of an intracloud lightning discharge. This study suggests that the polarization charges carried by the leader trees can lower the net charge in the different charge layers of the thundercloud and can decrease the total electric field significantly below the lightning initiation threshold.

Unified Theory of Lightning and Jet Discharges: Role of the Charge Imbalance

Chapter 2 introduces our fractal model of lightning and Chapter 3 demonstrates the validity of the model, while detailing the fundamental mechanisms by which the lightning leader channels propagate. In this chapter, we apply the same model in various cloud configurations to investigate the conditions under which cloud-to-ground lightning discharges, bolt-from-the-blue discharges, and blue and gigantic jets are formed. This work has been the subject of a paper that was published in *Nature Geoscience* [Krehbiel *et al.*, 2008].

4.1 Observations of Blue and Gigantic Jets

Blue jets develop upwards from cloud tops to terminal altitudes of about 40 km at speeds of the order 100 km/s and are characterized by a blue conical shape [Wescott *et al.*, 1995, 1998, 2001; Lyons *et al.*, 2003]. Blue starters are distinguished from blue jets by a much lower terminal altitude. They protrude upward from the cloud top (17–18 km) to a maximum 25.5 km in altitude [Wescott *et al.*, 1996, 2001]. Blue jets were originally documented and classified as such during airplane-based observations [Wescott *et al.*, 1995]. An earlier (October 21, 1989) observation of a phenomenon closely resembling blue jets using the payload bay TV cameras of

the space shuttle was reported by *Boeck et al.* [1995]. The storm, which produced this event, appeared to be a supercell storm with a thick anvil that obscured the illuminated cloud except along the side and at a central location, presumably an overshooting turret [*Boeck et al.*, 1995]. Ground observations of blue jets are believed to be difficult due to transmission of blue light through the atmosphere resulting in severe Rayleigh scattering [*Wescott et al.*, 1998; *Heavner et al.*, 2000, p. 74]. Several ground-based video recordings of blue jets, which also electrically connected a thundercloud with the lower ionosphere, have recently been reported [*Pasko et al.*, 2002; *Su et al.*, 2003; *Pasko*, 2003]. This type of event is now termed gigantic jets [*Su et al.*, 2003]. Recent photographic [*Wescott et al.*, 2001] and video [*Pasko et al.*, 2002] observations of blue jets at close range have clearly shown the small-scale streamer structure of blue jets, earlier predicted in [*Petrov and Petrova*, 1999]. *Petrov and Petrova* [1999] were first to propose that blue jets correspond qualitatively to the development of the streamer zone of a positive leader and therefore should be filled with a branching structure of streamer channels. These ideas have been further discussed and developed in [*Pasko and George*, 2002; *Pasko*, 2006; *Riousset et al.*, 2006a, 2007b; *Krehbiel et al.*, 2007a, b, c, 2008], and are accepted as an underlying hypothesis for the modeling studies of this chapter.

4.2 Lightning and Jets: New Observations and Unified Charge Imbalance Theory

Discharges that escape the storm are possible when the breakdown is triggered between adjacent unbalanced charge regions, such as occur in the lower and upper parts of storms [*Mazur and Ruhnke*, 1998; *Coleman et al.*, 2003; *Raizer et al.*, 2006]. Thus, breakdown triggered between the midlevel negative and lower positive charges usually escapes the storm downward to become a negative cloud-to-ground (−CG) discharge (Figure 4.1b) [*Marshall et al.*, 2005]. The ability of the discharge to continue through the lower positive charge region is aided by the presence of an overall negative charge imbalance in the storm, which biases the storm potentials negatively and imparts a strongly negative initial potential (‘×’ in Figure 4.1c) to the downward developing leader.

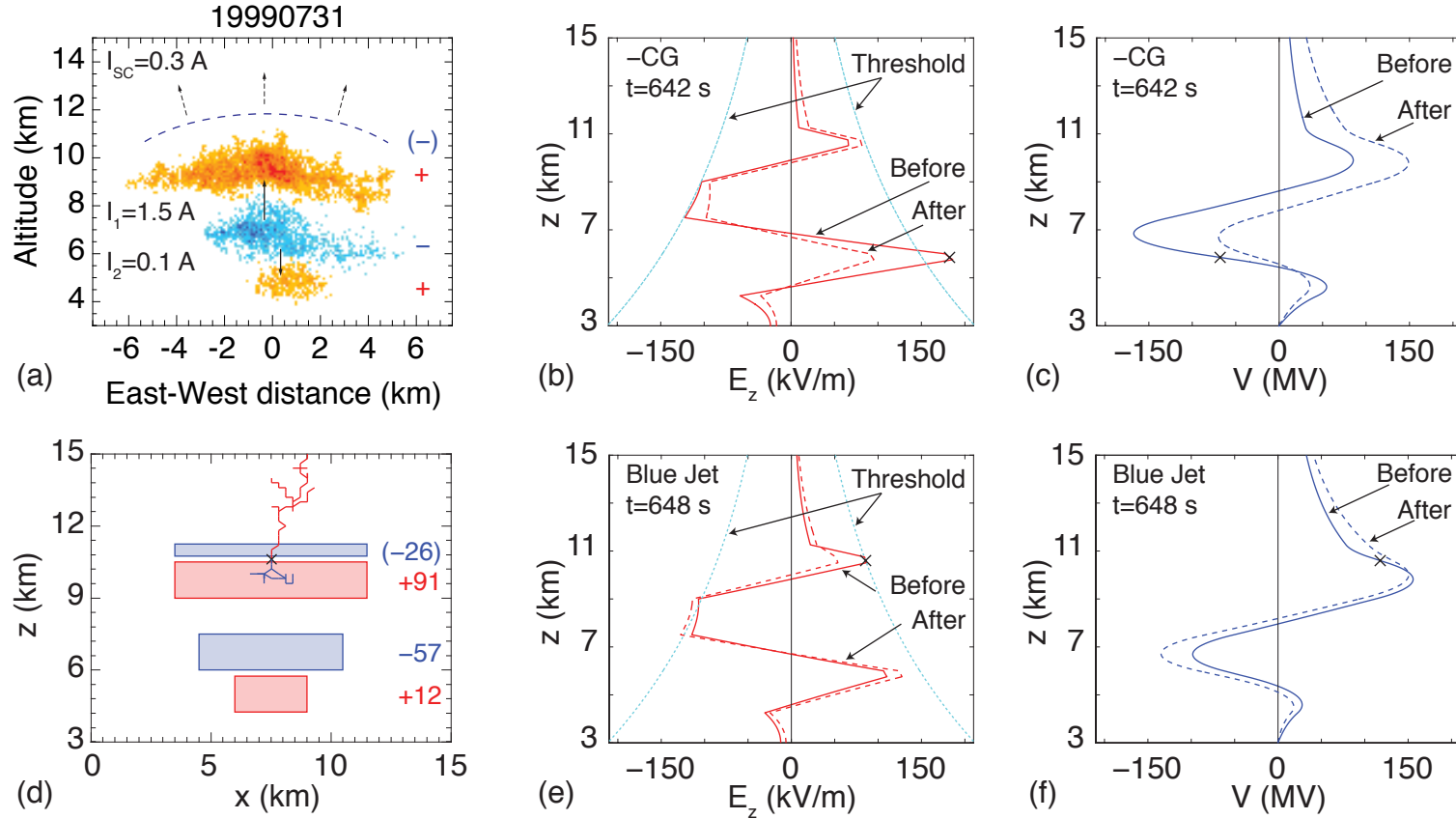


Figure 4.1. Basic scenario leading to blue jet formation. (a) Lightning-inferred charge structure [Marshall *et al.*, 2005] and model-estimated charging currents in a normally electrified storm over Langmuir Laboratory on July 31, 1999, including the expected screening charge at the upper cloud boundary (dashed line). (b,c) Vertical electric field (E_z) and potential (V) profiles before and after a negative cloud-to-ground discharge, showing how the discharge increases V and E_z in the upper part of the storm, and the assumed breakdown threshold vs. altitude. (d,e,f) Simulated and predicted occurrence of an upward discharge 6 s after the negative cloud-to-ground discharge. Here \times 's denote E_z and V where each discharge is initiated. The net charge content of each layer in C is indicated next to the charge region in panel (d) [Krehbiel *et al.*, 2008].

Normally electrified storms tend to develop an overall negative charge imbalance with time as a result of the screening negative charge flowing to the cloud top (I_{SC} in Figure 4.1a) [Wilson, 1921]. The negative charge is intermittently lowered to ground by negative cloud-to-ground discharges, thereby helping charge the global atmospheric electric circuit [Krehbiel, 1986]. Simple electrodynamic model calculations [Krehbiel *et al.*, 2008, Supplementary Information] show that the effect of a negative cloud-to-ground lightning is to suddenly change the storm net charge from negative to positive. As a result, the cloud potential quickly shifts toward positive values (Figure 4.1c) and the electric field is enhanced in the upper part of the storm (Figure 4.1b) [Wilson, 1956]. Continued charging can lead to a discharge being triggered in the upper part of the storm within a few seconds (Figure 4.1e,f) that would be expected to escape upward above the cloud top. The upward discharge would have the same polarity as the upper storm charge, namely positive for a normally electrified storm producing negative cloud-to-ground lightning. The triggering is suppressed if the screening charge is mixed into the upper storm charge, but if such mixing is weak or absent, then upward discharges are predicted to occur commonly. The fact that jets are infrequent implies that mixing of the screening charge is normally strong in storms.

That an upper level discharge, once triggered, would propagate upward above the cloud top is illustrated in Figure 4.1d using results from the stochastic lightning simulation model introduced in Chapter 2 [see also Rioussel *et al.*, 2007a]. The breakdown channel escapes upward because of the strong positive potential (~ 150 MV) in the upper part of the storm, which is imparted to the developing leader channel, coupled with the lack of a potential barrier for upward propagation (Figure 4.1f) [Raizer *et al.*, 2006]. Figure 4.2 shows observations of an upward jet that agree with the basic mechanism described above. The observation was obtained with a three-dimensional very high frequency (VHF) lightning mapping array [Rison *et al.*, 1999] during the Severe Thunderstorm Electrification and Precipitation Study (STEPS 2000) [Lang *et al.*, 2004], and was only recently discovered in the STEPS data. Until then no upward discharges had been seen or confirmed in the VHF mapping data. The jet occurred in a decaying storm system that had an inverted electrical structure [Rust *et al.*, 2005] and was producing intracloud (IC) discharges between an upper layer of negative charge and positive charge below

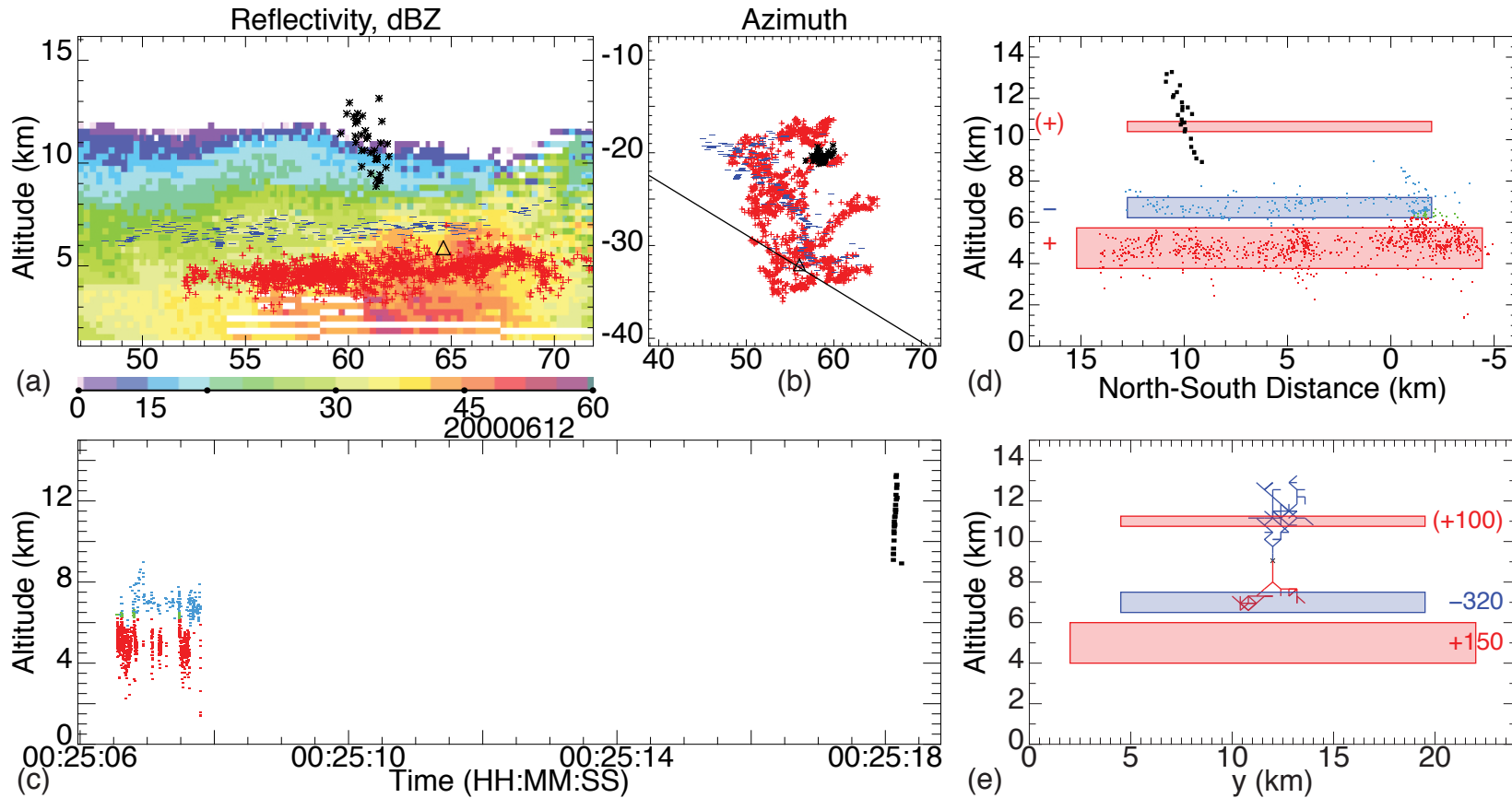


Figure 4.2. Upward negative jet from an inverted polarity storm on June 12 UTC during STEPS 2000. (a-d) VHF mapping observations of the jet (bold black sources) and preceding intracloud discharge, projected onto the closest vertical radar scan through the storm (panel a; line in plan projection, panel b). The jet developed ~ 2 km above the echo top, beginning immediately above where the intracloud discharge locally removed positive charge from the lower storm level (b). Plan radar scans show that the radar top was essentially constant at ~ 11.5 km altitude above the flash and in the vicinity of the jet. (e) Numerical simulation of the jet discharge. The net charge content of each layer in C is indicated next to the charge region. Red regions correspond to the positive charge centers, and blue regions represent the negative charge center. [Krehbiel *et al.*, 2008].

the negative. It was initiated midway between the upper negative charge and expected positive screening charge at the upper cloud boundary, 10 s after an intracloud discharge selectively removed positive charge from immediately below the initiation location (Figure 4.2b,c,d). The jet lasted 120 ms and propagated 4 km upward in the first 60 ms ($v=7\times 10^4$ m/s) to 13.5 km altitude, 2 km above the radar-detected echo top (Figure 4.2a). Its development was characteristic of an upward negative leader [Rison *et al.*, 1999; Behnke *et al.*, 2005] that would have been visible above the cloud top. The polarity is confirmed by low frequency (LF) electric field measurements of another, similar jet that occurred later in the same storm. Both discharges may have been similar to the optical ‘gnome’ observed later during STEPS [Lyons *et al.*, 2003].

The STEPS jet is well-simulated using a cylindrical disk charge configuration in which the lower positive charge is reduced relative to the upper negative charge, and capped by a thin positive screening charge (Figure 4.2e). Except for the polarities being reversed, the observations are fully consistent with the model of Figure 4.1. The intracloud discharge locally unbalanced the storm charge in the vicinity of the initiation region and the upward breakdown occurred 10 seconds later, directly above the unbalanced region (Figure 4.2b).

Other jets should have been detected by VHF mapping systems by now, but have not been. A possible explanation is that most blue-type jets are due to positive upward breakdown [Pasko and George, 2002; Wescott *et al.*, 2001; Raizer *et al.*, 2007] that radiates weakly at VHF [Rison *et al.*, 1999; Coleman *et al.*, 2003]. This inference agrees with optical observations of blue jets (BJs) as occurring in negative cloud-to-ground lightning-producing storms and being preceded by increases in negative cloud-to-ground discharge activity in the storm [Wescott *et al.*, 1995, 1998, 2001]. The breakdown likely starts as a leader that transitions within a few kilometers of exiting the cloud top to a streamer-dominated form [Pasko and George, 2002; Petrov and Petrova, 1999] that could continue to higher altitude. The downward negative breakdown that would accompany an upward positive blue jet (+BJ, Figure 4.1d) has not been identified in VHF mapping observations to

date.¹

A second mechanism exists for producing an upward discharge that may explain the occurrence of gigantic jets (GJs) [*Pasko et al.*, 2002; *Su et al.*, 2003]. Gigantic jets extend to higher altitude than blue jets (BJs) [*Wescott et al.*, 1995; *Boeck et al.*, 1995] and have a different appearance. The continuous positive leader-like propagation of optically observed blue jets [*Wescott et al.*, 1995, 1998, 2001] is contrasted with the impulsive rebrightening of gigantic jets [*Pasko et al.*, 2002], resembling negative leader processes. The estimated polarity of the gigantic jet observed by *Pasko et al.* [2002] was an issue of considerable uncertainty and debate [*Sukhorukov and Stubbe*, 1998; *Pasko and George*, 2002; *Raizer et al.*, 2007]. Subsequent additional evidence indicated that the gigantic jet was produced by a normally electrified storm and was of negative polarity [*Mathews et al.*, 2002]. The rebrightening events were accompanied by LF sferics corresponding to the upward transfer of negative charge, and the appearance of the gigantic jet in video was preceded 0.8 s earlier by an energetic positive narrow bipolar pulse (+NBP) characteristic of the onset of an upward negative intracloud flash [*Mathews et al.*, 2002; *Thomas et al.*, 2001; *Rison et al.*, 1999]. The inferred negative polarity agrees with subsequent measurements of gigantic jet sferics [*Su et al.*, 2003]. This point has since been confirmed by both ground observations of gigantic jets by *Cummer et al.* [2009] and satellite observations by *Kuo et al.* [2009]. In particular, *Cummer et al.* [2009] have been able to clearly determine the electromagnetic signature of the jet they observed and conclude that it had negative polarity.

The only way a negative gigantic jet (−GJ) could be produced by a normally electrified storm is that it originate in the midlevel negative storm charge. Evidence for how this can happen is provided by observations of ‘bolt-from-the-blue’ (BFB) lightning discharges (Figure 4.3a). VHF mapping observations show that bolt-from-the-blue discharges begin as regular, upward-developing intracloud flashes in normally electrified storms [*Rison et al.*, 1999; *Thomas et al.*, 2001; *Behnke et al.*, 2005]. Instead of terminating in the upper positive charge, however, the breakdown

¹Since the publication of this work, such VHF observations have been made. *Rison et al.* [2009] observed negative channels in the upper positive region of New Mexico thunderstorm of normal polarity without their positive counterpart in the central negative regions, leading the authors to conclude on the necessary development of these discharges in the form of upward positive blue jets.

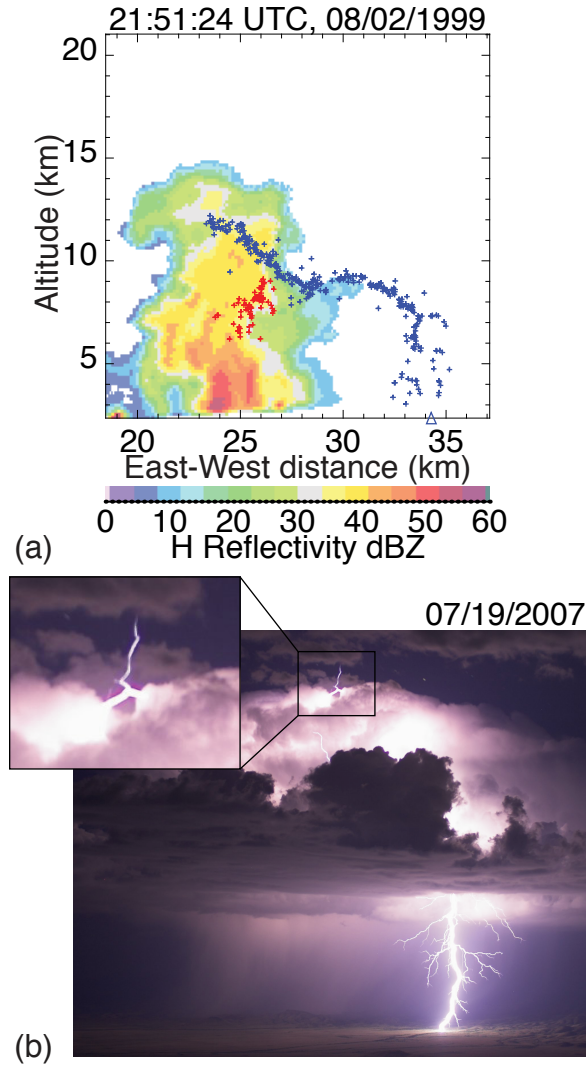


Figure 4.3. Two ‘bolt-from-the-blue’ (BFB) discharges. (a) Lightning mapping observations of a negative bolt-from-the-blue discharge, superimposed on a vertical radar scan through the storm. The lightning began as an upward intracloud discharge between midlevel negative charge (red sources) and upper positive charge (blue sources), then exited the cloud and went to ground as a negative leader, well away from the storm. ‘ Δ ’ denotes the negative cloud-to-ground strike point. (b) A cloud-enshrouded bolt-from-the-blue lightning that started to develop upward above the storm top before branching horizontally back into the upper part of the storm and turning downward to ground, causing a negative cloud-to-ground discharge on the lower right. The photograph of was taken with a 38 s time exposure from Langmuir laboratory at 3230 m altitude, 30 km distance from the storm, using an IR-modified 6-megapixel Canon 300D digital SLR fitted with a Nikon 35 mm/2.0 lens set at f/5.6. ISO-setting was 100, without noise reduction [Krehbiel *et al.*, 2008].

continues horizontally out the upper side of the storm and turns downward to ground. Although the lightning channel outside the cloud appears to originate in the upper positive charge, this visible section of the lightning is the negative counterpart of the positive leaders developing in the main negative charge region. This bright leader continues to be of negative polarity and the resulting cloud-to-ground stroke lowers negative charge to ground from the storm midlevel. The mapping observations show that bolt-from-the-blue discharges are surprisingly common in normally electrified storms.

The fact that bolt-from-the-blue discharges occur reveals a charge imbalance in which the upper positive charge is depleted in magnitude relative to the midlevel negative charge, most likely by mixing with the upper screening charge. In exiting the cloud and turning toward ground, bolt-from-the-blue discharges appear to be ‘guided’ by inferred positive screening charge attracted to the lateral cloud boundaries by the midlevel negative charge. This result is supported by simulation experiments, which find that substantial lateral charge is required to make the discharge turn downward to ground (Figure 4.4e). In the absence of guiding charge, the preferred discharge mode is upward, as indicated by the simulation of a negative gigantic jets in Figure 4.4f.

Thus, upward discharges can occur as a result of an intracloud flash that encounters depleted upper positive charge and propagates out the top of the storm. That such a discharge can exit the storm top and start developing upward is indicated by a bolt-from-the-blue photograph (Figure 4.3b). Once initiated, the upward discharge can become ‘gigantic’ because it has as its source the main negative charge of the storm, capable of producing highly energetic discharges. Negative gigantic jets are thus the upward analog of a downward negative cloud-to-ground discharge, with the role of the lower positive charge in triggering the discharge replaced by screening-depleted upper positive charge. In both cases, the lightning simulations show that continued propagation of the breakdown channels into the negative charge region maintains the channel potential at a sufficiently high negative value for the opposite end of the discharge to propagate through the potential well [Coleman *et al.*, 2003] associated with the lower or depleted upper positive charge (e.g., Figure 4.1c).

At present, gigantic jets have been recorded primarily at low latitudes and in

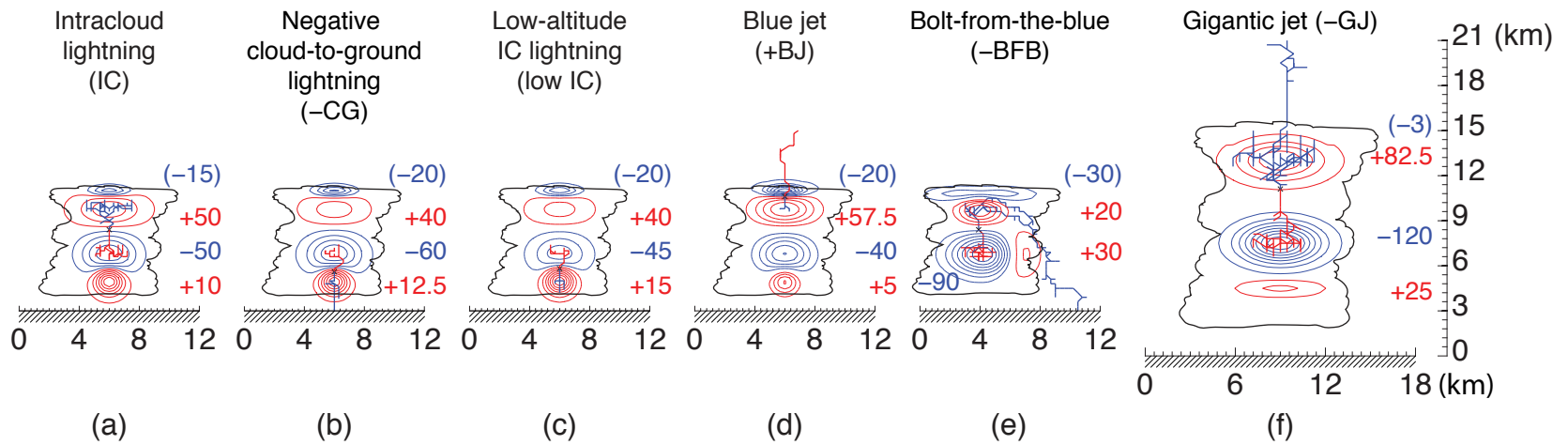


Figure 4.4. Simulated discharges illustrating the different known and postulated lightning types in a normally electrified storm (panels a–f). Blue and red contours and numbers indicate negative and positive charge regions and charge amounts (in C), respectively, each assumed to have a Gaussian spatial distribution. A partially analogous set of discharges occurs or would be predicted to occur in storms having inverted electrical structures (Figure B.1) [Krehbiel *et al.*, 2008].

storms extending to high altitudes (~ 15 km or more) [Pasko *et al.*, 2002; Su *et al.*, 2003]. This observation is possibly due to tropical clouds reaching high altitudes while remaining normally electrified [Williams *et al.*, 2006]. Optical observations of blue jets also show them emanating at similarly high altitudes from clouds [Wescott *et al.*, 1995, 1998]. Other things being equal, blue jets would be more readily initiated in taller storms due to the decrease in breakdown threshold with altitude (Figures 4.1b,e).

Figure 4.4 summarizes the results of simulating different types of discharges in normally electrified storms. In all cases, the type results from a competition concerning where breakdown is triggered first. Intracloud discharges usually win this competition because they occur between the two strongest charge regions during a storm convective stages (Figure 4.4a). Negative cloud-to-ground discharges (Figure 4.4b,e) occur as descending precipitation generates lower positive charge [Williams, 1989] or as the storm accumulates net negative charge, and can go either directly to ground or indirectly as a bolt-from-the-blue discharge. Negative gigantic jets (Figure 4.4f) provide an alternative way of relieving the midlevel negative charge, by discharging it to the upper atmosphere rather than to ground. Positive blue jets do the opposite, namely transport positive charge upward (Figure 4.4d). Thus, positive blue jets contribute to the charging of the global electric circuit, and negative gigantic jets discharge the circuit. Mixing of the screening charge at the cloud top with the upper level storm charge impedes the triggering of blue jets but encourages bolt-from-the-blue and gigantic jet-type discharges. The degree of mixing therefore likely plays a fundamental role in the occurrence and frequency of jet phenomena. Strong mixing appears to be the norm, as evidenced by the occurrence of bolt-from-the-blue discharges. Storms can get into the mode of producing blue jet-type breakdown [Wescott *et al.*, 1995; Lyons *et al.*, 2003]. The model calculations indicate that this regime can be the result of increased negative cloud-to-ground lightning production that drives the net storm charge positive, or to decreased mixing in stratiform regions [Krehbiel *et al.*, 2008, Supplementary Information]. In addition, the Figure 4.2 observations show that blue jets can be instigated by intracloud discharges. Finally, blue jet-type discharges are not necessarily confined to be lower-altitude cousins of gigantic jets, because both experience a similar, upwardly unconstrained potential environment

once they escape the cloud top.

The results of this study illustrate both the symmetries and asymmetries of the possible discharge types in convective storms [Williams *et al.*, 2006]. Although upward jets are symmetric analogs of downward cloud-to-ground discharges, they are substantially asymmetric in terms of their rate of occurrence. The discharge types are somewhat independent of polarity, giving rise for example to inverted intracloud and positive cloud-to-ground discharges in inverted polarity storms [Lang *et al.*, 2004; Rust *et al.*, 2005], as well as to the negative jet of Figure 4.2. Bolt-from-the-blue discharges have not been observed in inverted storms, but it is possible that positive gigantic jets (+GJs) could be produced by such storms (Figure B.1). A recent paper—currently under review—by van der Velde *et al.* [2010] present multi-instrumental observations of a positive gigantic jet produced by a winter thunderstorm in Europe. The storm that produced this positive gigantic jet also produced positive cloud-to-ground lightning and sprites, which are most common in inverted-polarity thunderstorms. This observation provides confirmation of the prediction made in this work of the existence of upward positive gigantic jets. Taken together, the upward breakdown types provide a set of scenarios that can be tested by further observations.

4.3 Summary of Results

In this chapter, we develop a self-consistent theory of lightning and jet discharges based on the concept of bi-directional, overall neutral and equipotential lightning leaders. The fractal model of Chapter 2 is applied to simulate typical lightning and jet discharges using realistic cloud configurations emphasizing charge imbalance as a principal factor allowing the formation of a leader with high enough potential that enables it to escape from the thundercloud. A new observation of an upward discharge observed by the lightning mapping array in a STEPS 2000 thunderstorm [Lang *et al.*, 2004] is also presented and successfully modeled. Finally, we develop a set of scenarios based on a single unified theory that are able to explain the development of classic lightning discharges and jet-type events observed to date. These scenarios also predict new cases expected to occur in both normal and inverted polarity thunderstorms. One of these, namely the occurrence of a positive

gigantic jet has been recently observed, i.e., after the publication of this work in [*Krehbiel et al.*, 2008].

Two-Dimensional Model for Studies of the Thundercloud Screening Charges in the Conducting Atmosphere

In this chapter, a two-dimensional axisymmetric model of charge relaxation in the conducting atmosphere is developed. The model accounts for time-dependent conduction currents and screening charges formed under the influence of the thundercloud charge sources. Particular attention is given to numerical modeling of the screening charges near the cloud boundaries. This model is used in Chapter 6 in conjunction with the lightning model introduced in Chapter 2 to demonstrate how realistic cloud electrodynamics lead to the development of blue and gigantic jets. The chapter consists of two parts: the first is devoted to a review of the fundamental principles of the charge relaxation in a conducting medium, and the second is dedicated to a detailed formulation of the quantitative model of charge relaxation as applicable to thundercloud dynamics in a realistic atmosphere. The output of the relaxation model is used to formulate inputs for lightning modeling using the approach described in Chapter 2. The results presented in this chapter have been published in [Riousset, 2010].

5.1 Fundamental Principles of Maxwellian Charge Relaxation

In Chapter 4, it is demonstrated how charge imbalances in the thundercloud lead to the development of various types of lightning discharges, including upward directed electrical discharges, so-called blue jets [Wescott *et al.*, 1995; Sentman and Wescott, 1995; Boeck *et al.*, 1995; Wescott *et al.*, 2001] and gigantic jets [Pasko *et al.*, 2002; Su *et al.*, 2003; van der Velde *et al.*, 2007; Chen *et al.*, 2008a, b; Kuo *et al.*, 2009]. The phenomenology of the different types of upward discharges observed to date has been recently reviewed by Mishin and Milikh [2008] and Pasko [2008, 2010]. In addition to local and global thundercloud charge imbalances created by cloud-to-ground or intracloud discharges prior to the initiation of jets, Krehbiel *et al.* [2008] also emphasize the role of the screening charge forming around the thundercloud boundaries in the development of both kinds of jets. The screening charge is responsible for two effects. First, it reduces the net overall charge content in the upper part of the storm by offsetting and mixing with the upper storm charge, as first suggested by Wilson [1921]. The screening charge results from electrical conduction currents to the cloud boundary and forms relatively rapidly around the upper boundary because of the significant increase in the atmospheric conductivity with altitude. When strongly mixed with the upper storm charge, the screening charge produces a charge imbalance that enables intracloud discharges to escape upward or outward from the storm as gigantic jets or bolt-from-the-blue discharges. The second effect is that, when not mixed or otherwise removed, the screening charge enhances the electric field immediately below the upper cloud boundary, by virtue of constituting an additional concentrated charge region. This last hypothesis was initially explored with Krehbiel *et al.*'s [2004] model to demonstrate how the enhanced electric field at the top of the thunderstorm explains the development of blue jets and is further investigated with an improved version of this model in [Krehbiel *et al.*, 2008, Supplementary Information].

The electrodynamic model of the study by Krehbiel *et al.* [2008] represents the effects of the cloud being embedded in a conductive atmosphere by determining the current density $J_z = \sigma(z_{\text{top}})E_z$ that would occur in the clear air immediately

above the cloud top. The current density is calculated from the electric field E_z on the axis of a cylindrical disk model due to the interior storm charges and from the atmospheric electric conductivity $\sigma(z=z_{\text{top}})$, where z is the vertical coordinate representing the altitude. The current density is assumed to be constant over the effective area A of the cloud-top charge disk and to thereby cause a total current $I_{\text{SC}}=J_z A$ that would accumulate at the upper cloud boundary as a screening charge. The presence of the screening charge in turn reduces the electric field above the storm top, which in the absence of interior charging causes the exterior field to relax exponentially with time with a time constant ε_0/σ . This model constitutes a one-dimensional approach for modeling atmospheric charge relaxation that is approximately correct for the parallel-plate cylindrical-charge model of the study.

In the present work, the charge relaxation process is modeled more accurately and in more detail using a fully two-dimensional axisymmetric model that takes into account the increase of atmospheric conductivity $\sigma(z)$ with altitude z in and around the cloud boundaries. In addition to describing the dynamical formation of the screening charge, the model provides a complete picture of the interior and exterior electric field, charges, and potential. The model also introduces self-consistent reassignment of the net charge contents in the cloud charge layers as a result of the occurrence of a sequence of lightning discharges. The relaxation determination employs a macroscopic approach similar to that used by *Pasko et al.* [1997] and does not involve or require explicit treatment of atmospheric ions [e.g., *Helsdon and Farley*, 1987]. Results of the cloud electrodynamic model are used as the basis for three-dimensional simulations of individual lightning discharges [*Riousset et al.*, 2007a], as an initial means for self-consistently determining the complete electrical evolution of a storm. The 2-D electrostatic formulation employed in this work does not allow the incorporation of dynamical cloud processes such as charge advection, storm top divergence, or deformation of charge layers by an updraft, but their potential effects are discussed in Chapter 6.

The two effects of the charge relaxation process, namely the magnification of electric field and dissipation of the upper storm charge can be illustrated by means of two examples, presented in Figures 5.1 and 5.2. The distributions of electric charges in the examples are purposely exaggerated and simplified in comparison with realistic distributions to accentuate the effects discussed later in this chapter

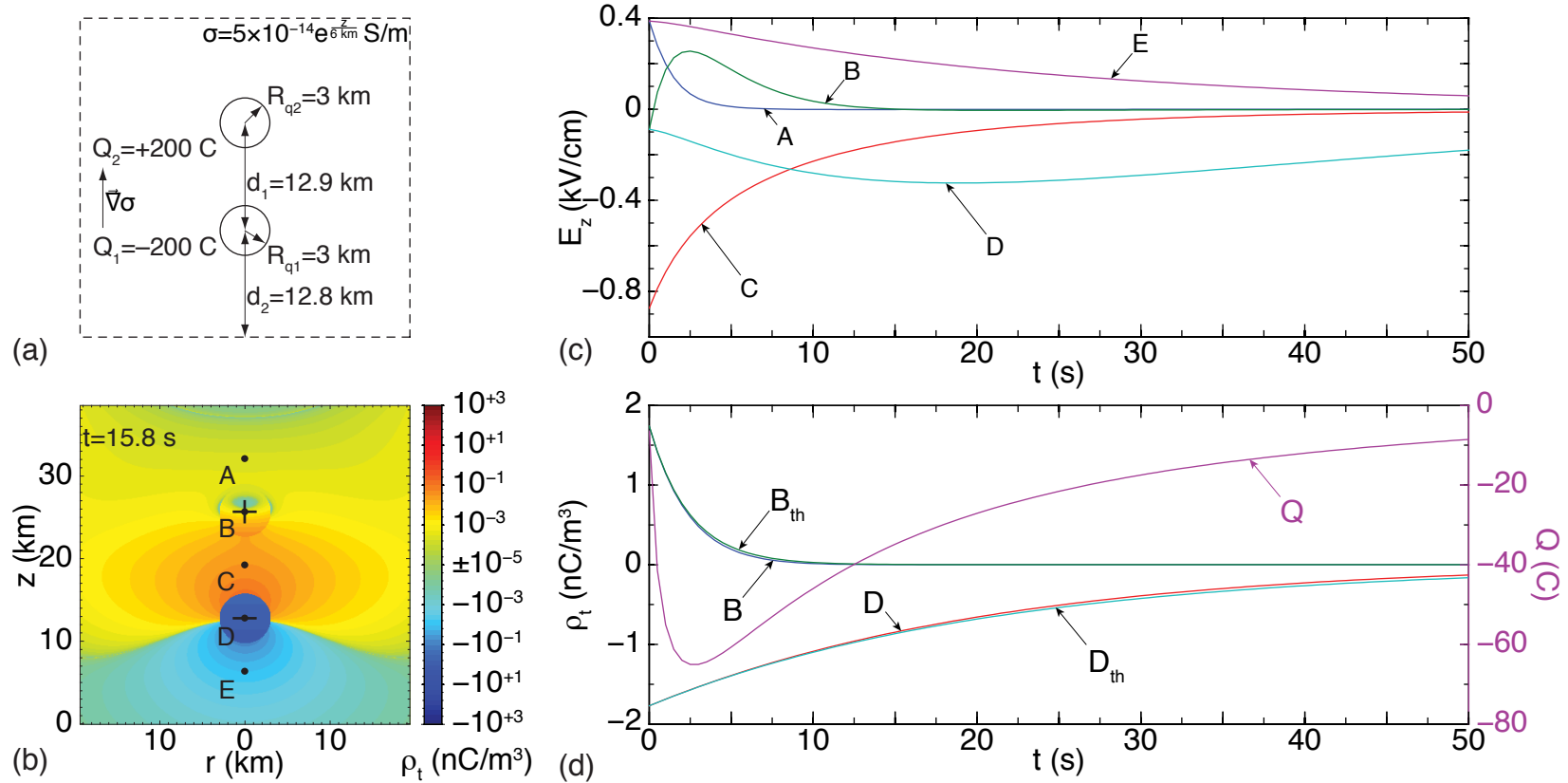


Figure 5.1. Charge dissipation in a conductive medium as a function of the altitude. (a) Geometry of the illustrative example. (b) Cross-sectional view of the charge density distribution at $t \sim 15.8 \text{ s}$. The positive charge (+) has almost disappeared and the negative charge (−) has only slightly dissipated. Letters A–E indicate the loci of observation of the evolution of the electric field and charge density in panels (c) and (d), respectively. In panel (d), B_{th} and D_{th} indicate the analytically calculated approximations of the evolutions of the charge densities at points B and D. The total charge Q in the simulation domain is represented using a solid purple line with corresponding scale shown on the right vertical axis. (See Supplementary Video 1 in [Riousset *et al.*, 2010a] for the animated version of panel (b) plot.)

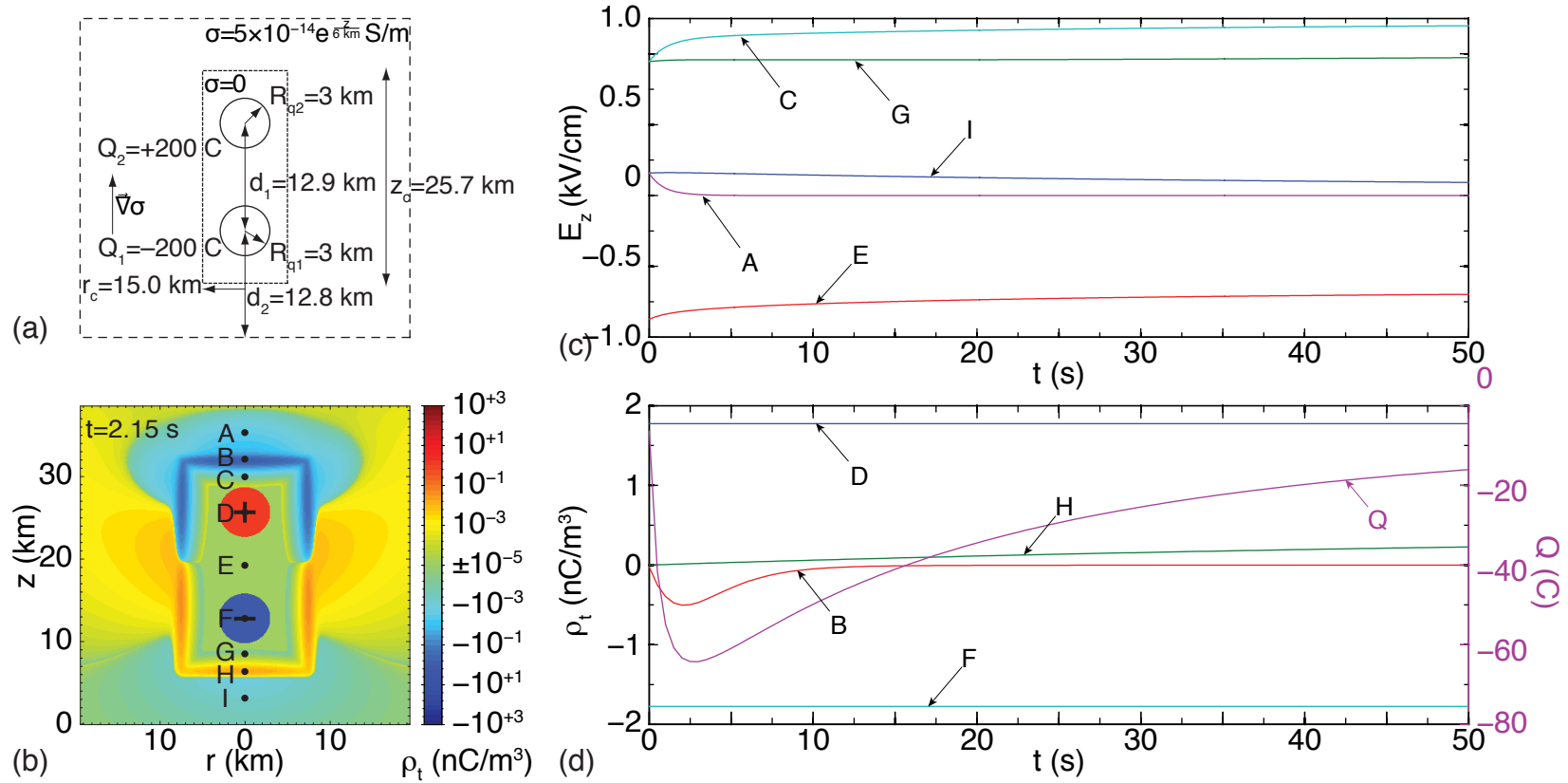


Figure 5.2. Formation of the screening charge at the boundary of a cylindrically symmetric thundercloud with reduced conductivity. (a) Geometry of the illustrative example. (b) Cross-sectional view of the charge density distribution at $t \sim 2.15$ s. The screening charge develops much faster on the upper boundary of the cylinder than on the lower one due to the exponential increase of conductivity with altitude z . Points A–I indicate the locations where the temporal evolution of the electric field and charge density are shown in panels (c) and (d), respectively. The total charge in the simulation domain Q is represented using a solid purple line with corresponding scale shown on the right vertical axis. (See Supplementary Videos 2a and 2b in [Riousset *et al.*, 2010a] for the animated version of panel (b) plot.)

and the following one in connection with the development of blue and gigantic jets.

Figure 5.1 illustrates how, when two equal and opposite polarity charges are placed in an infinite conductive medium with conductivity increasing with altitude, the overall system develops an excess of charge of the polarity of the lower charge due to the differences in relaxation time scales of charges at different altitudes [Wilson, 1921]. To simulate open boundary conditions, we adopt a formulation similar to that described in [Liu and Pasko, 2006]. For the case when conductivity increases with altitude, the timescale of the charge dissipation $\tau_\sigma(z)$ is given by $\tau_\sigma(z) = \varepsilon_0 / \sigma(z) = (\varepsilon_0 / \sigma_0) e^{-\frac{z}{h}}$, where ε_0 , $\sigma(z)$, σ_0 , and h are the free space permittivity, the conductivity of the medium as a function of the altitude z , the conductivity at sea level, and the conductivity characteristic height, respectively [e.g., Brown *et al.*, 1971; Pasko *et al.*, 1997, Appendix B]. Because σ increases with z , the upper positive charge (+) in Figure 5.1 dissipates faster than the lower negative charge (-), yielding an excess of negative charge in the system. In the example shown, $\tau_\sigma(25.6 \text{ km}) = \tau_\sigma^+ = 2.45 \text{ s}$ for the upper positive charge and $\tau_\sigma(12.8 \text{ km}) = \tau_\sigma^- = 20.8 \text{ s}$ for the lower negative charge. Figure 5.1b shows a cross-sectional view of the charge density after 15.8 s, i.e., after $\sim 6.5\tau_\sigma^+$ and $\sim .75\tau_\sigma^-$. By this time, the positive charge has almost completely dissipated, whereas the negative charge is comparatively mostly intact. The system develops an excess of negative charge after a few seconds as evidenced by the curve Q versus t shown in Figure 5.1d. Figure 5.1d also compares the charge densities at the centers of the two charge regions (points B and D in panel (b)) with the analytical results $\rho(z, t) = \rho_0(z) e^{-\frac{\sigma(z)t}{\varepsilon_0}}$ for an isolated charge in a uniformly conducting medium, and shows excellent agreement with the numerical results. The example illustrates a simple, plausible way in which storms develop a strong charge imbalance, leading to the occurrence of negative cloud-to-ground discharges (-CG) and to the formation of gigantic jets, as proposed by Krehbiel *et al.* [2008].

The second example, presented in Figure 5.2, illustrates the effects of embedding the charges in a cloud. Screening charges develop at the cloud boundaries due to conductivity gradients between the clear air outside the storm and the storm cloudy interior. The screening charges develop at different rates in the upper and lower part of the storm and enhance the electric field just inside the cloud boundary. These effects can be demonstrated using the same geometry as in Figure 5.1

with the difference that the dipole is now enclosed in a non-conducting dielectric cylinder. For purposes of illustration, the cylindrical dielectric region has a height (25.7 km) that is significantly greater than the altitude scale of the conductivity variation ($h=6$ km). Figure 5.2b shows the charge density distribution after 2.15 s. At this point, screening charges have had enough time to accumulate around the upper boundary of the zero-conductivity region [e.g., *Holzer and Saxon*, 1952] but not around the lower boundary, due to an approximate 70% conductivity difference between these two regions. The evolution of the charge densities at the upper and lower boundary points B and H in Figure 5.2b is shown in panel (d) and demonstrates the rate difference. As a result, a dipolar structure is formed between the upper positive charge at location D and the screening charge near point B that increases the electric field at point C between the two charge regions (curve ‘C’ in panel (c)). The local field increase is one of the fundamental effects leading to blue jet initiation discussed in [*Krehbiel et al.*, 2008]. In both the Figure 5.1 and Figure 5.2 examples, the screening process continues until sufficient charge has accumulated to neutralize externally the electric field of the source charge [*Wilson*, 1956; *Brown et al.*, 1971].

The effects discussed above provide additional insight into the initiation of blue and gigantic jets and are referred to in this chapter and in Chapter 6. Both blue and gigantic jet discharges are believed to be initiated in a conventional leader form [e.g., *Krehbiel et al.*, 2008]. Consequently, we use the 3-D Cartesian model of lightning discharge described by *Riousset et al.* [2007a] and in Chapter 2 of this dissertation to model initial development of leaders in specified charge configurations. The same first-principle techniques are used to determine both the lightning charge development and the charge relaxation presented in Figures 5.1 and 5.2. These techniques are more fully described in Section 5.2 below.

Classic, normally electrified thunderstorms have a dominant midlevel negative charge region (N) situated between a comparable upper positive charge region (P) above the negative charge, and lesser lower positive charge (LP) below the negative charge [e.g., *Williams*, 1989]. The three charge regions are illustrated in Figures 5.3a and 5.3b by blue and red rectangles, respectively. The charges and electric fields build up steadily with time as a result of the storm charging currents until a breakdown threshold is reached. The charging currents are believed to orig-

inate from convection-driven graupel-ice collisions in the presence of supercooled water droplets [e.g., *Williams*, 1989; *Rakov and Uman*, 2003, p. 85] and continue to be a topic of active research. Exceeding the breakdown threshold initiates a lightning discharge. Following initiation, bi-directional discharges develop, producing different lightning types depending on where the triggering happens to occur first [*Krehbiel et al.*, 2008]. The discharges suddenly reduce the net charges within the charge regions. The slow and fast time-varying charges in the thunderstorm cause the dynamical formation of induced free charges in the atmosphere and result in the development of so-called *Greifinger and Greifinger* [1976] boundaries. In an atmosphere with conductivity increasing with altitude, a *Greifinger and Greifinger* [1976] boundary separates the regions dominated by displacement current below the boundary and conduction current above the boundary. The location of this boundary depends on the electrodynamics of the thunderstorm in the troposphere. Fast charge rearrangements due to a lightning discharge result in downward moving boundaries and the slow charge build-up due to the storm charging currents leads to the formation of screening charges accumulating at the upper cloud boundary [e.g., *Pasko and George*, 2002], that can mix with the charge in the upper levels of the cloud. As described on a conceptual level earlier in this section, the screening layer can favor the development of either blue or gigantic jets, depending on the extent to which the screening charge is mixed with the upper storm charge [*Krehbiel et al.*, 2008]. After the jets are initiated as regular lightning leader channels, they convert to non-thermal, streamer zone dominated form at higher altitudes [*Petrov and Petrova*, 1999; *Kuo et al.*, 2009].

5.2 Formulation of the Charge Relaxation Model

To investigate the temporal electrodynamics of thunderclouds leading to the formation of jets, we have developed a 2-D axisymmetric model in which the storm charges are situated inside a cloud of zero electrical conductivity, with the storm as a whole being embedded in a conducting atmosphere of increasing conductivity with altitude. The model has radial and vertical domain extents of $L_r=64.5$ km and $L_z=72.25$ km, respectively, and is discretized using equidistant grids of 500 m

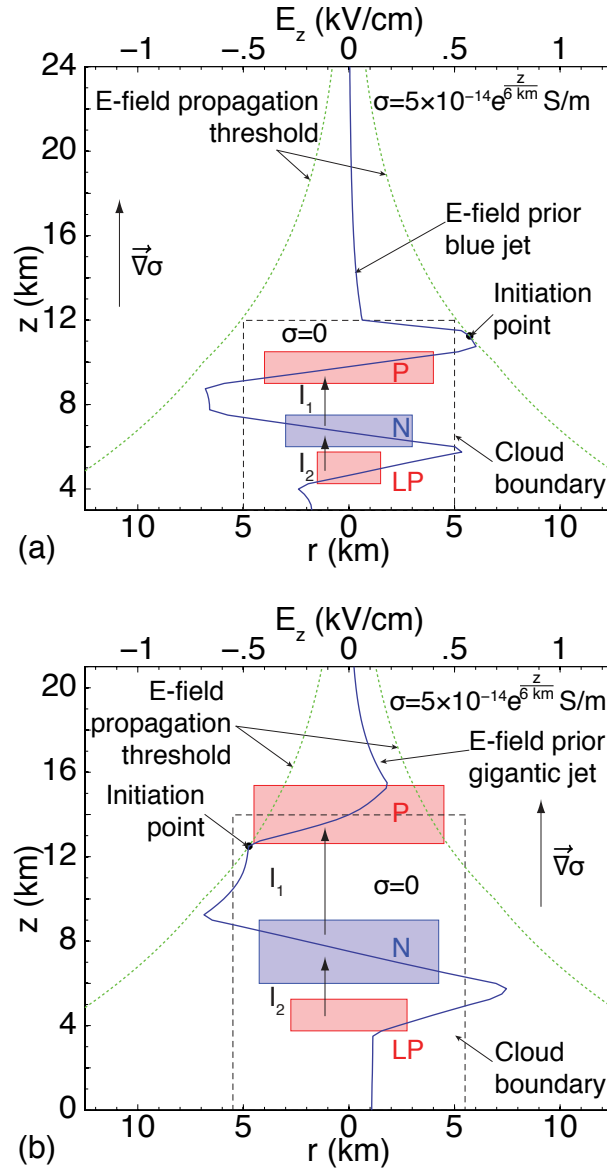


Figure 5.3. Geometry and conductivity distribution inside and nearby the model cloud employed for the simulation of (a) blue jets and (b) gigantic jets. Dashed green lines represent the electric field threshold E_{th}^{\pm} for lightning initiation. The solid blue lines represent the electric field at $r=0$ prior to the development of the jets. The solid rectangles marked LP, N and P depict the altitude and dimensions of the lower positive, central negative and upper positive thundercloud charge regions, respectively (Tables 5.1 and 5.2). The vertical arrows indicate the charging currents I_1 and I_2 .

and 250 m in the r - and z -directions (see Figures 5.3a and 5.3b and Table 5.1).

The thundercloud is assumed to have a classic tripolar charge structure (see Chapter 1 and [e.g., *Williams*, 1989]) enclosed in a dielectric cylinder of radius r_c and vertical extent z_c (Table 5.2) representing the limits of the cloud. The tripole is placed above a perfectly electrically conducting flat ground plane positioned at altitude $z=z_{\text{gnd}}$ (Table 5.1). The charge regions are modeled as axisymmetric cylindrical disks centered at altitudes z_{LP} , z_{N} , z_{P} , and characterized by radii R_{LP} , R_{N} , R_{P} , vertical extents d_{LP} , d_{N} , d_{P} (Table 5.2), and net charge contents Q_{LP} , Q_{N} , Q_{P} , respectively.

The storm charges are assumed to be generated by charging currents I_1 and I_2 between the N- and P-, and between the LP- and N-regions, respectively, as indicated in Figure 5.3. The source charges are uniformly distributed within each disk and their temporal variation produces time- and space-varying induced free charges ρ_f and electric potentials ϕ both inside and outside the storm. The basic set of equations relating ρ_f and ϕ to the source charge densities ρ_s are:

$$\nabla^2 \phi = -\frac{\rho_s + \rho_f}{\varepsilon_0} \quad (5.1)$$

Table 5.1. Parameters used in the simulations.

Name	Symbol	Units	+BJ	-GJ
Ground altitude	z_{gnd}	(km)	3	0
<i>2-D axisymmetric domain</i>				
Dimensions	L_r	(km)	64.5	64.5
	L_z	(km)	72.25	72.25
Discretization steps	δ_r	(m)	500	500
	δ_z	(km)	250	250
<i>3-D Cartesian domain</i>				
Dimensions	L_x	(km)	18.5	18.5
	L_y	(km)	18.5	18.5
	L_z	(km)	21.0	21.0
Discretization steps	δ_x	(m)	500	500
	δ_y	(m)	500	500
	δ_z	(m)	250	250

$$\frac{\partial \rho_f}{\partial t} - \nabla \sigma \cdot \nabla \phi = -\sigma \frac{\rho_s + \rho_f}{\varepsilon_0} \quad (5.2)$$

where σ is the atmospheric conductivity. The total charge density is $\rho_t = \rho_s + \rho_f$. The above equations express Gauss's Law and conservation of charge, in which the conduction current \vec{J} is assumed to be ohmic and replaced by $\vec{J} = \sigma \vec{E} = -\sigma \nabla \phi$ in (5.2).

The conductivity σ at any location (r, z) in the simulation domain is expressed by:

$$\sigma(r, z) = \underbrace{\sigma_0 e^{\frac{z + z_{\text{gnd}}}{h}}}_{\text{(I)}} \underbrace{\left(1 - \frac{1 - \tanh\left(\frac{r - r_c}{\alpha}\right)}{2} \times \frac{1 - \tanh\left(\frac{z - z_c}{\alpha}\right)}{2} \right)}_{\text{(II)}} \quad (5.3)$$

where the parameter α determines the thickness of the conductivity transition

Table 5.2. Geometrical and electrical parameters of the model thundercloud.

Name		Symbol	Unit	+BJ	-GJ
<i>Charge layer geometry</i>					
Lower positive	altitude ^a	z_{LP}	(km)	2.0	4.5
	radius	R_{LP}	(km)	1.5	2.75
	depth	d_{LP}	(km)	1.5	1.5
Central negative	altitude ^a	z_{N}	(km)	3.75	7.5
	radius	R_{N}	(km)	3.0	4.25
	depth	d_{N}	(km)	1.5	3.0
Upper positive	altitude ^a	z_{P}	(km)	6.75	14.0
	radius	R_{P}	(km)	4.0	4.5
	depth	d_{P}	(km)	1.5	2.75
<i>Cloud boundaries</i>					
Radius		r_c	(km)	5	5.5
Height ^a		z_c	(km)	9	14
Boundary thickness		α	(km)	0.15	0.75
<i>Charging currents</i>					
Upper charging current		I_1	(A)	+1.5	+3.0
Lower charging current		I_2	(mA)	-90	-250

^aaltitude above ground level

region between the cloud interior and the surrounding clear air. The conductivity outside the cloud increases exponentially with altitude z (term (I) in (5.3)) with an altitude scaling factor $h=6$ km and a conductivity at sea level $\sigma_0=5\times 10^{-14}$ S/m [e.g., *Pasko et al.*, 1997, and references therein]. Inside the cloud the conductivity is reduced to zero (term (II) in (5.3)), with a smooth transition at the boundary of width $\sim 2\alpha$. Two values of α are used in the simulations, 0.15 and 0.75 km (Table 5.2), so that the transition region typically contains several (3 to 7) grid points.

Few conductivity measurements have been made inside electrified clouds [*MacGorman and Rust*, 1998, p. 171, and references therein]. Because atmospheric ions quickly attach to cloud particles, clouds have a low electrical conductivity [e.g., *MacGorman and Rust*, 1998, pp. 170–172; *Rakov and Uman*, 2003, p. 91; *Rycroft et al.*, 2007]. Tests of the sensitivity of the simulation results for both gigantic jets and blue jets to the assumed cloud conductivity (zero and 10% of clear values – see discussion in [e.g., *MacGorman and Rust*, 1998, p. 172]) have shown that the results differ only by a slight increase in the charging current required to produce the same charge magnitudes.

The degree to which the screening charge is mixed with the interior, upper positive storm charge is an important factor in the production of blue and gigantic jets. The study by *Krehbiel et al.* [2008] indicates that blue jets occur most favorably in the absence of mixing, whereas gigantic jets are favored by strong mixing. The two scenarios are currently simulated in the model by having the upper boundary screening charge region overlap or not overlap the upper positive storm charge (Table 5.2 and Figure 5.3).

With σ given by (5.3), we can solve the system (5.1)–(5.2) for the two unknowns ϕ and ρ_f . Poisson’s equation (5.1) is solved using a red-black parallel Successive Overrelaxation Method (SOR) [*Niethammer*, 1989; *Zhang et al.*, 2005], and the continuity equation is solved using a parallel version of the classic Lax scheme [e.g., *Potter*, 1973, pp. 57 and 67].

The charging currents are chosen to reproduce typical intracloud (IC) and cloud-to-ground (CG) lightning rates in storms believed to produce the two types of jets. Blue jets (BJs) have been observed in electrically active continental storms that produce significant negative cloud-to-ground lightning (–CG) [e.g., *Lyons*

et al., 2003]. In contrast, gigantic jets (GJs), because they also discharge the N-charge region, are predicted to be suppressed by negative cloud-to-ground lightning [Krehbiel *et al.*, 2008]. The video recording of a gigantic jet observed from Puerto Rico by Pasko *et al.* [2002] shows the occurrence of several intracloud lightning discharges in a rapid succession prior to the jet initiation, implying an active main charging current I_1 . The Puerto Rico event occurred on September 14, 2001 approximately 200 km northwest of Arecibo observatory above a tropical oceanic thunderstorm [Pasko *et al.*, 2002]. Such systems typically produce little cloud-to-ground lightning [e.g., MacGorman and Rust, 1998, pp. 188 and 297] suggesting a relatively small I_2 compared with I_1 . It should be emphasized that the choice of specific values for the charging currents in the simulations do not alter the overall physical interpretation of the electrodynamics of jet-producing storms discussed here.

To model the bulk effect of lightning discharges on the thundercloud electrodynamics, three types of discharges are accounted for: (1) cloud-to-ground discharges (CG), which reduce the net charge content of the LP- and N-regions by 50% each, (2) intracloud discharges (IC), which cause a reduction of $\min(|Q_N|, |Q_P|)/2$ of the net charge in the N- and P-layers, and (3) blue jet discharges (BJ), which are assumed to produce a 50% reduction in the screening charge Q_{SC} and upper positive charge Q_P . These are the parameterizations used in the studies by Krehbiel *et al.* [2004, 2008]. For the gigantic jet simulations, where strong mixing is simulated by overlapping the screening charge with the upper positive charge, intracloud discharges are assumed to discharge the N- and P-layers by $\min(|Q_N|, |Q_P + Q_{mix}|)/2$, where Q_{mix} represents the amount of free induced screening charge (corresponding to ρ_f in (5.1)–(5.2)) that is present within the confines of the upper positive charge region. In addition, a fourth type of lightning discharge, the gigantic jet discharge, is introduced and assumed to reduce Q_N , Q_P and Q_{SC} each by a factor two, as detailed below in this section.

A discharge is assumed to occur when the electric field exceeds a predefined electric field threshold for initiation and propagation of positive and negative leaders, $E_{th}^\pm = 2.16 \times N(z + z_{gnd})/N_0$ kV/cm, where $N(z)$ and N_0 are the neutral densities at altitude z and at sea level, respectively [e.g., Marshall *et al.*, 1995; Rioussset *et al.*, 2007a, and references therein]. Discrimination between the different types of dis-

charges is based on their initiation altitudes. Breakdown that results from the electric field threshold being exceeded between the LP- and N-charge regions leads to a negative cloud-to-ground discharge (–CG) in the model that removes 50% of the charge content of the N- and LP-layers, causing net negative charge to be removed from the cloud (or, equivalently, positive charge to be added). Initiation that occurs between the N- and P-charge regions generates either an intracloud discharge or gigantic jet depending on the dynamic charge imbalances in the cloud and the geometrical structure of the charge regions. Finally, if the initial breakdown occurs above the P-layer, then the model leads to the development of a blue jet event.

A particularly important aspect of the investigations has been to determine when an intracloud discharge continues on out of the cloud to become a gigantic jet, in which case it behaves like a cloud-to-ground discharge and removes net negative charge from the cloud (–GJ), or if the discharge remains confined within the cloud and produces equal and opposite charge changes and zero net change to the overall storm charge. This determination is made on an *a posteriori* basis by using the fractal discharge model to simulate successive intracloud discharges until events are found that escape the cloud. From such simulations, an approximate empirical criterion has been developed and used in standalone simulations employing only the 2-D electrodynamic model. Whether an intracloud discharge becomes a gigantic jet depends largely on the relative magnitude of the negative Q_N charge and the mixing-depleted upper positive charge ($Q_P + Q_{\text{mix}}$). The fractal simulations indicate that gigantic jets occur when the charge ratio $|Q_P + Q_{\text{mix}}|/|Q_N| \lesssim 0.50$. This condition compares to the nominal criterion assumed for cloud-to-ground discharges which is that $|Q_{\text{LP}}|/|Q_N| < 1$, and a similar criterion for blue jets. We emphasize that gigantic jets have a more stringent criterion because the discharge has to propagate through two charge regions rather than one, with the unmixed screening charge being of negative polarity and therefore being repulsive to the escape. Finally, when a gigantic jet is determined or estimated to have occurred, the discharge is assumed in the electrodynamic model to reduce each of the three affected charges (Q_N , Q_P , and Q_{SC}) by half of their original values.

The specific values of the fractional reduction of net electric charge in the charge layers following a discharge are based on both observational and modeling

results and produce discharges with charge transfers that agree well with the estimates available in the referred literature. Intracloud discharges transfer a few tens of Coulombs between the N- and P-regions [e.g., *Krehbiel*, 1981; *Krehbiel et al.*, 1984a, b; *Helsdon et al.*, 1992; *Shao and Krehbiel*, 1996; *Rakov and Uman*, 2003, p. 325], and cloud-to-ground discharges lower similar amounts of charge to the ground in agreement with values reported in [*Rakov and Uman*, 2003, p. 146]. The model gigantic jet presented in Chapter 6 removed ~ 26 C net negative charge from the storm, consistent with estimates by *Su et al.* [2003]. The fractal model employed in this study has been shown to reproduce well the aforementioned charge transfers [*Riousset et al.*, 2006b, 2007a, and Chapter 6 of this dissertation]. When reported to the typical net charge content of the thundercloud charge regions [e.g., *Uman*, 2001, p. 60; *Rakov and Uman*, 2003, p. 79], the so-obtained estimates of the fractional charge reduction following a discharge are in a reasonable agreement with the values employed by the thundercloud dynamics model.

During model calculations, the side and top boundaries of the simulation domain are maintained at ground potential (Dirichlet boundary conditions). This hypothesis is fully justified for the ground and ionospheric boundaries [e.g., *Pasko et al.*, 1997] and introduces an error $< 10\%$ on the side boundary, decreasing as one approaches the center of the simulation domain at $r=0$, i.e., in the region of primary interest. The choice of boundary conditions as well as the choice of a 2-D axisymmetric model is related to the need for a large simulation domain and a very fine time resolution ($0.4 \text{ ms} < \varepsilon_0 / \sigma_{\text{max}}$, where σ_{max} is the maximum conductivity in the simulation domain), which involves a computational time that currently does not allow 3-D modeling.

At the moment of jet initiation, a “still picture” of the charge configuration is taken and converted to 3-D Cartesian coordinates to be used for simulation of the leader trees using the fractal model. The lightning simulation employs the stochastic model described in Chapter 2 in a reduced-size domain enclosing the cloud and its nearest surroundings (see Tables 5.1 and 5.2). The use of a simulation domain with reduced size requires Dirichlet open boundary conditions. The open boundary conditions employed in the present work follow procedures also described in Chapter 2.

5.3 Summary of Results

In this chapter, we developed a new 2-D axisymmetric model of charge relaxation in the conducting atmosphere. We also provide a discussion of the fundamental principles of Maxwellian charge relaxation in a conducting medium. These principles are applied to explain the formation of the screening charges at the boundary of the cloud. In Chapter 6, we investigate the role of the screening charge in the development of blue and gigantic jet discharges through self-consistent modeling.

Self-Consistent Modeling of Thundercloud Screening Charges: Implications for Blue and Gigantic Jets

In this chapter, the two-dimensional axisymmetric model of charge relaxation in the conducting atmosphere introduced in Chapter 5 is used in conjunction with the probabilistic lightning model developed in Chapter 2 to demonstrate how realistic cloud electrodynamics leads to the development of blue and gigantic jets. The model accounts for time-dependent conduction currents and screening charges formed under the influence of the thundercloud charge sources. Particular attention is given to numerical modeling of the screening charges near the cloud boundaries. The modeling results demonstrate the important role of the screening charges in local enhancement of the electric field and/or reduction of net charge in the upper levels of the thundercloud. The charge relaxation model presented in this work confirms the previous results obtained with a simpler model by *Krehbiel et al.* [2008], specifically that the accumulation of screening charges near the thundercloud top produces a charge configuration leading to the initiation of blue jets, and the effective mixing of these charges with the upper thundercloud charge may lead to the formation of gigantic jets. The material presented in this chapter has been

published in [Riousset *et al.*, 2010a].

6.1 Results of Modeling of Storm Dynamics and Jet Initiations

In this section, we present results from simulation runs leading to blue and gigantic jet events. The examples illustrate the limiting cases of no mixing between the screening and upper positive charges, and nearly complete mixing. These cases give rise to blue jets and gigantic jets relatively early and repeatedly in the simulations. In actual storms, the mixing is somewhere between the two limits. In addition, potential gigantic jets appear to be converted to bolt-from-the-blue (BFB) discharges, which are relatively common in normally electrified storms [Thomas *et al.*, 2002; Krehbiel *et al.*, 2008].

Figure 5.3 shows the charge geometry and electric field profiles for two different storms at the time of initiation of a blue jet (Figure 5.3a) and a gigantic jet (Figure 5.3b). For clarity of presentation, each figure is focused on the cloud and shows only a small part of the 2-D simulation domain. In both panels, the vertical arrows indicate the charging currents I_1 and I_2 . The dashed green lines represent the lightning initiation and propagation threshold E_{th}^{\pm} and the solid blue lines show the electric field at the time of initiation of the jets. The modeled storm of Figure 5.3a has charging currents of $[I_1, I_2] = [+1.5, -0.09]$ A and a charge structure in which the upper positive charge is separated from the upper cloud boundary and screening charge, so that no mixing occurs between the two. At ~300 seconds into the simulation, the initiation threshold is crossed at $z=11.25$ km, in the enhanced electric field region between the P-layer and screening charge and allowing for the development of an upward blue jet (Figures 6.1a and 6.2).

The storm of Figure 5.3b has a greater vertical extent and an upper cloud boundary centered within the P-layer to simulate mixing with the screening charge. The charging currents are also larger, at $[+3.0, -0.25]$ A. The presence of the screening charge within the P-layer results in the net P-charge becoming depleted with time relative to the N-charge (Figure 6.1b). The depletion is such that, ~46 s into the simulation, an intracloud discharge initiated at the base of the P-region

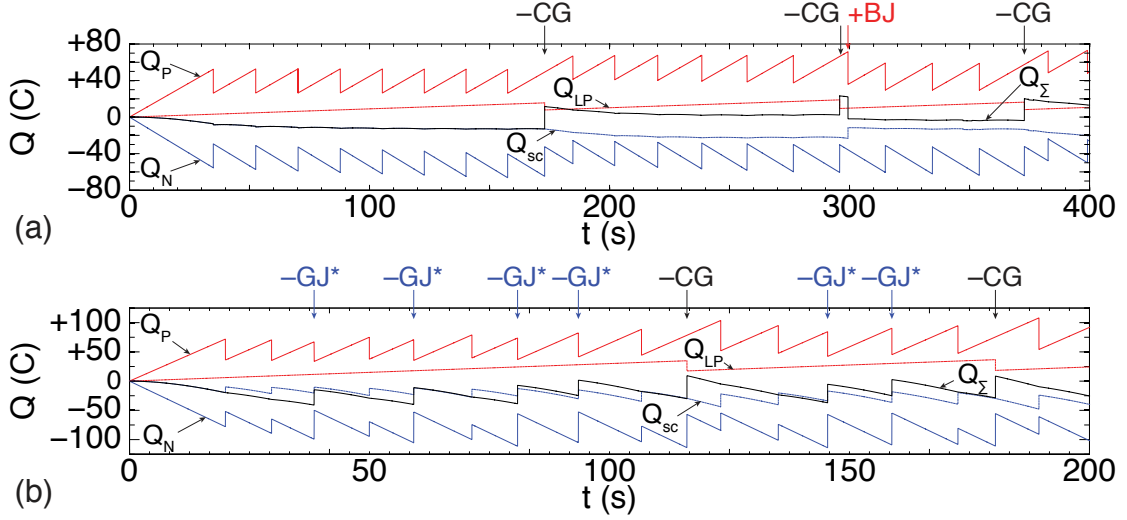


Figure 6.1. Model-calculated temporal variations of the storm charges leading to initiation of: (a) a blue jet discharge between the upper positive layer and the screening charge layer at $t=299.4$ s; (b) gigantic jet discharges between the central negative layer and upper positive charge layer reduced by the screening charge. The first gigantic jet occurs at $t \sim 46$ s. Sudden vertical jumps in the curves correspond to occurrence of intra-cloud discharges unless marked otherwise. Asterisks indicate that the gigantic jets could instead be bolt-from-the-blue discharges.

escapes the cloud as a gigantic jet (Figure 6.3).

Figure 6.1a shows the temporal evolution of the blue jet-producing storm of Figure 5.3a. The storm begins with a series of eight intracloud discharges between the N- and P-regions, seen as sudden changes in Q_N and Q_P (solid blue and red traces, respectively). During this time the lower positive charge Q_{LP} (dotted red trace) increases to the point where a negative cloud-to-ground discharge is initiated (at ~ 172 s) that changes the overall storm charge Q_Σ (the sum of the four charges Q_{LP} , Q_N , Q_P , and Q_{SC}) from a net negative to net positive value (black trace). The IC/CG sequence is repeated over the next ~ 2 min, after which point a positive blue jet (+BJ) is initiated (Figure 5.3a). The blue jet occurs ~ 4 s after the second negative cloud-to-ground discharge and is initiated by virtue of the negative cloud-to-ground lightning effectively adding positive charge to the storm, which suddenly increases the electric field in the storm upper levels (see Figure 4.1b). The additional 4 s of charging following the charge-imbalancing negative cloud-to-ground discharge causes the blue jet breakdown to be initiated

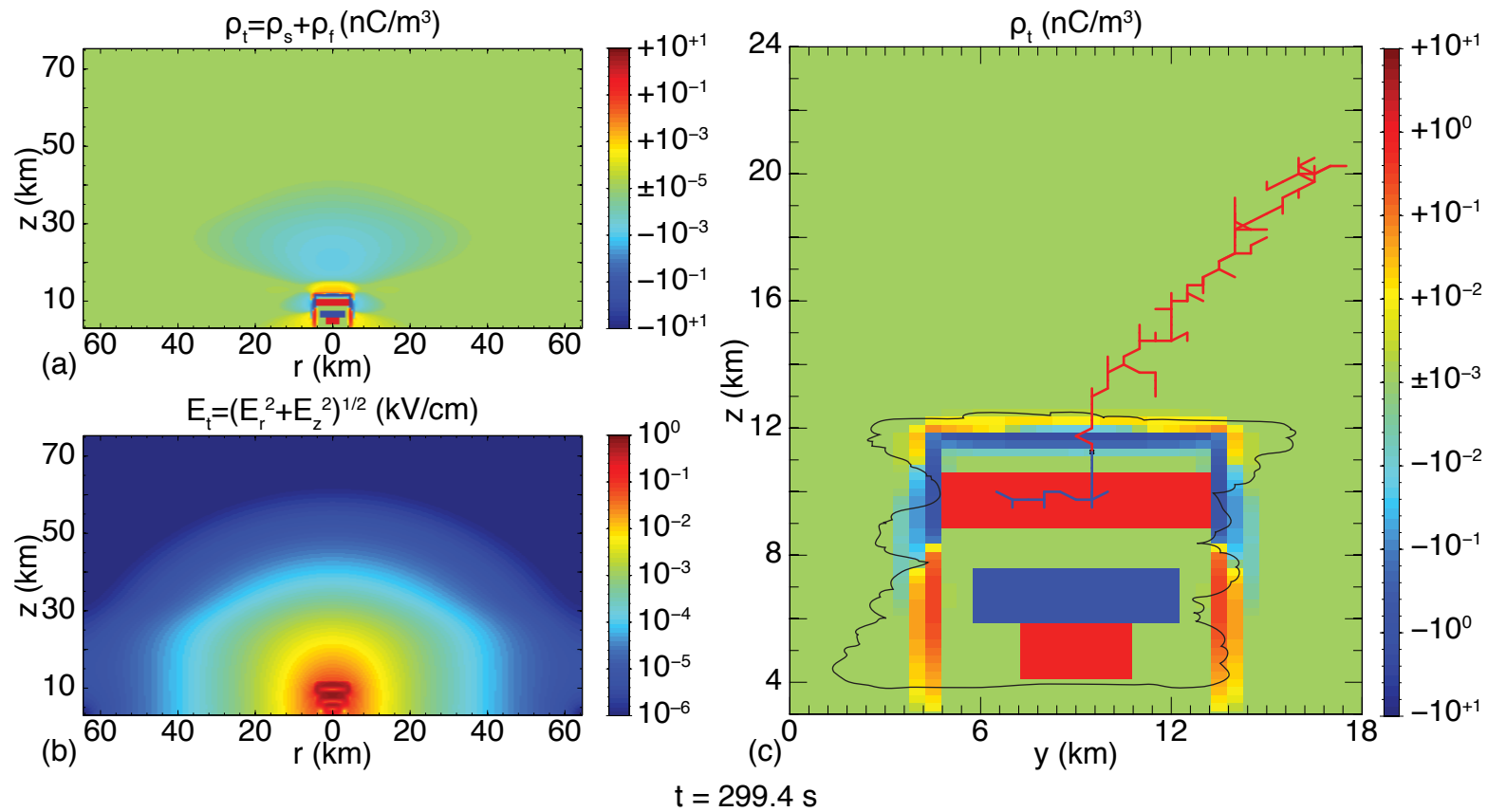


Figure 6.2. Total charge density (a), and electric field magnitude (b) at the moment of the blue jet initiation $t \sim 299.4$ s (see Figure 6.1a). At this instant, the electric field exceeds the lightning initiation threshold near the cloud upper boundary leading to an upward positive discharge (marked as +BJ in Figure 6.1a). (c) Modeling of the jet discharge using the 3-D fractal model, with charge densities as background. (See Supplementary Video 3 in [Riousset *et al.*, 2010a] for the animated version of panels (a) and (b).)

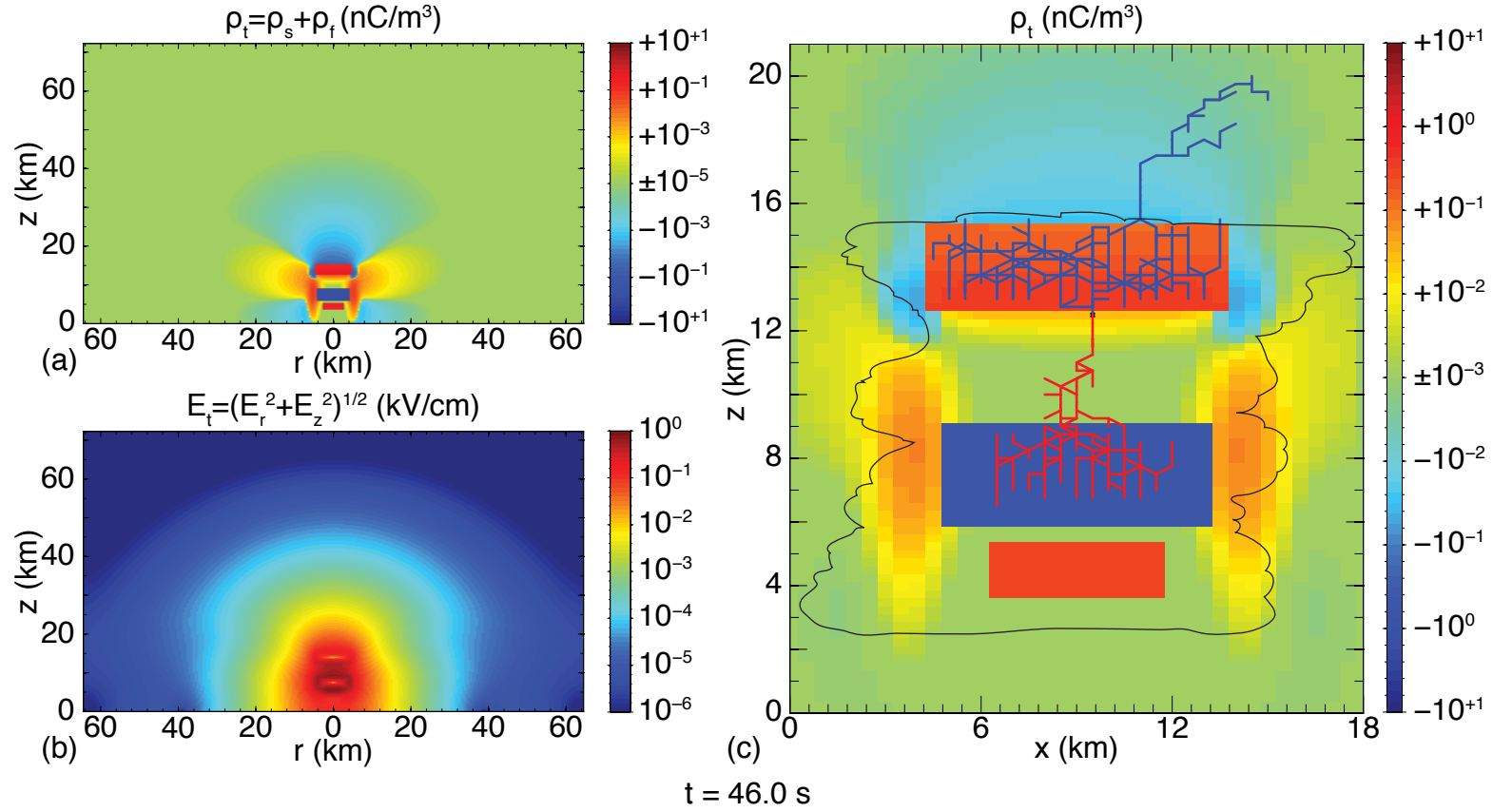


Figure 6.3. Same as Figure 6.2, except for the gigantic jet discharge at $t \sim 46$ s in Figure 6.1b, initiates between the central negative and screening depleted upper positive charge regions. (See Supplementary Video 4 in [Riousset *et al.*, 2010a] for the animated version of panels (a) and (b).)

before the next intracloud discharge, which are occurring at ~ 20 s intervals. The blue jet causes net positive charge to be removed from the storm, bringing the overall storm charge back close to neutrality. The blue jet also discharges part of the negative screening charge Q_{SC} (dotted blue line). We note that the accumulation of screening charge Q_{SC} above the cloud top facilitates the initiation of the blue jet. As a consequence of the screening charge being reduced by the blue jet, the next cloud-to-ground flash in the sequence does not initiate a blue jet. The screening charge does not start to rebuild until after the third negative cloud-to-ground discharge causes the storm to develop a net positive charge again. Similar results have been obtained using the 1-D model introduced in [Krehbiel *et al.*, 2004, 2008, Supplementary Information].

Figure 6.2a shows the total charge density ρ_t over the entire 2-D simulation domain at the instant of initiation of the blue jet, and Figure 6.2b shows the magnitude of the electric field at the same instant of time. The zoomed-in view of Figure 6.2c shows how the induced free charges of panel (a) largely consist of screening charges accumulated at the cloud boundary. Because of being spatially distributed, the negative component of the screening charge Q_{SC} of Figure 6.1a is calculated in the model as: $Q_{SC} = \iiint_V \rho_f(\vec{r}) dV$, where for simplicity the integration volume V consists of the entire half space above the lowest altitude $z_{\text{bottom}} \approx 12.5$ km of the upper positive charge region. The integral is dominated by the screening charges on the top and lateral upper cloud boundaries.

Figure 6.2c also shows a plane projection of the three-dimensionally modeled jet developing under the conditions given by the two-dimensional charge relaxation model. The initiation occurs at $z = 11.25$ km and the discharge develops bi-directionally from that point on, propagating through the screening charge at the top of the cloud, and further developing towards the ionosphere. The simulation is stopped when the discharge exits the simulation domain (through the $y = 0$ km boundary in the present situation, topping at ~ 21 km). Although not modeled in the present work, it is expected [e.g., Petrov and Petrova, 1999; Pasko and George, 2002; Krehbiel *et al.*, 2008] that the streamer corona of the thermalized leader section of the jet would expand up to higher altitudes, consistent with published observations of blue jets [e.g., Wescott *et al.*, 1995; Sentman and Wescott, 1995; Boeck *et al.*, 1995; Wescott *et al.*, 2001].

Figures 6.1b and 6.3 present analogous results for the gigantic jet-producing storm of Figure 5.3b. The larger values of the charging currents ($I_1=3.0$ A versus 1.5 A; $I_2=-0.25$ A versus -90 mA) cause the intervals between the initiations of intracloud lightning discharges to be shorter (every ~ 13 s) and the first negative cloud-to-ground discharge to be initiated after ~ 140 s (Figure 6.1b). In addition, the higher altitude of the storm causes the screening charge to form relatively rapidly and the storm to accumulate a substantial net negative charge (-40 C) 40 s into the simulation. By this time, the strong mixing of the screening charge produce an approximate 2:1 charge imbalance between the N- and P-charge regions, giving rise to a gigantic jet ~ 46 s into the simulation, as the third discharge of the storm. The net effect of the gigantic jet is to release ~ 26 C of negative charge from the storm, similar to a negative cloud-to-ground discharge but upward in the atmosphere rather than downward to ground. Under the assumptions (a) that gigantic jets remove only half of the N-charge and (b) continued strong mixing, the 3-D discharge model predicts about every other intracloud lightning discharge to produce an upward negative gigantic jet ($-GJ$). The first negative cloud-to-ground lightning discharge briefly interrupts the gigantic jet sequence by providing an alternative way of releasing the accumulated negative charge.

The numerous occurrences of gigantic jets in the simulation suggest that many discharges initiated in the midlevels of a thundercloud are able to escape. Such behavior is observed in New Mexico thunderstorms, as they commonly develop bolt-from-the-blue (BFB) dominated regimes [Thomas *et al.*, 2002]. Under these circumstances, bolt-from-the-blue lightning discharges become the main discharge process for releasing excess negative charge. The 2-D axisymmetric geometry of the relaxation model does not permit the development of asymmetric, locally enhanced lateral screening charge leading to the development of bolt-from-the-blue discharges [e.g., Krehbiel *et al.*, 2008, Figures 3 and 4e]. Instead, midlevel-initiated escaping discharges develop into gigantic jets. Therefore the repeated occurrence of gigantic jets in Figure 4b is to be expected, and should be compared with a BFB-dominated regime in light of the above argument.

Figure 6.3a shows the total charge density ρ_t over the entire 2-D simulation domain at the instant of initiation of the gigantic jet, and Figure 6.3b shows the magnitude of the electric field at the same instant of time. The focused view of

Figure 6.2c shows how the induced free charges of panel (a) are mixed with and largely contribute to the depletion of the P-layer. In this case, the portion Q_{SC} of the free induced charges mixed with the upper positive layer is calculated as $Q_{SC}=Q_{mix}=\iiint_{V_P} \rho_f(\vec{r})dV$, where the volume of integration V_P is restricted to the volume occupied by the P-region itself. Thus, Q_{SC} represents the charge content of the additional layer formed by accumulation of screening charge at the cloud top for the blue jet case, and the amount of screening charge Q_{mix} mixed with Q_P for the gigantic jet case.

Figure 6.3c shows a plane projection of the three-dimensional model of the first gigantic jet discharge at ~ 46 s. The discharge is initiated at $z=12.5$ km and develops bi-directionally within and through the N- and P-layers, respectively. The discharge escapes upward and, as in the blue jet case, the simulation is stopped as the jet reaches a boundary of the simulation domain (in this case, the side boundary at $y=0$ km). As expected for blue jets but not modeled here, the streamer corona of the leader part of gigantic jets is expected to propagate upward toward the ionosphere, consistent with published observations of gigantic jets [e.g., *Pasko et al.*, 2002; *Su et al.*, 2003; *Kuo et al.*, 2009].

6.2 Discussion

In this section, we provide a physical interpretation of the results presented above. In the simulations of blue and gigantic jets, the driving sources of all electrical discharges are the charging currents I_1 and I_2 . *Krider and Musser* [1982], *Williams* [1989] and *MacGorman and Rust* [1998, pp. 53–54] reported precipitation currents at the cloud base and at ground from 2–3 nA/m² up to 12 nA/m² or more. From the observationally inferred cross section of modeled thunderclouds ($\pi R_{LP}^2 \sim 7.0$ and 25 km² for simulation geometries of Figures 5.3a and 5.3b, respectively), the above current densities correspond to a lower altitude charging current I_2 ranging from ~ 15 mA up to 300 mA. The values of I_2 used in the simulations (90 and 250 mA) and given in Table 5.2 are therefore in good agreement with observational data. Simulations employing the assumed values of I_2 also give cloud-to-ground lightning flashing rates that are well within the range of observed values.

Few if any direct measurements are available for the main charging current I_1 , but the current can be estimated from intracloud lightning rates in the storm. Observational data and electrodynamic simulations show that intracloud discharges transfer up to 20–40 C per flash [Uman, 1969, pp. 96–101; Krehbiel, 1981, p. 143, Tables 8 and 16, and Figure 3.2.31; Uman, 1987, pp. 235–237; Rakov and Uman, 2003, p. 325]. A modest intracloud lightning flashing rate of one per 20 s (3 min^{-1}) would therefore require a charging current $I_1=1\text{--}2 \text{ A}$; higher flash rates such as are common in large storms (possibly with decreased charge transfer per flash) would require correspondingly larger charging currents. The values of I_1 used in the simulations (1.5 and 3.0 A) are consistent with such flashing rates.

The model-assumed storm charge densities are on the order of a few nC/m^3 (i.e., a few C/km^3), and are consistent with in-situ balloon measurements (e.g., 2–6.7 nC/m^3 in [Marshall and Stolzenburg, 1998]). The resulting electric field profiles and magnitudes, $\lesssim 10^5 \text{ V/m}$ (or 1 kV/cm), reasonably match those observed in thunderclouds [e.g., Marshall *et al.*, 1995, Figure 3; Marshall and Stolzenburg, 2001, Figure 2]. The modeled results constitute slight underestimates of the actual field strengths because the assumed threshold values E_{th}^\pm are breakeven values and do not attempt to incorporate an enhancement factor for initiating breakdown, which is not well known.

The conductivity of the moist air within a cloud is decreased due to ion attachment to hydrometeors [e.g., Brown *et al.*, 1971; Pruppacher and Klett, 1997, p. 798; Rakov and Uman, 2003, p. 91] compared with that of the surrounding dry, clear air. Consequently, a conductivity gradient appears at the cloud boundary (equation (5.3)) that causes a screening charge to form at the boundary [e.g., MacGorman and Rust, 1998, p. 71]. The location and thickness of the transition from higher to lower conductivity depends on factors such as overturning [e.g., Holton, 2004, p. 377] and storm maturity (a description of the thunderstorm evolution can be found in [e.g., Wallace and Hobbs, 1973, p. 351]).

Weak mixing between the upper-level screening charge and the cloud interior, due, for example, to weak overturning, causes a well-defined screening charge to accumulate around the upper cloud boundaries, as seen in Figures 5.2b and 6.2c. The screening charge is of negative polarity and locally enhances the electric field above the upper positive charge layer (Figure 5.2c). This field enhancement ul-

timately results in breakdown occurring in the uppermost part of the cloud that escapes the storm upward and becomes a blue jet. For the simulated storm of Figure 5.3a, no mixing takes place between the screening and upper positive charges and breakdown occurs quickly in the storm, at ~ 11 km altitude ~ 300 s into the simulation. The jet is triggered ~ 4 s after a negative cloud-to-ground discharge that transfers an estimated 20.9 C of negative charge to ground, leaving the storm with an overall net positive charge. The negative cloud-to-ground flash suddenly increases the electric field in the upper storm levels and enables the next breakdown event to occur above the positive charge region (giving rise to the jet) rather than below the positive charge region (which would have resulted in another intracloud lightning discharge).

At the time of the jet initiation, the lower positive, midlevel negative, upper positive, and cloud-top screening charges are $Q_{LP}=+9.7$ C, $Q_N=-35.8$ C, $Q_P=+71.5$ C and $Q_{SC}=-23.3$ C, respectively, corresponding to a net positive charge $Q_\Sigma=+22.1$ C. That the breakdown would result in an upward-escaping discharge is expected from Q_P being more than three times larger than Q_{SC} , and this difference is confirmed by the three-dimensional fractal modeling. Continued upward propagation is supported by the unconstrained potential profile above the cloud top (see Figure 4.1f) and by the quasi-exponential decrease of the breakdown threshold with increasing altitude (Figure 5.3).

Blue jet breakdown can also occur without the storm having a net positive charge [Krehbiel *et al.*, 2008], as confirmed by other simulations of this study. Although a positive charge imbalance helps, the most important factor is that an unmixed screening charge be present, without which the electric field strengths required to trigger breakdown are not reached. It is basically the same reason why lower positive charge is necessary for negative cloud-to-ground discharges to be initiated. That blue jets occur infrequently in storms, as suggested by the limited number of observations reported to date [e.g., Wescott *et al.*, 1995; Sentman and Wescott, 1995; Boeck *et al.*, 1995; Wescott *et al.*, 2001; Lyons *et al.*, 2003; Chen *et al.*, 2008b], implies that mixing of the screening and upper positive charges is normally strong, as would be expected in convective storms.

The opposite situation, that of strong mixing, results in the upper positive charge becoming depleted, and produces a substantial imbalance between the P-

and N-charges that enables gigantic jets to occur. Such a situation is expected to occur at or near overshooting tops, in which strong updrafts can loft charged particles high in the storm favoring mixing with the screening charge and leading to the charge structure described in Figure 5.3b. In effect, the upper positive charge is being relaxed away, as in the Figure 5.1 example. At the time of the initial gigantic jet in Figure 5.3b ($t=46.0$ s), $Q_{SC}=Q_{mix}=-20.4$ C of screening charge has mixed with an upper positive charge $Q_P=+67.2$ C, resulting in $+46.8$ C net charge in the upper positive region. By contrast, $Q_N=-99.3$ C, constituting an approximate 2:1 charge imbalance, and producing the first gigantic jet in the fractal simulations.

In a one-dimensional study of bi-directional breakdown processes, *Mazur and Ruhnke* [1998] observed that the upward negative leader of intracloud lightning could continue beyond the upper thundercloud boundary, in the manner of a gigantic jet as discussed above. They consequently recognized a possible relationship with prior observations of lightning extending from cloud tops to the stratosphere. They attribute their modeling results to the simplified one-dimensional representation of the leader channel in their model that does not allow for horizontal branching to pass through the upper positive charge region. The simplified model of *Mazur and Ruhnke* [1998] assumes a charge imbalance but the authors do not discuss the physical conditions related to the imbalance, nor do they recognize the role of the screening charge in allowing and/or enabling upward discharge.

Gigantic jets are observed most often above tropical oceanic storms [e.g., *Pasko et al.*, 2002; *Su et al.*, 2003; *Chen et al.*, 2008a, b; *Kuo et al.*, 2009], and only one observation of gigantic jet over land has been reported to date [*van der Velde et al.*, 2007]. Tropical oceanic thunderstorms typically reach to higher altitudes than do their continental counterparts and produce overall less lightning [*MacGorman and Rust*, 1998, p. 297]. This weaker lightning activity is believed to be related to the production of gigantic jets as discussed hereafter. Negative cloud-to-ground discharges are the primary means by which normally electrified storms release the excess negative charge resulting from the upper-level screening currents. Storms that have a deficit of normally-initiated negative cloud-to-ground discharges, coupled with strong mixing, would be favored to return their negative charge upward into the atmosphere by means of negative gigantic jets (or similarly, go indirectly to ground as negative bolts-from-the-blue). In addition, storms that reach relatively

high altitudes have their screening charges form relatively rapidly ($\tau_{\text{relax}}=17.2$ s at 14 km altitude) and the upper positive charge to be depleted relatively quickly, further favoring the occurrence of gigantic jets.

Similar to blue jets, the decrease in electric field threshold with altitude supports upward propagation of gigantic jets. We further note that a weak value of I_2 limits the occurrence of negative cloud-to-ground discharges, depriving the thunderstorm of its primary mechanism for eliminating the accumulating negative charge. Figure 6.1b shows intracloud activity prior to the occurrence of the jet, consistent with the observations of optical flashes recorded by *Pasko et al.* [2002, Supplementary Information, available at <http://pasko.ee.psu.edu/Nature/>] prior to the September 14, 2001 gigantic jet event and more recently by the ISUAL instrument [*Kuo et al.*, 2009].

To illustrate gigantic jet initiation in the model, the screening charge is allowed to form in the region of the upper positive charge (Table 5.2), leaving little screening charge that is not mixed with the upper positive charge. Depending on the degree of convective overturning, actual storms will have a partially unmixed negative screening charge above the positive that will serve to impede upward escape. In this case, lightning mapping observations indicate that the discharge escapes sideways out of the cloud to ground as a negative bolt-from-the-blue discharge [e.g., *Rison et al.*, 1999; *Thomas et al.*, 2001]. Positive lateral screening charge [e.g., *Krehbiel et al.*, 2008] (or, possibly, upper positive charge caught in a lateral downdraft) then turns the discharge to ground. Although the screening charge only partially overlaps the upper positive charge, in the presented model, only a small fraction of the screening charge is not mixed with the upper positive region, leading to relatively easy occurrence of gigantic jets. Bolt-from-the-blue discharges are commonly observed in normally electrified storms and appear to be directed downward by positive screening charge that would form laterally around the mid-level negative charge [*Krehbiel et al.*, 2008]. The cylindrically symmetric charge structures of this study do not produce bolt-from-the-blue discharges in the fractal simulations, indicating that asymmetrical screening charge accumulations and/or additional positive charge need to be present for bolt-from-the-blue lightning to occur. Tropical oceanic storms may be the primary producer of gigantic jets by virtue of having a tall ‘stovepipe’ structure with strong convective overturning

and the upper positive charge having a large vertical separation from the lateral screening charges associated with the midlevel negative charge.

Because of being two-dimensional, the electrodynamic model does not readily allow coupling of the results of the 3-D fractal lightning simulations back into the model to further investigate the interactions between lightning and charge structure. Future 3-D versions of the model would enable such studies and also allow the electrodynamic techniques developed in this study to be incorporated into 3-D cloud models. The present 2-D modeling demonstrates that charge structures are produced as an inevitable consequence of the cloud being embedded in a conductive atmosphere, for which expected charge accumulations are sufficient to produce blue- and gigantic-jet type breakdown. Although there may be other ways for creating jet-producing charge configurations, they are not necessary to the development of blue and gigantic jets. Meteorological processes such as high-altitude collisional particle charging, upper-level divergence, or wind shear from upstream charge regions may supplement or reduce the role of mixing in the formation of the needed charge configurations. In particular, storm-top divergence may play an additional or alternative role in advecting screening charge away from the upper cloud boundary, making it easier for gigantic jets to escape. Conversely, strong horizontal wind shear would primarily affect the screening charge rather than the upper positive charge and therefore would be a detriment to blue jets by preventing the screening charge from enhancing the upper level electric field, and to gigantic jets by preventing the screening charge from depleting the upper positive charge region. In addition, advection of the upper positive charge into the anvil would result in intracloud discharges developing into the anvil instead of going to ground as bolt-from-the-blue discharges or to the lower ionosphere as gigantic jets. In view of these issues, mixing has to be considered as having a strong effect on jet occurrences. The common occurrence of bolt-from-the-blue discharges provides clear evidence that the upper positive charge is depleted relative to the midlevel negative charge, which could be a result of mixing processes.

Observations of blue jets [Wescott *et al.*, 1995; Sentman and Wescott, 1995; Boeck *et al.*, 1995; Wescott *et al.*, 2001] and later gigantic jets [Pasko *et al.*, 2002; Su *et al.*, 2003] reveal a fine filamentary structure of these events identified as streamer channels [Pasko and George, 2002, and references therein]. The development of

such channels without a lightning leader would require an unrealistic amount of charge near the cloud top [*Pasko and George*, 2002; *RiOUSset et al.*, 2006a; *Raizer et al.*, 2007]. The modeling scenarios reported in the present work show how a lightning leader can propagate upward from the cloud, providing a stem above the thundercloud ($z=20$ km or higher) for development of the streamer corona up to the lower ionosphere, quantitatively demonstrating the idea first expressed by *Petrov and Petrova* [1999] and further developed in [*Krehbiel et al.*, 2008].

6.3 Summary of Results

In this chapter, we employ the model developed in Chapter 5 to simulate realistic thundercloud dynamics resulting in the initiation of blue and gigantic jets. Our results emphasize the role of the screening charges in the magnification of the electric field near the cloud top and/or the formation of charge imbalances. Blue and gigantic jets are modeled based on the concept of bi-directional, overall neutral and equipotential lightning leaders using realistic cloud configurations produced by the Maxwellian relaxation model. We demonstrate how the prior occurrence of intracloud discharges can prevent the development of a blue jet until a cloud-to-ground discharge enhances the excess of positive charge in the cloud by bringing negative charge to ground. The screening charge gradually developing at the cloud top leads to discharge initiation near the cloud upper boundary, but is insufficient to contain the lightning leader channel within the cloud resulting in occurrence of upward propagating blue-jet events. We also show that in thunderstorms for which convective overturning near the cloud top is sufficiently strong, the screening layer that allowed for blue jet initiation, gets mixed with the storm upper positive charge region, reducing the net positive charge in this region and causing a substantial charge imbalance between the two main layers of the thundercloud. Quantitative modeling of resulting discharge reveals that the leader channels cannot be contained in the volume enclosed within the cloud boundary and eventually escape upward to form a gigantic jet.

Model of Air Heating in Streamer Discharges Under Constant Applied Electric Field

In this chapter, we formulate a new 1-D, axisymmetric, air-density-dependent model of the streamer-to-spark transition. The model accounts for self-consistent effects of the dynamic expansion of the heated air on the reduced electric field E/N and resultant plasma kinetics in the streamer channel. In addition to ionization kinetics, involving the production and interaction of electrons and different types of positive and negative ions, the model accounts for self-quenching of $N_2(A^3\Sigma_u^+)$ excited molecules, and associative ionization processes involving $N_2(A^3\Sigma_u^+)$ and $N_2(a'^1\Sigma_u^-)$ species. The model also includes energy input in vibrational excitation of nitrogen molecules $N_2(v)$ and the vibrational–translational relaxation processes, and accounts for the effects of gains in electron energy in collisions with vibrationally excited $N_2(v)$ on the rate constants of processes involving electron impact collisions. The model is applied in Chapter 8 to perform a systematic study of gas dynamics and chemical kinetics involved in heating of air in streamer channels for a given air density N under assumption of constant applied electric field E .

7.1 Physics and Modeling of the Streamer-to-Spark Transition

The observed phenomenology of a subset of the recently recorded transient luminous events (TLEs) in the middle atmosphere, which originate from thundercloud tops [e.g., *Wescott et al.*, 2001; *Pasko et al.*, 2002; *Su et al.*, 2003; *Krehbiel et al.*, 2008; *Cummer et al.*, 2009; *Riousset et al.*, 2010a], indicate that these events, so-called blue and gigantic jets, may be related to conventional lightning leader processes as initially proposed by *Petrov and Petrova* [1999]. *Wescott et al.* [2001] have reported a two-minute time exposure color photograph of a jet event taken from St. Denis, Réunion Island in the Indian Ocean. The corresponding inverted black and white image from [*Wescott et al.*, 2001] is reproduced in Figure 7.1a and shows details of faint streamers diverging from the main body of the jet. Figure 7.1b shows an image obtained by averaging of 48 video fields extracted from the 24 frame video sequence corresponding to a similar event observed in Puerto Rico [*Pasko et al.*, 2002]. The image in Figure 7.1b effectively simulates how the observed event would look if captured on a photograph with an exposure time exceeding the total duration of the event (~ 0.8 s). Figure 7.1b shows a very similar structure to Figure 7.1a in terms of faint streamers diverging at large angles from the main body of the jet. The original video sequence presented in [*Pasko et al.*, 2002] indicates that these streamers are formed at the initial stage of the jet development. Therefore, the streamer structure in Figure 7.1a was likely formed at the initial stage of that event development, similarly to the event reported in [*Pasko et al.*, 2002] (Figure 7.1b). Figure 7.1b shows a very bright channel at the bottom of the image (between altitudes of approximately 16 and 20 km). We interpret the appearance of this bright feature in both Figures 7.1a and 7.1b as the streamer-to-leader transition involving strong heating and thermalization usually associated with a leader phenomenon. This interpretation is supported by the original color photograph in [*Wescott et al.*, 2001], in which the lower portion of the event in Figure 7.1a has a bright white color. Therefore, these events are believed to be associated with significant heating of the air in the regions of atmosphere near the cloud tops through which they propagate [*Pasko and George*, 2002]. The small-scale filamentary structures in the upper parts of the observed jets, identi-

cal to those observed in another type of TLEs at higher altitudes called sprites [e.g., *Stenbaek-Nielsen et al.*, 2007, and references therein], can be associated with corona streamers. Such streamer coronas are expected to constitute an essential part of the streamer zone of the parent lightning leader [e.g., *Bazelyan and Raizer*, 1998, pp. 204, 238, and 253] as hypothesized by *Petrov and Petrova* [1999].

Recently, *Krehbiel et al.* [2008] discussed the charge imbalances in thunderstorms as a fundamental condition allowing propagation of leaders downward as cloud-to-ground lightning or upward as jet discharges. This work, reviewed in Chapter 4, demonstrates that upward discharges are analogous to cloud-to-ground lightning and provides a unified view on how lightning escapes from a thundercloud. *Krehbiel et al.* [2008] note that in accordance with existing experimental evidence, the lightning initiation usually happens between adjacent charge regions of different polarity where the electric field is the highest. If the negative and positive charge centers are approximately equal in magnitude, then the bidirectional discharge propagates in the form of positive leaders inside of negative charge region and in the form of negative leaders inside of the positive charge region [e.g., *Riousset et al.*, 2007a]. In this situation, the leader system, which is assumed to be overall equipotential and neutral, remains at nearly zero potential [*Riousset et al.*, 2007a]. *Krehbiel et al.* [2008] demonstrate that when the two charges are not balanced, the leader potential can be significantly shifted in the direction defined by the charge with dominant magnitude, and the propagation of the leader becomes essentially independent from the weaker charge center, allowing it to penetrate through the weaker charge center and to escape from the thundercloud. To further support the ideas advanced by *Krehbiel et al.* [2008], *Riousset et al.* [2010a] introduce a two-dimensional axisymmetric model of charge relaxation in the conducting atmosphere and apply this model in conjunction with the three-dimensional lightning model proposed in [*Riousset et al.*, 2007a] to illustrate how blue and gigantic jet discharges are produced above cloud tops. The results of *Krehbiel et al.* [2008] and *Riousset et al.* [2010a] provide a quantitative picture of how the lightning leader can escape the cloud upward and serve as the initiation of blue and gigantic jets. The exact details of the transition from the hot leader channel near the cloud top to the streamer-dominated forms observed in jets at high altitude are not understood at present, and one of the goals of the studies of

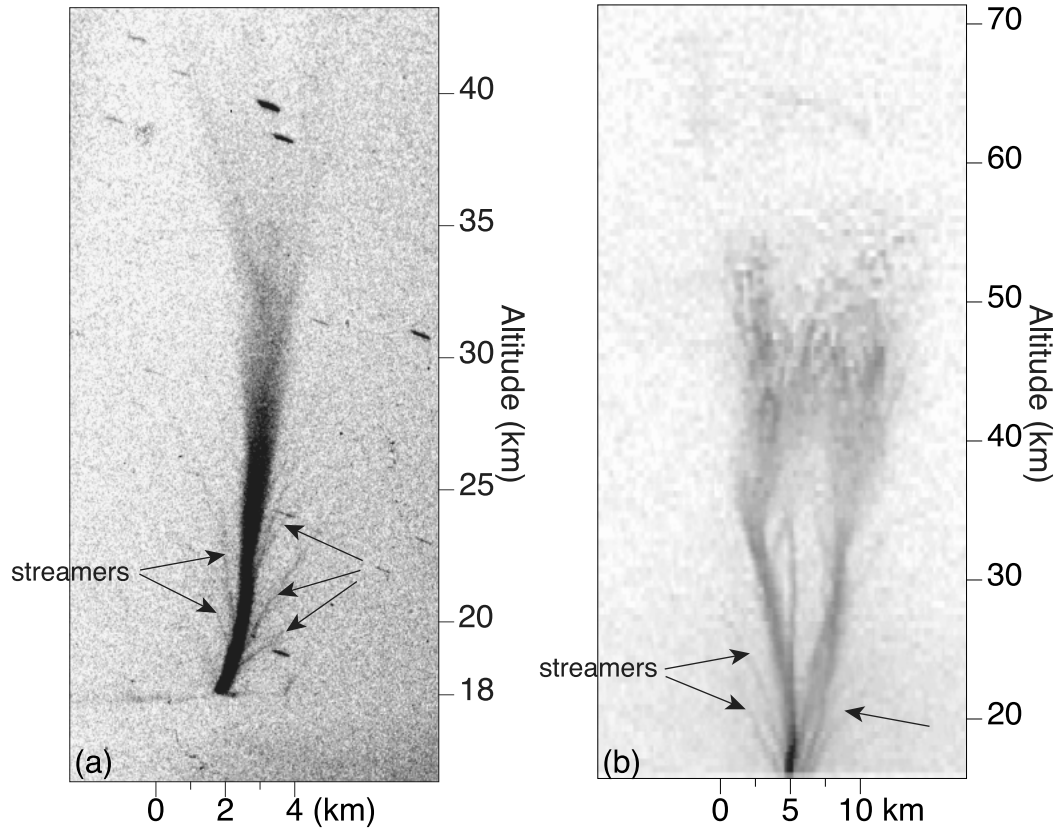


Figure 7.1. (a) A black and white image of a 2-min time exposure of a blue jet [Wescott *et al.*, 2001]. The image is provided through the courtesy of G. Wescott, University of Alaska. (b) Processed image obtained by averaging of sequence of video fields from observations reported in [Pasko *et al.*, 2002, <http://pasko.ee.psu.edu/Nature/>]. Reprinted from [Pasko and George, 2002] with permission from American Geophysical Union.

this chapter and the following one (Chapter 8) is to make a first quantitative step in understanding the elementary scaling of the heating processes associated with streamers and leaders as a function of the ambient air density (or equivalently, as a function of the altitude).

After appropriate scaling with air density, the corona streamers observed in Figure 7.1 are fully analogous to those that initiate spark discharges in relatively short (several cm) gaps at near ground pressure [Liu *et al.*, 2009, and references therein] and that are known to constitute building blocks of streamer zones of conventional lightning leaders and leaders in long gaps in laboratory experiments [e.g., Gallimberti, 1979; Bazelyan and Raizer, 1998, pp. 204, 238, and 253; Gallimberti

et al., 2002]. The scaling of the parameters of streamer discharges as a function of air density N (e.g., streamer radius $r_s \propto 1/N$, streamer electron density $n_{e,s} \propto N^2$, and dielectric relaxation time in the streamer body $\tau_s \propto 1/N$) has been discussed for sprite discharges in the middle atmosphere and can be readily used to establish a similarity law for the Joule heating timescale (i.e., its scaling with neutral density) [Pasko *et al.*, 1998]. Indeed, assuming for simplicity of presentation that air density N , streamer electron density n_e and the electric field in the streamer channel \vec{E} remain constant, and that all Joule energy is transferred directly to heating of the gas, one can write an equation for the air temperature T_g in the form:

$$\frac{dNk_B T_g}{dt} = (\gamma - 1) \vec{J} \cdot \vec{E} \quad (7.1)$$

where $\vec{J} = q_e n_e \mu_e \vec{E}$ is the current density, q_e is electron charge, γ is the specific heat ratio and μ_e is the electron mobility. The scaling of streamer electron density with air density N is defined with respect to ground value N_0 as $n_e = n_{e,0} N^2/N_0^2$, where $n_{e,0}$ is the streamer electron density at the ground level. Other physical quantities can be expressed in similar form as $\mu_e = \mu_{e,0} N_0/N$ and $E = E_0 N/N_0$ [e.g., Pasko *et al.*, 1998]. Having substituted these expressions in the above equation one can represent time variation of air temperature T_g in the form:

$$\frac{dT_g}{d(tN^2/N_0^2)} = \frac{(\gamma - 1)q_e}{k_B} n_{e,0} \mu_{e,0} E_0^2 \quad (7.2)$$

that directly indicates that for reduced air density $N < N_0$ it takes a factor of N_0^2/N^2 longer time to produce the same increment in gas temperature T_g (e.g., 5000 K, see further discussion below). Therefore, the general scaling of the Joule heating timescale in the streamer channels as a function of air density is $\tau_h \propto 1/N^2$ [e.g., Achat *et al.*, 1992; Tardiveau *et al.*, 2001; Pasko, 2006]. Therefore, it is generally expected that the heating processes and resulting streamer-to-spark transition should be delayed with a reduction of air pressure (i.e., at higher altitudes in the Earth atmosphere), and it should be possible to define a set of specific conditions (i.e., altitude range, reduced electric field E/N , etc.) in the Earth atmosphere for which the transition becomes impossible. The heating of the streamer channel depends not only on the Joule heating but also on the relaxation of vibrationally excited N_2

molecules, on the complicated kinetics of electron detachment from negative ions, on the gas dynamics expansion of the channel, and on other factors as discussed in Chapter 8. Consequently, a simple similarity law for heating timescale cannot be simply deduced from the similarity laws for streamers.

Unlike the neutral gas density N , the pressure p is easily measured, and therefore commonly used for reference in experimental studies on the streamer-to-spark transition [e.g., *Achat et al.*, 1992; *Larsson*, 1998]. During the initial stages of the heating, the gas temperature T_g can be considered as constant so that p becomes equivalent to N , with their relationship obeying the classical law of perfect gases, $p = Nk_B T_g$, where k_B is the Boltzmann constant. When thermal gas expansion effects are accounted for, it is important to use the reduced electric field E/N , instead of E/p [e.g., *Tardiveau et al.*, 2001]. Consequently, in the present work, we use reduced parameters as functions of the neutral gas density N similar to those used in other experimental [*Tardiveau et al.*, 2001] and theoretical [e.g., *Naidis*, 2005; *Popov*, 2009] works. In this work, we investigate the similarity law of heating timescale in the streamer-to-spark transition, i.e., its scaling with neutral gas density. The model developed for the studies reported in this chapter builds on previous theoretical modeling of streamer-to-spark transition, a review of which is given below. It also complements experimental investigations of the pressure effects on the development of electric discharges in small gaps by *Achat et al.* [1992] and *Tardiveau et al.* [2001].

The earliest qualitative model description of a streamer-to-spark transition by *Marode* [1983, and references therein] focuses solely on a thermal transition (i.e., based on gas dynamics expansion of the channel leading to a reduction in the gas density and to an increase in E/N). Later studies either include chemical kinetic processes as an alternative or a companion mechanism to the thermal mechanism. *Mnatsakanyan and Naidis* [1991] discuss the foundations of the chemistry models of electrical discharges. The first comprehensive kinetics scheme of the non-equilibrium discharge in nitrogen–oxygen mixtures is reported by *Kossyi et al.* [1992]. Many subsequent models of streamer breakdown in short gaps involving chemical kinetics [e.g., *Aleksandrov et al.*, 1997, 1998, 2001; *Naidis*, 1999, 2005, 2008; *Popov*, 2001, 2003, 2009; *Flitti and Pancheshnyi*, 2009] benefit from the exhaustive list of reactions investigated in this pioneering work.

The first models of plasma heating by *Aleksandrov et al.* [1997, 1998] were developed in the framework of breakdown (by streamer or leader channel, respectively) in long air gaps ($>5\text{--}10$ m). *Aleksandrov et al.*'s [1997] 0-D model accounts for the influence of the electric field and gas temperature on the ionization kinetics to study the response time of a leader parameters to a step change in the gas temperature. It does not account for vibrational–translational relaxation of vibrational energy of N_2 molecules, which was introduced in [*Aleksandrov et al.*, 1998], following the principles discussed in [e.g., *Mnatsakanyan and Naidis*, 1985]. *Aleksandrov et al.*'s [1998] 1.5-D model accounts for the fact that the Joule heating owing to the current flow in the channel is not solely used to increase the temperature of the background gas. Instead, only a small fraction of the Joule heating energy, denoted η_T , is used to heat the channel in the so-called “fast heating” process mainly associated with relaxation of electronically excited states of N_2 and O_2 molecules; a significant fraction η_V of the Joule energy is transferred to and stored in the vibrational energy levels of the nitrogen molecules. *Aleksandrov et al.* [1998] conclude that the rapid gas heating is associated with a conversion of the energy of the electronically excited molecular states into heat via quenching of the excited molecules.

Aleksandrov et al. [1998] consider that the effect of hydrodynamic expansion of the streamer channel on the streamer-to-spark transition is negligible because of the fairly short time of the channel formation. *Naidis* [1999] employs a similar model in 0-D involving 14 species including electrons, positive and negative ions, and excited radicals to propose two possible origins of the increase in plasma conductivity leading to the spark formation during streamer-to-spark transition [*Naidis*, 1999, 2005, and references therein]. The first one is a thermal mechanism, which leads to lowering of the gas number density N inside the channel due to the expansion of the heated gas [*Marode et al.*, 1979; *Marode*, 1983; *Bastien and Marode*, 1985]. As already noted above, this process leads to the growth of the mean reduced field E/N and therefore to an increase in the ionization rate. The second one is a kinetic mechanism related to the accumulation of active particles (radicals and excited molecules) changing the balance between the rates of generation and loss of electrons due to the acceleration of the detachment, stepwise and associative ionization [e.g., *Aleksandrov et al.*, 1998]. Both of these factors act simultaneously,

but for practical analysis, it is possible to identify different parameter regimes when only one of these factors dominates. Recent analysis accounting for both of these factors conducted in [Naidis, 2005] indicates that at relatively high electric field values $EN_0/N > 20$ kV/cm in the streamer channel during the streamer-to-spark transition, the kinetic mechanism is dominant, and related problems can be solved with sufficient accuracy assuming that the gas density N is neutral. At lower electric field values $EN_0/N < 17$ kV/cm, the approximation based on constant pressure (i.e., allowing the growth of gas temperature and the associated decrease of N) can be employed [Naidis, 2005].

A model by Flitti and Pancheshnyi [2009] employs 44 species participating in about 430 reactions to study the gas heating in fast-pulsed discharges in N_2 - O_2 mixtures. This work pays particular attention to the estimation of the fractions η_T and η_V , which are obtained with the BOLSIG+ solver of the Boltzmann equation for electrons in weakly ionized gases [Hagelaar and Pitchford, 2005]. Using this model, Flitti and Pancheshnyi [2009] show that higher electron density, electric field or partial pressure of oxygen leads to a faster gas heating, but that the heating rate associated with excitation of vibrational and electronic degrees of freedom is almost independent of the value of the applied electric field, in the range of fields studied. These authors also do not detect significant pressure dependence of the η_T and η_V parameters, in agreement with the results presented in [Popov, 2001].

The investigation of the effects of the channel expansion discussed by Naidis [1999] requires suitable modeling of the gas dynamics of the plasma channel, and so a spatial dimension of the discharge needs to be introduced. Under the assumptions of a constant, uniform field along the channel axis, and of an axial symmetry of the discharge, one-dimensional time varying simulations of the streamer-to-spark transition have been shown to adequately model the heating of the channel [e.g., Naidis, 2005]. The 1-D axisymmetric, axially invariant model of the streamer-to-spark transition by Aleksandrov *et al.* [2001] adopts a 1-D time dependent hydrodynamic model under the isobaric approximation coupled to a 0-D kinetics scheme. Aleksandrov *et al.* [2001] employ a time- and space-dependent heat equation and a time-dependent homogeneous electron-density balance equation and suggest that kinetic mechanisms prevail over thermal processes (i.e., processes related to gas dynamic expansion). Popov [2001] developed a similar model involving a 0-D

kinetics scheme coupled to 1-D time- and space-dependent system of equations comprising the equations of conservation of energy and electron number density (n_e) under the assumption of a constant neutral density. The salient difference between the equations of balance of electrons as it appears in *Naidis's* [1999] and *Popov's* [2001] model resides in the spatial dependence of n_e that is described in the latter by the ambipolar diffusion equation. The model is used to investigate the contribution of the vibrational–translational relaxation to the rapid gas heating in nitrogen–oxygen mixtures and concludes that the contribution of the vibrational–translational relaxation reactions to the total rate of gas heating should increase with gas pressure because of the increase in the concentration of $O(^3P)$ atoms [*Popov*, 2001].

The assumptions of constant pressure and constant neutral density indeed correspond to two heating regimes of the discharge according to whether the breakdown time τ_{br} , defined as the time to heat the channel from ambient temperature (~ 300 K) to the temperature at which the thermal ionization becomes important ($T_{br} \sim 5000$ K), is more or less than the ratio of the streamer radius r_s to the sound velocity c_s . When $\tau_{br} \leq r_s/c_s$, the role of the channel expansion is small, so that the assumption of constant neutral density employed in 0-D models [e.g., *Naidis*, 1999] and 1-D models [e.g., *Popov*, 2001] is fully justified. At $\tau_{br} > r_s/c_s$, the effects related to the reduction of neutral gas density due to channel expansion become important [*Naidis*, 1999]. At ground pressure, these conditions correspond to breakdown times $\gtrsim 1 \mu s$ [e.g., *Naidis*, 1999], i.e., similar to the gas dynamics timescales on the order of $0.1\text{--}1 \mu s$ quoted by *Aleksandrov et al.* [2001], and long enough for equalization of the pressure on timescales of $\sim 1 \mu s$ as discussed in [*Popov*, 2003]. This last regime can be regarded as occurring under isobaric conditions [*Naidis*, 2005].

Further investigation of the conditions for the appearance of these regimes is made possible by introducing full one-dimensional gas dynamics, i.e., suppressing the hypotheses of either constant pressure or density in the channel. In comparison with the work by *Popov* [2001], *Popov* [2003] introduces an advection term in the time- and space-dependent equation of electron balance, and uses it to further study the role of each of the two heating regimes described by *Naidis* [1999] in the initiation and development of a leader channel in air. It is shown that, during the initial stage of the channel formation, kinetics effects largely govern the parameters

of the heating process. In contrast the rapid increase in the electron density near the axis leads to a decrease in the gas density. As a result, the discharge contracts toward the channel axis and evolves into a highly conducting thin column [Popov, 2003].

Naidis [2005] extends the 1-D steady state models previously developed by *Benilov and Naidis* [2003, 2005] for investigation of low-current discharges in atmospheric-pressure air, and discharges in a flow of preheated air. *Naidis* [2005] tests the conditions of existence of the heating regimes under the assumption of constant pressure or constant neutral gas density. This model is employed in the framework of the study of the dynamics of streamer breakdown of short non-uniform air gap and leads to the conclusion that streamer-to-spark transition at values of $E/N \gtrsim 80$ Td may be described with sufficient accuracy under the approximation of constant gas density; at $E/N \lesssim 70$ Td, the transition may be described under the approximation of constant pressure [Naidis, 2005]. The obtained model breakdown times are compared with experimental results obtained by Černák *et al.* [1995] and Larsson [1998].

Using a model similar to that introduced in [Popov, 2003], Popov [2009] recently suggested that the formation of a leader channel in air, and consequently the heating of streamer discharges occurs in two stages: one based on the kinetics processes occurring at an essentially constant gas density on timescales much shorter than the characteristic gas-dynamic time, and another in which gas dynamic rarefaction of the channel becomes dominant. In other words, this work suggests that the two regimes described by *Naidis* [2005] would occur successively rather than simultaneously.

The model developed in this chapter includes all the components previously incorporated in the model of spark discharges and summarized in the literature review above. Our kinetic approach does not directly adopt the most recent complex kinetics schemes involving several tens of species and several hundreds of reactions [e.g., Sentman *et al.*, 2008a, b; Flitti and Pancheshnyi, 2009] but it identifies the dominant reactions relevant to the problem of air heating in the streamer channel and investigates their impact on the streamer-to-spark transition dynamics. There are two principal approaches that are used in the existing literature for modeling studies of air heating effects in streamer discharges. Marode [1983] provides

an excellent review of related approaches including their relevance to practical systems and the external circuit considerations driving the discharge. The first approach postulates either a time-dependent or a stationary current and derives time dynamics of the electric field, conductivity and other parameters of the channel assuming continuity of the current along the channel [e.g., *Aleksandrov et al.*, 2001; *Benilov and Naidis*, 2003; *Bazelyan et al.*, 2007; *Popov*, 2001, 2003, 2009]. The second approach assumes a constant value of the electric field in the channel and then self-consistently evaluates dynamics of other discharge parameters (i.e., conductivity, current, gas temperature, etc) [*Marode et al.*, 1979; *Bastien and Marode*, 1985; *Aleksandrov et al.*, 1998; *Naidis*, 1999, 2005]. As is demonstrated in the above cited literature, the second approach describes very well a situation after the streamer bridges a relatively short gap with a constant applied voltage, and there are several related experiments conducted under controlled laboratory conditions at ground and near ground air pressures in which streamer-to-spark transition times have been accurately measured [e.g., *Černák et al.*, 1995; *Larsson*, 1998]. The present study reports results relevant to the second approach. The related model set up is motivated by the possibility to carefully test the model-calculated transition times in comparison with experimental data. The goal of the present investigation is to conduct a systematic study of the gas dynamics and chemical kinetics of the streamer-to-spark transition at different air densities. The set up of our model is similar to that reported by *Naidis* [2005]. We extend this previous work by studying scaling properties of air heating for a broad range of air densities corresponding to altitudes of 0–70 km in the Earth atmosphere.

7.2 Formulation of the Model of Streamer-to-Spark Transition

The model, which we developed for the studies of the effective time τ_{br} of the initial stage of air heating in the streamer channel up to temperature $T_{\text{br}}=5000$ K, is one-dimensional (1-D) axisymmetric and axially invariant (i.e., only dependent on the time t and the radial coordinate r in the cylindrical coordinate system). The model couples a zero-dimensional kinetics scheme with a fully one-dimensional

gas dynamics model. It allows the investigation of streamer-to-spark transition at various air densities, or equivalently at various altitudes in the Earth atmosphere. At ground pressure (10^5 Pa), the discharge is modeled in a short air gap of size $d=1$ cm with the constant applied voltage U . During most of the heating time, after the streamer bridged the gap, the applied electric field E in the gap can be assumed to be uniform along the axis [e.g., *Naidis*, 1999, 2005] and is given by $E = (U - U_c)/d$, where U_c is the voltage drop at the cathode ($U_c=0.2$ kV). The channel has a radius r_s taken to be equal to 0.2 mm. In addition, the radial distribution of the electronic conductivity σ_e and ionic conductivity σ_i is assumed to be Gaussian: $\sigma_{e,i} = \sigma_{e,i}^0 e^{-r^2/r_s^2}$, where $\sigma_{e,i}^0$ are the values of the electronic and ionic conductivities on the axis of the channel at $r=0$ [e.g., *Naidis*, 1999]. This approximation differs from that of *Popov* [2001, 2003], who assumed that the radial dependence of the electron density (and hence of the conductivity) was governed by the advection with the ambient air velocity and by the ambipolar diffusion processes. To model self-similar discharges, such as those in the experimental work by *Tardiveau et al.* [2001], it is necessary to scale the parameters of the model with the neutral density. This scaling is done based on the similarity relations summarized in [*Pasko*, 2006]. The scaling of the different parameters of the model and their scaling properties are given in Table 7.1.

The gas dynamics in the model is governed by the Euler equations [e.g., *Marode*, 1983, p. 142; *Brown*, 1991, p. 267; *Popov*, 2003, 2009] and includes the equations of conservation of mass, momentum, and energy and the equation of balance of the vibrational energy of N_2 (equations (7.3), (7.4), (7.5), and (7.6), respectively):

$$\frac{\partial \rho}{\partial t} + \nabla \cdot (\rho \vec{v}) = 0 \quad (7.3)$$

$$\frac{\partial}{\partial t} (\rho \vec{v}) + \nabla \cdot (\rho \vec{v} \vec{v}) = -\nabla p \quad (7.4)$$

$$\frac{\partial \varepsilon}{\partial t} + \nabla \cdot \{(\varepsilon + p) \vec{v}\} = \eta_T Q_e + Q_i + Q_{VT} \quad (7.5)$$

$$\frac{\partial \varepsilon_v}{\partial t} + \nabla \cdot (\varepsilon_v \vec{v}) = \eta_V Q_e - Q_{VT} \quad (7.6)$$

where ρ , \vec{v} , p , ε , and ε_v represent the mass density, velocity, pressure, energy density, and vibrational energy density of N_2 , in the channel, respectively. The

total Joule energy deposition rate per unit volume Q is divided into its electronic component $Q_e = \sigma_e E^2$ and ionic component $Q_i = \sigma_i E^2$, such that $Q = Q_e + Q_i$. The Q_{VT} term in equations (7.5) and (7.6) describes the transfer of energy from the vibrational energy levels of nitrogen to the translational energy of the gas. The energy density ε is defined as $\varepsilon = \rho (\vec{v} \cdot \vec{v}) / 2 + p / (\gamma - 1)$, where γ is the specific heat ratio, assumed to be constant and equal to 1.4. In fact, the specific heat ratio depends on the gas composition and varies with temperature, in particular, for $T_g \gtrsim 2000$ K. But for all the results presented in this work, $T_g \gtrsim 2000$ K means that

Table 7.1. Parameters for the model of streamer-to-spark transition.

Parameter	Symbol	Value at sea level	Scaling property
Domain size	L_r	2 mm	$\propto (N/N_0)^{-1}$
Streamer radius	r_s	0.2 mm	$\propto (N/N_0)^{-1}$
Space step	δr	4 μm	$\propto (N/N_0)^{-1}$
Time step	δt	$0.1 \times \min(\delta r / c_s, \tau_{VT_{N_2, O_2}}, \tau_{VT_O})$	$\propto (N/N_0)^{-1}$
Electron mobility ^a	μ_e	$\sim 5 \times 10^{-2} \text{ V} \cdot \text{m}^2 \text{s}^{-1}$	$\propto (N/N_0)^{-1}$
Positive ion mobility	μ_+	$2.5 \times 10^{-4} \text{ V} \cdot \text{m}^2 \text{s}^{-1}$	$\propto (N/N_0)^{-1}$
Negative ion mobility	μ_-	$2.2 \times 10^{-4} \text{ V} \cdot \text{m}^2 \text{s}^{-1}$	$\propto (N/N_0)^{-1}$
Initial gas temperature	T_g	300 K	$\propto (N/N_0)^0$
Initial vibrational temperature of N_2	T_v	300 K	$\propto (N/N_0)^0$
Final gas temperature	T_{br}	5000 K	$\propto (N/N_0)^0$
Fraction of N_2 in air	x_{N_2}	0.79	$\propto (N/N_0)^0$
Fraction of O_2 in air	x_{O_2}	0.21	$\propto (N/N_0)^0$
Average mass of air particle	m_g	$4.82 \times 10^{-26} \text{ kg}$	$\propto (N/N_0)^0$
Quantum of vibrational energy	ΔE_v	0.29 eV	$\propto (N/N_0)^0$
Applied electric field	E	14–24 kV/cm	$\propto (N/N_0)^1$
Initial gas density	N	$2.5 \times 10^{19} \text{ cm}^{-3}$	$\propto (N/N_0)^1$
Initial pressure	p	10^5 Pa	$\propto (N/N_0)^1$
Initial O_2^+ density	$n_{O_2^+}$	$2 \times 10^{14} \text{ cm}^{-3}$	$\propto (N/N_0)^2$
Initial electron density	n_e	$2 \times 10^{14} \text{ cm}^{-3}$	$\propto (N/N_0)^2$

^aThe electron mobility depends on the reduced electric field E/N [e.g., *Morrow and Lowke, 1997*].

the system already enters the phase of exponential increases of the gas temperature and is close to the spark stage (see discussion in Section 8.1 and Figures 8.3a and 8.5a). Thus, the change of the specific heat ratio has a small influence on our results. The quantities η_T and η_V are the fractions of the Joule energy transferred directly to gas heating (“fast heating”) and to the vibrational energy levels of the nitrogen molecules, respectively. In our calculations of η_T and η_V , we assume an air mixture consisting of 78.11% of nitrogen, 20.91% oxygen, and 0.98% argon. The rates of energy losses by electrons per unit volume (in $\text{eV m}^{-3} \text{s}^{-1}$) in the various collisional processes (see below) are obtained from the BOLSIG+ software [Hagelaar and Pitchford, 2005]. They include the energy losses in: elastic collisions, excitation of rotational, vibrational and electronic levels, and ionization of N_2 molecules, denoted $q_{\text{ela}}^{\text{N}_2}$, $q_{\text{rot}}^{\text{N}_2}$, $q_{\text{vib}}^{\text{N}_2}$, $q_{\text{elec}}^{\text{N}_2}$, and $q_{\text{ion}}^{\text{N}_2}$, respectively; elastic collisions, excitation of rotational, vibrational and electronic levels, and ionization of O_2 molecules, denoted $q_{\text{ela}}^{\text{O}_2}$, $q_{\text{rot}}^{\text{O}_2}$, $q_{\text{vib}}^{\text{O}_2}$, $q_{\text{elec}}^{\text{O}_2}$, and $q_{\text{ion}}^{\text{O}_2}$, respectively; and, elastic collisions, excitation of electronic levels, and ionization of Ar atoms, denoted $q_{\text{ela}}^{\text{Ar}}$, $q_{\text{elec}}^{\text{Ar}}$, and $q_{\text{ion}}^{\text{Ar}}$, respectively. After introducing the fractions η_β^α for energy losses for a given species α in the process β as $\eta_\beta^\alpha = q_\beta^\alpha / \sum_{\alpha,\beta} q_\beta^\alpha$, the quantities η_T and η_V are given by the following equations :

$$\eta_T = (\eta_{\text{ela}}^{\text{N}_2} + \eta_{\text{ela}}^{\text{O}_2} + \eta_{\text{ela}}^{\text{Ar}}) + (\eta_{\text{rot}}^{\text{N}_2} + \eta_{\text{rot}}^{\text{O}_2}) + \eta_{\text{vib}}^{\text{O}_2} + 0.3 \times (\eta_{\text{elec}}^{\text{N}_2} + \eta_{\text{elec}}^{\text{O}_2} + \eta_{\text{elec}}^{\text{Ar}}) \quad (7.7)$$

$$\eta_V = \eta_{\text{vib}}^{\text{N}_2} \quad (7.8)$$

In our calculations of η_T represented by (7.7), we assumed that 30% of the energy expended on the excitation of the electronic degrees of freedom of the molecules is directly transferred to gas heating [Aleksandrov *et al.*, 1998; Naidis, 1999; Popov, 2001]. Figure 7.2 shows the values of η_T and η_V for the range of reduced electric field E/N from 3.72×10^{-2} Td (1 Td = 10^{-17} V·cm²) to 3.72×10^2 Td calculated from (7.7) and (7.8). We note that in our model E is assumed to be uniform and constant and N varies with r and t . These variations are reflected in the changes in η_T and η_V entering in equations (7.5) and (7.6).

The electronic conductivity at $r=0$ is defined as: $\sigma_e^0 = q_e \mu_e n_e$, where q_e , μ_e , and n_e are the electronic charge, mobility, and number density of electrons obtained using the kinetics scheme. Similarly, the ionic conductivity at $r=0$ is defined as:

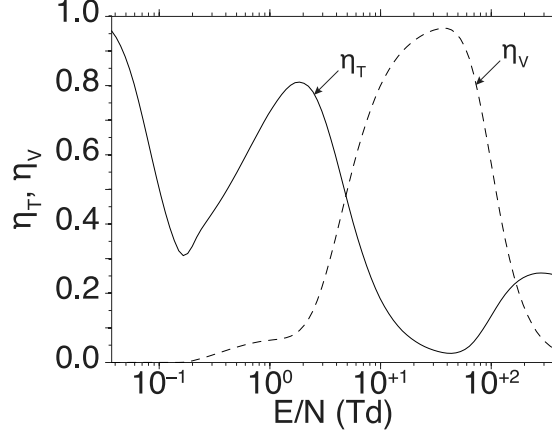


Figure 7.2. Fractions of Joule energy spent in fast heating η_T (solid line), and vibrational excitation of N_2 molecules η_v (dashed line) as a function of the applied reduced field E/N in Td. The results are based on BOLSIG+ software calculations [Hagelaar and Pitchford, 2005].

$\sigma_i^0 = \sum_{\alpha} q_{\alpha} \mu_{\alpha} n_{\alpha}$, where α represents the following ions: O_2^+ , O_4^+ , $O_2^+N_2$, O^- , O_2^- , and O_3^- , and where q_{α} , μ_{α} and n_{α} are the charge, mobility, and number density of the species α also obtained using the kinetics scheme (see discussion below in this section). The positive and negative ions mobilities are given by $\mu_+ = 2.5 \times 10^{-4} \text{ V} \cdot \text{m}^2 \text{s}^{-1}$ and $\mu_- = 2.2 \times 10^{-4} \text{ V} \cdot \text{m}^2 \text{s}^{-1}$ at ground pressure and scale inversely proportionally with the gas density ($\propto N_0/N$) [Zhao *et al.*, 1995]. The electronic mobility μ_e is calculated as a function of the reduced electric field E/N using the approach specified in [Morrow and Lowke, 1997]. Similarly to the approach used in [Naidis, 2005] the radial dependence of the electronic and ionic Joule energy deposition rates (Q_e and Q_i , respectively) is assumed to be Gaussian along the r -axis, and the related terms are expressed as $Q_e = \sigma_e^0 E^2 e^{-r^2/r_s^2}$ and $Q_i = \sigma_i^0 E^2 e^{-r^2/r_s^2}$, respectively.

The transfer of energy from the vibrational energy levels of molecular nitrogen to translational energy Q_{VT} is expressed as $Q_{VT} = [\varepsilon_v - \varepsilon_{v,eq}(T_g)] / \tau_{VT}$, where $1/\tau_{VT} = 1/\tau_{VT_{N_2, O_2}} + 1/\tau_{VT_O}$. The quantities T_g , T_v , ε_v , and $\varepsilon_{v,eq}(T_g)$ are the gas temperature, the vibrational temperature of N_2 molecules, vibrational energy per unit volume of nitrogen molecules at T_v , and the equilibrium value of ε_v at the temperature $T_v = T_g$, respectively [e.g., Naidis, 1999; Popov, 2003]. The timescales $\tau_{VT_{N_2, O_2}}$ and τ_{VT_O} are the timescales describing the relaxation of the vibrational energy of the vibrationally excited N_2 molecules into the translational energy of air molecules. We note that our model formulation explicitly includes a term con-

taining τ_{VT_O} , which describes the efficient quenching of vibrational excitation of N_2 by atomic oxygen [Aleksandrov *et al.*, 1997, and references therein]. From [e.g., Naidis, 2007], we have: $\varepsilon_v = n_{N_2} \Delta E_v / (e^{\Delta E_v / k_B T_v} - 1)$, where ΔE_v is the quantum of vibrational energy of N_2 molecules ($\Delta E_v = 0.29$ eV), and k_B is the Boltzmann constant. The timescale $\tau_{VT_{N_2, O_2}}$ is related to the gas temperature and pressure as $\tau_{VT_{N_2, O_2}} = 6.5 \times 10^{-4} e^{137/T_g [K]} / p [Pa]$ s [e.g., Mnatsakanyan and Naidis, 1985], and τ_{VT_O} depends on both the gas temperature T_g and the number density of atomic oxygen n_O as: $\tau_{VT_O} = 1 / (n_O [cm^{-3}] 1.07 \times 10^{-10} e^{-69.9/T_g [K]^{1/3}})$ s [e.g., Taylor, 1974]. We note that T_v , T_g , and $\tau_{VT_{N_2, O_2}}$ radial dependencies can be calculated from ρ , \vec{v} , ε , and ε_v . We use the on-axis value of n_O provided by the 0-D kinetics scheme (see below) to estimate the value of τ_{VT_O} . The results of the present work are not sensitive to this approximation.

The system of equations (7.3)–(7.6) is discretized using a finite-difference method [e.g., Potter, 1973, pp. 15–17] and solved using a second-order Lax-Wendroff scheme [e.g., Press *et al.*, 1992, p. 844]. The time step δt is related to the space step δr and to the timescales of the vibrational–translational relaxation through the relationship: $\delta t < \min(\delta r / c_s, \tau_{VT_{N_2, O_2}}, \tau_{VT_O})$, where c_s is the sound velocity in the gas: $c_s = \sqrt{\gamma p / \rho}$. This condition satisfies the Courant-Friedrichs-Lewy stability criterion [e.g., Courant *et al.*, 1928; Potter, 1973, p. 63]. At the beginning of each time step, the gas dynamics model takes for input the values of ρ , \vec{v} , ε , and ε_v at the end of the previous step to calculate the quantities η_T , η_V , Q_{VT} , and p . The terms Q_e , Q_i , and Q_{VT} are obtained from the electron, ion, and atomic oxygen densities calculated by the 0-D kinetics scheme described hereafter.

The kinetics scheme developed for the studies presented in this work involves 17 species (electrons e; neutral particles N_2 , O_2 , O, N, NO, $O_2(a^1\Delta_g)$, $N_2(A^3\Sigma_u^+)$, $N_2(B^3\Pi_g)$, $N_2(C^3\Pi_u)$, $N_2(a^1\Sigma_u^-)$; negative ions O^- , O_2^- , O_3^- ; and positive ions O_2^+ , O_4^+ , $O_2^+N_2$) with 67 reactions summarized in Table 7.2. The model rates are taken from [Vallance-Jones, 1974; Kossyi *et al.*, 1992; Lowke, 1992; Walter *et al.*, 1994; Aleksandrov *et al.*, 1995; Morrow and Lowke, 1997; Popov, 2001; Benilov and Naidis, 2003; Liu and Pasko, 2004]. The model accounts for the effects of gains in electron energy in collisions with vibrationally excited N_2 on the rate constants of processes involving electron impact collisions (reactions R2–R3 and R28–R30 in

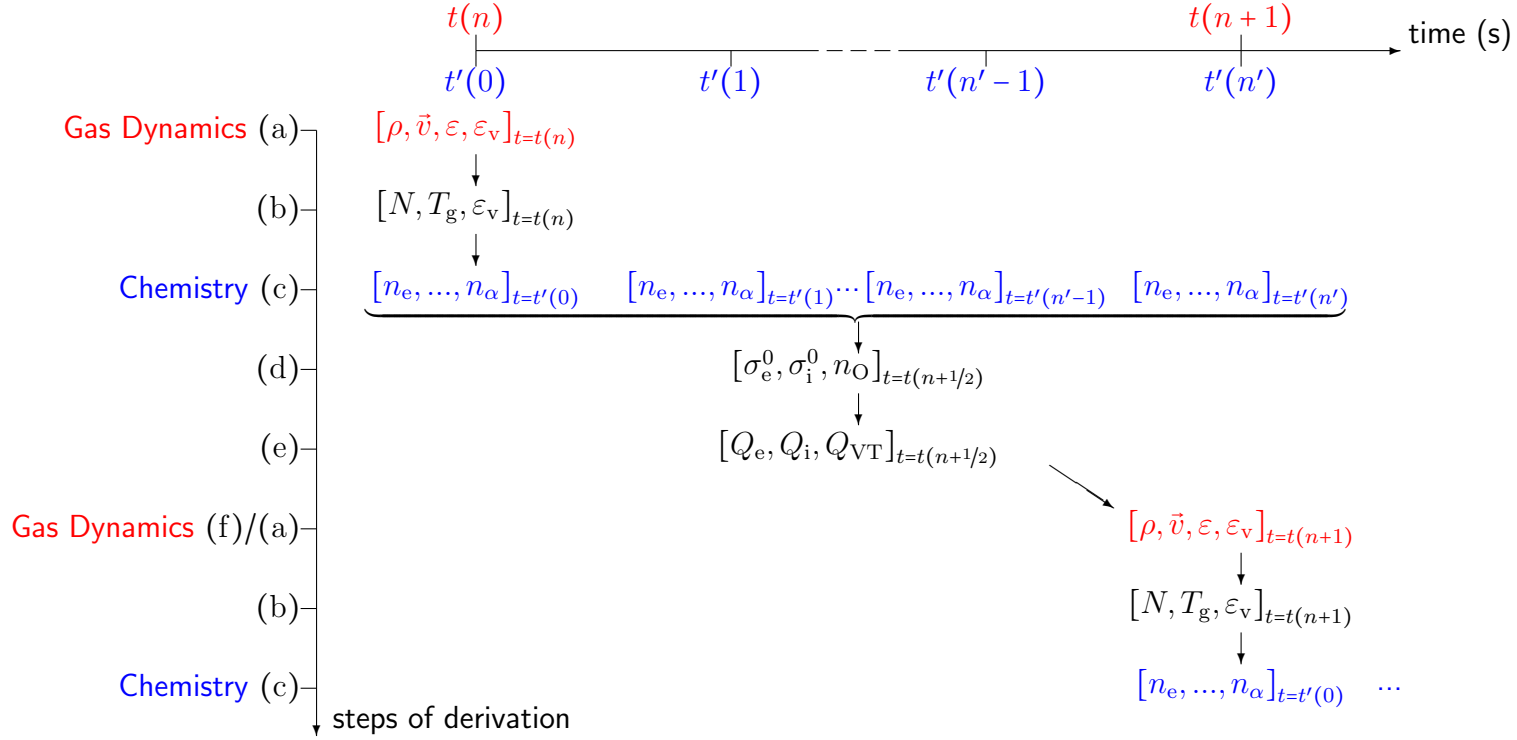


Figure 7.3. Algorithm for the 1-D axisymmetric, axially invariant model of streamer-to-spark transition. The time notation t represents the timeline for the gas dynamics model, and t' denotes that of the kinetics scheme. If ρ , \vec{v} , ε , ε_v are known at $t(n)$ (step (a)), then the model calculates the values of N , T_g , and ε_v at step (b) and uses them as input values for the kinetics scheme to derive the densities of each species α in the interval $[t'(0), t'(n')]$ (step (c)). Then the model calculates the electronic and ionic conductivities of the plasma σ_e^0 and σ_i^0 and density of atomic oxygen on the axis ($r=0$) at $t(n+1/2)$ by averaging the values of σ_e^0 , σ_i^0 and n_O calculated at $t=t'(0)$ and $t=t'(n')$ (step (d)). Afterward, the terms corresponding to the electronic and ionic Joule energy deposition per unit volume Q_e and Q_i and energy transfer from the vibrational energy levels of nitrogen to translational energy Q_{VT} per unit volume are calculated at every point r of the simulation domain at $t=t(n+1/2)$ (step (e)). Finally the values of ρ , \vec{v} , ε , ε_v are calculated at $t(n+1)$ using the quantities obtained from steps (a) and (e) (step (f)/(a)). The process is repeated until T_g reaches a breakdown value $T_{br}=5000$ K.

Table 7.2: List of reactions

Reactants			→	Products		Rate constant		Units	References	#	Comments
Generation of electrons by direct ionization: F_{ion}											
R1	M	+e	→O ₂ ⁺	+e	+e	ν_1	(1/s)	[Morrow and Lowke, 1997]	(A1/A2)	$\nu_1=k_{\text{iz},\text{O}_2}[\text{O}_2]+k_{\text{iz},\text{N}_2}[\text{N}_2]$; M=N ₂ , O ₂	
Generation of electrons by stepwise and associative ionizations: F_{step}											
R2 ^a	NO	+e	→NO ⁺	+e	+e	$5.0\times10^{-9}\exp(-460/(E/N))F$	(cm ³ /s)	[Benilov and Naidis, 2003]	(3)		
R3 ^a	O	+e	→O ⁺	+e	+e	$4.0\times10^{-9}\exp(-713/(E/N))F$	(cm ³ /s)	[Benilov and Naidis, 2003]	(4)	O ⁺ +O ₂ →O ₂ ⁺ +O	
R4	N ₂ (A)+N ₂ (a')		→N ₄ ⁺	+e		5×10^{-11}	(cm ³ /s)	[Kossyi et al., 1992]	(25)	N ₄ ⁺ +O ₂ →O ₂ ⁺ +N ₂ +N ₂	
R5	N ₂ (a')+N ₂ (a')		→N ₄ ⁺	+e		2×10^{-10}	(cm ³ /s)	[Kossyi et al., 1992]	(26)	N ₄ ⁺ +O ₂ →O ₂ ⁺ +N ₂ +N ₂	
Loss of electrons by two and three-body attachment processes: $F_{\text{a}_2}+F_{\text{a}_3}$											
R6	O ₂	+e	→O ⁻	+O		ν_{a_2}	(1/s)	[Morrow and Lowke, 1997]	(A3/A4)	$\nu_{\text{a}_2}=k_{\text{a}_2}[\text{O}_2]$	
R7	O ₂	+e	+M→O ₂ ⁻	+M		ν_{a_3}	(1/s)	[Morrow and Lowke, 1997]	(A5)	$\nu_{\text{a}_3}=k_{\text{a}_3}[\text{O}_2][\text{M}]$; M=N ₂ , O ₂	
R8	O ₂	+O	+e→O	+O ₂ ⁻		10^{-31}	(cm ⁶ /s)	[Kossyi et al., 1992]	(48)		
Loss of electrons by electron-ion recombination: F_{rec}											
R9	O ₂ ⁺	+e	→O	+O		$2\times10^{-7}(300/T_{\text{e}})$	(cm ³ /s)	[Kossyi et al., 1992]	(40)		
R10	O ₂ ⁺	+e	+M→O ₂	+M		$6\times10^{-27}(300/T_{\text{e}})^{1.5}$	(cm ⁶ /s)	[Kossyi et al., 1992]	(44)	A=O ₂ ⁺ ; M=O ₂ , N ₂	
R11	O ₄ ⁺	+e	→O ₂	+O ₂		$1.4\times10^{-6}(300/T_{\text{e}})^{1/2}$	(cm ³ /s)	[Kossyi et al., 1992]	(30)		
R12	O ₂ ⁺ N ₂	+e	→O ₂	+N ₂		$1.3\times10^{-6}(300/T_{\text{e}})^{1/2}$	(cm ³ /s)	[Kossyi et al., 1992]	(34)		
Generation of electrons by detachment: F_{d}											
R13	O ₂ ⁻	+O ₂ (a)	→O ₂	+O ₂	+e	2×10^{-10}	(cm ³ /s)	[Kossyi et al., 1992]	(58)		
R14	O ₂ ⁻	+N ₂ (A)	→O ₂	+N ₂	+e	2.1×10^{-9}	(cm ³ /s)	[Kossyi et al., 1992]	(60)		
R15	O ⁻	+N ₂	→N ₂ O	+e		9×10^{-13}	(cm ³ /s)	[Benilov and Naidis, 2003]	(22)		
R16	O ⁻	+O	→O ₂	+e		5×10^{-10}	(cm ³ /s)	[Benilov and Naidis, 2003]	(23)		
R17	O ₂ ⁻	+O	→O ₃	+e		1.5×10^{-10}	(cm ³ /s)	[Benilov and Naidis, 2003]	(25)		
R18	O ₃ ⁻	+O	→O ₂	+O ₂	+e	3×10^{-10}	(cm ³ /s)	[Benilov and Naidis, 2003]	(26)		
R19	O ⁻	+O ₂ (a)	→O ₃	+e		3×10^{-10}	(cm ³ /s)	[Kossyi et al., 1992]	(62)		
R20	O ⁻	+N ₂ (A)	→O	+N ₂	+e	2.2×10^{-9}	(cm ³ /s)	[Kossyi et al., 1992]	(64)		
R21	O ⁻	+NO	→NO ₂	+e		2.6×10^{-10}	(cm ³ /s)	[Benilov and Naidis, 2003]	(24)		
R22	O ₂ ⁻	+O ₂	→O ₂	+O ₂	+e	$2\times10^{-10}e^{-0.52/T_{\text{ef}2}}\frac{1-e^{-4\theta}}{1-e^{-\theta}}$ $\theta=0.13(1/T_{\text{g}}[\text{eV}]-1/T_{\text{ef}2})$ $T_{\text{ef}2}=T_{\text{g}}[\text{eV}]+5.2\times10^{-6}(E/N)^2[\text{eV}]$	(cm ³ /s)	[Benilov and Naidis, 2003]	(21)		

Continued on Next Page...

Table 7.2 – Continued

Reactants			→	Products		Rate constant		Units	References	#	Comments
Electron impact excitation of metastable state: F_{ex}											
R23	O ₂	+e	→O ₂ (a)	+e		$\nu_{\text{O}_2(\text{a})}$		(1/s)	[Aleksandrov et al., 1995]	(8)	$\nu_{\text{O}_2(\text{a})}=k_{\text{O}_2(\text{a})}[\text{O}_2]$
R24	N ₂	+e	→N ₂ (A)	+e		$\nu_{\text{N}_2(\text{A})}$		(1/s)	[Aleksandrov et al., 1995]	(4)	$\nu_{\text{m},\text{N}_2}=k_{\text{N}_2(\text{A})}[\text{N}_2]$
R25	N ₂	+e	→N ₂ (a')	+e		$\nu_{\text{N}_2(\text{a}')}$		(1/s)	[Aleksandrov et al., 1995]	(6)	$\nu_{\text{N}_2,\text{a}}=k_{\text{N}_2(\text{a}')}[\text{N}_2]$
R26	N ₂	+e	→N ₂ (B)	+e		$\nu_{1\text{P}}$		(1/s)	[Aleksandrov et al., 1995]	(5)	$\nu_{1\text{P}}=k_{1\text{P}}[\text{N}_2]$
R27	N ₂	+e	→N ₂ (C)	+e		$\nu_{2\text{P}}$		(1/s)	[Aleksandrov et al., 1995]	(7)	$\nu_{2\text{P}}=k_{2\text{P}}[\text{N}_2]$
Electron impact dissociation: F_{di}											
R28 ^a	N ₂	+e	→N	+N	+e	$5.0\times10^{-9}\exp(-646/(E/N))F$		(cm ³ /s)	[Benilov and Naidis, 2003]	(5)	
R29 ^a	O ₂	+e	→O(³ P)	+O(³ P)	+e	$F\nu_{\text{O}(\text{3P})}$		(1/s)	[Aleksandrov et al., 1995]	(10)	[Benilov and Naidis, 2003, (6)]
R30 ^a	O ₂	+e	→O(³ P)	+O(¹ D)	+e	$F\nu_{\text{O}(\text{1D})}$		(1/s)	[Aleksandrov et al., 1995]	(11)	
Ground states chemistry: F_{gd}											
R31	N	+NO	→O	+N ₂		$1.1\times10^{-10}T_{\text{g}}[\text{eV}]^{1/2}$		(cm ³ /s)	[Benilov and Naidis, 2003]	(15)	
R32	N	+O ₂	→O	+NO		$1.2\times10^{-10}T_{\text{g}}[\text{eV}]\exp(-0.27/T_{\text{g}}[\text{eV}])$		(cm ³ /s)	[Benilov and Naidis, 2003]	(17)	
Active states chemistry and collisional and radiative deactivation: F^*											
R33 ^b	N ₂ (B)		→N ₂ (A)	+ $h\nu(1\text{PN}_2)$		1.7×10^5		(1/s)	[Liu and Pasko, 2004]		[Walter et al., 1994]
R34 ^b	N ₂ (C)		→N ₂ (B)	+ $h\nu(2\text{PN}_2)$		2.0×10^7		(1/s)	[Liu and Pasko, 2004]		[Walter et al., 1994]
R35 ^b	N ₂ (B)+N ₂		→N ₂	+N ₂		1.0×10^{-11}		(cm ³ /s)	[Vallance-Jones, 1974]		Table 4.7
R36 ^b	N ₂ (C)+O ₂		→N ₂	+O ₂		3.0×10^{-10}		(cm ³ /s)	[Vallance-Jones, 1974]		Table 4.7
R37	O ₂ (a)+O ₂		→O ₂	+O ₂		$2.2\times10^{-18}(T_{\text{g}}/300)^{0.8}$		(cm ³ /s)	[Kossyi et al., 1992]	(123)	[Lowke, 1992, (6)]
R38	N ₂ (A)+O		→NO	+N(¹ D)		7×10^{-12}		(cm ³ /s)	[Kossyi et al., 1992]	(102)	
R39 ^b	N ₂ (A)+N ₂ (A)		→N ₂ (B)	+N ₂		7.7×10^{-11}		(cm ³ /s)	[Popov, 2001]	(4)	[Kossyi et al., 1992, (104)]
R40 ^b	N ₂ (A)+N ₂ (A)		→N ₂ (C)	+N ₂		1.6×10^{-10}		(cm ³ /s)	[Popov, 2001]	(3)	[Kossyi et al., 1992, (104)]
R41	N ₂ (A)+O		→N ₂	+O(¹ S)		2.1×10^{-11}		(cm ³ /s)	[Kossyi et al., 1992]	(108)	
R42	N ₂ (A)+O ₂		→N ₂	+O	+O	2.54×10^{-12}		(cm ³ /s)	[Kossyi et al., 1992]	(100)	
R43	N ₂ (a')+O ₂		→N ₂	+O	+O	2.8×10^{-11}		(cm ³ /s)	[Kossyi et al., 1992]	(115)	
Ion-ion recombination: F_{ii}											
	A ⁻	+B ⁺	→A	+B		$2\times10^{-7}(300/T_{\text{g}})^{0.5}$		(cm ³ /s)	[Kossyi et al., 1992]	(I)	
R44	O ⁻	+O ₂ ⁺	→O	+O ₂							A ⁻ =O ⁻ ; B ⁺ =O ₂ ⁺
R45	O ₂ ⁻	+O ₂ ⁺	→O ₂	+O ₂							A ⁻ =O ₂ ⁻ ; B ⁺ =O ₂ ⁺
R46	O ₃ ⁻	+O ₂ ⁺	→O ₃	+O ₂							A ⁻ =O ₃ ⁻ ; B ⁺ =O ₂ ⁺

Continued on Next Page...

Table 7.2 – Continued

	Reactants		→	Products		Rate constant	Units	References	#	Comments
	A^-	$+BC^+$	$\rightarrow A$	$+B$	$+C$	10^{-7}	(cm^3/s)	[Kossyi et al., 1992]	(II)	
R47	O^-	$+O_2^+$	$\rightarrow O$	$+O$	$+O$					$A^-=O^-$; $BC^+=O_2^+$
R48	O^-	$+O_4^+$	$\rightarrow O$	$+O_2$	$+O_2$					$A^-=O^-$; $BC^+=O_4^+$
R49	O^-	$+O_2^+N_2$	$\rightarrow O$	$+O_2$	$+N_2$					$A^-=O^-$; $BC^+=O_2^+N_2$
R50	O_2^-	$+O_2^+$	$\rightarrow O_2$	$+O$	$+O$					$A^-=O_2^-$; $BC^+=O_2^+$
R51	O_2^-	$+O_4^+$	$\rightarrow O_2$	$+O_2$	$+O_2$					$A^-=O_2^-$; $BC^+=O_4^+$
R52	O_2^-	$+O_2^+N_2$	$\rightarrow O_2$	$+O_2$	$+N_2$					$A^-=O_2^-$; $BC^+=O_2^+N_2$
R53	O_3^-	$+O_2^+$	$\rightarrow O_3$	$+O$	$+O$					$A^-=O_3^-$; $BC^+=O_2^+$
R54	O_3^-	$+O_4^+$	$\rightarrow O_3$	$+O_2$	$+O_2$					$A^-=O_3^-$; $BC^+=O_4^+$
R55	O_3^-	$+O_2^+N_2$	$\rightarrow O_3$	$+O_2$	$+N_2$					$A^-=O_3^-$; $BC^+=O_2^+N_2$
<i>Positive ions chemistry: F_i^+</i>										
R56	O_4^+	$+O_2(a)$	$\rightarrow O_2^+$	$+O_2$	$+O_2$	10^{-10}	(cm^3/s)	[Kossyi et al., 1992]	(228)	
R57	O_4^+	$+O$	$\rightarrow O_2^+$	$+O_3$		3×10^{-10}	(cm^3/s)	[Kossyi et al., 1992]	(229)	
R58	O_2^+	$+O_2$	$+O_2 \rightarrow O_4^+$	$+O_2$		$2.4 \times 10^{-30} (300/T_g)^{3.2}$	(cm^6/s)	[Kossyi et al., 1992]	(167)	
R59	$O_2^+N_2$	$+O_2$	$\rightarrow O_4^+$	$+N_2$		10^{-9}	(cm^3/s)	[Kossyi et al., 1992]	(232)	
R60	O_2^+	$+N_2$	$+N_2 \rightarrow O_2^+N_2$	$+N_2$		$0.9 \times 10^{-30} (300/T_g)^2$	(cm^6/s)	[Kossyi et al., 1992]	(168)	
R61	O_4^+	$+N_2$	$\rightarrow O_2^+N_2$	$+O_2$		$4.61 \times 10^{-12} (300/T_g)^{2.5} \exp(-2650/T_g)$	(cm^6/s)	[Kossyi et al., 1992]	(226)	
R62	$O_2^+N_2$	$+N_2$	$\rightarrow O_2^+$	$+N_2$	$+N_2$	$1.1 \times 10^{-6} (300/T_g)^{5.3} \exp(-2357/T_g)$	(cm^6/s)	[Kossyi et al., 1992]	(231)	
R63	O_4^+	$+O_2$	$\rightarrow O_2^+$	$+O_2$	$+O_2$	$3.3 \times 10^{-6} (300/T_g)^4 \exp(-5030/T_g)$	(cm^6/s)	[Kossyi et al., 1992]	(227)	
<i>Negative ions chemistry: F_i^-</i>										
R64	O^-	$+O_2(a)$	$\rightarrow O_2^-$	$+O$		10^{-10}	(cm^3/s)	[Kossyi et al., 1992]	(242)	
R65	O_2^-	$+O$	$\rightarrow O_2$	$+O^-$		3.3×10^{-10}	(cm^3/s)	[Kossyi et al., 1992]	(237)	
R66	O_3^-	$+O$	$\rightarrow O_2^-$	$+O_2$		3.2×10^{-10}	(cm^3/s)	[Kossyi et al., 1992]	(247)	
R67	O^-	$+O_2$	$+M \rightarrow O_3^-$	$+M$		$2.8 \times 10^{-32} T_{\text{efl}}^{-1}$	(cm^6/s)	[Benilov and Naidis, 2003]	(27)	$M=N_2, O_2$
						$T_{\text{efl}}=T_g[\text{eV}] + 6.9 \times 10^{-6} (E/N)^2 [\text{eV}]$				

^aA correction to account for gains in electron energy in collisions with vibrationally excited nitrogen molecules is introduced by means of the factor: $F=e^{Cz/(E/N)^2}$ where $C=6.5 \times 10^3 \text{ Td}^2$ and $z=e^{-\Delta E_v/k_B T_v}$ [Benilov and Naidis, 2003].

^bReactions R32, R33, R34, R35, R38 are used to derive the densities of $N_2(B)$ and $N_2(C)$ in a steady state approximation.

Table 7.2) [Benilov and Naidis, 2003]. The system of kinetic equations is solved to describe the time dynamics of the density of each species α on the axis of the discharge, i.e., using a 0-D approximation [Naidis, 1999, 2005]. In particular, the general balance equation for the electron number density ($\alpha=e$) can be written in the form [Naidis, 1999]:

$$\frac{dn_e}{dt} = (F_{\text{ion}} + F_{\text{step}} + F_d - F_{a_2} - F_{a_3} - F_{\text{rec}}) n_e \quad (7.9)$$

where F_{ion} is the rate of direct ionization of N_2 and O_2 ; F_{step} is the sum of the rates of ionization of radicals by the electron impact and associative ionization in collisions of excited N_2 ; F_d , F_{a_2} , F_{a_3} , and F_{rec} are the rates of detachment, two- and three-body attachment, and electron-ion recombination, respectively. The source terms corresponding to associative ionization and detachment are not proportional to the electron number density n_e , but the representation of the corresponding terms in the form of (7.9) is very convenient for purposes of comparison of different processes [Naidis, 1999].

In summary, the model employs a fully 1-D axisymmetric, axially invariant gas dynamics model coupled to a 0-D kinetics scheme according to the algorithm schematically represented in Figure 7.3. The time integration is ended when the gas temperature T_g reaches the predefined breakdown temperature $T_{\text{br}}=5000$ K. The laboratory data on timescales of air heating in streamer channels at ground and near-ground pressures [Larsson, 1998], and related modeling studies [Naidis, 1999, 2005] indicate that the experimentally measured and previously calculated τ_{br} values are in good agreement with our model results for the range $18 < EN_0/N < 24$ kV/cm (see the results presented in Section 8.1). We emphasize that the combined action of uncertainties in the initial streamer electron density ($n_e|_{t=0}=1-3 \times 10^{14} \text{ cm}^{-3}$), the initial densities of active species in the streamer after the passage of the high electric field pulse associated with the streamer head, and the cathode voltage drop (U_c) lead to an estimated combined uncertainty of a factor of two for the model breakdown times τ_{br} reported in the next section. In this work, we choose the same initial conditions as in [Naidis, 2005] ($n_e|_{t=0}=2 \times 10^{14} \text{ cm}^{-3}$, $U_c=0.2$ kV, and zero initial densities of active species) to demonstrate performance of our model in comparison with results given in [Naidis,

1999, 2005]. The conclusions derived in the present work on air-density-dependent scaling of the discharge properties are not sensitive to these assumptions.

7.3 Summary of Results

In this chapter, we develop an air-density-dependent model of streamer-to-spark transition. The model accounts for the effects of the dynamic expansion of the heated air on the reduced electric field E/N and of the resultant plasma kinetics in the streamer channel. It also includes the transfer of energy through vibrational-translational relaxation of N_2 molecules, and a realistic partition of input energy into gas heating and vibrational excitation of N_2 molecules during the streamer-to-spark transition dynamics. In addition to ionization kinetics, involving the production and interaction of electrons and different types of positive and negative ions, the model accounts for self-quenching of $N_2(A^3\Sigma_u^+)$ excited molecules, and associative ionization processes involving $N_2(A^3\Sigma_u^+)$ and $N_2(a'^1\Sigma_u^-)$ species. The model also accounts for the effects of gains in electron energy in collisions with vibrationally excited $N_2(v)$ on the rate constants of processes involving electron impact collisions. The model self-consistently couples a fully 1-D axisymmetric, axially invariant gas dynamics model to a 0-D kinetics scheme involving 17 species in more than 60 reactions through the derivation of the Joule heating and of the related energy participating in the channel. In Chapter 8, we investigate the mechanisms of air heating in the streamer channel and compare our results with previously published experimental and modeling results.

Investigation of Timescales of Air Heating in Streamer Discharges at Different Altitudes in the Earth Atmosphere

In this chapter, we apply the model developed in Chapter 7 to investigate the streamer-to-spark transition as a function of the air density. The model allows investigation of effective timescales τ_{br} of the initial stage of air heating in streamer channels up to 5000 K at which the thermal ionization becomes important. This work constitutes a first step toward the understanding of the conversion of hot leader channels driven by thermal ionization near cloud tops to non-thermal streamer forms observed at higher altitudes in blue and gigantic jets (see discussion in Chapters 4 and 6). For the present study, the model conditions are set up to closely resemble those realized in laboratory experiments in order to carefully test the model-calculated streamer-to-spark transition times in comparison with the available experimental data at ground and near-ground pressures. We also investigate the scaling of effective heating times with the air density N .

8.1 Results of Modeling of the Streamer-to-Spark Transition

In this section, we present results of simulations of the streamer-to-spark transition at various altitudes, or equivalently air densities. The results are obtained assuming that the discharge occurs in a domain with radius $L_r=2$ mm at ground pressure. Based on their experimental results, *Tardiveau et al.* [2001] suggested that in studies of similarity laws, the entire system should be scaled, and consequently L_r is scaled with neutral density ($L_r \propto 1/N$, see Table 7.1). The breakdown time τ_{br} is always much less than the ratio $L_r/c_s \simeq 10 \mu s$ at ground pressure, so that the boundary effects are negligible in the results presented in this work. The scaling of L_r with altitude ensures that this result holds at any altitude.

The 1-D axisymmetric, axially invariant simulation domain of radius L_r is then discretized using 500 space steps of length δr , and consequently δr scales inversely with the neutral density, too ($\delta r \propto 1/N$). The time step δt used in the Lax-Wendroff algorithm in the gas dynamics model (see Figure 7.3) is chosen as: $\delta t = 0.1 \times \min(\delta r/c_s, \tau_{VT_{N_2, O_2}}, \tau_{VT_O})$ and therefore satisfies the Courant-Friedrichs-Lewy condition for stability of the finite-difference numerical scheme as already discussed in Chapter 7. The initial conditions and the other parameters of the model are summarized in Table 7.1 with their respective scaling properties.

Figure 8.1a displays the breakdown times τ_{br} at normal and reduced pressure as a function of the applied voltage U . Results are compared with experimental data obtained by *Černák et al.* [1995] and *Larsson* [1998]. The solid lines represent the model breakdown times under normal pressure ($p=10^5$ Pa) and reduced pressure ($p=0.75 \times 10^5$ Pa). The dashed line shows the breakdown time in a constant neutral gas density channel assuming a constant conductivity of the channel and that all the power from the system Q is directly used for heating of the plasma. The symbols ‘◻’ show experimental results reported by *Černák et al.* [1995], and ‘◊’ and ‘●’ show the results obtained by *Larsson* [1998]. The data obtained by *Larsson* [1998] are obtained for a 1-cm-long air gap under a constant voltage and are particularly interesting because they represent the experimental setup closest to the model formulated in Chapter 7. Figure 8.1 shows very good agreement between the model results and the experimental data. In comparison, the estimates based on pure

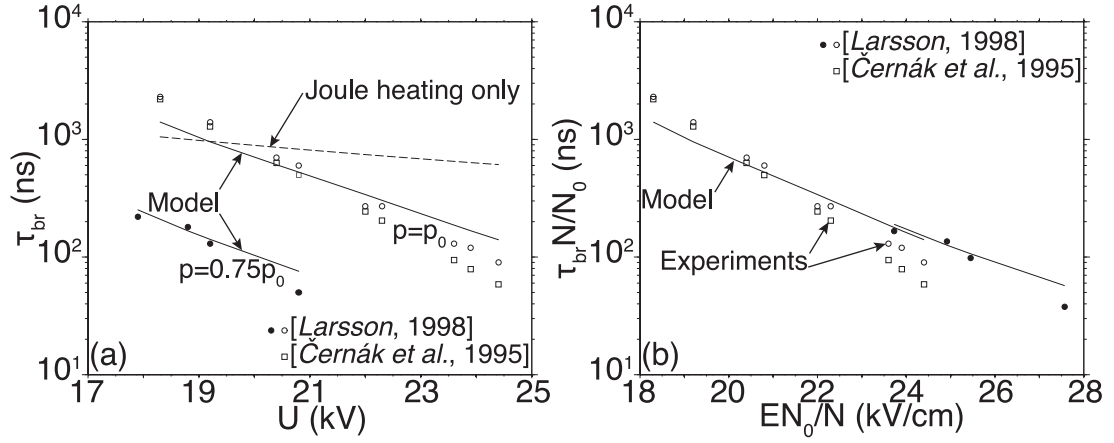


Figure 8.1. (a) Experimental and model streamer-to-spark transition times for various applied voltages. The solid lines represent the transition times under normal pressure ($p=10^5$ Pa) and reduced pressure ($p=0.75 \times 10^5$ Pa). The broken line shows the breakdown time of a Joule heated channel with constant neutral gas density corresponding to $p=10^5$ Pa and assuming a constant plasma conductivity in the channel. The symbols ‘ \square ’ show the experimental results obtained by Černák *et al.* [1995], and ‘ \circ ’ and ‘ \bullet ’ show the results obtained by Larsson [1998]. The data obtained reduced density are shown with full circle ‘ \bullet ’, while data taken at atmospheric pressure are shown with open circles ‘ \circ ’. (b) Same model and experimental data as in panel (a) but using reduced values of the applied field (EN_0/N) and of the transition times ($\tau_{br}N/N_0$).

Joule heating (dashed line) demonstrate a completely different slope of variation of τ_{br} as a function of the applied voltage and no good quantitative agreement with the observations. Figure 8.1b presents the same results but scaled with the neutral density. Both experimental and model transitions times are scaled with N as $\tau_{br}N/N_0$ (which is a good estimate of the scaling factor as is shown below in Figure 8.9), and the applied electric field is represented in its usual reduced form as EN_0/N . We note that the model curves and the data points obtained at two different pressures both form a monotonic continuous set when represented in the $\tau_{br}N/N_0$ versus EN_0/N format. These results indicate that experimentally measured and modeled transition times agree, and both scale approximately as $1/N$.

Figure 8.2 compares the streamer-to-spark transition times obtained using a 0-D model under the assumption of constant density N (dashed lines), a 0-D model under the assumption of a constant pressure p (dot-dashed lines), and the 1-D

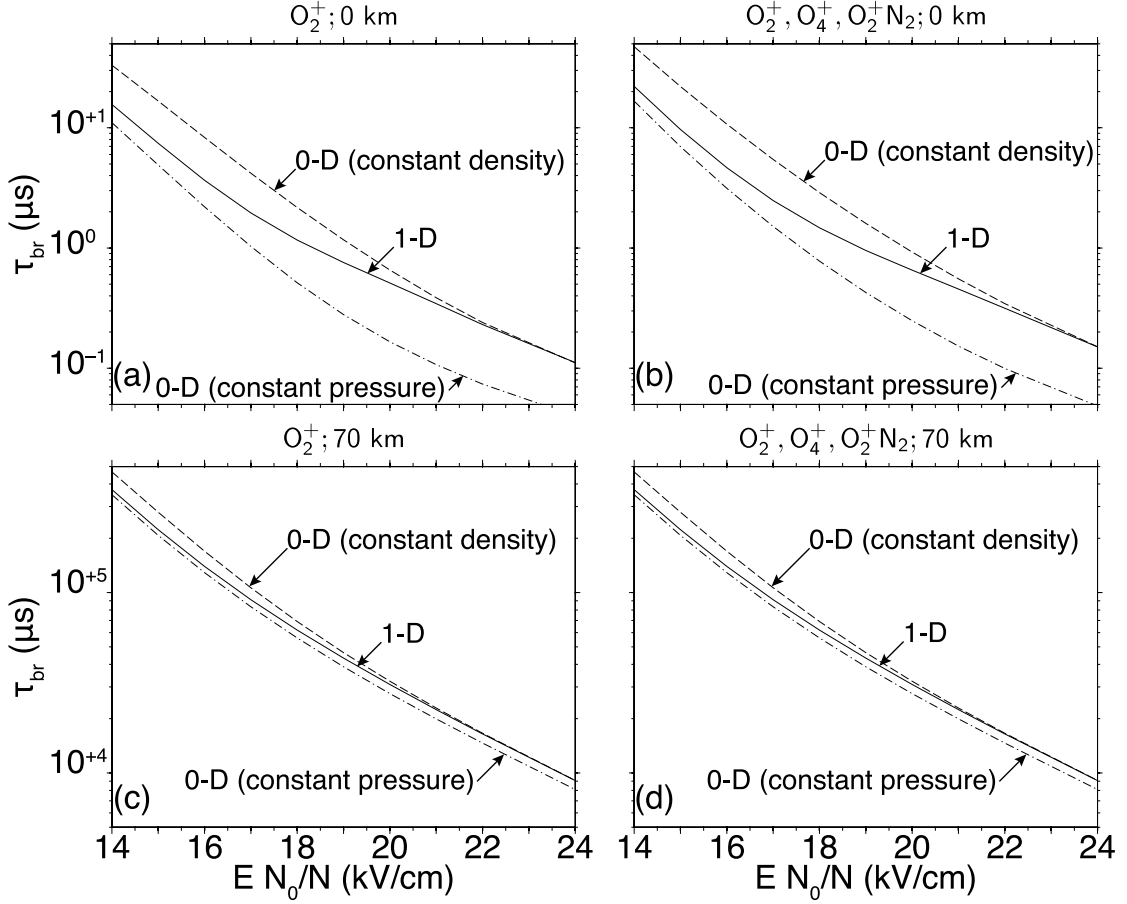


Figure 8.2. Comparison of 0-D models under constant pressure p , constant density N , and 1-D model of Chapter 7 at different altitudes and for two different kinetic schemes: including O_2^+ only at $z=0$ km (a) and $z=70$ km (c); and including O_2^+ , O_4^+ , and O_2^+N_2 at $z=0$ km (b) and $z=70$ km (d).

model described in Chapter 7 (solid lines). The model results are obtained at different altitudes (0 km in panels (a) and (b)) and 70 km (in panels (c) and (d)) for two kinetic schemes including electrons, neutral species N_2 , O_2 , O , N , NO , negative ions O^- , O_2^- , O_3^- , and excited species $\text{O}_2(\text{a}^1\Delta_g)$, $\text{N}_2(\text{A}^3\Sigma_u^+)$, $\text{N}_2(\text{B}^3\Pi_g)$, $\text{N}_2(\text{C}^3\Pi_u)$, $\text{N}_2(\text{a}^1\Sigma_u^-)$. The two kinetic schemes differ only through the treatment of positive ions. Only O_2^+ ions are included in the cases of Figure 8.2a and 8.2c. The related chemical kinetics can be considered as similar to that presented in [Naidis, 1999] where O_2^+ was observed as the dominant positive ion. The cases of Figures 8.2b and 8.2d include a more complete set of ions: O_2^+ , O_4^+ , and O_2^+N_2 . The N_2^+ ions produced as result of electron impact ionization of the N_2 , and the N_4^+

ions produced in associative ionization reactions R4 and R5 (Table 7.2) are usually assumed to readily convert into O_2^+ ions due to fast-charge-exchange reactions [e.g., *Aleksandrov and Bazelyan*, 1999; *Sentman et al.*, 2008a, b]. This approximation is fully justified by the timescale of these conversions (~ 1 ns at altitude 0 km), which is much shorter than the timescale of the streamer-to-spark transition. Therefore, we assume in our model that the electron impact ionization of N_2 and the associative ionization reactions directly lead to the production of O_2^+ ions. Similarly, we assume that atomic oxygen ions O^+ produced in reaction R3 (Table 7.2) very quickly convert to O_2^+ ions via a charge exchange reaction $O^+ + O_2 \rightarrow O_2^+ + O$ that has timescale ~ 30 ns at 0 km and ~ 0.4 ms at 70 km [*Sentman et al.*, 2008a, b].

The O_2^+ ions quickly convert into O_4^+ ions through the reaction R58 (Table 7.2) and into $O_2^+N_2$ ions through the reaction R60 (Table 7.2). The rate of conversion of $O_2^+N_2$ ions into O_4^+ via the three-body reaction R59 is also very high leading to the predominance of this ion at high air densities (low altitudes). Figures 8.4 and 8.6 presented below illustrate that the O_4^+ ion dominates at altitude 0 km, but O_2^+ dominates at 70 km. The importance of O_4^+ ions at high air pressures is underscored by the fact that these ions have a very high recombination rate with electrons (R11, Table 7.2) leading to a slower streamer-to-spark transition. This is confirmed by the direct comparison of the results presented in Figure 8.2a, which are obtained assuming O_2^+ ions only, and those presented in Figure 8.2b based on a complete positive ion chemistry including O_2^+ , O_4^+ , and $O_2^+N_2$ ions. We note that although electron impact ionization of NO (R2) is explicitly included in our model, under the studied conditions NO^+ ions do not make any significant contribution to streamer-to-spark transition dynamics.

Figure 8.2 shows that at any altitude and for both schemes, the 1-D model converges toward the 0-D model under constant density at high-applied electric fields and toward the 0-D model under constant pressure at lower applied electric field. A significant difference appears from the comparison of the situations described in Figure 8.2: although at low pressures (panels (c) and (d)) the differences between constant density and constant pressure streamer-to-spark transition times do not exceed $\sim 25\%$, the results produced by the different models can differ by as much as a factor 2 to 3 at ground pressure. In the next section, we discuss the reasons for those differences.

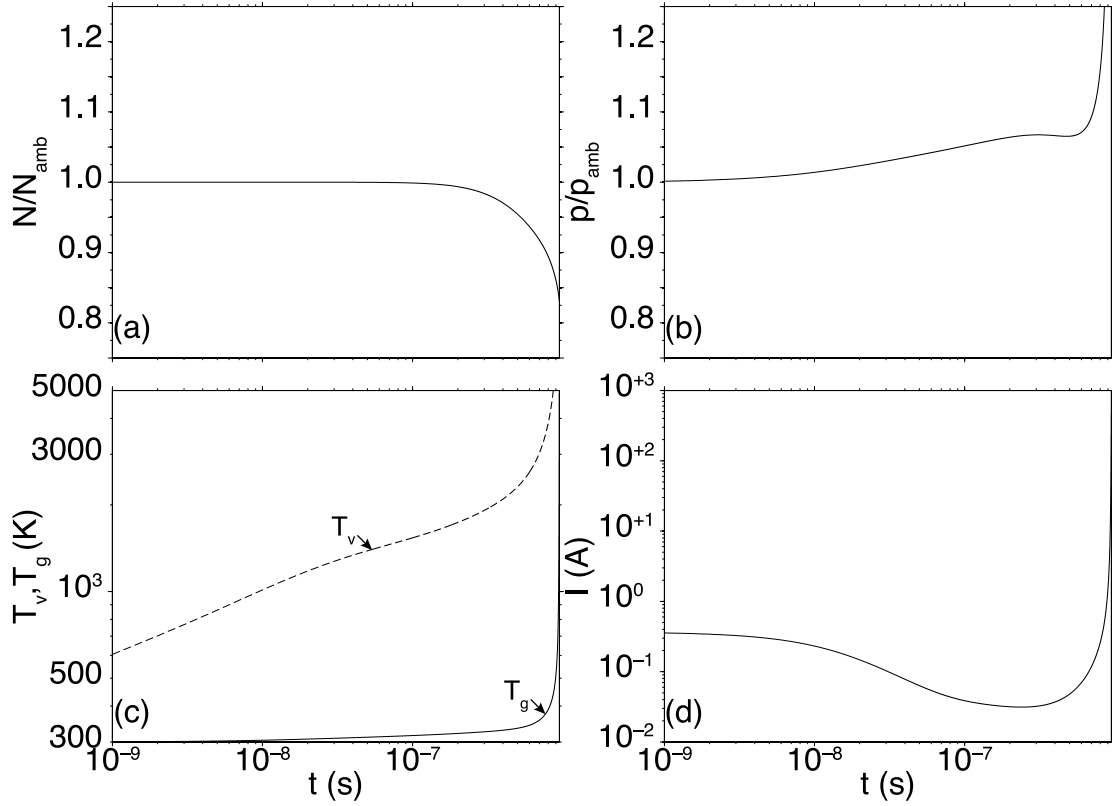


Figure 8.3. Time dynamics of the streamer-to-spark transition at altitude 0 km and $EN_0/N=19$ kV/cm. (a) Changes in the reduced neutral gas density N/N_0 at the axis of the channel; (b) Variations of the reduced pressure p/p_0 at the axis of the channel, where p_0 is the ambient pressure at the altitude considered; (c) evolution of the neutral gas temperature T_g (solid line) and vibrational temperature T_v of N_2 at the axis of the channel (dashed lined); (d) Electric current flowing along the channel and defined as $I=\pi r_s^2 (\sigma_e^0 + \sigma_i^0) E^2$.

Figures 8.3, 8.4, and 8.7a illustrate the temporal dynamics of the streamer-to-spark transition at altitude 0 km (i.e., at ground pressure $p=10^5$ Pa) assuming $EN_0/N=19$ kV/cm and full O_2^+ , O_4^+ , and $O_2^+N_2$ ion chemistry kinetics. The time by which the gas temperature reaches 5000 K is $\tau_{\text{br}}=0.95 \mu\text{s}$ in this case. Figures 8.3a and 8.3b represent the evolution of the neutral gas density normalized with the ambient gas density N_{amb} and of the gas pressure p normalized with the ambient pressure p_{amb} at the altitude of the simulation (0 km). The ratio N/N_{amb} remains constant until $t=0.2 \mu\text{s}$, then drops quickly just before reaching the spark stage. Conversely, the ratio p/p_{amb} increases slowly until $t=0.2 \mu\text{s}$, when it reaches a

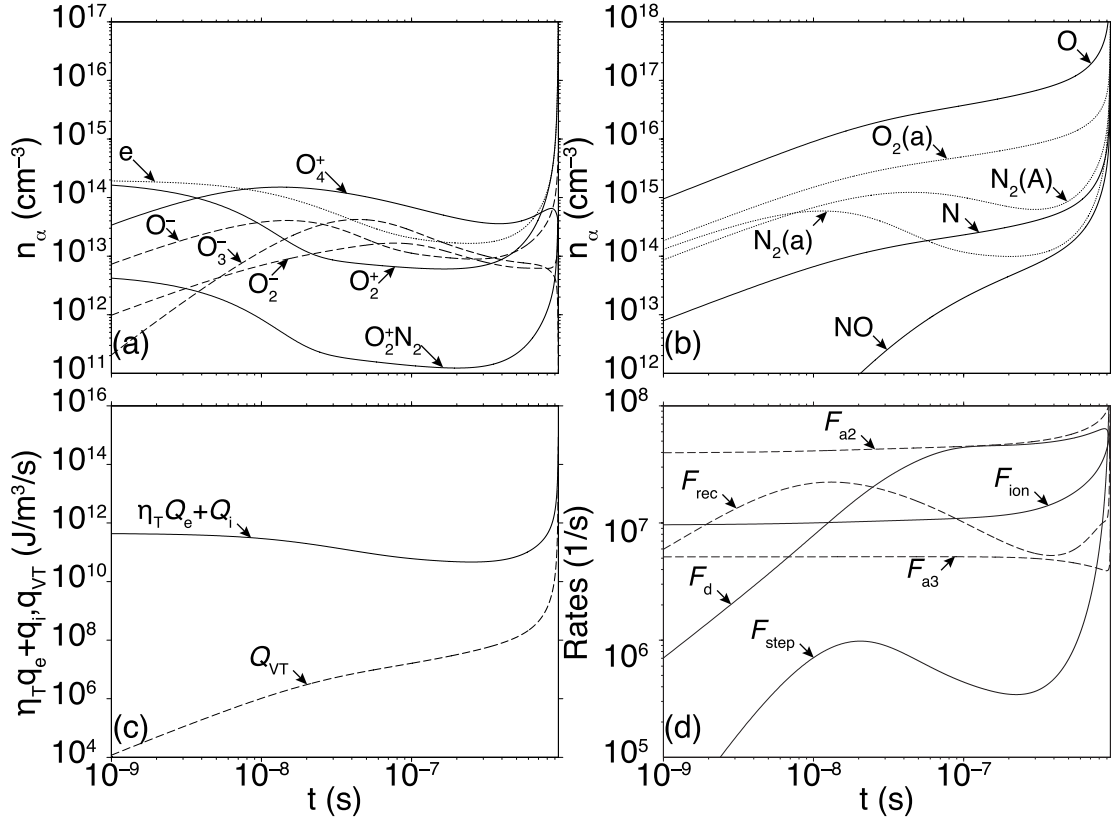


Figure 8.4. Time dynamics of the streamer-to-spark transition at altitude 0 km and $EN_0/N=19$ kV/cm (cont. from Figure 8.3). (a), (b) densities of charged species (e , O_2^- , O_3^- , O_2^+ , O_4^+ , and $O_2^+N_2$), and densities of neutral species (O , N , NO , $O_2(a^1\Delta_g)$, $N_2(A^3\Sigma_u^+)$, and $N_2(a^1\Sigma_u^+)$) at the axis of the discharge, respectively. (c) Contributions from the fast heating ($\eta_T Q_e = \eta_T \sigma_e^0 E^2$), ionic Joule heating ($Q_i = \sigma_i^0 E^2$), and vibrational–translational relaxation energy transfer (Q_{VT}) (in $\text{eV m}^{-3} \text{s}^{-1}$) appearing on the right hand side of the equation for translational energy (7.5). (d) Rates of generation and loss of electrons as a function of time.

plateau for ~ 200 ns, and then increases exponentially. Figure 8.3c shows the time evolution of the gas temperature T_g (solid line) and of the vibrational temperature T_v of N_2 (dashed line) at the axis of the channel. The temperature T_g increases almost linearly by a few tens of Kelvins until $t \sim 0.5 \mu\text{s}$, when it starts increasing exponentially. A similar observation can be made about T_v . These dynamics are in good quantitative agreement with those reported previously in [Naidis, 1999, 2005]. The current flowing in the channel $I = \pi r_s^2 (\sigma_i^0 + \sigma_e^0) E^2$ is represented in panel (d) of Figure 8.3.

Figures 8.4a and 8.4b show the evolution of the densities of charged and neu-

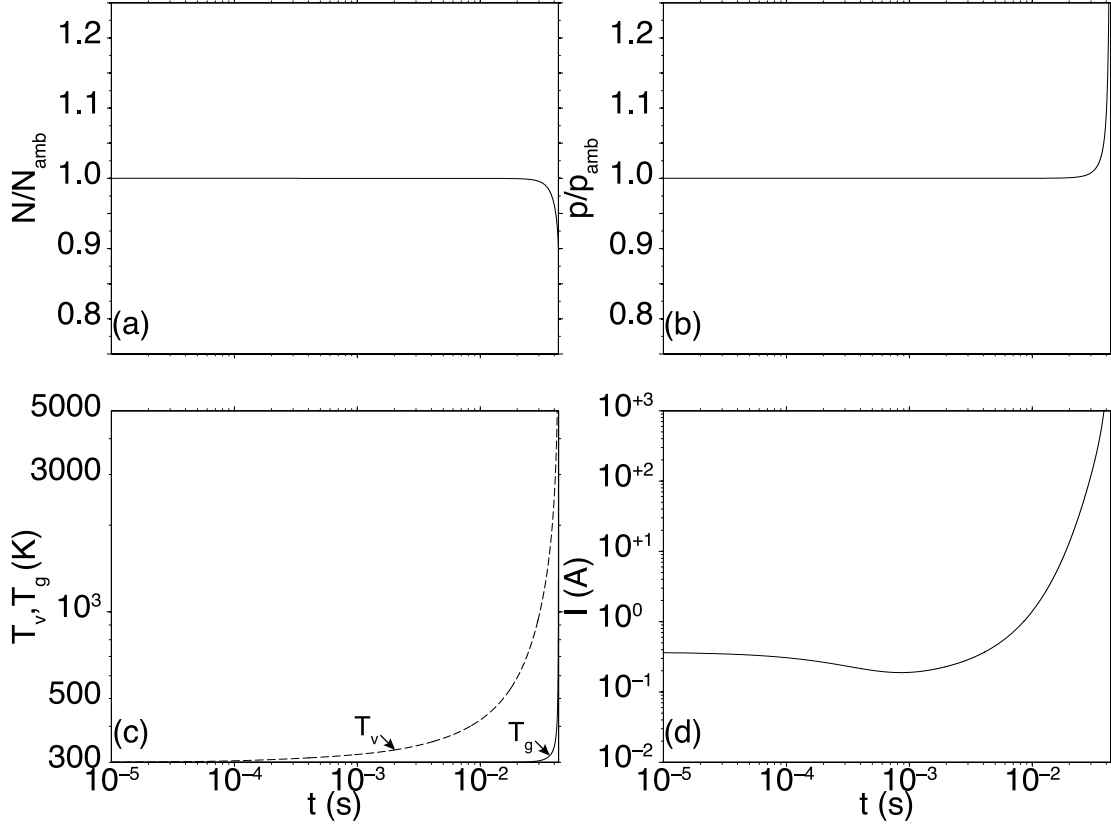


Figure 8.5. Time dynamics of the streamer-to-spark transition at altitude 70 km and $EN_0/N=19$ kV/cm. (a)–(d) Same as in Figure 8.3.

tral particles with time. Note that O_4^+ is the dominant species after 10 ns and until the end of the simulation (i.e., $T_g \geq T_{\text{br}}$). In panel (c), we illustrate the contributions from the fast heating and the vibrational–translational relaxation to the increase of energy density (and therefore to the neutral gas temperature). The contribution from the fast heating and ionic Joule heating remains largely dominant over the energy transfer from vibration–translational relaxation until the time of the transition. Figure 8.4d shows the electron generation and loss rates during the transition, and emphasizes the relative importance of the detachment and stepwise ionization processes in the growth of electron density during the streamer-to-spark transition. It is believed that the fast release of electrons in detachment collisions is a critically important process for the fast gas heating in streamer channels [e.g., Aleksandrov *et al.*, 1997; Naidis, 1999; Vidal *et al.*, 2002; Comtois *et al.*, 2003]. Figure 8.7a illustrates the contributions of different processes to the total rate of

detachment F_d shown in Figure 8.4d, indicating in particular the dominant role of $O^- + N_2$, $O^- + O$, and $O_3^- + O$ interactions (reactions R15, R16, and R18 in Table 7.2, respectively) in the rapidly growing detachment rate. These results are in good agreement with the conclusions reached by *Naidis* [1999] indicating that the major cause of spark formation is an increase with time in the electron detachment rate due to the accumulation of oxygen atoms and other active species.

Figures 8.5, 8.6, and 8.7b provide the same information as Figures 8.3, 8.4, and 8.7a at $EN_0/N=19$ kV/cm only for the altitude 70 km (i.e., at pressure $p \approx 7$ Pa). In this case, $\tau_{br}=43.3$ ms. Figure 8.5c reveals that the initial linear increase in T_g is no longer present, instead, T_g remains constant until the very last stage of the streamer-to-spark transition; then at $t \sim 30$ ms, it increases exponentially. Similarly, the neutral gas density remains constant until the time of exponential increase of T_g , at which point it decreases rapidly (Figure 8.5a). Inter-

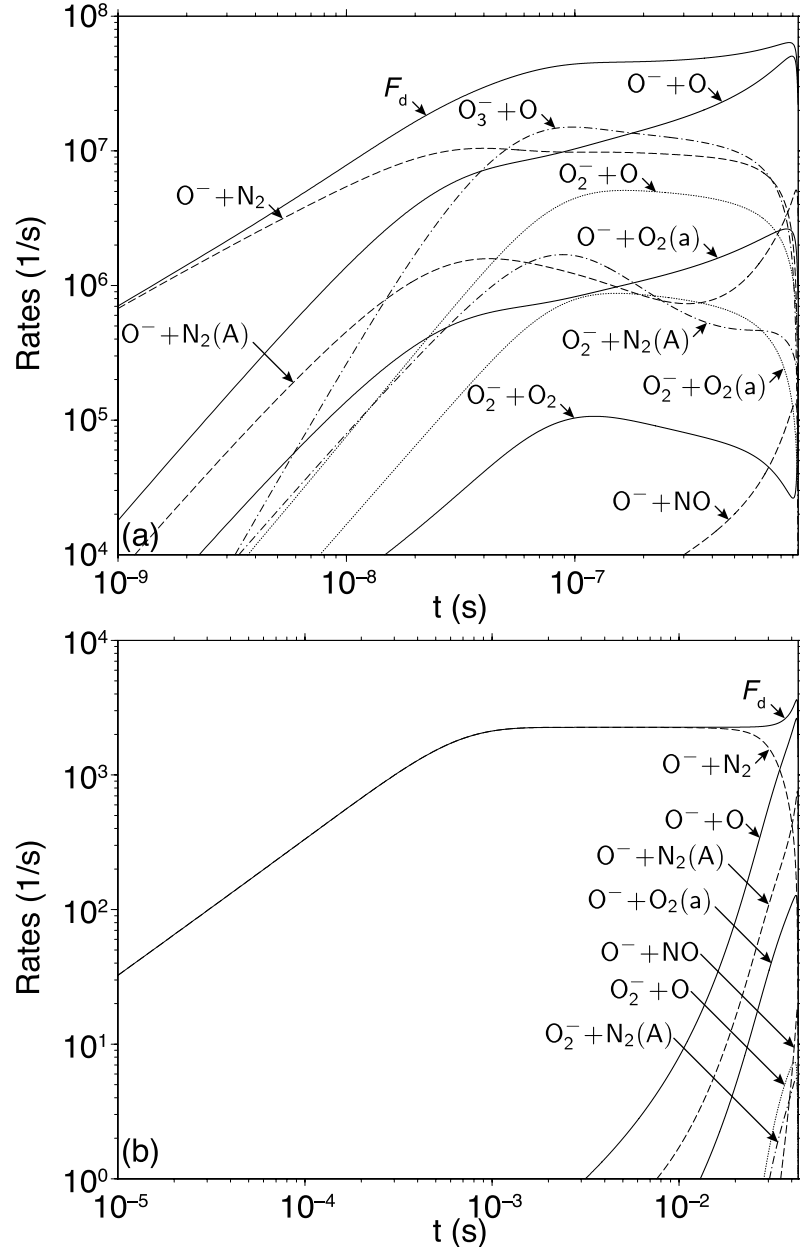


Figure 8.7. Contributions of all reactions of detachment (R13–R22 in Table 7.2) to the total detachment rate F_d throughout the duration of the streamer-to-spark transition at 0 km (a), and 70 km (b).

estingly, the behavior of the ratio p/p_{amb} in Figure 8.5b is significantly simpler than at 0 km, as it presents no variations until $t \sim 30$ ms. Although O_4^+ prevails at 0 km in Figure 8.4a, Figure 8.6a emphasizes that O_2^+ remains the dominant positive ion throughout the entire duration of the streamer-to-spark transition at 70 km because

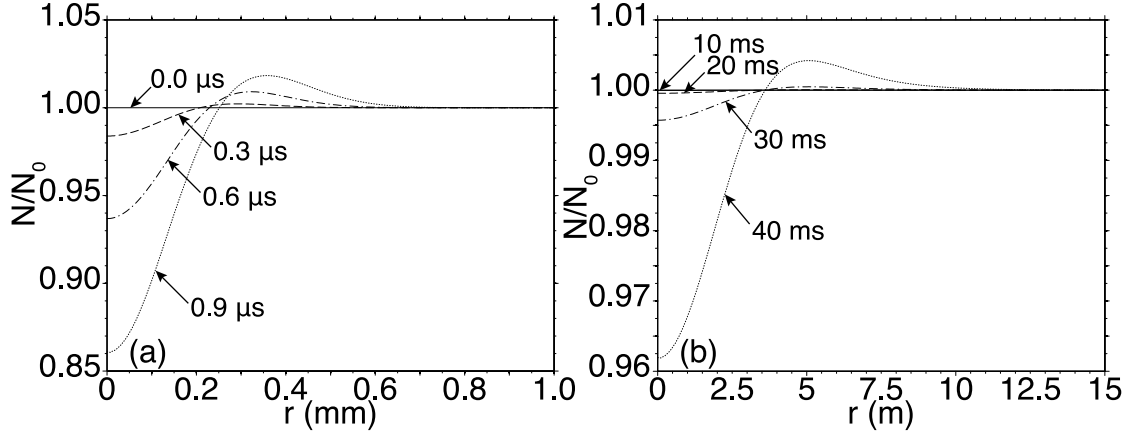


Figure 8.8. Distribution of the reduced gas density on the radial coordinate (a) at 0 km at $t=0, 0.3, 0.6$, and $0.9 \mu\text{s}$, and (b) at 70 km at $t=10, 20, 30$, and 40 ms .

of the disappearance of three-body interactions leading to more complex ions, as already noted above. Figure 8.6d emphasizes the disappearance of the three-body attachment and dramatic reduction in the recombination loss rate of electrons at low air pressures. We emphasize that the reduction of the recombination rate as documented in Figure 8.6d at low air density in comparison with ground level results shown in Figure 8.4d is one of the fundamental reasons for acceleration of heating observed at reduced air densities and reported in this chapter. The recombination process is described in kinetic equations by terms that contain products of electron and ion densities and therefore these terms can be approximately viewed as quadratic with respect to streamer electron density. Because electron density itself scales with air density as $\sim N^2$, the contribution of these quadratic terms quickly becomes negligible in comparison with other processes (i.e., two-body attachment) with reduction of air density N . The two-body attachment process, for example, enters in electron balance equation (7.9) as $-F_{a_2}n_e$, where $F_{a_2}=\nu_{a_2}$ and ν_{a_2} scales proportionally to N . The recombination term enters in the same equation as $-F_{\text{rec}}n_e$, where F_{rec} is itself proportional to n_e and therefore scales as N^2 , becoming negligible in comparison with two-body processes at low air densities at high altitudes (see Figure 8.6d). Figure 8.7b shows that the detachment rate F_d at 70 km is almost exclusively governed by the $\text{O}^- + \text{N}_2$ interaction (reaction R15 in Table 7.2) until the very last stage of the transition, when the $\text{O}^- + \text{O}$ interaction (reaction R16 in Table 7.2) becomes dominant.

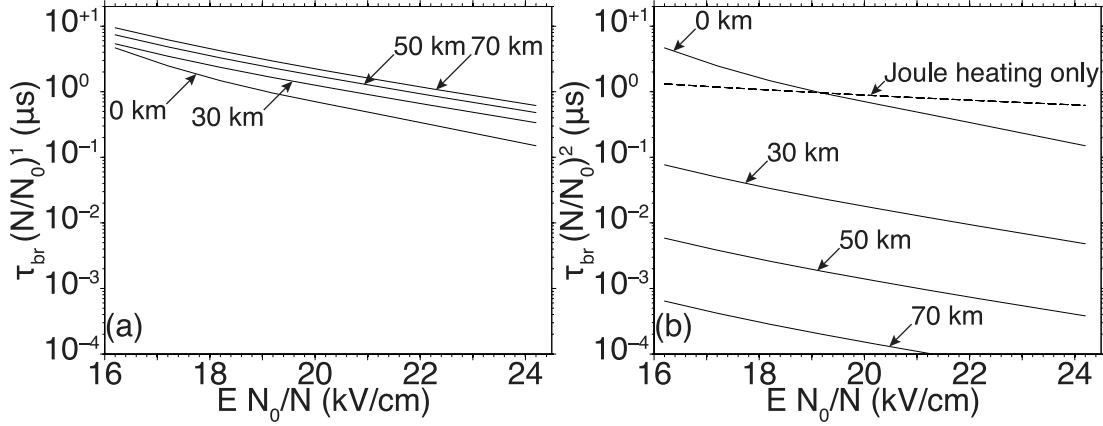


Figure 8.9. Scaling of the breakdown times as a function of the neutral density for various applied electric fields and altitudes (0, 30, 50, and 70 km). (a) $\tau_{br} \propto 1/N^1$: the scaling is the same as that of the vibrational–translational relaxation timescale. (b) $\tau_{br} \propto 1/N^2$: the scaling is the same as that of the Joule heating timescale, assuming constant air density N and time independent conductivity of the channel.

Figure 8.8 shows the distribution of the reduced gas density N/N_{amb} as a function of the radial coordinate at 0 km at $t=0, 0.3, 0.6$, and 0.9 μs (panel (a)), and at 70 km at $t=10, 20, 30$ and 40 ms (panel (b)). It demonstrates that at higher altitudes the neutral gas density remains almost constant for most of the transition (within $\sim 1\%$ of the initial value until $t \gtrsim 30$ ms), and almost no radial expansion of the channel occurs until the very last stage of the streamer-to-spark transition (panel (b)). At higher air density at lower altitudes, the gas dynamics effect becomes pronounced much earlier during the transition (panel (a)).

Figure 8.9 shows τ_{br} at 0, 30, 50 and 70 km altitudes for the reduced field range $16 < E N_0/N < 24$ kV/cm. We emphasize that Figures 8.9a and 8.9b show the same exact values τ_{br} using different ways of scaling them with N . Figure 8.9a presents the results assuming that the transition times scale similarly to the vibrational–translational relaxation time (i.e., $\propto 1/N$) and Figure 8.9b presents the results assuming that the breakdown times scale similarly to the Joule heating timescale (i.e., $\propto 1/N^2$ [e.g., *Achat et al.*, 1992]). The curves shown in Figure 8.9a and Figure 8.9b would coincide if the heating followed the vibrational–translational or the Joule heating similarity laws, respectively. Therefore, the results shown in Figure 8.9b indicate a significant acceleration of the heating with reduction of air pressure. Figure 8.9a and 8.9b demonstrate that τ_{br} scales closer to $1/N$ than to

$\propto 1/N^2$. This result agrees with conclusions reached in [Naidis, 2005, Figure 6].

8.2 Discussion

The model introduced in Chapter 7, whose results are presented in Section 8.1, allows us to investigate the influence of the treatment of positive ions in the kinetics scheme on the streamer-to-spark transition. It also permits us to quantitatively evaluate the scaling properties of the streamer-to-spark transition time. In this section, we discuss related questions and analyze the sensitivity of the model to the different employed approximations.

8.2.1 Comparison with experimental data, and approximations of constant pressure and gas density

The timescales of streamer-to-spark transition are compared with the experimental measurements in Figure 8.1. The model results appear to be in excellent agreement with the experimental data under both normal and reduced pressure conditions (10^5 Pa and 0.75×10^5 Pa, respectively). In comparison, numerical modeling does not fit experimental data under the conditions of Joule heating assuming constant neutral density and constant conductivity of the channel (dashed line in Figure 8.1). The comparison of theoretical and experimental curves (solid lines and ‘ \square ’, ‘ \circ ’, and ‘ \bullet ’ marks) with each other and with the results obtained for the Joule heated channel at constant density and channel conductivity therefore emphasizes the necessity of including the time-dependent chemical kinetics and partitioning of energy between fast heating and vibrational excitation in order to reproduce the experimentally observed results (see Figure 8.1).

At low applied voltage, the gas dynamics, which leads to the expansion of the channel and to the reduction of the air density N , plays a dominant role. Under these conditions the pressure p stays approximately constant with the increase in the gas temperature T_g . Low applied voltages correspond to longer breakdown times allowing the pressure to be equalized on the timescale of the streamer-to-spark transition, i.e., allowing us to make the assumption that the channel remains under constant pressure. The high-applied voltages lead to very small τ_{br} such that

$\tau_{br} \ll r_s/c_s$, allowing us to assume that the neutral density barely varies during the time of the transition. Therefore, it is expected that the 1-D model (including the gas dynamics) converges towards the 0-D model under assumption of constant pressure at lower applied voltage, and towards the 0-D model under constant density for higher applied voltage (Figure 8.2), consistent with previous results by *Naidis* [2005]. In the latter case, the transition occurs too fast to allow the gas dynamics to play any significant role. From this result, it follows that the effects of the gas dynamics can be neglected at high reduced electric field E/N , i.e., when the timescale of the variation of the neutral gas density is too slow to compete with that of the kinetics effects. When the neutral gas density varies on a timescale comparable to that of the streamer-to-spark transition, the gas dynamics effects act in parallel with the kinetics mechanisms and increase the ionization (through an increase of the reduced electric field), resulting in a faster transition. Consequently, the gas dynamics is able to accelerate the transition to spark at low applied voltage.

Another interesting fact in Figure 8.2 lies in the differences of the transition times between 0-D constant density and constant pressure models at 0 and 70 km. At ground level, they can differ by a factor ~ 2 to 3, but at higher altitude, their difference does not exceed $\sim 25\%$ as evidenced by Figure 8.2. Figure 8.3c shows that at high air density, the temperature increases steadily throughout most of the duration of the transition (until $t=0.5 \mu s$) and then increases exponentially. Therefore the variations of T_g are too large to be negligible in this case, and the pressure p cannot be assumed to be simply proportional the air density N ($p \propto N$) (see Figures 8.3a and 8.3b). Hence, the 0-D models under assumptions of constant pressure or density differ significantly for any applied electric field and for both kinetic models (Figures 8.2a and 8.2b). At higher altitude (Figures 8.2c and 8.2d), the gas temperature remains almost constant until the very last stages of the transition when it rapidly increases exponentially (Figures 8.5c). Hence, both the pressure and air density remain quasi-constant (see Figures 8.5a and 8.5b) and such that effectively $p \propto N$ most of the time. Consequently there is little difference between the two 0-D models as observed in Figures 8.2c and 8.2d. It is shown earlier in this section that our 1-D model is bounded by the two 0-D models; therefore, it can be stated that at high altitude, the three models are approximately equivalent.

The fundamental physical reason for this equivalence is that the air temperature increases very rapidly in comparison with the gas dynamic expansion time (i.e., $\tau_{\text{br}} \leq r_s/c_s$) so no significant changes in air density are observed.

The observed model variations in the dynamics of the gas temperature reveal the existence of two heating phases: one, a regime of steady, linear increase of the gas temperature, and another manifested in exponential growth of the temperature. Figure 8.3c shows that both phases exist at high air density, and Figure 8.5c emphasizes that only the latter exists at lower air density. This observation is related to the rate of increase in electron number density that increases by two orders of magnitude at high air density and by as much as four orders of magnitude at lower air density, leading to a more sudden transition to spark in the second case than in the first one.

8.2.2 Role of $\text{N}_2(\text{B}^3\Pi_g)$ and $\text{N}_2(\text{C}^3\Pi_u)$ excited species

In comparison with [Naidis, 1999, 2005], the present study includes B and C excited states of N_2 . Although at ground pressure the effects of these states on heating timescales are negligible, it is important to consider their quenching altitude, defined as the altitude at which the collisional quenching timescale is equal to the timescale of de-excitation by radiation. The quenching altitude of the C state is 30 km and that of the B state is 50 km [e.g., Vallance-Jones, 1974, p. 119]. At low air pressures, we observed a slight acceleration of the heating (increasing from ~5 to 10% at 70 km for EN/N_0 ranging between 14 and 21 kV/cm) owing to enhancement of the density of $\text{N}_2(\text{A}^3\Sigma_u^+)$ species due to the cascade from the B state (R33 in Table 7.2) (also enhanced by the cascade from C state (R34 in Table 7.2)).

8.2.3 Role of atomic oxygen in detachment collisions

Figures 8.4d and 8.6d show that the streamer-to-spark transition is accompanied by an increase in the detachment rate of electrons F_d . At 0 km, this is correlated with an increase of the detachment of O^- ions in collision with atomic oxygen (R16) (Figure 8.7a), which increases in turn with the concentration of oxygen atoms n_{O} . The importance of the accumulation of oxygen atoms for the fast transition to

spark was emphasized by *Naidis* [1999].

8.2.4 Role of ambient NO, O₃, O, and CO₂

For all the simulations presented in this chapter, we assumed zero initial densities for the active species. In particular, this means that we neglected the ambient density of O₃ and NO in the upper atmosphere. At 70 km, $n_{\text{O}_3} \simeq 6 \times 10^8 \text{ cm}^{-3}$ and $n_{\text{NO}} \simeq 1.2 \times 10^7 \text{ cm}^{-3}$ [e.g., *Sentman et al.*, 2008a, Table 2]. Whether these initial densities are introduced in the model or not does not produce any noticeable change in the time of streamer-to-spark transition for applied $EN_0/N = 14\text{--}24 \text{ kV/cm}$, and altitude range between 0 and 70 km. The initial densities of O₃ and NO are maintained to their initial values until the last stages of the transition, when the behavior of n_{O_3} and n_{NO} with non-zero initial conditions closely follow the dynamics of these species with zero initial densities. The study of the dynamics of O₃ requires to include reactions of production and destruction of O₃. Based on the estimations of the timescales of several reactions of production and destruction of O₃, it can be shown that O₃ is primarily produced by collisions of atomic oxygen with O₂ in the reaction: $\text{O} + \text{O}_2 + \text{O}_2 \rightarrow \text{O}_2 + \text{O}_3$ (with constant of reaction $k_f = 8.6 \times 10^{-31} T_g [\text{K}]^{-1.25} \text{ cm}^6 \cdot \text{s}^{-1}$) and destroyed in the reaction $\text{O}_2 + \text{O}_3 \rightarrow \text{O} + \text{O}_2 + \text{O}_2$ (with constant of reaction $k_d = 73 \times 10^{-11} e^{-11400/T_g [\text{K}]} \text{ cm}^3 \cdot \text{s}^{-1}$) [*Parissi et al.*, 2000]. *Parissi et al.* [2000] emphasized that the dependence of k_f and k_d on the temperature T_g implies that the ozone destruction reaction is favored for high temperature. Using $n_{\text{O}_3} \simeq 6 \times 10^8 \text{ cm}^{-3}$ [*Sentman et al.*, 2008a] and $n_{\text{O}} \simeq 2 \times 10^{10} \text{ cm}^{-3}$ [e.g., *Harlow and Riehl*, 1991] for the initial concentrations in O₃ and O at 70 km, our simulation results demonstrate that destruction of O₃ is favored for gas temperature above $\sim 600 \text{ K}$. If the initial temperature is high enough, then we observe a destruction of the initially present O₃ molecules, in agreement with the above discussion.

Similarly, if the ambient density of atomic oxygen at 70 km is accounted for ($n_{\text{O}} \simeq 2 \times 10^{10} \text{ cm}^{-3}$ [e.g., *Harlow and Riehl*, 1991]), then the number density of O remains close to its initial value until the last stages of the transition, when the difference between the dynamics of atomic oxygen with and without the initial ambient density of O is no longer significant. Quantitatively, the addition of the initial n_{O} density produces a small acceleration of the streamer-to-spark transition

by decreasing the breakdown times by $\lesssim 1\%$ for applied $EN/N_0=14\text{--}24$ kV/cm.

The concentration of CO_2 molecules at 70 km in the Earth atmosphere is on the order of $5 \times 10^{11} \text{ cm}^{-3}$ [e.g., *Sentman et al.*, 2008a] and non-radiating vibrationally excited $\text{N}_2(v)$ molecules are expected to efficiently transfer their energy to $\text{CO}_2(\nu_3)$ vibrational states that then radiate infrared emissions at $4.3 \text{ }\mu\text{m}$ [e.g., *Kumer*, 1977; *Picard et al.*, 1997, and references therein]. The transfer of vibrational energy from N_2 to CO_2 takes from several seconds at 70 km to a minute at 90 km altitude [e.g., *Picard et al.*, 1997]. Although the lifetime of $\text{CO}_2(\nu_3)$ is very short (~ 2 ms), in the mesosphere the effective lifetime of $\text{CO}_2(\nu_3)$ and relaxation time of $\text{N}_2(v)$ are both lengthened considerably by reabsorption of $4.3 \text{ }\mu\text{m}$ photons (radiation trapping) and by the reverse VV process in which the vibrational energy is passed back to N_2 . The effective relaxation times of $\text{N}_2(v)$ are in the range of 5–7 min at 70–90 km altitude [*Kumer*, 1977; *Picard et al.*, 1997]. These timescales exceed by several orders of magnitude the heating timescales reported in the present work and therefore related processes are not included in the present model.

8.2.5 Effects of positive ion chemistry

The comparison of Figures 8.2a and 8.2b emphasizes the effects of different positive ions included in the model. For the simulation results presented in this work, N_2^+ and N_4^+ ions are readily converted into O_2^+ ions [e.g., *Naidis*, 1999]. This hypothesis has been tested and simulation results (not presented here for the sake of brevity) have shown that nitrogen positive ions remain in negligible quantity at any moment of the simulation at any altitude. The densities of the positive ions in Figures 8.4a and 8.6a reveal that O_4^+ is the dominant ion at low altitude, and O_2^+ is the main positive ion at high altitude. The O_4^+ ion is produced in a three-body process R58 and is lost in two-body processes (R11, R48, R51, R54, R56, R57, R61, and R63). The O_2^+N_2 ion is produced in the three-body process R60 and can lead to O_4^+ ion via a two-body reaction R59. Therefore, the production of both O_4^+ and O_2^+N_2 ions fundamentally occurs in three-body interactions. The O_2^+ ion is produced in direct electron impact ionization (R1) and in charge transfer reactions involving N_2^+ and N_4^+ ions [e.g., *Sentman et al.*, 2008a, b] that are two-body processes. The O_2^+ ion is lost in both two-body processes (R9, R44–R47, R50, and R53) and

three-body processes (R10, R58, and R60). The decrease of neutral density with altitude reduces the importance of three-body processes compared with two-body processes (as evidenced, in particular, in Figures 8.4d and 8.6d for two- and three-body attachment), and makes O_2^+ the dominant positive ion at higher altitude (see Figure 8.6a). Our model results indicate that whether or not positive ions O_4^+ and $O_2^+N_2$ are explicitly included in the model has direct consequences on the streamer-to-spark transition time. In particular, as already emphasized in Section 8.1, at ground conditions the transition into spark is significantly longer when O_4^+ and $O_2^+N_2$ ions are taken into account (see Figures 8.2a and 8.2b), mainly due to the fast recombination of electrons with these ions and resultant reduction in electron conductivity. At higher altitude, there is no noticeable difference between the kinetics schemes including O_2^+ only or the full O_2^+ , O_4^+ , and $O_2^+N_2$ positive ion chemistry (Figures 8.2c and 8.2d, respectively). Indeed, Figure 8.6a shows that even when O_4^+ and $O_2^+N_2$ are accounted for in the kinetics scheme, they are negligible at all times during the transition in comparison with O_2^+ ions.

The refined treatment of the chemistry of the plasma including O_4^+ and $O_2^+N_2$ is expected to improve the accuracy of the results, yet it involves reactions of ion–ion recombinations, whose rates are still poorly known. The works by *Kossyi et al.* [1992] and *Sentman et al.* [2008a, b] provide a significant number of reactions of ion–ion recombination, but their lists are not exhaustive, as for example the recombinations of complex ions such as O_4^+ with O^- are not included.

The kinetic scheme presented in Chapter 7 does not include three-body ion–ion recombination reactions (for example, reactions (V) and (VI) in [*Kossyi et al.*, 1992]). If three-body ion–ion recombinations were included, then the number of unknown rates of reactions would increase significantly and therefore would introduce an additional source of uncertainty. We restrain the reactions of ion–ion recombination in the kinetic scheme to well-documented two-body reactions (R44–R55 in Table 7.2). *Benilov and Naidis* [2003] even further simplified the treatment of ion–ion interactions in their model by treating all ion–ion recombinations through a unique reaction denoted $X^+ + Y^- \rightarrow X + Y$, where X^+ and Y^- represent any positive and negative ions, respectively.

8.2.6 Role of associative ionization reactions

Popov [2003] emphasizes the role of the reactions of associative ionization (R4–R5 in Table 7.2) in the explosive increase in the electron density leading to the transition to spark. The comparisons of breakdown times τ_{br} produced by our model for $EN_0/N=14\text{--}24$ kV/cm at 0 and 70 km altitude show that ignoring these reactions would affect the transition time most significantly at high reduced electric field E/N . For $EN_0/N=14$ kV/cm, τ_{br} increases by a few percents ($<2\%$) if R4–R5 are neglected, because the timescales of the reactions of associative ionization ($\tau_{\text{R4-R5}} \gtrsim 50 \mu\text{s}$ at 0 km and $\tau_{\text{R4-R5}} \gtrsim 10$ s at 70 km) are longer than the streamer-to-spark transition times ($\tau_{\text{br}}=26.7 \mu\text{s}$ at 0 km and $\tau_{\text{br}}=0.37$ s at 70 km). At higher reduced fields, for $EN_0/N=24$ kV/cm, the timescales of the reactions R4 and R5 are on the order of $0.1\text{--}1 \mu\text{s}$ and $\gtrsim 1$ s at 0 and at 70 km altitudes, respectively. These timescales are comparable with the streamer-to-spark transition time, suggesting a significant effect of the reactions of associative ionization on the dynamics of the transition under these conditions. This observation is confirmed by the model results, which show that in the absence of R4 and R5, the breakdown time is delayed by up to $\sim 40\%$ at 0 km altitude for $EN_0/N=24$ kV/cm, when $\tau_{\text{R4-R5}} \ll \tau_{\text{br}}$.

8.2.7 Scaling of heating time with air density, and thermal conduction and diffusion losses

The effective timescale of the cooling of the streamer channel due to the thermal conduction effects scales with ambient air density as $1/N$, and previous studies have established that the effective Joule heating time in streamer channels under conditions of constant channel conductivity and air density scales as $1/N^2$, therefore leading to a better heat confinement and an easier transition to spark at higher gas pressures in comparison with low pressures [*Achat et al.*, 1992].

Because the adjusted heating time scaling factor for the breakdown time ($\tau_{\text{br}} \propto 1/N^{1.11}$) lies between the scaling factor of the vibrational–translational relaxation ($\propto 1/N$) and that of the Joule heating timescale ($\propto 1/N^2$), our results and those in [*Naidis*, 2005, Figure 6] demonstrate that kinetic effects lead to a significant acceleration of the heating, with effective heating times appearing to scale closer to $1/N$ than to $1/N^2$, which is predicted on the basis of simple similarity

laws for Joule heating [Achat *et al.*, 1992].

These results have significant consequences for the evaluation of the importance of different processes for gas heating in streamer channels at low gas pressures. Specifically, they imply that all the processes, which have effective times that scale proportionally to $1/N$ and which are determined to be unimportant for streamer-to-spark transition at ground pressure, can still be ignored at lower pressures. These processes include, in particular, the thermal conduction processes, which lead to the cooling of the streamer channel [Achat *et al.*, 1992; Tardiveau *et al.*, 2001], the diffusion of charged and neutral species [Naidis, 2005] and losses related to the radial drift of ions [Naidis, 2005]. In the same vein it is important to emphasize that the vibrational–translational relaxation time τ_{VT} scales as $1/N$ and since heating time also scales close to $1/N$ there is no significant acceleration of the heating due to transfer of vibrational energy from N_2 molecules, as would be expected if heating time scaled as $1/N^2$.

8.3 Summary of Results

In this chapter, the model developed in Chapter 7 is applied to investigate the streamer-to-spark transition as a function of the air density. The model results are successfully compared with experimental data obtained by Černák *et al.* [1995] and Larsson [1998] at ground and near-ground pressure. The model results confirm the previous results by other authors obtained at ground pressure that the fast release of electrons in detachment collisions is a critically important process for fast gas heating in streamer channels during the streamer-to-spark transition. Classic 0-D models under assumptions of constant gas density or constant pressure, and the 1-D model are also compared, and it is shown that the three models lead to similar results at lower air density (i.e., at high altitudes), but differ significantly at higher air density. The results indicate that at low ambient air densities the channel conductivity and the air temperature increase very rapidly in comparison with gas dynamic expansion time (i.e., $\tau_{br} \leq r_s/c_s$, where r_s is the streamer channel radius and c_s is speed of sound) so both constant density and constant pressure approximations to channel dynamics commonly used in previous studies at ground pressure lead to nearly identical streamer-to-spark transition times. It is shown

that at lower applied electric field, the 1-D model (including the gas dynamics) converges towards the 0-D model under the assumption of constant pressure while for higher applied electric field it converges towards the 0-D model under constant density. At ground and near-ground pressure, these results are in excellent agreement with the prior results on this topic reported by *Naidis* [2005]. The present work demonstrates that for a broad range of air densities studied (between altitudes 0 and 70 km), the streamer-to-spark transition time scales with neutral density as: $\tau_{\text{br}} \propto N^{-1.11}$, i.e., faster than the timescale of Joule heating assuming constant air density and conductivity in the streamer channel ($\propto N^{-2}$) but slower than that of the vibrational–translational relaxation ($\propto N^{-1}$). The obtained model heating times for the altitude range indicate substantial relative (i.e., scaled with $1/N^2$) acceleration of the air heating, when compared with the ground level. This acceleration is attributed to strong reduction in electron losses due to three-body attachment and electron–ion recombination with reduction of air pressure. The vibrational–translational relaxation time τ_{VT} scales as $1/N$ and since heating time also scales close to $1/N$ there is no significant acceleration of the heating due to transfer of vibrational energy from N_2 molecules, as would be expected if heating time scaled as $1/N^2$.

These results have significant consequences for the evaluation of the importance of different processes for gas heating in streamer channels at low air densities. Specifically, all the processes, which are determined to be unimportant for the streamer-to-spark transition at ground pressure and which have effective times, which scale proportionally to $1/N$, can still be ignored at lower pressures. These include, in particular, the thermal conduction processes, the diffusion of charged and neutral species, and losses related to the radial drift of ions. In the same vein it is important to emphasize that the vibrational–translational relaxation time τ_{VT} scales as $1/N$ and since heating time also scales close to $1/N$ there is no significant acceleration of the heating due to transfer of vibrational energy from N_2 molecules, as would be expected if heating time scaled as $1/N^2$. The results indicate that at low ambient air densities the channel conductivity and the air temperature increase very rapidly in comparison with gas dynamic expansion time (i.e., $\tau_{\text{br}} \leq r_s/c_s$, where r_s is the streamer channel radius and c_s is speed of sound) so both constant density and constant pressure approximations to channel dynamics

commonly used in previous studies at ground pressure lead to nearly identical streamer-to-spark transition times.

Conclusions

In this chapter, we summarize the scientific contributions developed throughout this dissertation, and suggest several possible directions for the continuation to the studies realized to date.

9.1 Summary of Results

Here we summarize the principal results and contributions, which follow from the studies presented in this dissertation.

9.1.1 Fractal Modeling of an Intracloud Discharge

In Chapter 2, a new model of intracloud lightning discharge is presented, based on *Kasemir's* [1960] hypotheses of equipotentiality and neutrality of the channel, and on the dielectric breakdown model proposed by *Niemeyer et al.* [1984]. Using a realistic thundercloud charge distribution in Chapter 3, the model is able to reproduce a realistic pattern of an intracloud discharge (in particular, the altitude of initiation and the extensive horizontal propagation of leader channels) comparable to an actual discharge observed over Langmuir Laboratory on July 31, 1999. It is shown that parameters of the discharge such as the charge carried, dipole moment and average linear charge density associated with the leader trees, are in good agreement with previous modeling and related measurements reported in the refereed literature. The model is applied to study the reduction of the electric field in

the thunderstorm due to the growth of the bipolar structure of leader trees resembling development of an intracloud lightning discharge. This study suggests that the polarization charges carried by the leader trees could lower the net charge in the different charge layers of the thundercloud and could decrease the total electric field significantly below the lightning initiation threshold.

9.1.2 Unified Theory of Lightning and Jet Discharges

In Chapter 4, we develop a self-consistent theory of lightning and jet discharges based on the concept of bi-directional, overall neutral and equipotential lightning leaders. The fractal model of Chapter 2 is applied to simulate typical lightning and jet discharges using realistic cloud configurations emphasizing charge imbalance as a principal factor allowing the formation of a leader with high enough potential that enables it to escape from the thundercloud. A new observation of an upward discharge observed by the lightning mapping array in a STEPS 2000 thunderstorm [Lang *et al.*, 2004] is also presented and successfully modeled. Finally, we develop a set of scenarios based on a single unified theory that are able to explain the development of the classic lightning discharges and jet-type events that have been observed to date. These scenarios also predict new cases expected to occur in both normal and inverted polarity thunderstorms. One of these, namely the occurrence of a positive gigantic jet, has been recently observed by *van der Velde et al.* [2010], i.e., after the publication of this work in [Krehbiel *et al.*, 2008].

9.1.3 Self-Consistent Modeling of Thundercloud Screening Charges: Implications for Blue and Gigantic Jets

In Chapter 5, we introduce a 2-D axisymmetric model of charge relaxation in the conducting atmosphere. In Chapter 6, the model is applied in conjunction with *Riousset et al.*'s [2007a] fractal model of lightning to illustrate how blue and gigantic jet discharges are produced above cloud tops. Moreover, the role of the screening charge in the development of each kind of jet discharge is explained through self-consistent modeling. In particular, we demonstrate how the prior occurrence of intracloud discharges can prevent the development of a blue jet until a cloud-to-ground discharge enhances the excess of positive charge in the

cloud by bringing negative charge to the ground. The screening charge gradually developing at the cloud top leads to breakdown initiation near the cloud upper boundary, but is insufficient to contain the lightning leader channel within the cloud resulting in occurrence of upward propagating blue jet events. Furthermore, in thunderstorms for which convective overturning near the cloud top is sufficiently strong, the screening layer that allows for blue jet initiation, gets mixed with the storm upper positive charge region, reducing the net positive charge in this region and causing a substantial charge imbalance between the two main layers of the thundercloud. Quantitative modeling of the resulting discharge reveals that the leader channels cannot be contained in the volume enclosed within the cloud boundary and eventually escape upward to form a gigantic jet, consistent with the ideas first expressed by *Krehbiel et al.* [2008].

9.1.4 Investigations of the Timescales of Air Heating in Streamer Discharges at Different Altitudes in the Earth Atmosphere

In Chapter 7, we introduce an air-density-dependent model of the streamer-to-spark transition. It accounts for the effects of gas dynamics, transfer of energy through vibrational–translational relaxation of N_2 molecules, and realistic partition of input energy into gas heating and vibrational excitation of N_2 molecules during the streamer-to-spark transition dynamics. The model self-consistently couples a fully 1-D axisymmetric, axially invariant gas dynamics model to a 0-D kinetics scheme involving 17 species in 67 reactions. The model results are presented in Chapter 8 and are successfully compared with experimental data obtained by *Černák et al.* [1995] and *Larsson* [1998] at ground and near-ground pressure. We also compare classic 0-D models under assumptions of constant gas density or constant pressure and the 1-D model. We show that the three models lead to similar results at lower air density (i.e., at high altitudes), but differ significantly at higher air density. We show that at a lower applied electric field, the 1-D model (including the gas dynamics) converges towards the 0-D model under assumption of constant pressure but for a higher applied electric field it converges towards the 0-D model under constant density. At ground and near-ground pressure, these

results are in excellent agreement with the prior results on this topic reported by *Naidis* [2005].

The present work demonstrates that for a broad range of air densities studied (between altitudes 0 and 70 km), the streamer-to-spark transition time scales with neutral density as: $\tau_{\text{br}} \propto N^{-1.11}$, i.e., faster than the timescale of Joule heating assuming constant air density and conductivity in the streamer channel ($\propto N^{-2}$), but slower than that of the vibrational–translational relaxation ($\propto N^{-1}$). The obtained model heating times for the altitude range indicate substantial relative (i.e., scaled with $1/N^2$) acceleration of the air heating, when compared with ground level. This acceleration is attributed to strong reduction in electron losses due to three-body attachment and electron–ion recombination with reduction of air pressure.

9.2 Suggestions for Future Research

The studies summarized in Section 9.1 invite further investigation in the following areas:

9.2.1 Modeling of the Dynamics of the Thunderstorm

The model of the charge relaxation introduced in Chapter 5 produces 2-D axisymmetric simulations of the dynamics of the electrical structure of the thundercloud. The so-created 2-D structures are then projected onto a 3-D Cartesian space for use in the 3-D fractal model of the lightning discharge described in Chapter 2. This 3-D model allows us to validate *a posteriori* the correspondence between the nature of the events predicted to occur in the 2-D model (namely, cloud-to-ground or intracloud lightning, blue or gigantic jets) with the 3-D discharges produced by the fractal model of lightning. A 3-D model of charge relaxation in the conducting atmosphere would allow to implement the 3-D fractal model of lightning directly into the simulation of the thundercloud dynamics. Therefore, the criteria that we currently use for establishing whether an intracloud lightning develops into a gigantic jet or whether a classic cloud-to-ground discharge remains trapped into the cloud to produce a low intracloud discharge (see Figure 4.4) would no longer be necessary. These criteria are based on the local charge imbalances between the

charge layers and also checked *a posteriori*. They would be replaced by actual discharges produced by the 3-D fractal model which can provide the exact location of the charge removal, and therefore suppresses the assumption of a uniform charge reduction in the charge layers to model the bulk effect of a discharge on the electrical structure of the thundercloud.

9.2.2 Modeling of the Streamer-to-Spark Transition

The model of the streamer-to-spark transition introduced in Chapter 7 couples a fully 1-D gas dynamics model to a 0-D kinetics scheme. To calculate the electronic and ionic Joule energies on one hand, and the energy transfer from the vibrational energy levels of nitrogen to the translational energy of the gas on the other hand, we need to derive the radial distribution of the densities of electron and atomic oxygen, respectively. The use of a 0-D chemistry model permits the calculations of these densities on the axis of the streamer channel. Thus, in the model described in Chapter 7, the on-axis value of the density of atomic oxygen is used for the estimation of the energy transfer through vibrational–translation relaxation, and a Gaussian radial distribution in the case of electron density is assumed to calculate the electronic and ionic Joule energies. The development of a 1-D chemistry model would permit direct implementation of the plasma chemistry in the current 1-D model of gas dynamics. It would also make the previous approximations unnecessary and would eventually allow us a more detailed investigation of the effects of additional mechanisms, such as diffusion of the species, on the streamer-to-spark transition time.

Appendix **A**

Flowchart Representations of the Numerical Models

In this appendix, we represent the fractal model of lightning discharge, the model of Maxwellian charge relaxation, and the model of streamer-to-spark transition, developed in Chapters 2, 5, and 7, respectively, in the form of flowchart diagrams (Figures A.1, A.2, and A.3).

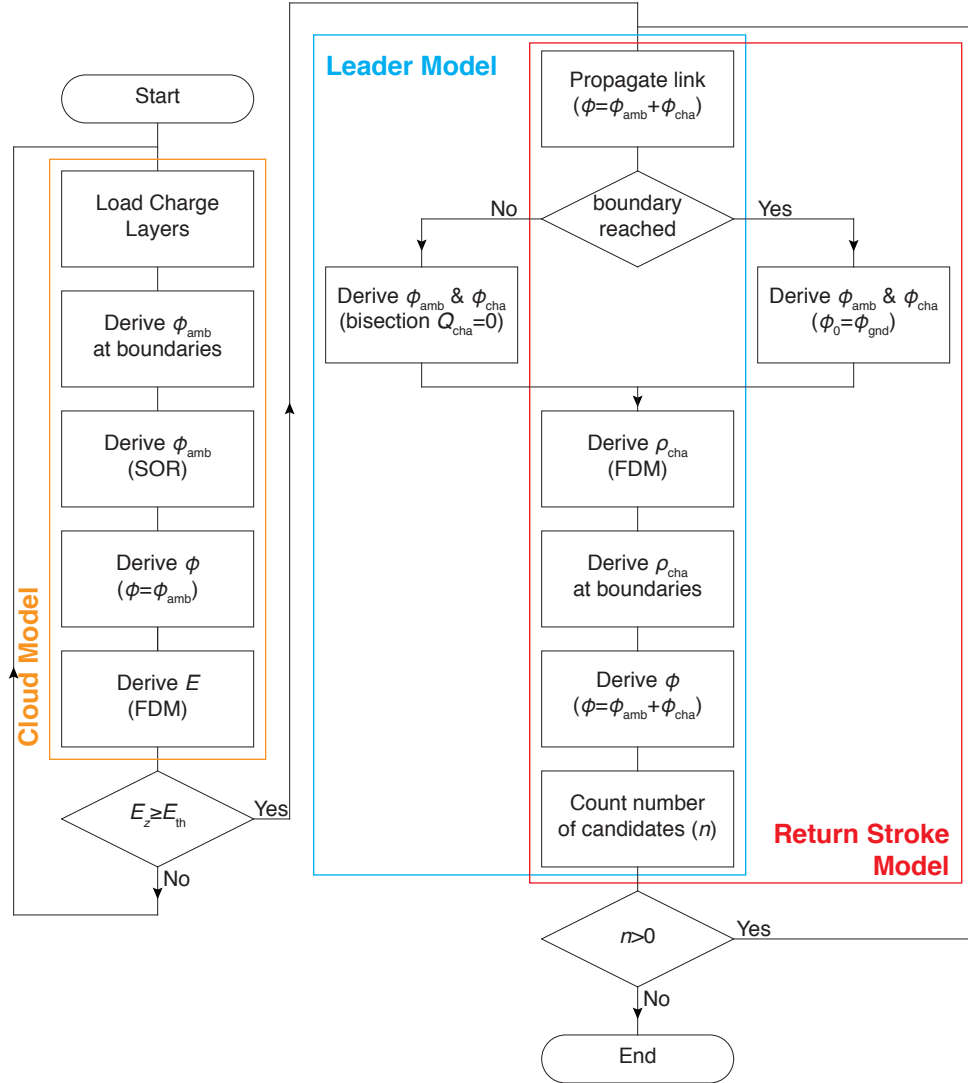


Figure A.1. Algorithm for development of the discharge trees [Riousset *et al.*, 2007a, and Chapter 2 of this document](based on hypotheses by Kasemir [1960] and Niemeyer *et al.* [1984]).

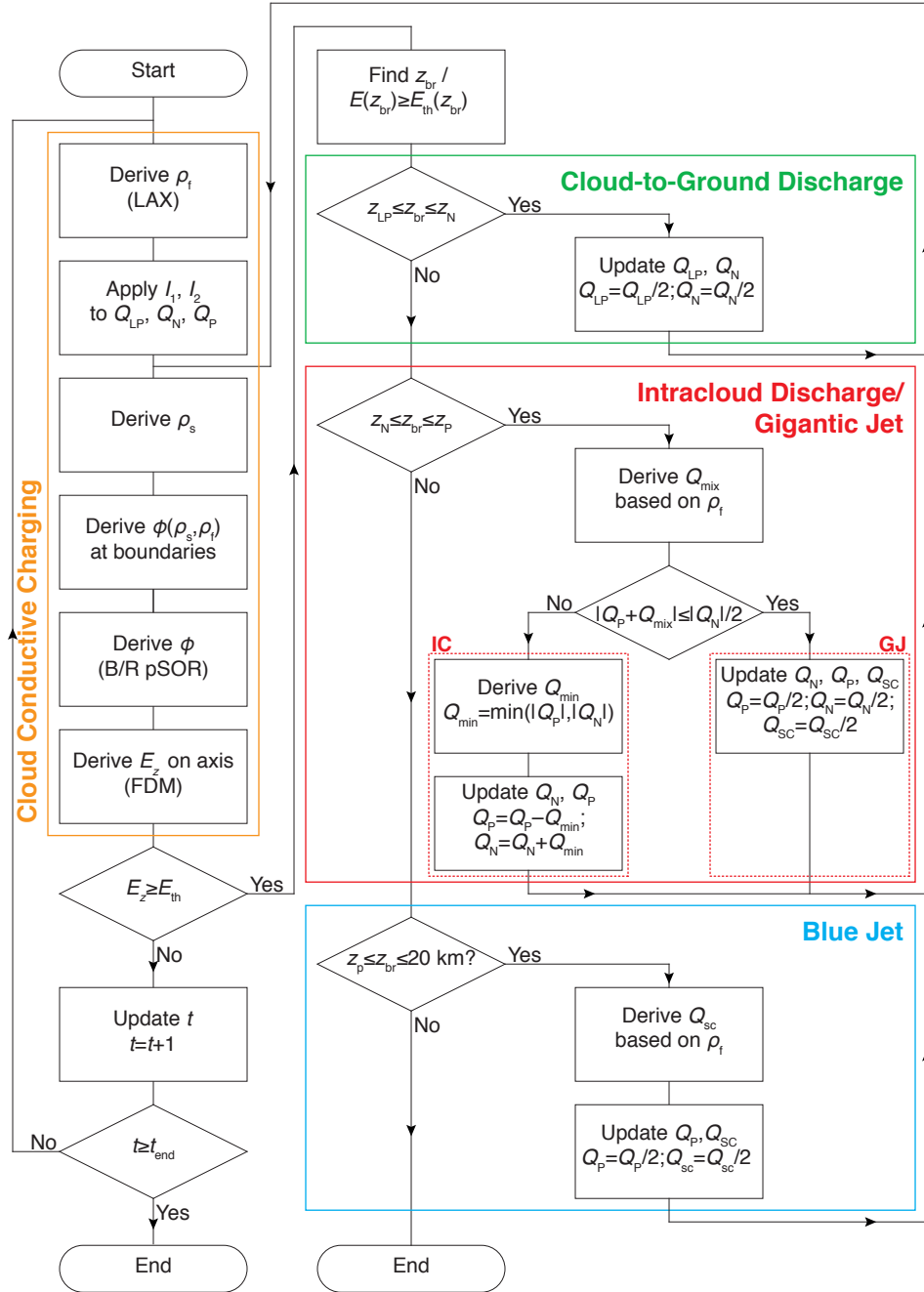


Figure A.2. Flowchart of the model of Maxwellian relaxation of the atmosphere. The charge reduction is based on [Krehbiel *et al.*, 2004, 2008].

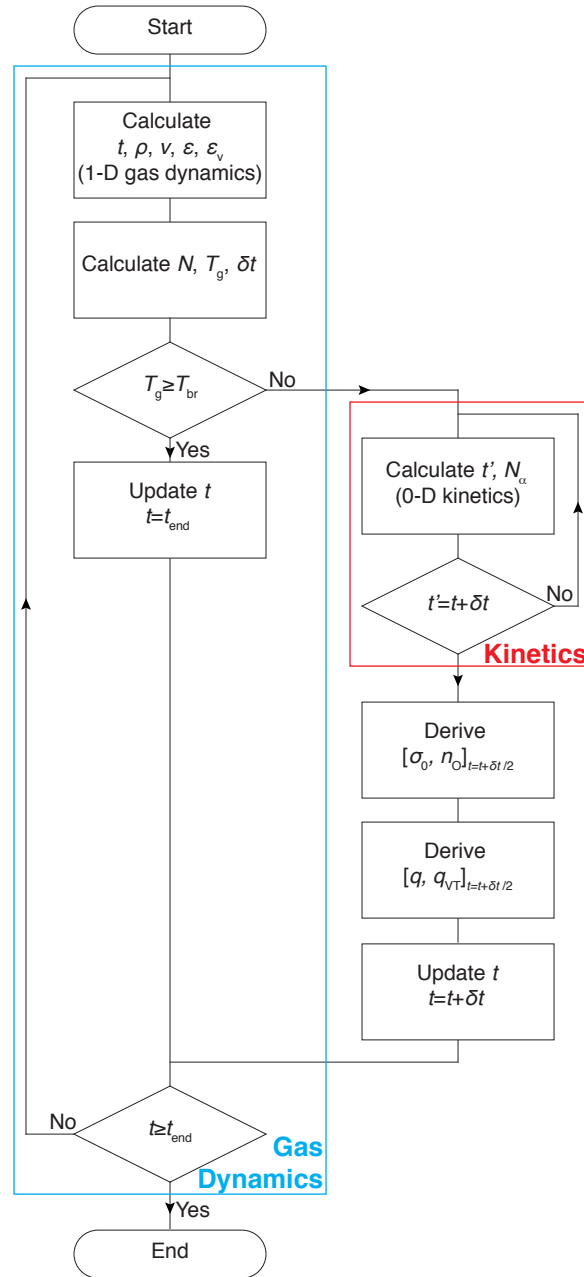


Figure A.3. Flowchart of the model of streamer-to-spark transition.

Supplementary Information for the Unified Theory of Lightning and Jet Discharges

The material presented in this appendix has been published as Supplementary Information in [Krehbiel *et al.*, 2008].

B.1 Lightning mapping and radar observations

The lightning observations of Figure 4.1a and 4.3a were obtained at Langmuir Laboratory using the New Mexico Tech Lightning Mapping Array (LMA) [Rison *et al.*, 1999]. The arrival times of impulsive radiation events in the 60–66 MHz VHF band were measured at six or more ground-based stations and used to determine the development of individual lightning discharges in three-dimensional space and time. Differences in the radiation and propagation characteristics of negative and positive breakdown were used to determine the polarity of the lightning channels (Figure 4.2a–d and Figure 4.3a) [Rison *et al.*, 1999] and to infer the charge structure of an example storm (Figure 1a) [Coleman *et al.*, 2003; Rust *et al.*, 2005; Marshall *et al.*, 2005]. Vertical radar scans from the NCAR S-Pol (10 cm) radar and New Mexico Tech (3 cm) dual-polarization radar provided the structure of the parent storm (Figures 4.2a and 4.3a, respectively).

B.2 Electrodynamic Model

Here we briefly discuss the model developed by *Krehbiel et al.* [2004]. The electrodynamic model (further detailed in Supplementary Information of [*Krehbiel et al.*, 2008]) uses the lightning polarity data of Figure 1.2a as input to estimate the location and extent of the storm charge regions. It represents the charge structure as a vertical sequence of axially aligned, uniformly charged cylindrical disks (Figure 1.2b), for which the electric field and potential profiles are calculated along the axis. The storm charging currents are represented by two current sources, I_1 between the mid-level negative and upper positive storm charges, and I_2 between the negative and lower positive charges, whose values are determined by running the model in time and matching the average flashing rates of intracloud (IC) and cloud-to-ground (CG) discharges to the observed flashing rates. An above-cloud, ohmic screening current I_{sc} is calculated by the model to simulate the formation of a screening charge at the upper cloud boundary. Lightning is assumed to occur when the on-axis electric field exceeds a specified altitude-dependent electric field threshold. Depending on the initiation location, intracloud, cloud-to-ground, or upward jet discharges occur and the charge content of the appropriate layers is decreased accordingly. The results reveal the role of the screening charge and mixing currents in the occurrence of upward discharges (see Chapter 4 and Supplementary Information in [*Krehbiel et al.*, 2008]).

B.3 Jets in Normal and Inverted-Polarity Thunderclouds

We have classified upward discharges into two basic categories or types: ‘blue’ jets (BJs) and ‘gigantic’ jets (GJs). Heretofore, the two types have been distinguished primarily in terms of their maximum altitudes, and possibly their polarities, and blue jets (including blue starters) developing up to lower altitudes than gigantic jets, and appearing to transport positive charge upward, while gigantic jets appearing to transport negative charge upward. If it is assumed that the two types are produced by normally electrified storms, as the observational information has indicated, then the present study indicates that the distinguishing characteristic

between them is where they are initiated relative to the storm charges. The resulting breakdown scenarios give rise to positive blue jets (+BJs) and negative gigantic jets (−GJs).

In addition to the above, the observations of Fig. 2 show that negative upward jets can be produced by inverted polarity storms. We identify this as a negative blue jet (−BJ) based on where it is initiated relative to the storm charges. By extension, the inverted-storm analog of a −GJ would be a +GJ, with each polarity of GJ having as its source the main or mid-level charge of the storm. The four possible types of upward discharges are summarized in Figure B.1.

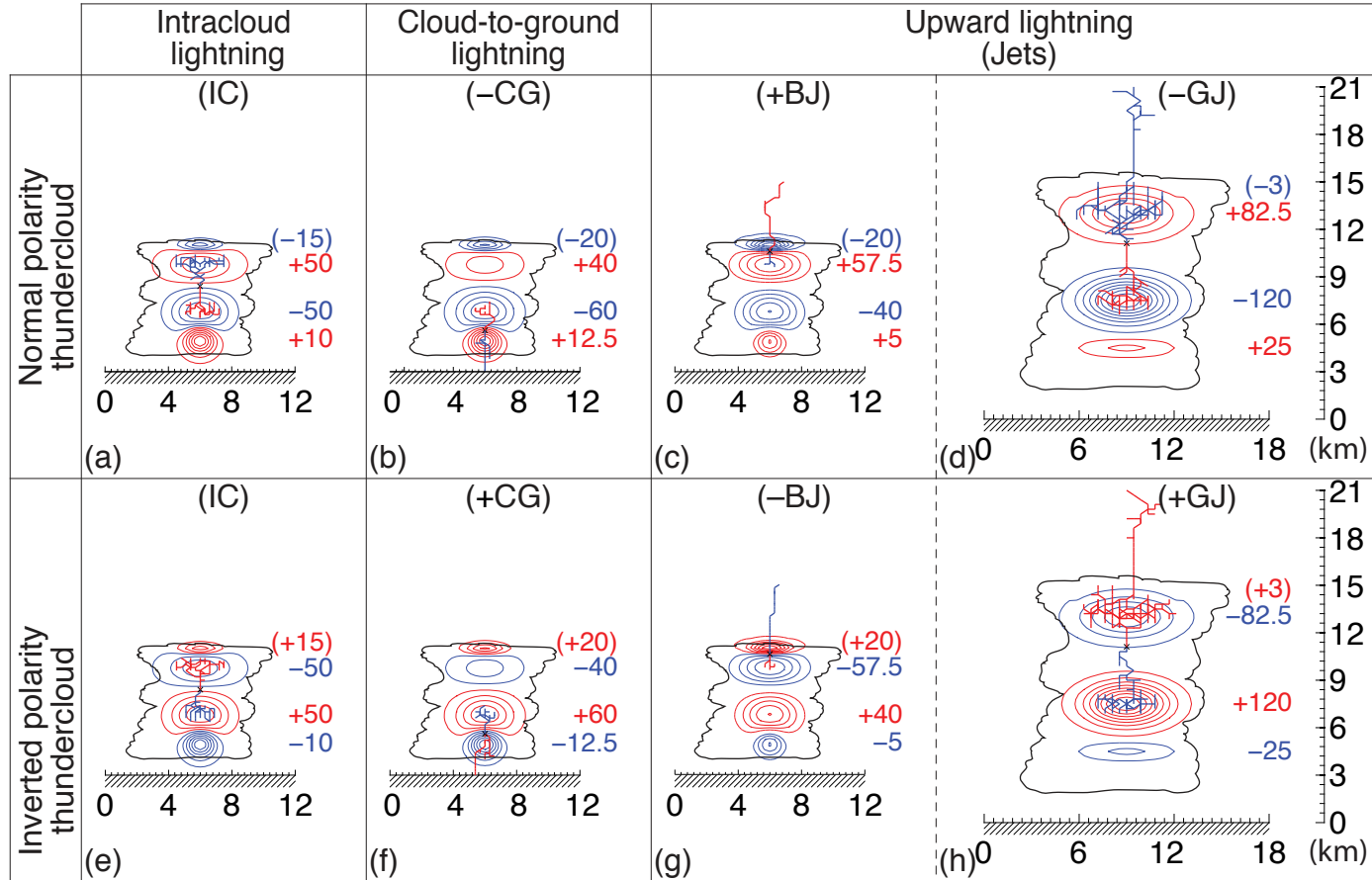


Figure B.1. Illustrative lightning simulations for normal- and inverted-polarity storms, showing the four possible types of upward discharges, classified by initiation mechanism (blue jet and gigantic jet) and upward polarity (+ and -). Blue and red contours and numbers indicate negative and positive charge regions and charge amounts (in C), respectively, each assumed to have a Gaussian spatial distribution. Also shown for reference are the common forms of IC and CG flashes in normal and inverted storms. Blue jets will tend to be initiated by a precursor discharge (either CG or IC) that causes a charge imbalance in the storm [Krehbiel *et al.*, 2008, Supplementary Information].

Supplementary Information for the Maxwellian Charge Relaxation Model

C.1 Necessity of Charge Compensation in a Con- ducting Medium

The model proposed in Chapter 5 is based on the Poisson and continuity equations to simulate the Maxwellian charge relaxation in the conducting atmosphere. In this section, we show how the source charges ρ_s dissipate if no compensation is accounted for. The following derivations are based on [Pasko *et al.*, 1997].

We start with the following system of equations:

$$\left\{ \begin{array}{lcl} \frac{\partial \rho_f + \rho_s}{\partial t} + \nabla \cdot (\vec{J}_c + \vec{J}_s) & = & 0 \\ \nabla^2 \phi & = & -\frac{\rho_f + \rho_s}{\varepsilon_0} \end{array} \right. \quad (\text{C.1})$$

where \vec{J}_s is the source current, $\vec{J}_c = -\sigma \nabla \phi$ the conduction current, and ϕ the electric potential. If we recall that:

$$\frac{\partial \rho_s}{\partial t} + \nabla \cdot \vec{J}_s = 0 \quad (\text{C.2})$$

then,

$$\left\{ \begin{array}{l} \frac{\partial \rho_f}{\partial t} - \nabla \sigma \cdot \nabla \phi + \sigma \frac{\rho_f + \rho_s}{\varepsilon_0} = 0 \\ \nabla^2 \phi = -\frac{\rho_f + \rho_s}{\varepsilon_0} \end{array} \right. \quad (\text{C.3})$$

For testing purposes, we assume $\nabla \sigma = 0$, and then the system becomes:

$$\left\{ \begin{array}{l} \frac{\partial \rho_f}{\partial t} + \sigma \frac{\rho_f + \rho_s}{\varepsilon_0} = 0 \\ \nabla^2 \phi = -\frac{\rho_f + \rho_s}{\varepsilon_0} \end{array} \right. \quad (\text{C.4})$$

If ρ_s is constant ($\rho_s(t) = \rho_s(0)$), then $\frac{\partial \rho_f}{\partial t} + \sigma \frac{\rho_f + \rho_s}{\varepsilon_0} = 0$ can be rewritten as:

$$\frac{\partial \rho_f + \rho_s}{\partial t} + \sigma \frac{\rho_f + \rho_s}{\varepsilon_0} = 0 \quad (\text{C.5})$$

and finally the total charge density $\rho_f + \rho_s$ decays as:

$$(\rho_f + \rho_s)(t) = \rho_s(0) e^{-t/\tau_f} \quad \text{where } \tau_f = \frac{\varepsilon_0}{\sigma} \quad (\text{C.6})$$

To maintain the total charge $\rho_s + \rho_f$ equal to the charge brought by the source current \vec{J}_s , we introduce a complementary source current \vec{J}'_s to compensate the dissipation of the source charge $-\partial \rho_s / \partial t$, then \vec{J}_s and \vec{J}'_s are related by the following relationship:

$$-\frac{\partial \rho_s}{\partial t} = \nabla \cdot \vec{J}'_s = \nabla \cdot \vec{J}_s + \frac{\rho_s \sigma}{\varepsilon_0} \quad (\text{C.7})$$

and charge conservation for the source charges is expressed as:

$$\nabla \cdot \vec{J}_s = -\frac{\partial \rho_s}{\partial t} - \frac{\rho_s \sigma}{\varepsilon_0} \quad (\text{C.8})$$

then, if we plug (C.8) into (C.1), (C.3) becomes:

$$\left\{ \begin{array}{l} \frac{\partial \rho_f}{\partial t} - \nabla \sigma \cdot \nabla \phi + \sigma \frac{\rho_f}{\varepsilon_0} = 0 \\ \nabla^2 \phi = -\frac{\rho_f + \rho_s}{\varepsilon_0} \end{array} \right. \quad (\text{C.9})$$

As previously, if we assume for testing purposes that $\nabla\sigma = 0$, then, with $\rho_f(0)=0$ we have:

$$\frac{\partial\rho_f}{\partial t} + \sigma\frac{\rho_f}{\varepsilon_0} = 0 \quad (\text{C.10})$$

$$\Rightarrow \rho_f(t) = \rho_f(0)e^{-\frac{t}{\tau_f}} = 0 \quad (\text{C.11})$$

If we additionally assume a constant source charge density ($\rho_s(t)=\rho_s(0)$), then (C.11) yields:

$$(\rho_s + \rho_f)(t) = \rho_s(0) \quad (\text{C.12})$$

and therefore the total charge density $\rho_f + \rho_s$ is maintained constant.

C.2 Performance of the Charge Relaxation Model: Comparison with the Results of *Holzer and Saxon* [1952]

In this section, we provide a demonstration of the performance of the Maxwellian charge relaxation model developed in Chapter 5. We simulate the electric field created by a sphere of radius a , uniformly charged with the charge Q , and enclosed in a sphere of radius b and conductivity σ' , which is placed in an infinite medium of conductivity σ (see Figure C.1). We compare our numerical results with the analytical solution to this problem provided by *Holzer and Saxon* [1952] and reproduced hereafter.

For the sake of clarity, we convert the expressions originally given in [*Holzer and Saxon*, 1952] in CGS units to SI units used in all the material presented in this dissertation. We start with the Maxwell–Gauss equation:

$$\nabla \cdot \vec{D} = \rho \quad (\text{C.13})$$

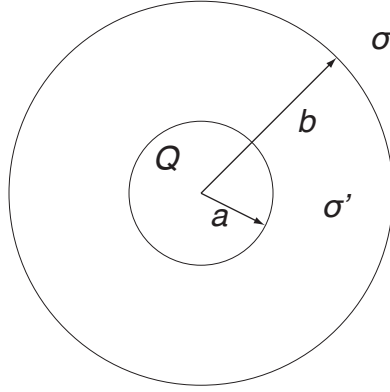


Figure C.1. A spherical charge Q of radius a placed in the center of a sphere of conductivity σ' and radius b embedded in a medium of conductivity σ .

or equivalently in integral form:

$$\oiint_s \vec{D} \cdot d\vec{S} = Q \quad (\text{C.14})$$

In the remainder of this section, we denote r as the radial coordinate in the cylindrical coordinate system and \mathfrak{r} as the radial coordinate in the spherical coordinate system. For obvious reasons of symmetry, we have $\vec{D} = D_{\mathfrak{r}} \hat{\mathfrak{r}}$, and consequently

$$D_{\mathfrak{r}} = \frac{Q}{4\pi\mathfrak{r}^2} \quad \text{at } \mathfrak{r} \geq a \quad (\text{C.15})$$

If we assume that the medium has a permittivity equal to the permittivity of free space then, $D_{\mathfrak{r}} = \varepsilon_0 E_{\mathfrak{r}}$ and because $\vec{J} = \sigma' \vec{E}$, in the medium of conductivity σ' we have:

$$J_{\mathfrak{r}} = \sigma' \frac{Q}{4\pi\varepsilon_0 a^2} \quad \text{at } \mathfrak{r} = a \quad (\text{C.16})$$

In steady state, the continuity equation can be simplified as follows:

$$\frac{\partial \overset{0}{\rho}}{\partial t} + \nabla \cdot \vec{J} = 0 \Rightarrow \frac{\partial \mathfrak{r}^2 J_{\mathfrak{r}}}{\partial \mathfrak{r}^2} = 0 \quad (\text{C.17})$$

and therefore:

$$J_{\mathfrak{r}} = \begin{cases} \frac{C_1}{\mathfrak{r}^2} & \text{for } a \leq \mathfrak{r} \leq b \\ \frac{C_2}{\mathfrak{r}^2} & \text{for } \mathfrak{r} \geq b \end{cases} \quad C_1, C_2 \text{ are two constants} \quad (\text{C.18})$$

Recall that because $J_{\mathfrak{r}}(a) = \sigma' \frac{Q}{4\pi\epsilon_0 a^2}$, then $C_1 = \sigma' \frac{Q}{4\pi\epsilon_0}$. Subsequently, $J_{\mathfrak{r}}(b) = \sigma' \frac{Q}{4\pi\epsilon_0 b^2}$ and $C_2 = \sigma' \frac{Q}{4\pi\epsilon_0}$ as well. Consequently, we have:

$$J_{\mathfrak{r}} = \sigma' \frac{Q}{4\pi\epsilon_0 \mathfrak{r}^2} \quad \text{for } \mathfrak{r} \geq b \geq a \quad (\text{C.19})$$

This results yields the following expression in the media of conductivity σ for the electric field $E_{\mathfrak{r}} = J_{\mathfrak{r}}/\sigma$:

$$E_{\mathfrak{r}} = \frac{\sigma'}{\sigma} \frac{Q}{4\pi\epsilon_0 \mathfrak{r}^2} \quad \text{for } \mathfrak{r} \geq b \quad (\text{C.20})$$

Finally, the total current flowing through the boundary $\mathfrak{r}=b$ can be expressed as:

$$\begin{aligned} I(b) &= \iint_{\mathfrak{s}} \vec{J} \cdot d\vec{S} \\ &= \int_{\theta=0}^{\pi} \int_{\phi=0}^{2\pi} \vec{J} \cdot \hat{\mathfrak{r}} b^2 \sin(\theta) d\phi d\theta \\ &= 4\pi \sigma \overbrace{\frac{\sigma'}{\sigma} \frac{Q}{4\pi\epsilon_0 b^2}}^{E_{\mathfrak{r}}(b)} b^2 \\ &\Rightarrow I(b) = \frac{\sigma'}{\sigma} \left(Q \frac{\sigma}{\epsilon_0} \right) \end{aligned} \quad (\text{C.21})$$

Thus, the field intensity and current flow in the medium of conductivity σ can be

expressed as:

$$\left\{ \begin{array}{l} E_{\mathfrak{r}} = \frac{\left(\frac{\sigma'}{\sigma}Q\right)}{4\pi\epsilon_0\mathfrak{r}^2} \quad \text{for } \mathfrak{r} \geq b \\ I(b) = \left(\frac{\sigma'}{\sigma}Q\right) \frac{\sigma}{\epsilon_0} \end{array} \right. \quad (\text{C.22})$$

to be compared with the same values if the media of conductivity σ' were removed:

$$\left\{ \begin{array}{l} E_{\mathfrak{r}} = \frac{Q}{4\pi\epsilon_0\mathfrak{r}^2} \quad \text{for } \mathfrak{r} \geq b \\ I(b) = Q \frac{\sigma}{\epsilon_0} \end{array} \right. \quad (\text{C.23})$$

The comparison of (C.22) and (C.23) confirms the results stated by *Holzer and Saxon* [1952] that “both the field intensity and current flow in the medium of conductivity σ are the same as if the medium of conductivity σ' were removed and the charge Q replaced by $Q \frac{\sigma'}{\sigma}$.”

The last part of this section is devoted to the comparison of the numerical and analytical solutions of the problem. To avoid numerical instabilities, we introduce a smooth transition between the two media of conductivity σ and σ' , which is achieved in a way similar to that of Section 5.2:

$$\sigma(r, z) = \sigma' + (\sigma - \sigma') \underbrace{\frac{1 + \tanh\left(\frac{\mathfrak{r} - b}{\alpha}\right)}{2}}_{\text{transition at } \mathfrak{r}=b} \quad \mathfrak{r} = \sqrt{r^2 + (z - h)^2} \quad (\text{C.24})$$

where h is the position of the sphere along the z -axis and the parameter α determines the thickness of the transition region between the two media of conductivities σ and σ' .

In Figure C.2, we use $Q=200$ C, $a=2$ km, $b=3$ km, $\alpha=150$ m, $\sigma=5 \times 10^{-14}$ S/m, and $\sigma'=0.5 \times 10^{-14}$ S/m. The sphere is placed at the center of an axisymmetric domain with dimension $L_r \times L_z = 9.7$ km \times 19.5 km, discretized using 98 and 196 points in the r - and z -directions, respectively. Panel (a) shows the total charge density in the simulation domain $\rho_t = \rho_s + \rho_f$, where ρ_s and ρ_f are the source and

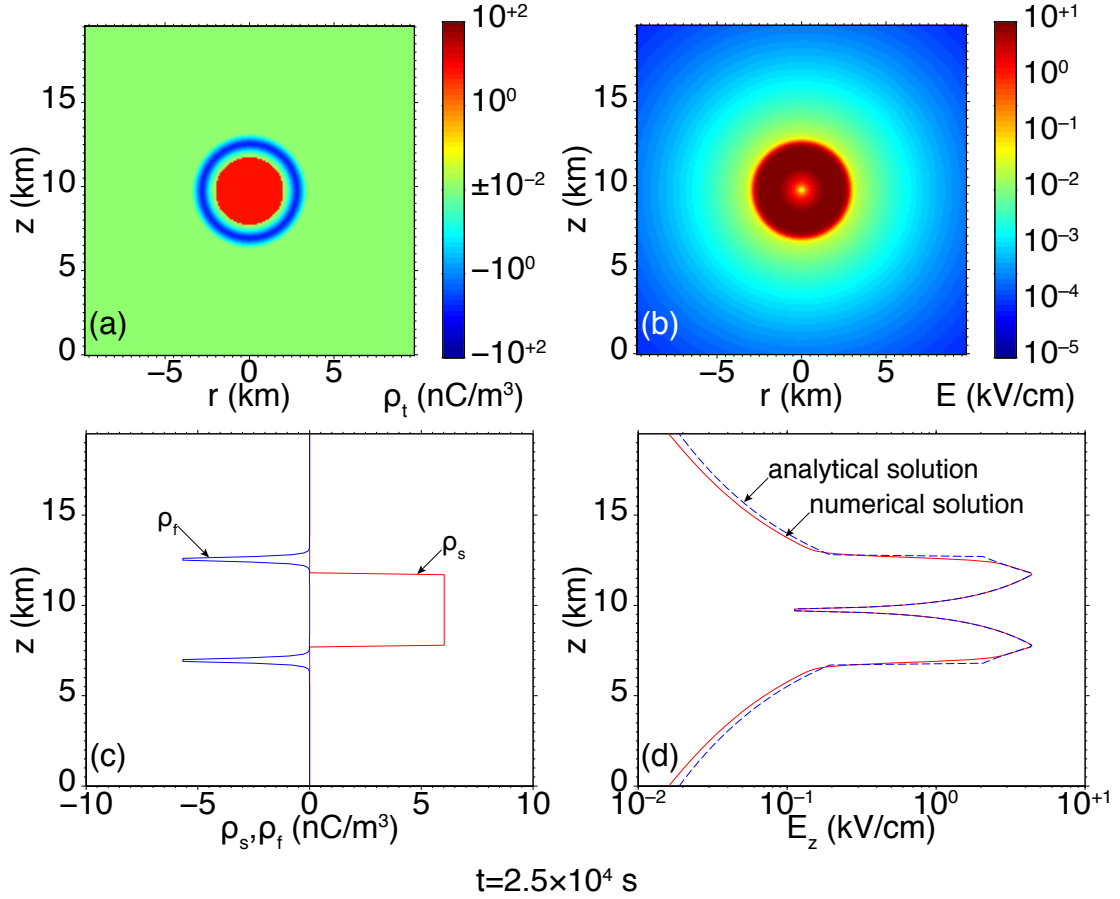


Figure C.2. Comparison of numerical and analytical solutions to the problem of Figure C.1 at $t = 2.5 \times 10^4$ s. (a) Total charge density $\rho_t = \rho_s + \rho_f$. (b) Amplitude of the electric field $E = \sqrt{E_r^2 + E_z^2}$, where E_r and E_z are the horizontal and vertical component of the electric field. (c) Source and free induced charge densities (ρ_s and ρ_f , respectively) at $r = 0$ km. (d) Numerical (solid line) and analytical (broken line) solutions for the amplitude of the vertical component of the electric field E_z at $r = 0$ km.

free induced charge densities, respectively. Panel (b) displays the amplitude of the electric field in the domain. Panel (c) compares the source and free induced charge density along the axis $r = 0$ km. Panel (d) compares the numerical and analytical solutions for the electric field along the axis $r = 0$ km.

From Figure C.2, it appears that the analytical and numerical solutions are in excellent agreement. We verified that the small error is numerical, and decreases when the resolution is improved. In addition, Figure C.2a shows the formation of screening charges at the boundary between the domains of conductivity σ and σ' .

A similar result discussed in Chapter 5 leads to the same conclusion. This simple case study allowed us to verify the validity of our model when applied to problems, for which an analytical solution is achievable.

References

- Achat, S., Y. Teisseyre, and E. Marode (1992), The scaling of the streamer-to-arc transition in a positive point-to-plane gap with pressure, *J. Phys. D: Appl. Phys.*, *25*(4), 661–668.
- Agoris, D. P., V. P. Charalambakos, E. Pyrgloti, and S. Grzybowski (2004), A computational approach on the study of Franklin rod height impact on striking distance using a stochastic models, *J. Electrostat.*, *60*(2–4), 175–181, doi:10.1016/j.elstat.2004.01.020.
- Aleksandrov, N., E. Bazelyan, N. Dyatko, and I. Kochetov (1998), Streamer breakdown of long air gaps, *Plasma Phys. Rep.*, *24*(7), 541–555.
- Aleksandrov, N. L., and E. M. Bazelyan (1999), Ionization processes in spark discharge plasmas, *Plasma Sources Sci. Technol.*, *8*, 285–294.
- Aleksandrov, N. L., A. E. Bazelyan, E. M. Bazelyan, and I. V. Kochetov (1995), Modeling of long streamers in atmospheric-pressure air, *Plasma Phys. Rep.*, *21*(60), 57–75.
- Aleksandrov, N. L., E. M. Bazelyan, I. V. Kochetov, and N. A. Dyatko (1997), The ionization kinetics and electric field in the leader channel in long air gaps, *J. Phys. D: Appl. Phys.*, *30*(11), 1616–1624, doi:10.1088/0022-3727/30/11/011.
- Aleksandrov, N. L., E. M. Bazelyan, and A. M. Konchakov (2001), Plasma parameters in the channel of a long leader in air, *Plasma Phys. Rep.*, *27*(10), 875–885.
- Altaratz, O., T. Reisin, and Z. Levin (2005), Simulation of the electrification of winter thunderclouds using the three-dimensional regional atmospheric modeling system (RAMS) model: Single cloud simulations, *J. Geophys. Res.*, *110*(D20205), doi:10.1029/2004JD005616.
- Barthe, C., G. Molinié, and J.-P. Pinty (2005), Description and first results of an explicit electrical scheme in a 3D cloud resolving models, *Atmos. Res.*, *76*(1-4), 95–113, doi:10.1016/j.atmosres.2004.11.021.

- Bastien, F., and E. Marode (1985), Breakdown simulation of electronegative gases in non-uniform field, *J. Appl. Phys.*, *18*(3), 377–393.
- Bazelyan, E. M., and Y. P. Raizer (1998), *Spark Discharge*, 294 pp., Chemical Rubber Company Press, New York, NY.
- Bazelyan, E. M., and Y. P. Raizer (2000), *Lightning Physics and Lightning Protection*, 400 pp., IoP Publishing Ltd, Bristol, UK and Philadelphia, PA.
- Bazelyan, E. M., Y. P. Raizer, and N. L. Aleksandrov (2007), The effect of reduced air density on streamer-to-leader transition and on properties of long positive leader, *J. Phys. D: Appl. Phys.*, *40*(14), 4133.
- Behnke, S. A., R. J. Thomas, P. R. Krehbiel, and W. Rison (2005), Initial leader velocities during intracloud lightning: Possible evidence for a runaway breakdown effect, *J. Geophys. Res.*, *110*(D12), D10207, doi:10.1029/2004JD005312.
- Benilov, M., and G. Naidis (2005), Modelling of discharges in a flow of preheated air, *Plasma Sources Sci. Technol.*, *14*(1), 129–133, doi:10.1088/0963-0252/14/1/015.
- Benilov, M. S., and G. V. Naidis (2003), Modelling of low-current discharges in atmospheric-pressure air taking account of non-equilibrium effects, *J. Phys. D: Appl. Phys.*, *36*(15), 1834–1841, doi:10.1088/0022-3727/36/15/314.
- Boeck, W. L., O. H. Vaughan, R. J. Blakeslee, B. Vonnegut, M. Brook, and J. McKune (1995), Observations of lightning in the stratosphere, *J. Geophys. Res.*, *100*, 1465.
- Brown, K. A., P. R. Krehbiel, C. B. Moore, and G. N. Sargent (1971), Electrical screening layers around charged clouds, *J. Geophys. Res.*, *76*(12), 2825–2835.
- Brown, R. A. (1991), *Fluid mechanics of the atmosphere, International geophysics series*, vol. 47, 2nd ed., 489 pp., Academic Press, San Diego, CA.
- Černák, M., E. M. van Veldhuizen, I. Morva, and W. R. Rutgers (1995), Effect of cathode surface properties on glow-to-arc transition in a short positive corona gap in ambient air, *J. Phys. D: Appl. Phys.*, *28*(6), 1126–1132.
- Chen, A. B., C.-L. Kuo, Y.-J. Lee, H.-T. Su, R.-R. Hsu, J.-L. Chern, H. U. Frey, S. B. Mende, Y. Takahashi, H. Fukunishi, Y.-S. Chang, T.-Y. Liu, and L.-C. Lee (2008a), Global distributions and occurrence rates of transient luminous events, *J. Geophys. Res.*, *113*(A8), doi:10.1029/2008JA013101.
- Chen, A. B., L. Tsai, L. Lee, J. Chou, H. Su, R. Hsu, C. Wu, P. Lin, S. B. Mende, H. U. Frey, Y. Takahashi, and L. Lee (2008b), Meteorological aspects of elves and jets, *Eos Trans. AGU*, *89*(53), Fall Meet. Suppl., Abstract AE13A-0303.

- Coleman, L. M., T. C. Marshall, M. Stolzenburg, T. Hamlin, P. R. Krehbiel, W. Rison, and R. J. Thomas (2003), Effects of charge and electrostatic potential on lightning propagation, *J. Geophys. Res.*, *108*(D9), 4298, doi:10.1029/2002JD002718.
- Comtois, D., H. Pépin, F. Vidal, F. A. Rizk, C. Y. Chien, T. W. Johnston, J. C. Kieffer, B. La Fontaine, C. Potvin, P. Couture, H. P. Mercure, A. Bondiou-Clergerie, P. Lalande, and I. Gallimberti (2003), Triggering and guiding of an upward positive leader from a ground rod with an ultrashort laser pulse—II: Modeling, *IEEE Trans. Plasma Sci.*, *31*(3), 387–395, doi:10.1109/TPS.2003.811649.
- Courant, R., K. Friedrichs, and H. Lewy (1928), Partial differential equations of mathematical physics, *Mathematische Annalen*, *100*, 32–74.
- Cummer, S. A., J. B. Li, F. Han, G. P. Lu, N. Jaugey, W. A. Lyons, and T. E. Nelson (2009), Quantification of the troposphere-to-ionosphere charge transfer in a gigantic jet, *Nature Geoscience*, *2*(9), 617–620, doi:10.1038/ngeo607.
- Dwyer, J. R. (2003), A fundamental limit on electric fields in air, *Geophys. Res. Lett.*, *30*(20), 2055, doi:10.1029/2003GL017781.
- Dwyer, J. R., H. K. Rassoul, M. Al-Dayeh, L. Caraway, A. Chrest, B. Wright, E. Kozak, J. Jerauld, M. A. Uman, V. A. Rakov, D. M. Jordan, and K. J. Rambo (2005), X-ray bursts associated with leader steps in cloud-to-ground lightning, *Geophys. Res. Lett.*, *32*, L01803, doi:10.1029/2004GL021782.
- Femia, N., L. Niemeyer, and V. Tucci (1993), Fractal characteristics of electrical discharges: Experiments and simulations, *J. Phys. D: Appl. Phys.*, *26*(4), 619–627, doi:10.1088/0022-3727/26/4/014.
- Flitti, A., and S. Pancheshnyi (2009), Gas heating in fast pulsed discharges in N₂–O₂ mixtures, *Eur. Phys. J. Appl. Phys.*, *45*(2), 21,001, doi:10.1051/epjap/2009011.
- Gallimberti, I. (1979), The mechanism of the long spark formation, *J. Phys. Coll.*, *40*(C7), 193–250.
- Gallimberti, I., G. Bacchiega, A. Bondiou-Clergerie, and P. Lalande (2002), Fundamental processes in long air gap discharges, *C. R. Physique*, *3*(10), 1335–1359, doi:10.1016/S1631-0705(02)01414-7.
- Gilmore, F. R. (1965), Potential energy curves for N₂, NO, O₂ and corresponding ions, *J. Quant. Spectrosc. Radiat. Transfer*, *5*(2), 369–389, doi:10.1016/0022-4073(65)90072-5.

- Greifinger, C., and P. Greifinger (1976), Transient ULF electric and magnetic fields following a lightning discharges, *J. Geophys. Res.*, *81*(13), 2237–2247.
- Gurevich, A. V., and K. P. Zybin (2001), Runaway breakdown and electric discharges in thunderstorms, *Phys. Uspekhi*, *44*(11), 1119–1140.
- Gurevich, A. V., G. M. Milikh, and R. A. Roussel-Dupré (1992), Runaway electron mechanism of air breakdown and preconditioning during a thunderstorm, *Phys. Lett. A.*, *165*(5–6), 463–468, doi:10.1016/0375-9601(92)90348-P.
- Hagelaar, G. J. M., and L. C. Pitchford (2005), Solving the Boltzmann equation to obtain electron transport coefficients and rate coefficients for fluid models, *Plasma Sources Sci. Technol.*, *14*(4), 722–733.
- Hager, W. W., J. S. Nisbet, J. R. Kasha, and W.-C. Shann (1989), Simulation of electric fields within a thundercloud, *J. Atmos. Sci.*, *46*(23), 3542–3558.
- Harlow, H. B., and J. P. Riehl (1991), Recovery of atomic oxygen density and temperature of the thermosphere by numerical inversion of simulated infrared radiance data with Gaussian noise, *Planet. Space Sci.*, *39*(8), 1155–1162, doi:10.1016/0032-0633(91)90167-9.
- Heavner, M. J., D. D. Sentman, D. R. Moudry, and E. M. Wescott (2000), Sprites, blue jets, and elves: Optical evidence of energy transport across the stratopause, in *Atmospheric Science Across the Stratopause, Geophysical Monograph Series*, vol. 123, edited by D. E. Siskind, S. D. Eckermann, and M. E. Summers, pp. 69–82, American Geophysical Union, Washington DC.
- Helsdon, J. H., and R. D. Farley (1987), A numerical modeling study of a Montana thunderstorm: 2. Model results versus observations involving electrical aspects, *J. Geophys. Res.*, *92*, 5661–5675, doi:10.1029/JD092iD05p05661.
- Helsdon, J. H., and K. Poeppel (2005), A 3D non grid-point-dependent lightning scheme, *Eos Trans. AGU*, *86*(52), Fall Meet. Suppl., Abstract AE41A-0147.
- Helsdon, J. H., Jr., G. Wu, and R. D. Farley (1992), An intracloud lightning parameterization scheme for a storm electrification model, *J. Geophys. Res.*, *97*(D5), 5865–5884.
- Helsdon, J. H., Jr., S. Gattaleeradapan, R. D. Farley, and C. C. Waits (2002), An examination of the convective charging hypothesis: Charge structure, electric fields, and Maxwell currents, *J. Geophys. Res.*, *107*(D22), 4630, doi:10.1029/2001JD001495.
- Hockney, R., and J. Eastwood (1981), *Computer Simulation Using Particles*, 540 pp., McGraw-Hill, New York, NY.

- Holton, J. R. (2004), *An Introduction to Dynamic Meteorology, International Geophysics*, vol. 88, 4th ed., 535 pp., Academic Press, New York, NY.
- Holzer, R., and D. Saxon (1952), Distribution of electrical conduction currents in the vicinity of thunderstorms, *J. Geophys. Res.*, *57*(2), 207–216.
- Kasemir, H. W. (1960), A contribution to the electrostatic theory of a lightning discharge, *J. Geophys. Res.*, *65*(7), 1873–1878.
- Kossyi, I. A., A. Y. Kostinsky, A. A. Matveyev, and V. P. Silakov (1992), Kinetic scheme of the non-equilibrium discharge in nitrogen-oxygen mixtures, *Plasma Sources Sci. Technol.*, *1*(3), 207–220.
- Krehbiel, P., W. Rison, R. Thomas, T. Marshall, M. Stolzenburg, W. Winn, and S. Hunyady (2004), Thunderstorm charge studies using a simple cylindrical charge model, electric field measurements, and lightning mapping observations, *Eos Trans. AGU*, *85*(47), Fall Meet. Suppl., Abstract AE23A-0843.
- Krehbiel, P. R. (1981), An analysis of the electric field change produced by lightning, Ph.D. thesis, University of Manchester Institute of Science and Technology, Manchester, UK.
- Krehbiel, P. R. (1986), The electrical structure of thunderstorms, in *The Earth's Electrical Environment*, pp. 90–113, National Academy Press, Washington, D.C.
- Krehbiel, P. R., R. Tennis, M. Brook, E. W. Holmes, and R. Comes (1984a), A comparative study of the initial sequence of lightning in a small Florida thunderstorm, in *Proc. VIIth Intn'l. Conf. Atmos. Elec., Albany, NY*, pp. 279–285.
- Krehbiel, P. R., M. Brook, S. Khanna-Gupta, C. Lennon, and R. Lhermitte (1984b), Some results concerning VHF lightning radiation from the real-time LDAR system at KSC, Florida, in *Proc. VIIth Intn'l. Conf. Atmos. Elec., Albany, NY*, pp. 388–393.
- Krehbiel, P. R., J. A. RiOUSset, V. P. Pasko, R. J. Thomas, W. Rison, and M. A. Stanley (2007a), Upward electrical discharges from thunderstorms, *Leiden Workshop, Poster Session*, Leiden, Netherlands, Oct. 8.
- Krehbiel, P. R., J. A. RiOUSset, V. P. Pasko, R. J. Thomas, W. Rison, and M. A. Stanley (2007b), Upward electrical discharges from thunderstorms, *Leiden Workshop, Presentation*, Leiden, Netherlands, Oct. 11.
- Krehbiel, P. R., J. A. RiOUSset, V. P. Pasko, R. J. Thomas, W. Rison, M. A. Stanley, and H. E. Edens (2007c), Upward electrical discharges from thunderstorms, *Eos Trans. AGU*, *88*(52), Fall Meet. Suppl., Abstract AE23A-0891.

- Krehbiel, P. R., J. A. RiOUSset, V. P. Pasko, R. J. Thomas, W. Rison, M. A. Stanley, and H. E. Edens (2008), Upward electrical discharges from thunderstorms, *Nature Geoscience*, *1*(4), 233–237, doi:10.1038/ngeo162.
- Krider, E. P., and J. A. Musser (1982), Maxwell currents under thunderstorms, *J. Geophys. Res.*, *87*(C13), 11,171–11,176.
- Kumer, J. (1977), Theory of CO₂ 4.3- μ m-aurora and related phenomena, *J. Geophys. Res.*, *82*(16), 2203–2209.
- Kuo, C. L., J. K. Chou, L. Y. Tsai, A. B. Chen, H. T. Su, R. R. Hsu, S. A. Cummer, H. U. Frey, S. B. Mende, Y. Takahashi, and L. C. Lee (2009), Discharge processes, electric field, and electron energy in ISUAL-recorded gigantic jets, *J. Geophys. Res.*, *114*(A4), doi:10.1029/2008JA013791.
- Kupershtokh, A. L., V. Charalambakos, D. Agoris, and D. I. Karpov (2001), Simulation of breakdown in air using cellular automata with streamer to leader transition, *J. Phys. D: Appl. Phys.*, *34*(6), 936–946, doi:10.1088/0022-3727/34/6/315.
- Lalande, P., A. Bondiou-Clergerie, G. Bacchiega, and I. Gallimberti (2002), Observations and modeling of lightning leaders, *C. R. Physique*, *3*(10), 1375–1392, doi:10.1016/S1631-0705(02)01413-5.
- Lang, T. J., L. J. Miller, M. Weisman, S. A. Rutledge, L. J. Barker III, V. N. Bringi, V. Chandrasekar, A. Detwiler, N. Doesken, J. Helsdon, C. Knight, P. Krehbiel, W. A. Lyons, D. MacGorman, E. Rasmussen, W. Rison, W. D. Rust, and R. J. Thomas (2004), The severe thunderstorm electrification and precipitation study, *Bull. Am. Meteorol. Soc.*, *85*(8), 1107–1125, doi:10.1175/BAMS-85-8-1107.
- Larsson, A. (1998), The effect of a large series resistance on the streamer-to-spark transition in dry air, *J. Phys. D: Appl. Phys.*, *31*(9), 1100.
- Lehtinen, N. G., T. F. Bell, and U. S. Inan (1999), Monte Carlo simulation of runaway MeV electron breakdown with application to red sprites and terrestrial gamma ray flashes, *J. Geophys. Res.*, *104*(A11), 24,699–24,712, doi:10.1029/1999JA900335.
- Lieberman, M. A., and A. J. Lichtenberg (2005), *Principles of Plasma Discharges and Materials Processing*, 2nd ed., John Wiley & Sons, Inc., New York, NY.
- Liu, N. Y., and V. P. Pasko (2004), Effects of photoionization on propagation and branching of positive and negative streamers in sprites, *J. Geophys. Res.*, *109*, A04301, doi:10.1029/2003JA010064.
- Liu, N. Y., and V. P. Pasko (2006), Effects of photoionization on similarity properties of streamers at various pressures in air, *J. Phys. D: Appl. Phys.*, *39*, 327–334, doi:10.1088/0022-3727/39/2/013.

- Liu, N. Y., V. P. Pasko, K. Adams, H. C. Stenbaek-Nielsen, and M. G. McHarg (2009), Comparison of acceleration, expansion, and brightness of sprite streamers obtained from modeling and high-speed video observations, *J. Geophys. Res.*, *114*, A00E03, doi:10.1029/2008JA013720.
- Liu, X. S., and P. R. Krehbiel (1985), The initial streamer of intracloud lightning flashes, *J. Geophys. Res.*, *90*(ND4), 6211–6218.
- Lowke, J. J. (1992), Theory of electrical breakdown in air—The role of metastable oxygen molecules, *J. Phys. D: Appl. Phys.*, *25*, 202–210.
- Lyons, W. A., CCM, T. E. Nelson, R. A. Armstrong, V. P. Pasko, and M. A. Stanley (2003), Upward electrical discharges from thunderstorm tops, *Bull. Am. Meteorol. Soc.*, *84*(4), 445–454, doi:10.1175/BAMS-84-4-445.
- MacGorman, D. R., and W. D. Rust (1998), *The Electrical Nature of Storms*, 432 pp., Oxford Univ. Press, New York, NY.
- MacGorman, D. R., J. M. Straka, and C. L. Ziegler (2001), A lightning parameterization for numerical cloud models, *J. Appl. Meteor.*, *40*(3), 459–478.
- Mansell, E. R., D. R. MacGorman, C. L. Ziegler, and J. M. Straka (2002), Simulated three-dimensional branched lightning in a numerical thunderstorm model, *J. Geophys. Res.*, *107*(D9), 4075, doi:10.1029/2000JD000244.
- Mansell, E. R., D. R. MacGorman, C. L. Ziegler, and J. M. Straka (2005), Charge structure and lightning sensitivity in a simulated multicell thunderstorm, *J. Geophys. Res.*, *110*, D12101, doi:10.1029/2004JD005287.
- Marode, E. (1983), The glow-to-arc transition, in *Electrical Breakdown and Discharges in gases: Macroscopic Processes and Discharges, Series B—Physics*, vol. B, edited by L. H. Luessen and E. E. Kunhardt, pp. 119–166, Plenum Press, New York, NY, proc. of Adv. Sci. Inst. 1981, Les Arcs, France.
- Marode, E., F. Bastien, and M. Bakker (1979), Model of the streamer-induced spark formation based on neutral dynamics, *J. Atmos. Terr. Phys.*, *50*(1), 140–146.
- Marshall, T. C., and W. D. Rust (1993), Two types of vertical electrical structures in stratiform precipitation regions of mesoscale convective systems, *Bull. Am. Meteorol. Soc.*, *74*(11), 2159–2170.
- Marshall, T. C., and M. Stolzenburg (1998), Estimates of cloud charge densities in thunderstorms, *J. Geophys. Res.*, *103*(D16), 19,769–19,775, doi:10.1029/98JD01674.

- Marshall, T. C., and M. Stolzenburg (2001), Voltages inside and just above thunderstorms, *J. Geophys. Res.*, *106*(D5), 4757–4768.
- Marshall, T. C., M. P. McCarthy, and W. D. Rust (1995), Electric field magnitudes and lightning initiation in thunderstorms, *J. Geophys. Res.*, *100*(D4), 7097–7104, doi:10.1029/95JD00020.
- Marshall, T. C., M. Stolzenburg, W. D. Rust, E. R. Williams, and R. Boldi (2001), Positive charge in the stratiform cloud of a mesoscale convective system, *J. Geophys. Res.*, *106*(D1), 1157–1164, doi:10.1029/2000JD900625.
- Marshall, T. C., M. Stolzenburg, C. R. Maggio, L. M. Coleman, P. R. Krehbiel, T. Hamlin, R. J. Thomas, and W. Rison (2005), Observed electric fields associated with lightning initiation, *Geophys. Res. Lett.*, *32*(3), L03813, doi:10.1029/2004GL021802.
- Mathews, J. D., M. A. Stanley, V. P. Pasko, T. G. Wood, U. S. Inan, M. J. Heavner, and S. A. Cummer (2002), Electromagnetic signatures of the Puerto Rico blue jet and its parent thunderstorms, *Eos Trans. AGU*, *83*(47), Fall Meet. Suppl., Abstract A62D-02.
- Mazur, V., and L. H. Ruhnke (1998), Model of electric charges in thunderstorms and associated lightning, *J. Geophys. Res.*, *103*(D18), 23,299–23,308.
- McCarthy, M. P., and G. K. Parks (1992), On the modulation of X-ray fluxes in thunderstorms, *J. Geophys. Res.*, *97*(D5), 5857–5864.
- Mishin, E. V., and G. M. Milikh (2008), Blue jets: Upward lightning, *Space Sci. Rev.*, *137*(1–4), 473–488, doi:10.1007/s11214-008-9346-z.
- Mnatsakanyan, A. K., and G. V. Naidis (1985), The vibrational-energy balance in a discharge in air, *High Temp.*, *23*(4), 506–513.
- Mnatsakanyan, A. K., and G. V. Naidis (1991), Charged particle production and loss processes in nitrogen–oxygen plasmas, in *Reviews of Plasma Chemistry*, vol. 1, edited by B. M. Smirnov, Consultants Bureau, New York.
- Morrow, R., and J. J. Lowke (1997), Streamer propagation in air, *J. Phys. D: Appl. Phys.*, *30*, 614–627.
- Naidis, G. V. (1999), Simulation of streamer-to-spark transition in short non-uniform air gaps, *J. Phys. D: Appl. Phys.*, *32*, 2649–2654.
- Naidis, G. V. (2005), Conditions for inception of positive corona discharges in air, *J. Phys. D: Appl. Phys.*, *38*, 2211–2214.

- Naidis, G. V. (2007), Simulation of convection-stabilized low-current glow and arc discharges in atmospheric-pressure air, *Plasma Sources Sci. Technol.*, *16*(2), 297–303, doi:10.1088/0963-0252/16/2/012.
- Naidis, G. V. (2008), Simulation of spark discharges in high-pressure air sustained by repetitive high-voltage nanosecond pulses, *J. Phys. D: Appl. Phys.*, *41*(23), doi:10.1088/0022-3727/41/23/234017.
- Niemeyer, L., and H. J. Wiesmann (1987), Modeling of leader branching in electronegative gases, in *Gaseous Dielectrics V: Proceedings of the Fifth International Symposium on Gaseous Dielectrics*, pp. 134–139, Knoxville, TN, 3–7 May.
- Niemeyer, L., L. Pietrono, and H. J. Wiesmann (1984), Fractal dimension of dielectric breakdown, *Phys. Rev. Lett.*, *52*(12), 1033–1036, doi:10.1103/PhysRevLett.52.1033.
- Niemeyer, L., L. Pietrono, and H. J. Wiesmann (1986), Fractal dimension of dielectric breakdown—Response, *Phys. Rev. Lett.*, *57*(5), 650, doi:10.1103/PhysRevLett.57.650.
- Niemeyer, L., L. Ullrich, and N. Wiegart (1989), The mechanism of leader breakdown in electronegative gases, *IEEE Trans. Dielectr. Electr. Insul.*, *24*(2), 309–324, doi:10.1109/14.90289.
- Niethammer, W. (1989), The SOR method on parallel computers, *Numer. Math.*, *56*, 247–254.
- Ogawa, T., and M. Brook (1964), Mechanism of intracloud lightning discharge, *J. Geophys. Res.*, *69*(24), 5141.
- Parissi, L., E. Odic, A. Goldman, M. Goldman, and J.-P. Borra (2000), Temperature effects on plasma chemical reactions—Application to VOC removal from flue gases by dielectric-barrier discharges, in *Electrical discharges for environmental purposes: Fundamentals and applications*, edited by E. M. van Veldhuizen, chap. 11, pp. 279–313, Nova Science Publishers, Huntington, NY.
- Pasko, V. P. (2003), Electric jets, *Nature*, *423*, 927–929.
- Pasko, V. P. (2006), Theoretical modeling of sprites and jets, in *Sprites, Elves and Intense Lightning Discharges*, *NATO Science Series II: Mathematics, Physics and Chemistry*, vol. 225, edited by M. Füllekrug, E. A. Mareev, and M. J. Rycroft, pp. 253–311, Springer, Heidelberg, Germany.
- Pasko, V. P. (2008), Blue jets and gigantic jets: Transient luminous events between thunderstorm tops and the lower ionosphere, *Plasma Phys. Control. Fusion*, *50*(12), 124,050, doi:10.1088/0741-3335/50/12/124050.

- Pasko, V. P. (2010), Recent advances in theory of transient luminous events, *J. Geophys. Res.*, *115*, doi:10.1029/2009JA014860.
- Pasko, V. P., and J. J. George (2002), Three-dimensional modeling of blue jets and blue starters, *J. Geophys. Res.*, *107*(A12), 1458, doi:10.1029/2002JA009473.
- Pasko, V. P., U. S. Inan, T. F. Bell, and Y. N. Taranenko (1997), Sprites produced by quasi-electrostatic heating and ionization in the lower ionosphere, *J. Geophys. Res.*, *102*(A3), 4529–4561, doi:10.1029/96JA03528.
- Pasko, V. P., U. S. Inan, and T. F. Bell (1998), Spatial structure of sprites, *Geophys. Res. Lett.*, *25*, 2123–2126.
- Pasko, V. P., U. S. Inan, and T. F. Bell (2000), Fractal structure of sprites, *Geophys. Res. Lett.*, *27*(4), 497–500, doi:10.1029/1999GL010749.
- Pasko, V. P., U. S. Inan, and T. F. Bell (2001), Mesosphere-troposphere coupling due to sprites, *Geophys. Res. Lett.*, *28*(19), 3821–3824, doi:10.1029/2001GL013222.
- Pasko, V. P., M. A. Stanley, J. D. Matthews, U. S. Inan, and T. G. Wood (2002), Electrical discharge from a thundercloud top to the lower ionosphere, *Nature*, *416*, 152–154, doi:10.1038/416152a.
- Petrov, N. I., and G. N. Petrova (1993), Physical mechanisms for intracloud lightning discharges, *Tech. Phys. Lett.*, *38*(4), 287–290.
- Petrov, N. I., and G. N. Petrova (1999), Physical mechanisms for the development of lightning discharges between a thundercloud and the ionosphere, *Tech. Phys. Lett.*, *44*, 472–475.
- Petrov, N. I., G. N. Petrova, and F. D'Alessandro (2003), Quantification of the probability of lightning strikes to structures using a fractal approach, *IEEE Trans. Dielectr. Electr. Insul.*, *10*(4), 641–654, doi:10.1109/TDEI.2003.1219649.
- Picard, R., U. Inan, V. Pasko, J. Winick, and P. Wintersteiner (1997), Infrared glow above thunderstorms?, *Geophys. Res. Lett.*, *24*(21), 2635–2638.
- Poeppel, K. (2005), A 3D lightning parameterization with branching and charge induction, Master's thesis, South Dakota School of Mines and Technology, Rapid City, SD.
- Popov, N. A. (2001), Investigation of the mechanism for rapid heating of nitrogen and air in gas discharges, *Plasma Phys. Rep.*, *27*(10), 886–896, doi:10.1134/1.1409722.

- Popov, N. A. (2002), Spatial structure of the branching streamer channel in a corona discharge, *Plasma Phys. Rep.*, *28*(7), 615–622, doi:10.1134/1.1494061.
- Popov, N. A. (2003), Formation and development of a leader channel in air, *Plasma Phys. Rep.*, *29*(8), 695–708, doi:10.1134/1.1601648.
- Popov, N. A. (2009), Study of the formation and propagation of a leader channel in air, *Plasma Phys. Rep.*, *35*(9), 785–793, doi:10.1134/S1063780X09090074.
- Potter, D. (1973), *Computational Physics*, 304 pp., John Wiley & Sons, Inc., New York, NY.
- Poulos, S. T., J. A. Rioussset, and V. P. Pasko (2008), Modeling of realistic thundercloud charge structure and application to simulation of lightning discharges, *NSF EE REU Penn State Annual Research Journal*, *6*, 61–78.
- Press, W. H., B. P. Flannery, S. A. Teukolsky, and W. T. Vetterling (1992), *Numerical Recipes in C: The Art of Scientific Computing*, 2nd ed., 1020 pp., Cambridge Univ. Press, New York, NY.
- Proctor, D. E. (1981), VHF radio pictures of cloud flashes, *J. Geophys. Res.*, *86*(NC5), 4041–4071.
- Proctor, D. E. (1983), Lightning and precipitation in a small multicellular thunderstorm, *J. Geophys. Res.*, *88*(NC9), 5421–5440.
- Proctor, D. E. (1997), Lightning flashes with high origins, *J. Geophys. Res.*, *102*(D2), 1693–1706, doi:10.1029/96JD02635.
- Pruppacher, H. R., and J. D. Klett (1997), *Microphysics of Clouds and Precipitation*, *Atmospheric and Oceanographic Sciences Library*, vol. 18, 2nd rev. and enl. ed., 954 pp., Kluwer Academic Publishers, Boston, MA.
- Raizer, Y. P. (1991), *Gas Discharge Physics*, 449 pp., Springer-Verlag, New York, NY.
- Raizer, Y. P., G. M. Milikh, and M. N. Shneider (2006), On the mechanism of blue jet formation and propagation, *Geophys. Res. Lett.*, *33*(23), L23801, doi:10.1029/2006GL027697.
- Raizer, Y. P., G. M. Milikh, and M. N. Shneider (2007), Leader–streamers nature of blue jets, *J. Atmos. Sol. Terr. Phys.*, *69*(8), 925–938, doi:10.1016/j.jastp.2007.02.007.
- Rakov, V. A., and M. A. Uman (2003), *Lightning: Physics and Effects*, 850 pp., Cambridge Univ. Press, Cambridge, U.K.; New York, NY.

- Riousset, J. A. (2006), Fractal modeling of lightning discharges, Master's thesis, The Pennsylvania State University, University Park, PA.
- Riousset, J. A. (2010), *Fractal Modeling of Lightning Discharges: A Thesis in Electrical Engineering Submitted for the Degree of Master of Science*, 132 pp., LAP Lambert Academic Publishing, Saarbrücken, Germany.
- Riousset, J. A., V. P. Pasko, P. R. Krehbiel, R. J. Thomas, and W. Rison (2006a), Electrical structure of thunderclouds leading to formation of blue jets and gigantic jets, *CEDAR Workshop Poster Sessions Booklet*, 2, COUP-05, Santa Fe, NM, June 22.
- Riousset, J. A., V. P. Pasko, P. R. Krehbiel, R. J. Thomas, and W. Rison (2006b), Three-dimensional fractal modeling of intracloud lightning discharge in a New Mexico thunderstorm and comparison with lightning mapping observations, *Eos Trans. AGU*, 87(52), Fall Meet. Suppl., Abstract AE21A-0996.
- Riousset, J. A., V. P. Pasko, P. R. Krehbiel, R. J. Thomas, and W. Rison (2007a), Three-dimensional fractal modeling of intracloud lightning discharge in a New Mexico thunderstorm and comparison with lightning mapping observations, *J. Geophys. Res.*, 112(D15203), doi:10.1029/2006JD007621.
- Riousset, J. A., V. P. Pasko, P. R. Krehbiel, R. J. Thomas, and W. Rison (2007b), Physical mechanisms of blue jets and gigantic jets, *CEDAR Workshop Poster Sessions Booklet*, 2, SPR-01, Santa Fe, NM, June 26.
- Riousset, J. A., V. P. Pasko, P. R. Krehbiel, W. Rison, and M. A. Stanley (2010a), Modeling of thundercloud screening charges: Implications for blue and gigantic jets, *J. Geophys. Res.*, 115, A00E10, doi:10.1029/2009JA014286.
- Riousset, J. A., V. P. Pasko, and A. Bourdon (2010b), Air heating associated with transient luminous events, *J. Geophys. Res.*, in review.
- Rison, W., R. J. Thomas, P. R. Krehbiel, T. Hamlin, and J. Harlin (1999), A GPS-based three-dimensional lightning mapping system: Initial observations in central New Mexico, *Geophys. Res. Lett.*, 26(23), 3573–3576, doi:10.1029/1999GL010856.
- Rison, W., P. R. Krehbiel, R. J. Thomas, and M. F. Brown (2009), Observations of precursor breakdown prior to intracloud lightning discharges, *Eos Trans. AGU*, 90(52), Fall Meet. Suppl., Abstract AE32A-02.
- Roussel-Dupré, R. A., A. V. Gurevich, T. Tunnel, and G. M. Milikh (1994), Kinetic theory of runaway breakdown, *Phys. Rev. E*, 49(3), 2257–2271, doi:10.1103/PhysRevE.49.2257.

- Rust, W. D., and T. C. Marshall (1996), On abandoning the thunderstorm tripole-charge paradigm, *J. Geophys. Res.*, *101*(D18), 23,499–23,504.
- Rust, W. D., D. R. MacGorman, E. C. Bruning, S. A. Weiss, P. R. Krehbiel, R. J. Thomas, W. Rison, T. Hamlin, and J. Harlin (2005), Inverted-polarity electrical structures in thunderstorms in the severe thunderstorm electrification and precipitation study (STEPS), *Atmos. Res.*, *76*(1–4), 247–271.
- Rycroft, M. J., A. Odzimek, N. F. Arnold, M. Füllekrug, A. Kulak, and T. Neubert (2007), New model simulations of the global atmospheric electric circuit driven by thunderstorms and electrified shower clouds: The roles of lightning and sprites, *J. Atmos. Sol. Terr. Phys.*, *69*(17–18), 2485–2509, doi:10.1016/j.jastp.2007.09.004.
- Satpathy, S. (1986), Fractal dimension of dielectric breakdown—Comment, *Phys. Rev. Lett.*, *57*(5), 649, doi:10.1103/PhysRevLett.57.649.
- Sentman, D. D., and E. M. Wescott (1995), Red sprites and blue jets: Thunderstorm-excited optical emissions in the stratosphere, mesosphere, and ionosphere, *Phys. Plasmas*, *2*(6), 2514–2522, doi:10.1063/1.871213.
- Sentman, D. D., H. C. Stenbaek-Nielsen, M. G. McHarg, and J. S. Morrill (2008a), Plasma chemistry of sprite streamers, *J. Geophys. Res.*, *113*(D11), doi:10.1029/2007JD008941.
- Sentman, D. D., H. C. Stenbaek-Nielsen, M. G. McHarg, and J. S. Morrill (2008b), Correction to “Plasma chemistry of sprite streamers” (vol. 113, art. D11112, 2008), *J. Geophys. Res.*, *113*(D14), doi:10.1029/2008JD010634.
- Shao, X. M., and P. R. Krehbiel (1996), The spatial and temporal development of intracloud lightning, *J. Geophys. Res.*, *101*(D21), 26,641–26,668.
- Shao, X. M., M. Stanley, P. R. Krehbiel, W. Rison, G. Gray, and V. Mazur (1996), Results of observations with the New Mexico Tech lightning interferometer, in *Proc. Xth Intn’l. Conf. Atmos. Elec., Osaka, Japan*, pp. 317–320.
- Shepherd, T. R., W. D. Rust, and T. C. Marshall (1996), Electric fields and charges near 0 degrees C in stratiform clouds, *Mon. Wea. Rev.*, *124*(5), 919–938.
- Stenbaek-Nielsen, H. C., M. G. McHarg, T. Kammae, and D. D. Sentman (2007), Observed emission rates in sprite streamer heads, *Geophys. Res. Lett.*, *34*, L11105, doi:10.1029/2007GL029881.
- Stolzenburg, M., W. D. Rust, and T. C. Marshall (1998a), Electrical structure in thunderstorm convective regions—1. Mesoscale convective systems, *J. Geophys. Res.*, *103*(D12), 14,059–14,078, doi:10.1029/97JD03546.

- Stolzenburg, M., W. D. Rust, and T. C. Marshall (1998b), Electrical structure in thunderstorm convective regions-2. Isolated storms, *J. Geophys. Res.*, *103*(D12), 14,079–14,096, doi:10.1029/97JD03547.
- Stolzenburg, M., W. D. Rust, and T. C. Marshall (1998c), Electrical structure in thunderstorm convective regions-3. Synthesis, *J. Geophys. Res.*, *103*(D12), 14,097–14,108, doi:10.1029/97JD03545.
- Stolzenburg, M., T. C. Marshall, W. D. Rust, E. Bruning, D. R. MacGorman, and T. Hamlin (2007), Electric field values observed near lightning flash initiations, *Geophys. Res. Lett.*, *34*(4), L04804, doi:10.1029/2006GL028777.
- Su, H. T., R. R. Hsu, A. B. Chen, Y. C. Wang, W. S. Hsiao, W. C. Lai, L. C. Lee, M. Sato, and H. Fukunishi (2003), Gigantic jets between a thundercloud and the ionosphere, *Nature*, *423*, 974–976, doi:10.1038/nature01759.
- Sukhorukov, A. I., and P. Stubbe (1998), Problems of blue jet theories, *J. Atmos. Sol. Terr. Phys.*, *23*(13), 7–9, doi:10.1016/S1364-6826(98)00021-2.
- Tardiveau, P., E. Marode, A. Agneray, and M. Cheaib (2001), Pressure effects on the development of an electric discharge in non-uniform fields, *J. Phys. D: Appl. Phys.*, *34*, 1690–1696.
- Taylor, R. L. (1974), Energy transfer processes in the stratosphere, *Can. J. Chem.*, *52*, 1436.
- Thomas, R. J., P. R. Krehbiel, W. Rison, T. Hamlin, J. Harlin, and D. Shown (2001), Observations of VHF source powers radiated by lightning, *Geophys. Res. Lett.*, *28*(1), 143–146.
- Thomas, R. J., S. Behnke, T. Hamlin, J. Harlin, P. Krehbiel, and W. Rison (2002), New Mexico thunderstorms observed by the lightning mapping array, an overview of one season, *Eos Trans. AGU*, *83*(47), Fall Meet. Suppl., Abstract A71B-0097.
- Uman, M. A. (1969), *Lightning*, 264 pp., McGraw-Hill, New York, NY.
- Uman, M. A. (1984), *Lightning*, reprint ed., 298 pp., Dover, Mineola, NY, originally published: New York: McGraw-Hill, 1969.
- Uman, M. A. (1987), *The Lightning Discharge, International geophysics series*, vol. 39, 377 pp., Academic Press, Orlando, FL.
- Uman, M. A. (2001), *The Lightning Discharge*, unabridged ed., 377 pp., Dover, Mineola, NY.
- Vallance-Jones, A. V. (1974), *Aurora*, D. Reidel Publishing Co., Norwell, MA.

- van der Velde, O. A., W. A. Lyons, T. E. Nelson, S. A. Cummer, J. Li, and J. Bunnell (2007), Analysis of the first gigantic jet recorded over continental North America, *J. Geophys. Res.*, *112*, D20104, doi:10.1029/2007JD008575.
- van der Velde, O. A., J. Bór, J. Li, S. A. Cummer, E. Arnone, F. Zanotti, M. Füllekrug, C. Haldoupis, S. Naitamor, and T. Farges (2010), Multi-instrumental observations of a positive gigantic jet produced by a winter thunderstorm in Europe, *J. Geophys. Res.*, doi:10.1029/2007JD008575, in review.
- Vidal, F., I. Gallimberti, F. A. M. Rizk, T. W. Johnston, A. Bondiou-Clergerie, D. Comtois, J. C. Kieffer, B. La Fontaine, H. P. Mercure, and H. Pépin (2002), Modeling of the air plasma near the tip of the positive leader, *IEEE Trans. Plasma Sci.*, *30*(3), 1339–1349, doi:10.1109/TPS.2002.801538.
- Vonnegut, B. (1983), Deductions concerning accumulations of electrified particles in thunderclouds based on electric field changes associated with lightning, *J. Geophys. Res.*, *88*(NC6), 3911–3912.
- Wallace, J. M., and P. V. Hobbs (1973), *Atmospheric Science, An Introductory Survey, International Geophysics*, vol. 92, 2nd ed., 504 pp., Academic Press, New York, NY.
- Walter, C. W., P. C. Cosby, and H. Helm (1994), Predissociation quantum yields of singlet nitrogen, *Phys. Rev. A*, *50*, 2930–2936.
- Wescott, E. M., D. Sentman, D. Osborne, D. Hampton, and M. Heavner (1995), Preliminary results from the Sprites94 aircraft campaign: 2. Blue jets, *Geophys. Res. Lett.*, *22*(10), 1209–1212.
- Wescott, E. M., D. D. Sentman, M. J. Heavner, D. L. Hampton, D. Osborne, and O. H. Vaughan Jr. (1996), Blue starters: Brief upward discharges from an intense Arkansas thunderstorms, *Geophys. Res. Lett.*, *23*(16), 2153–2156, doi: 10.1029/96GL01969.
- Wescott, E. M., D. D. Sentman, M. J. Heavner, D. L. Hampton, and O. H. Vaughan Jr. (1998), Blue jets: Their relationship to lightning and very large hailfall, and their physical mechanisms for their production, *J. Atmos. Sol. Terr. Phys.*, *60*, 713–724.
- Wescott, E. M., D. Sentman, H. C. Stenbaek-Nielsen, P. Huet, M. J. Heavner, and D. R. Moudry (2001), New evidence for the brightness and ionization of blue jets and blue starters, *J. Geophys. Res.*, *106*(A10), 21,549–21,554, doi: 10.1029/2000JA000429.

- Wiesmann, H. J., and H. R. Zeller (1986), A fractal model of dielectric breakdown and prebreakdown in solid dielectrics, *J. Appl. Phys.*, *60*(5), 1770–1773, doi:10.1063/1.337219.
- Williams, E., R. Boldi, J. Bór, G. Sători, C. Price, E. Greenburg, Y. Takahashi, K. Yamamoto, Y. Matsudo, Y. Hobara, M. Hayakawa, T. Chronis, E. Anagnostou, D. M. Smith, and L. Lopez (2006), Lightning flashes conducive to the production and escape of gamma radiation to space, *J. Geophys. Res.*, *111*, D16209, doi:10.1029/2005JD006447.
- Williams, E. R. (1989), The tripolar structure of thunderstorms, *J. Geophys. Res.*, *94*(D11), 13,151–13,167.
- Williams, E. R., C. M. Cooke, and K. A. Wright (1985), Electrical discharge propagation in and around space charge clouds, *J. Geophys. Res.*, *90*(D4), 6059–6070.
- Wilson, C. T. R. (1921), Investigations on lightning discharges and on the electric field of thunderstorms, *Philos. Trans. R. Soc. London, Ser. A*, *221*, 73–115.
- Wilson, C. T. R. (1956), A theory of thundercloud electricity, *Proc. R. Soc. London, Ser. A*, *236*, 297.
- Winn, W. P., and L. G. Byerley (1975), Electric field growth in thunderclouds, *Q. J. R. Met. Soc.*, *101*, 979–994.
- Zahn, M. (1987), *Electromagnetic Field Theory: A Problem Solving Approach*, reprint ed., 723 pp., R.F. Krieger, Malabar, FL, reprint. Originally published: New York: Wiley, 1979.
- Zhang, C., H. Lan, Y. Pe, and B. D. Estrade (2005), Parallel SOR iterative algorithms and performance evaluation on a Linux cluster, in *Proceedings of the International Conference on Parallel and Distributed Processing Techniques and Applications, PDPTA 2005*, vol. 1, edited by H. R. Arabnia, pp. 263–269, CSREA Press, Las Vegas, NV, June 27–30.
- Zhao, X. M., J. C. Diels, C. Y. Wang, and J. M. Elizondo (1995), Femtosecond ultraviolet laser pulse induced lightning discharge in gases, *IEEE J. Quantum Electron.*, *31*, 599–612.
- Ziegler, C. L., and D. R. MacGorman (1994), Observed lightning morphology relative to modeled space charge and electric field distributions in a tornadic storm, *J. Appl. Meteor.*, *51*(6), 833–851.

Vita

Jérémy A. Rioussset

Jérémy Rioussset received his high school ‘Baccalauréat’ with Honors from Lycée A. Daudet, Tarascon, France. He graduated from a double degree program in August and October 2006. He received the ‘Diplôme d’ingénieur de l’École Centrale de Lyon’ (equivalent M.Eng. Engineering Sciences) from the École Centrale de Lyon, Écully, France and the M.S. in Electrical Engineering from Penn State University, University Park, PA. He recently finished in August 2008 a Ph.D. in Electrical Engineering at Penn State University.

Jérémy received second prize at the CEDAR poster competition in 2006 and ranked first in the same competition in 2007. He also received an honorable mention for his work presented at the American Geophysical Union Fall Meeting in 2006 and 2008 in San Francisco and the second prize at the 2009 NRSM-URSI student paper competition. Jérémy was awarded the A. J. Ferraro Graduate Research Awards in recognition of excellence in M.S. (2007) and Ph.D. (2009) research in the areas of remote sensing, communications and space sciences.

Jérémy has been a member of the American Geophysical Union since December 2005 and a member of Tau Beta Pi since December 2008.